WAVE AND CURRENT INDUCED MOTIONS ON TLP-TAD MULTIBODY SYSTEM

Miguel Angel Moya Ramirez

Tese de Doutorado apresentada ao Programa de Pós-graduação em Engenharia Oceânica, COPPE, da Universidade Federal do Rio de Janeiro, como parte dos requisitos necessários à obtenção do título de Doutor em Engenharia Oceânica.

Orientador: Antonio Carlos Fernandes

Rio de Janeiro
Maio de 2017

WAVE AND CURRENT INDUCED MOTIONS ON
TLP-TAD MULTIBODY SYSTEM

Miguel Angel Moya Ramirez

TESE SUBMETIDA AO CORPO DOCENTE DO INSTITUTO ALBERTO LUIZ COIMBRA DE PÓS-GRADUAÇÃO E PESQUISA DE ENGENHARIA (COPPE) DA UNIVERSIDADE FEDERAL DO RIO DE JANEIRO COMO PARTE DOS REQUISITOS NECESSÁRIOS PARA A OBTENÇÃO DO GRAU DE DOUTOR EM CIÊNCIAS EM ENGENHARIA OCEÂNICA.

Examinada por:

_____
Prof. Antonio Carlos Fernandes, Ph.D.

_____
Prof. Carlos Antonio Levi da Conceição, Ph.D.

_____
Prof. Juan Bautista Villa Wanderley, Ph.D.

_____
Prof. Gilberto Bruno Ellwanger, D.Sc.

_____
Eng. Allan Carré de Oliveira, D.Sc.

_____
Prof. André Luís Condino Fujarra, D.Sc.

RIO DE JANEIRO, RJ – BRASIL
MAIO DE 2017

Ramirez, Miguel Angel Moya

Wave and Current Induced Motions on TLP-TAD Multibody System/ Miguel Angel Moya Ramirez. – Rio de Janeiro: UFRJ/COPPE, 2017.

IX, 240 p.: il.; 29,7 cm.

Orientador: Antonio Carlos Fernandes

Tese (doutorado) – UFRJ/ COPPE/ Programa de Engenharia Oceânica, 2017.

Referências Bibliográficas: p. 223-230.

1. Dynamics of Multi-body Systems. 2. Nonlinear Wave Loads. 3. Vortex Induced Motions. 4. VIM Mitigation Devices. I. Fernandes, Antonio Carlos. II. Universidade Federal do Rio de Janeiro, COPPE, Programa de Engenharia Oceânica. III. Título.

Unaquaeque enim arbor de fructu suo cognoscitur

Luca, 6, 44

Acknowledgments

I offer my gratitude to God.

I express my respect and gratitude to Professor Antonio Carlos Fernandes, who is more than a supervisor and has been both a friend and a father.

I very much appreciate the time and effort of committee members Dr. Carlos Levi, Dr. Juan Wanderley, Dr. Gilberto Ellwanger, Dr. Allan Carré and Dr. André Fujarra.

I am very grateful for the guidance, and encouragement of my family, my mother, father, brothers, and sister.

I express my deepest gratitude to BrasFELS, KOMtech, Keppel FELS, FloaTEC and $F(K)^N$ (FloaTEC, Keppel and NUS cooperative laboratory at LOC) for the very enriching experiences and growth opportunities. Special thanks to Mr. Aziz Merchant, Mr. Anis Hussain, Mr. Ankit Choudhary and Mr. Too Lye for their kindness, support, and cooperation in the development of this thesis.

I gratefully acknowledge the professors and the entire staff of the Ocean Engineering Program of the Federal University of Rio de Janeiro.

I am especially appreciative of Dr. Miguel Celis and Dr. Joel Sena for their friendship and vast insight and knowledge of offshore structures and hydrodynamics. The outstanding crew of the Laboratory of Waves and Currents (LOC/COPPE-UFRJ) kindly assisted the experimental test campaigns. I gratefully acknowledge Luis Antonio Ferreira and Igor Santos Carvalho.

To my dear friends Caterina, Laura, Jose, Dani, Mendo, Jota, Isabel, Anita, Macarena, Soledad, Bruna, Mari, Diego, Rafael and Ana Paula. Conmigo vais, mi corazón os lleva.

I extend my gratitude to my friends and colleagues at the Laboratory of Waves and Currents of the Federal University of Rio de Janeiro.

Resumo da Tese apresentada à COPPE/UFRJ como parte dos requisitos necessários para a obtenção do grau de Doutor em Ciências (D.Sc.)

MOVIMENTOS INDUZIDOS POR ONDAS E CORRENTES NO SISTEMA MULTICORPO TLP-TAD

Miguel Angel Moya Ramirez

Maio/2017

Orientador: Antonio Carlos Fernandes
Programa: Engenharia Oceânica

Este trabalho apresenta uma extensa análise experimental e numérica dos movimentos induzidos pelas ondas e correntes no sistema multicorpo TLP-TAD.

Estudaram-se as forças de primeira e segunda ordem devido às ondas atuantes no sistema com auxílio da teoria potencial. O acoplamento hidrodinâmico entre os corpos é analisado tanto no domínio do tempo quanto no domínio da frequência.

Avaliou-se experimentalmente o efeito de sombra nas forças médias da corrente sobre os corpos. Além disso, examinaram-se numericamente os efeitos de escala e bloqueio nos coeficientes de força das correntes atuantes sobre o sistema.

Por outro lado, estudaram-se, mediante técnicas experimentais em escala reduzida, os movimentos induzidos pela corrente VIM e Galloping no sistema TLP-TAD, analisando as diferenças no comportamento das plataformas entre os casos sozinho, multicorpo desconectado e multicorpo conectado com amarras.

Finalmente, testaram-se vários dispositivos com o objetivo de mitigar o VIM da TLP analisando as influências do amortecimento, da frequência natural e das forças de arrasto.

Abstract of Thesis presented to COPPE/UFRJ as a partial fulfillment of the requirements for the degree of Doctor of Science (D.Sc.)

WAVE AND CURRENT INDUCED MOTIONS ON
TLP-TAD MULTIBODY SYSTEM

Miguel Angel Moya Ramirez

May/2017

Advisor: Antonio Carlos Fernandes
Department: Ocean Engineering

This work presents an extensive experimental and numerical analysis with the aim of investigating wave and current induced motions of a tension leg platform – tender assisted drilling multibody system.

The study includes an analysis of first and second-order wave loads on the system using the potential wave theory. It also analyzes the wave coupling effects by using frequency and time domain approaches.

The analysis of current loads includes experimental tests to quantify shielding or interaction effects and numerical simulations using Computational Fluid Dynamics (CFD) to evaluate scale and blockage effects in the multi-body system considering several current velocities and angles of attack.

Furthermore, this thesis includes an experimental study of vortex induced motions (VIM) and Galloping instabilities of the multi-body system when subject to currents. The motions developed by the TLP and the TAD in single-body cases are compared to multi-body cases when the floaters are disconnected and connected by a hawser system.

Finally, with the aim of reducing the VIM response of the TLP, the work includes an analysis of several VIM mitigation devices investigating the influences of damping, natural frequencies, average current loads and the amplitude of the motions of the TLP.

CONTENTS

CHAPTER I. INTRODUCTION

This work presents experimental and numerical analyses of the dynamic behavior of a Tension Leg Platform (TLP) – Tender Assisted Drilling (TAD) multi-body system subject to waves and currents. This chapter contents the motivation, aim, and scope of the thesis below. Furthermore, it includes a survey of relevant previous works.

1.1 MOTIVATION

The heart of the success of the oil and gas industry lies in its continual search for innovative solutions and advanced technology. The constant evolution of more efficient and economical techniques enables us to develop safer and more profitable projects.

In this context, the use of Tender Assisted Drilling (TAD) units is one of the most promising developments. The use of TADs during the drilling phase of a field development, in support of the main unit (Spar or TLP) provides several advantages over a traditional production platform with a fully functional drilling unit [13], [18], [54], and [85]. The most notable advantages are summarized below.

- TADs decrease space requirements on the main production platform deck. Consequently, operators can significantly reduce the operating weight of the rig, which is particularly relevant for deep water installations.
- TADs provide additional accommodation for the crew, power source, crane facilities, pumping, and helideck.
- TADs increase the storage capacity for equipment and material operations.
- TADs improve safety because administrators can transfer the crew to this unit in hazardous situations.
- TADs are versatile, and operators can use the same unit in different projects.

Tension Leg Platform (TLP) is expected to be the candidate that can benefit most from the TAD concept since it is more sensitive to the topside weight [10]. Additionally, the small

vertical motions of a TLP make the connection with the TAD easier. Finally, the probability of interference between TAD mooring lines and TLP tendons is relatively low [96].

Since the semi-submersible Seahawk was converted from a mobile offshore drilling unit (MODU) to TAD in 1992, the first in the world, researchers have faced several challenges in the development of this concept. Therefore, the complex scenario of two floaters moored in close proximity requires an extensive and careful hydrodynamic analysis to guarantee the successful execution of the TLP-TAD system.

Researchers have conducted several studies focusing on the hydrodynamic interactions of two floating structures positioned close to each other and subject to waves, for instance, [14], [17], [91], and [97]. The results of these studies show that coupling effects can induce larger motions in the floaters of the multi-body system. However, few works [92] focus on the wave hydrodynamic interactions of a TLP – TAD system.

Additionally, scholars have recognized the importance of second-order loads in the design of mooring systems for offshore structures due to pioneering works such as [27], [65], [72] and [74]. However, few studies have assessed the behavior of the second-order loads in multi-body systems; none were found focused on the TLP-TAD system. Consequently, it is not clear how the presence of a second body modifies the second-order loads and affects the dynamic behavior of the floaters.

Furthermore, few works have assessed the average current loads on multi-body systems. Koop [48] analyzed two vessels in a side by side arrangement; the results presented showed significant shielding or interaction effects. In some situations, the current loads on the vessel in the downstream position decrease significantly and can even change their direction. Furthermore, the scale effects due to the differences in flow regimes between model-scale and full-scale predictions have generated increasing interest in the last few years.

Finally, there are several studies of flow induced motions in offshore floating structures such as Spars, TLPs, and Semi-submersibles, including [51], [93], [95], and [98]. The results have shown that those floaters are susceptible to different types of flow-induced vibrations such as Vortex Induced Motions (VIM) and Galloping instabilities. However, it is not clear how such complex phenomena affect a multi-body system.

Because of the lack of experimental and numerical analysis focused on the TLP-TAD multi-body system, the coupling effects in waves and currents are unknown.

1.2 AIM AND SCOPE

Based on the challenges described prior, the aim of this thesis is to investigate the hydrodynamic coupling effects due to current and waves in a TLP-TAD multi-body system with extensive numerical and experimental analyses. The results of this work are intended to pave the way for future optimization studies and provide a better understanding of how hydrodynamic coupling effects influence the dynamic behavior of TLP-TAD systems.

Eight chapters compose this thesis.

In Chapter 1, as an introduction, the motivation, aim, and scope of the work are presented. Furthermore, a survey of relevant previous studies is performed.

In Chapter 2, a brief review of the theoretical background is presented.

In Chapter 3, the main characteristics of the case study are presented; including the geometrical and physical aspects of both floaters. Additionally, the values of stiffness and natural periods are estimated using analytical and numerical approaches.

In Chapter 4, first and second-order wave loads on the system are investigated numerically using the potential wave theory. Wave coupling effects are analyzed using frequency domain (FD) and time domain (TD) approaches. Comparisons of the dynamic behavior of the floaters between single-body and multi-body cases are presented throughout the chapter. Moreover, in the computation of the second-order loads, the importance of the free surface integral (FSI) is proved, the accuracy of the Newman approximation (NA) is tested, and the importance of second-order loads in time simulations is confirmed.

In Chapter 5, the average current forces and moments on the multi-body system are investigated experimentally and numerically. Shielding effects are investigated for several current velocities, angles of attack and different relative positions between the floaters. Furthermore, scale and blockage effects are studied for both floaters using Computational Fluid Dynamics.

In Chapter 6, the dynamic behavior of the TLP-TAD multi-body system, when subject to currents, is experimentally investigated. The motions developed for the TLP and TAD in the single-body cases are compared with the behavior of the floaters in multi-body arrangements considering two cases: disconnected and connected by a hawser system.

In Chapter 7, several devices are tested experimentally with the aim of reducing the motions induced in the TLP by currents. The influence of damping, natural frequencies, average current loads and dynamic motions are considered.

Finally, in Chapter 8, the main conclusions of this work are presented. Furthermore, suggestions for future work in this field are also provided.

1.3 LITERATURE REVIEW

The analysis of the dynamic behavior of the TLP-TAD multibody system involves several aspects of the offshore hydrodynamics. The most relevant studies concerning the topics covered in this research are included in the literature review presented below.

1.3.1 Wave Loads

Dallinga et. al. [22] discussed the methodologies for determining extreme value responses in the calculation of mooring lines and noted that second-order forces are not limited to the horizontal modes but also influence the vertical modes.

Hauteclocque et. al. [41] tested the accuracy of several approaches to determine the low-frequency loads on a vertical cylinder and a floating body in shallow water. They concluded that the accuracy of the techniques depends on the natural frequency of the body. Thus, in deep water, for natural frequencies below 0.005 Hz, the Newman approximation (NA) is satisfactory. In shallow water, the second-order loads present significant variations, even for natural frequencies below 0.005 Hz. Consequently, the Newman approximation (NA) may not be applicable in this case.

Maruo [53] proposed the far-field method to estimate the horizontal mean drift loads in a stationary body subject to regular waves. Momentum and energy conservation principle constitute the basis of this theory.

Ogilvie [68] developed analytic expressions to estimate the second-order forces based on potential theory in two-dimensions. Ogilvie also calculated the vertical forces of the first and second-order on a fixed cylinder.

Ogilvie [69] presented a review of the most important methodologies for the computation of second-order loads and noted that in vertical motions, the Newman

approximation (NA) is not valid because these modes normally have natural periods in the range of 30 to 60 seconds.

Pinkster [71] proposed the near-field approach to estimate the mean drift forces in six degrees of freedom using pressure integration. The near-field method presents better convergence than previous approaches and considers both horizontal and vertical loads on the bodies.

Pinkster [72] described the hydrodynamic theory of 3D bodies in waves and proposed expressions for the estimation of mean drift forces and slow drift forces in six degrees of freedom through pressure integration on the body surface. This approach divides the second-order force into five components corresponding to (1) the relative wave elevation (2) the first-order fluid velocities (the quadratic velocity term in Bernoulli's equation) (3) the product of the gradient of first-order pressure and body motions (4) the product of first-order angular movements of the body and inertia forces (5) and the contribution from the second-order potential. Additionally, Pinkster suggested an approximation to the second-order potential based on the hypothesis that the greatest contribution to the slow drift forces is the undisturbed incident wave potential; consequently, the radiation and diffraction second-order potentials are negligible.

1.3.2 Semi-Submersible Hydrodynamics

Ahilan and Harrison [1] investigated the influence of the current speed on slowly varying responses and found that these responses increase with decreasing current speeds. Moreover, they showed that the effect of slowly varying forces on mooring line tensions was approximately 15-20%. Although these forces are not significant in terms of the overall integrity of the mooring system, they magnify the dynamic offset of the unit and can be a critical issue in cases in which the semi-submersible unit is operating in close proximity to other installations.

Gueydon et. al. [38] analyzed second-order loads in a semi-submersible. They concluded that the difference-frequency term dominates the motion response because it excites the underdamped Surge mode at its natural period. Additionally, because semi-submersibles have natural periods for Pitch that are slightly higher than the

typical wave periods in random sea, vertical motions are susceptible to slow-drift loads as well.

Matos et. al. [56] presented a comparison between five approaches to the determination of second-order loads on semi-submersible platforms, focusing on vertical motions. They used experimental data to validate their numerical predictions. They concluded that the Newman approximation (NA) and methods that neglected the second-order potential effects on the second-order loads do not provide accurate estimations of the vertical modes. However, a solution that neglects the quadratic free surface forcing terms is suitable and efficient when computation time is critical. The white-noise approximation provides an excellent agreement for Heave and Pitch motions.

Takagi et. al. [86] presented a comparison between several computational algorithms to calculate the motions of semi-submersibles in waves. They showed that the majority of the programs provide accurate results for the calculations of Surge and Sway motions. Moreover, the predictions of these codes agree well with experimental tests. However, Heave, Roll, Pitch, and Yaw present significant differences. Programs based on the Morison equation present accurate results, implying that viscous effects are relevant for these modes.

1.3.3 Tension Leg Platform Hydrodynamics

Chen et. al. [15] analyzed second-order wave loads on TLPs using a numerical code combined with semi-analytical solutions. Their results show that there is no simple way to predict the second-order diffraction loads acting on TLPs. Additionally, they reported that the contribution of the second-order diffraction potential is not negligible and that approximations that use the results of simple bodies such as vertical cylinders may provide incorrect results. Furthermore, interactions between TLP columns lead to rapid variations of second-order loads with wave frequencies and wave headings.

Faltinsen et.al. [29] proposed a regular long wave method to compute the forces on a vertical cylinder caused by the third order potential. They based this method on the asymptotic expansion of a small parameter that they defined as a product of the

wavenumber and the column radius. However, this model is limited to small wavenumber values.

Gurley and Kareem [39] demonstrated that marine structures with natural frequencies in the range of 1 to 5 seconds might experience two types of resonant response: Springing responses due to sum-frequency wave effects and transient ringing responses. Additionally, they showed that variations in the draft and the vertical position of the center of rotation could mitigate the ringing. The addition of damping causes a quicker decay in ringing but does not prevent its occurrence.

Kim [45] numerically analyzed the sum-frequency wave loads on the stationary International Ship Structures Committee (ISSC) Tension-Leg Platform (TLP) and compared the numerical predictions for the full TLP with approximate estimation based on the results for a single column and four columns floater. Both estimation approaches neglected the effects of wave interaction between the four columns and the influence of the pontoons. Kim concluded that, despite a substantial savings of computing time, approximations of sum-frequency forces based on the numerical results for the single column or four columns could lead to a gross error for both regular and bi-chromatic incident waves. Therefore, the wave interaction between columns and the influence of pontoons are relevant for the computation of high-frequency excitations and motions of TLPs.

Molin et.al. [61] solved the third order diffraction theory to calculate the third order forces in a consistent way. Unfortunately, this model is limited to the triple frequency of third order forces in regular waves and is incompatible with the analysis in irregular sea states.

Morgan and Malaeb [64] analyzed the dynamic response of a TLP subject to waves and demonstrated that coupling between Surge and Heave motions (set-down) could introduce asymmetric terms into the stiffness matrix for symmetric platforms.

1.3.4 Multi-Body Hydrodynamics

Chen and Mahrenholtz [14] studied the dynamic responses of twin bodies with and without connections under the action of beam waves. Additionally, they studied the influence of stiffness, relative distance, and water depth and validated their results

with experimental tests. They found that when the distance between the bodies increases, the maximum response corresponds to longer waves. However, Sway motions increase significantly when the water depth decreases. Finally, they found a weak relation between the stiffness and body response.

Choi and Hong [17] analyzed numerically hydrodynamic interactions of two bodies in close proximity for three cases: two rectangular barges, two VLCC arranged in tandem and, two VLCCs arranged side by side. Their results showed weak coupling effects for Surge in head seas. In the case of rectangular barges, coupling effects for Roll and Sway were strong in beam seas. Additionally, they observed strong coupling effects in the mean drift forces for beam seas. For the tandem arrangement, they observed weak coupling effects. For side-by-side moored vessels, they found intensive interactions, particularly for Roll motions and mean drift forces.

Cruz [21] developed a numerical model to represent the dynamic behavior of a multibody system composed of a TLWP and a FPSO subjected to regular waves. The numerical predictions were validated with experimental tests. The numerical model provides a reasonable accuracy for some wave conditions, however, fails to represent the Yaw motion of the TLWP and the Sway-Yaw coupled motions of the multibody system.

Eatock-Taylor and Hung [26] performed a theoretical assessment of the mean wave drift forces on groups of vertical circular cylinders. They found that interaction effects between the cylinders have a strong influence on the total horizontal drift force. Moreover, at low frequencies, the drift force tends to equal the force on an isolated cylinder multiplied by the square of the number of cylinders in the group. In addition, they concluded that wave diffraction is primarily responsible for mean drift forces and that, in principle, hydrodynamic interactions can lead to substantial increases in drift forces.

Menezes [58] presented a review of the numerical methods applied to analyze multibody systems subject to waves, currents and wind using the frequency and time domain approaches. Additionally, numerically investigated the hydrodynamic and structural coupling effects in two multibody systems. Menezes concluded that a FPSO

could influence the hydrodynamic behavior of a TLP, even for large distances, in the order of 400 m.

Rivera [78] analyzed a multibody system composed of a TLWP coupled to a FPSO in regular waves. Previous experiments revelated, at a given range of wave periods. Rivera developed a mathematical model with nonlinearities in damping and restoring actions to represent the parametric resonance observed in the experiments, and concluded that the mooring lines of the TLP play a relevant role in the coupling of the Surge and Yaw motions. In addition, the coupled motions for Sway and Yaw is caused by the connection with the FPSO.

Teigen and Sclavounos [91] numerically investigated coupled slow drift motions of a floating system comprising a mini-TLP and a tender barge in close proximity for long-crest and short-crest seas. They considered second-order loads in time domain (TD) simulations. Their results show a slight sensitivity to the grid sizes used for the multi-body diffraction analysis. However, the presence of a barge significantly disturbs the exciting forces on the TLP. The researchers found a moderate reduction in the total Surge motion for short-crest waves relative to long-crest waves. However, Sway motions present the opposite behavior. Thus, the assumption of a short-crest sea is not conservative. Finally, Yaw motion of the TLP is relatively strong for a wave heading of 135°.

Xu et. al. [97] examined the motion responses and wave drift forces in the frequency domain (FD) on three barges positioned in a side-by-side arrangement. They used the middle-field and the near-field methods to calculate wave drift forces. Their results present reasonable agreement with experimental tests, and the middle-field method offers higher accuracy and better convergence. The near-field method overestimates the drift forces at most of the frequencies. Comparisons between multi-body and single-body cases show that hydrodynamic interactions are significant. In head sea conditions, the motions of the multi-body cases are larger than that of the single-body cases. The lateral drift forces are relevant in the multi-body cases but are nearly zero in the single-body cases. In beam sea conditions, each barge in the multi-body cases undergoes larger drift forces at low frequencies and smaller forces at high frequencies.

1.3.5 Current and Wind Loads

Croonenborghs et al. [20] performed a comparison of experimental and numerical methods for the assessment of wind and current loads on a semi-submersible. They compared results from two different wind tunnels, full-scale CFD, and towing tests. For current loads, they found reasonable agreement between the first wind tunnel and the towing tests. CFD calculations were in excellent agreement despite some discrepancies at the peak values. The second wind tunnel captured the same trends as the first one but fell systematically below the other results in absolute values. For wind loads, they found the same pattern for the two wind tunnels and CFD but observed only small differences at the peak values. They analyzed several factors to explain the differences, among which the more relevant are the transducers calibration, modeling of the uniform flow and modeling of the vertical wind profile.

Koop and Bereznitski [47] investigated the applicability, cost, and accuracy of CFD to obtain the current coefficients in semi-submersibles. Furthermore, they studied scale effects on the current coefficients using experimental data from wind tunnels and an offshore basin. The results show that CFD can provide reliable and accurate solutions. The model-scale force coefficients were not strongly dependent on the grid resolution. However, full-scale studies require deeper investigations into the effects of grid refinement. The full-scale values were approximately 15-20% lower than the model-scale values.

Silva [82] investigated the flow around a supply boat considering current, wind loads and ship resistance. Silva validated the numerical predictions with experimental data provided by a towing tank and a wind tunnel. CFD accurately predicted the winds loads. Small discrepancies were found for near-lateral winds in the longitudinal force and moment. For current loads, in general, excellent agreement was found, except for the range of near beam currents. A deep analysis demonstrated that it is worthwhile to apply transient simulations for near beam current conditions. In addition, the use of different turbulence models does not significant modify the force coefficient. Finally, for ship resistance, excellent agreement was achieved, and results demonstrate that the free-surface can introduces variations in the order of 8% of the resistance value.

Teigen et al. [90] conducted numerical investigations into the effects of current headings on TLPs. Their results showed shielding effects between the TLP columns, and they determined that the critical angle of the incident current occurs in the range of 20° to 30°.

Vaz et al. [94] studied current loads on a semi-submersible unit using experimental tests, semi-empirical models and numerical methods. The results of the experimental tests showed that downstream columns spontaneously moved forward into the wake of the upstream column. Additionally, downstream columns underwent larger fluctuations in the drag force than upstream columns. The semi-empirical results were in reasonable agreement with experimental data. However, the model requires the calibration of parameters such as turbulence intensity and roughness. For CFD, the authors used three different viscous-flow codes: CFX, STAR-CCM+, and ReFreSCo. All of the results underestimated the average current coefficient relative to the experimental results. The differences between the CFD results were smaller than the differences between the best CFD result and the average experimental result. Furthermore, the unsteady behavior of the drag coefficient is underestimated by all CFD computations.

1.3.6 Vortex Induced Motion

Gonçalves et al. [35] conducted experimental investigations on VIM with a semi-submersible platform with square columns, focusing on the effects of angle of attack and hull appendages. Their results show a typical bell VIV curve. However, the maximum response and the corresponding reduced velocity are dependent on the incident angle. Additionally, they showed hull appendages to have a decisive influence on the VIM response.

Gonçalves et al. [36] conducted an experimental investigation on VIM of a semi-submersible platform with square columns, focusing on the effects of surfaces waves, external damping, and draft conditions. This work is particularly notable because the analysis includes waves interacting with currents. Their results show that regular waves are associated with VIM suppression. In addition, current with irregular waves showed lower VIM responses than in the case without waves. Furthermore, external

damping reduced the VIM response considerably, and the low draft condition attenuated the VIM completely.

Gonçalves et al. [37] investigated the effects of column shapes on the VIM response of deep-draft semi-submersibles, considering square and circular column sections. They observed that the Sway responses were of the same order of magnitude regardless of the columns shape; however, the responses occurred at different incident angles. In contrast, Yaw motion of the circular column section was slightly higher than that of the square column section.

Leverette et al. [51] demonstrated that VIV could affect not only tendons and risers but also entire single column or multi-column TLPs. Subsequently, they analyzed the impact of the VIM response on the complete structural system using the Finite Element Method (FEM) and validated their results with full-scale data. Finally, they concluded that VIM could excite structural resonant modes within the platform with frequencies above those traditionally analyzed during the design stages.

Tan et al. [88] investigated the effects of hull appurtenances on a multi-column TLP designed for the Southeast Asian environment. Numerical and experimental results show that the response amplitudes for the hull without appurtenances are higher than those for the hull with appurtenances for the same reduced velocities. Moreover, the responses for the hull with appurtenances for most current headings increase with reduced speed, indicating galloping behavior in the TLP

Walls et al. [95] analyzed the dynamic behavior of multicolumn floaters in currents and demonstrated that the lower mass ratios of conventional TLPs cause a wider range of response that is slightly higher than that of deep draft semi-submersibles. Additionally, they show that the flow induced motions can involve a combination between VIM and galloping instabilities. Finally, they concluded that small differences in the floater geometry might vary the VIM responses and that the column length determines the order of magnitude of the motions. Thus, when they reduced the column height by 50% almost, they observed almost no flow induced motions.

CHAPTER II. THEORETICAL BACKGROUND

In this chapter, the theoretical background of this work is presented including a brief review of first and second-order wave potential theory, the linear and second-order loads on offshore structures and the Newman Approximation for low-frequency second-order loads. In additional, a brief review of the coupled analysis of a floating body with mooring lines is presented. Finally, select aspects of current induced motions by current are discussed.

2.1. HYDROSTATIC EQUILIBRIUM

Archimedes' principle establishes that the buoyant force on a body submerged in a fluid is equal to the displaced weight of the fluid in which the body moves. Thus, a free-floating ship in equilibrium as shown in Fig. 2.1 has a static equilibrium given by Eqn. (2.1).

$$\rho \cdot g \cdot \nabla_{SHIP} = M_{SHIP} \cdot g \tag{2.1}$$

where M_{SHIP} is the mass of the ship, g is the acceleration of gravity, ρ is the sea water density, and ∇_{SHIP} is the volume of the submerged part of the ship. In the case of moored floating structures, the mooring line forces on the body must be considered. Thus, for a TLP, Eqn. (2.1) becomes Eqn. (2.2).

$$\rho \cdot g \cdot \nabla_{TLP} = M_{TLP} \cdot g + \sum_{i=1}^{n} Tt_n \tag{2.2}$$

where ∇_{TLP} is the TLP displacement, M_{TLP} is the TLP mass, and Tt_n is the pre-tension load on the n-th tendon of the TLP. Similarly, for TAD Eqn. (2.3) is obtained.

$$\rho \cdot g \cdot \nabla_{TAD} = M_{TAD} \cdot g + \sum_{i=1}^{n} T_{V_n} \tag{2.3}$$

where ∇_{TAD} is the TAD displacement, M_{TAD} is the TAD mass and T_{V_n} is the vertical component of the pre-tension load T_{O_n} on the n-th mooring line of TAD.

In addition, the hydrostatic force acting on the small layer over the water-plane area gives the restoring forces and moment for small vertical displacement and inclinations [44].

Thereby, Eqns. (2.4) to (2.6) describe Heave, Roll, and Pitch restoring coefficients, respectively.

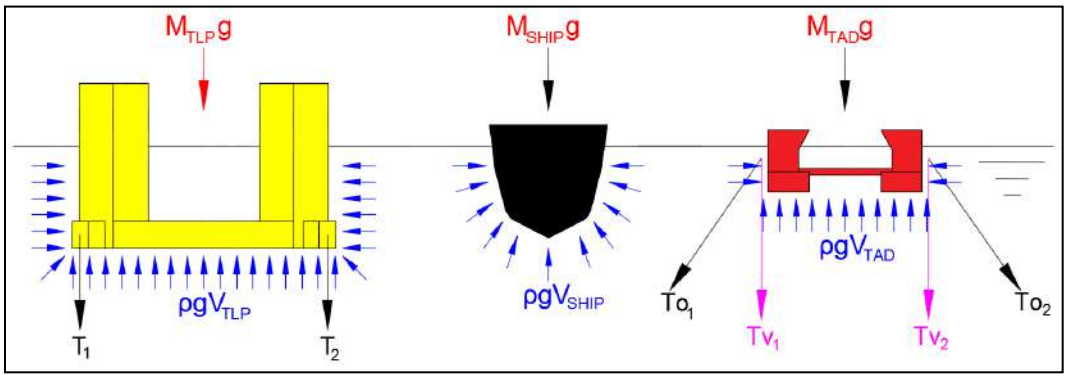

Figure 2.1 Archimedes' principle for floating bodies.

$$C_{33} = \rho g A_{WP} \tag{2.4}$$

$$C_{44} = \rho g \nabla \overline{KM}_T - gM\overline{KG} \tag{2.5}$$

$$C_{55} = \rho g \nabla \overline{KM}_L - gM\overline{KG} \tag{2.6}$$

where A_{WP} is the water plane, ∇ is the submersed volume, KG is the vertical position of the center of gravity, and M is the mass of the floater. Note that, C_{44} and C_{55} were modified from [28] to include the mooring line forces. $\overline{KM}_T$ and $\overline{KM}_L$ are hydrostatic characteristics of the floaters and are given by Eqns. (2.7) and (2.8)

$$\overline{KM}_T = \overline{KB} + \overline{BM}_T = \overline{KB} + \frac{I_T}{\nabla} \tag{2.7}$$

$$\overline{KM}_L = \overline{KB} + \overline{BM}_T = \overline{KB} + \frac{I_L}{\nabla} \tag{2.8}$$

where $\overline{KB}$ is the position of the center of buoyancy and I_T and I_L are the area moments of inertia of the water plane in relation to the x-axis and y-axis, respectively. As noted above, these restoring coefficients are valid only for infinitesimal motions. However, these expressions give reasonable approximations of dynamic motions [44].

The mooring systems also provide restoring forces in six degrees of freedom. These coefficients are computed analytically or numerically. [80] deduced in a simple manner the analytic expression for the stiffness of TLP tendons presented below. Note that, nonsymmetrical terms of the stiffness matrix were not included here.

$$K_{11} = K_{22} = \sum_{i=1}^{n} \frac{Tt_n}{L_n} \quad 2.9$$

$$K_{33} = \sum_{i=1}^{n} \frac{(EA)_n}{L_n} \Rightarrow K_{33}^G = K_{33} + C_{33} \quad 2.10$$

$$K_{44} = \sum_{i=1}^{n} \frac{(EA)_n}{L_n} y_n^2 \Rightarrow K_{44}^G = K_{44} + C_{44} \quad 2.11$$

$$K_{55} = \sum_{i=1}^{n} \frac{(EA)_n}{L_n} x_n^2 \Rightarrow K_{55}^G = K_{55} + C_{55} \quad 2.12$$

$$K_{66} = \sum_{i=1}^{n} \frac{Tt_n}{L_n} (x_n^2 + y_n^2) \quad 2.13$$

where L_n is the tendon length, $(EA)_n$ is the axial stiffness, and x_n and y_n are the coordinates of connection of the n-th tendon of the TLP. Note that, for Heave, Roll and Pitch, the global stiffness is obtained by a linear superposition of both hydrostatic and tendon stiffness.

2.2 WAVE BODY INTERACTION

2.2.1 Wave Theory

In the development of this theory, the fluid is considered incompressible and inviscid. Moreover, wave flow is assumed to be irrotational. Thus, a velocity potential Φ is used to describe the fluid velocity at each point; the velocity potential Φ must satisfy the Laplace equation (2.14) [28].

$$\nabla^2\Phi = \frac{\partial^2\Phi}{\partial x^2} + \frac{\partial^2\Phi}{\partial y^2} + \frac{\partial^2\Phi}{\partial z^2} = 0 \quad 2.14$$

Additionally, the fluid must satisfy the kinematic boundary condition, which establishes that any particle in contact with the free surface remains on it. The dynamical boundary condition defines the pressure on the free surface boundary between air and water to be continuous. Finally, the nonpenetration boundary condition applies on the bottom. These conditions are expressed as follows:

$$\frac{\partial\eta}{\partial t} + \frac{\partial\Phi}{\partial x}\cdot\frac{\partial\eta}{\partial t} + \frac{\partial\Phi}{\partial y}\cdot\frac{\partial\eta}{\partial y} - \frac{\partial\Phi}{\partial z} = 0 \; on \; z = -\eta \quad 2.15$$

$$\frac{\partial\Phi}{\partial t} + \frac{1}{2}\nabla\Phi\cdot\nabla\Phi + g\cdot z = 0 \; on \; z = -\eta \quad 2.16$$

$$\frac{\partial\Phi}{\partial z} = 0 \; on \; z = -d \quad 2.17$$

where η is the free surface, g is the gravitational acceleration, and d is the water depth. This set of equations constitute the boundary value problem (BVP) [44].

With the assumption of a perturbation solution in terms of a small wave slope of the incident waves, the velocity potential Φ and associated variables, such as wave elevation, dynamic pressure, and particle velocities are expanded in the following form:

$$\Phi = \epsilon \cdot \Phi^{(1)} + \epsilon^2 \cdot \Phi^{(2)} + \epsilon^3 \cdot \Phi^{(3)} + O(\epsilon^4) \quad 2.18$$

$$\eta = \epsilon \cdot \eta^{(1)} + \epsilon^2 \cdot \eta^{(2)} + \epsilon^3 \cdot \eta^{(3)} + O(\epsilon^4) \quad 2.19$$

where ϵ is the so-called perturbation parameter. Thus, by substituting Eqns. (2.18) and (2.19) into Eqns. (2.15) to (2.17), and grouping the equations into sets with the same order ϵ, ϵ^2 and so on. The problem is solved easily. Equations. (2.20) and (2.21) present the first-order potential and wave elevation.

$$\Phi^{(1)} = \frac{gA}{\omega} \frac{cosh\, k(z+d)}{\cosh(kd)} \sin(kx - \omega t) \quad 2.20$$

$$\eta^{(1)} = \mathrm{A} \cdot \cos(kx - \omega t) \quad 2.21$$

where A is the wave amplitude, ω is the wave frequency and k is the wave number. ω and k are related by the dispersion equation as follows:

$$\omega^2 = gk \tanh(kh) \quad 2.22$$

Equations (2.23) and (2.24) present the second-order potential and wave elevation.

$$\Phi^{(2)} = A^2 \frac{3\omega}{8} \frac{cosh\, 2k(z+d)}{\sinh^4(kd)} \sin 2(kx - \omega t) \quad 2.23$$

$$\eta^{(2)} = \frac{A^2 k}{4} \frac{cosh\,(kd)(2 + cosh 2kd)}{\sinh^3(kd)} \cos 2(kx - \omega t) \quad 2.24$$

2.2.2 Linear wave loads

The hydrodynamic wave pressure creates hydrodynamic forces consisting of motion-induced hydrodynamic inertia and hydrodynamic damping forces that are proportional to the acceleration and velocity of the body, respectively, and the exciting wave force on the structure assumed to be fixed in waves [44]. The exciting wave force consists of the Froude-Krylov and diffraction forces. The hydrodynamic wave

pressure is computed assuming a linear superposition among incident, diffracted and radiated velocity potential functions as follows:

$$\Phi^{(1)} = \Phi_I^{(1)} + \Phi_D^{(1)} + \Phi_R^{(1)} \quad 2.25$$

This linear superposition divides the potential into two parts. The first is the radiation potential, which assumes that the body oscillates harmonically at frequency ω in calm water in six degrees of freedom. The second is the sum of the incident and the diffraction velocity potentials, which satisfies the kinematical boundary condition at the mean body position as shown in Eqn. (2.26) [28].

$$\frac{\partial \Phi_D^{(1)}}{\partial n} = -\frac{\partial \Phi_I^{(1)}}{\partial n} \quad 2.26$$

To solve the radiation problem, the body oscillates harmonically in calm water in its six degrees of freedom with a particular frequency ω is assumed. It is possible to demonstrate that the velocity potential per unit velocity amplitude corresponds to:

$$\Phi_R^{(1)} = \sum_{j=1}^{6} Re\left[\varphi_j(x,y,z)e^{-i\omega t}\right] \quad 2.27$$

The radiation potential φ_j satisfies the Laplace equation, the boundary conditions of Eqns. (2.15) to (2.17), and two additional boundary conditions. The first is in terms of the surface body, as shown in Eqn. (2.28), and the second is in the form of the radiation condition, which establishes that the radiation and diffraction potentials must vanish at a great distance from the structure [20] as shown in Eqn. (2.29)

$$\frac{\partial \varphi_j^{(1)}}{\partial n} = n_j \, , j = 1,2,\ldots,6 \; on \; body \; surface \quad 2.28$$

$$\lim_{R\to\infty} \sqrt{R}\left(\frac{\partial Re[\varphi_{R,D}^{(1)}]}{\partial R} + \frac{\omega^2}{g} Im[\varphi_{R,D}^{(1)}]\right) = 0 \, , on \; R \quad 2.29$$

where R is the radial distance from the center of the body in all directions. The hydrodynamic force F_{jk} is obtained solving this set of equations and it consists of two forces: one proportional to the acceleration and one to the velocity. Thus,

$$F_{jk} = -\omega^2 \cdot u_k \cdot A_{jk} - i\omega \cdot u_k \cdot B_{jk} \quad 2.30$$

where F_{jk} represents the j-th mode force due to the k-th mode motion, u_k is the generalized displacement amplitude of the k-th mode, A_{jk} are the constants called

added mass proportional to the acceleration $A_k = -\omega^2 \cdot u_k$, and B_{jk} are the constants called potential damping proportional to the velocity $V_k = -i\omega \cdot u_k$. As in the case of the force, the suffix jk indicates the j-th mode of added mass or damping due to the k-th mode motion. Similarly, the diffraction wave potential must satisfy the Laplace equation, the boundary conditions of Eqns. (2.15) to (2.17). The far field condition of Eqn. (2.29) and the body surface of Eqn. (2.26). Once the potential function and the hydrodynamic pressure are calculated, the wave exciting force is given by Eqn. (2.31)

$$F = \int_{\sigma} p \cdot n \cdot d\sigma \cdot e^{i\omega t} = -i\rho\omega \int_{\sigma} \left(\varphi_I^{(1)} + \varphi_D^{(1)}\right) n \cdot d\sigma \cdot e^{i\omega t} \qquad 2.31$$

where p is the hydrodynamic pressure, σ is the body surface, and n is the unit outward normal on the body surface. Substituting Eqn. (2.28) into Eqn. (2.31), Eqn. (2.32) is obtained.

$$F_j = -i\rho\omega \int_{\sigma} \left(\varphi_I^{(1)} + \varphi_D^{(1)}\right) \frac{\partial \varphi_j^{(1)}}{\partial n} \cdot d\sigma \cdot e^{i\omega t}, j = 1, \dots, 6 \qquad 2.32$$

The exciting wave force includes the contributions of the incident wave potential and the diffraction wave potential, which are the Froude-Krylov force of Eqn. (2.33) and the diffraction force in Eqn. (2.34), respectively.

$$F_{FK_j} = -i\rho\omega \int_{\sigma} \varphi_I^{(1)} \cdot \frac{\partial \varphi_j^{(1)}}{\partial n} \cdot d\sigma \cdot e^{i\omega t}, j = 1, \dots, 6 \qquad 2.33$$

$$F_{D_j} = -i\rho\omega \int_{\sigma} \varphi_D^{(1)} \cdot \frac{\partial \varphi_j^{(1)}}{\partial n} \cdot d\sigma \cdot e^{i\omega t}, j = 1, \dots, 6 \qquad 2.34$$

$$\Phi_{I,D}^{(1)} = \varphi_{I,D}^{(1)} e^{i\omega t} \qquad 2.35$$

2.2.3 Haskind Relation

By considering the vector function $A = (\mathrm{X}, \mathrm{Y}, \mathrm{Z})$ to be continuously differentiable, defined in the volume v and enclosed by the surface τ. Gauss' theorem establishes the following:

$$\int_{v} \nabla \cdot A \cdot dv = \int_{\tau} \mathrm{n} \cdot A \cdot d\tau \qquad 2.36$$

where ∇ is the vector differential operator, and n is the unit outward normal on the surface τ. Now, consider two scalar functions, φ_1 and φ_2, defined in the domain v and

on surface τ, both differentiable up to second-order with continuous derivate functions. Replacing A by $\varphi_1 \nabla \varphi_2$ in Eqn. (2.36), The first form of Green's theorem is obtained.

$$\int_v (\nabla\varphi_1 \cdot \nabla\varphi_2 + \varphi_1 \nabla^2 \varphi_2) dv = \int_\tau \mathrm{n} \cdot \varphi_1 \nabla \varphi_2 \cdot d\tau = \int_\tau \varphi_1 \frac{\partial \varphi_2}{\partial n} d\tau \qquad 2.37$$

Interchanging φ_1 and φ_2 in Eqn. (2.37), Eqn. (2.38) is obtained. Thus, subtracting Eqn. (2.37) from Eqn. (2.38), Eqn. (2.39) is obtained, the second form of Green's theorem.

$$\int_v (\nabla\varphi_2 \cdot \nabla\varphi_1 + \varphi_2 \nabla^2 \varphi_1) dv = \int_\tau \varphi_2 \frac{\partial \varphi_1}{\partial n} d\tau \qquad 2.38$$

$$\int_v (\varphi_2 \nabla^2 \varphi_1 - \varphi_1 \nabla^2 \varphi_2) dv = \int_\tau \left(\varphi_2 \frac{\partial \varphi_1}{\partial n} - \varphi_1 \frac{\partial \varphi_2}{\partial n}\right) d\tau \qquad 2.39$$

If φ_1 and φ_2 are harmonic or regular, then $\nabla^2 \varphi_{1,2} = 0$ and Eqn. (2.40), known as Green's second identity is obtained.

$$\int_\tau \left(\varphi_2 \frac{\partial \varphi_1}{\partial n} - \varphi_1 \frac{\partial \varphi_2}{\partial n}\right) d\tau = 0 \qquad 2.40$$

By replacing φ_1 and φ_2 with the diffraction $\varphi_D^{(1)}$ and radiation $\varphi_R^{(1)}$velocity potentials in the fluid domain v enclosed by the surface τ, Eqn. (2.41) is obtained. Since the integral vanishes except on the body boundary surface, the integrals can be considered on the body surface σ. Additionally, substituting the diffraction boundary condition Eqn. (2.26) into Eqn. (2.41), Eqn. (2.42) is obtained.

$$\int_\tau \varphi_R^{(1)} \frac{\partial \varphi_D^{(1)}}{\partial n} d\tau = \int_\tau \Phi_D^{(1)} \frac{\partial \varphi_R^{(1)}}{\partial n} d\tau \qquad 2.41$$

$$-\int_\sigma \varphi_R^{(1)} \frac{\partial \varphi_I^{(1)}}{\partial n} d\tau = \int_\sigma \varphi_D^{(1)} \frac{\partial \varphi_R^{(1)}}{\partial n} d\tau \qquad 2.42$$

Using Eqn. (2.42) in Eqn. (2.32), Eqn. (2.43) is obtained, known as the Haskind relation. It establishes that, given the incident and radiation potential, it is possible to determine the exciting wave forces without computing the diffraction potential.

$$F_j = -i\rho\omega \int_\sigma \left(\varphi_I^{(1)} \frac{\partial \varphi_j^{(1)}}{\partial n} - \varphi_R^{(1)} \frac{\partial \varphi_j^{(1)}}{\partial n}\right) \cdot d\sigma \cdot e^{i\omega t}, j = 1, \dots, 6 \qquad 2.43$$

2.3 MEAN DRIFT FORCES

Three different formulations have developed to estimate the mean drift forces. The first is the far-field approach, which once can derive by applying the momentum theorem to the fluid domain. Although efficient and offering satisfactory convergence, it is restricted to providing only three components of the horizontal modes and cannot be used to estimate the forces on individual bodies when they are part of a multi-body system. The second is the near-field approach based on direct pressure integration on the body surface. This approach provides the mean drift forces in all six degrees of freedom and is compatible with one single-body or multi-body systems. The third is the middle-field approach, which represents the application of Gauss' theorem in limited domains by control surfaces.

2.3.1 Far-Field Formulation

By applying the conservative principle of linear and angular momentum to the fluid domain bounded by a body surface σ, water free surface n and limiting surface at the far-end S_∞, Maruo [53] presented a formulation to calculate the mean drift forces on the horizontal modes (i.e., Surge, Sway and Yaw). Subsequently, Newman [65] extended the formulation presented by Maruo as follows:

$$\mathrm{MDF}_x = \overline{\frac{\rho g}{2}\int_{F_\infty} \eta^{(1)^2} n_1 dl + \int_{S_\infty} \left(\rho \phi_n^{(1)} \phi_x^{(1)} + P n_1\right) ds} \quad 2.44$$

$$\mathrm{MDF}_y = \overline{\frac{\rho g}{2}\int_{F_\infty} \eta^{(1)^2} n_2 dl + \int_{S_\infty} \left(\rho \phi_n^{(1)} \phi_y^{(1)} + P n_2\right) ds} \quad 2.45$$

$$\mathrm{MDM}_z = \overline{\frac{\rho g}{2}\int_{F_\infty} \eta^{(1)^2} n_6 dl + \int_{S_\infty} \left(\rho \phi_n^{(1)} \left((x-x_0)\phi_y^{(1)} - (y-y_0)\phi_x^{(1)}\right) + P n_6\right) ds} \quad 2.46$$

where n_j with (j=1,2,6) are the normal vectors for each mode, F_∞ is the upper boundary that vertically touches the mean free surface of the water, $\phi_n^{(1)} = \partial\phi^{(1)}/\partial n$, $\phi_x^{(1)} = \partial\phi^{(1)}/\partial x$, $\phi_y^{(1)} = \partial\phi^{(1)}/\partial y$, x_0 and y_0 are the coordinates of the reference point of rotation, and P is given by Eqn. (2.47). Note that the mean drift forces represent the average value during one wave period.

$$p = \rho \frac{\partial \Phi^{(1)}}{\partial t} + \frac{1}{2}\rho\left(\nabla \Phi^{(1)}\right)^2 \quad 2.47$$

2.3.2 *Near-Field Formulation*

With the near-field formulation, the mean drift forces can be calculated by direct integration of the pressure on the body surface at its mean position. The hydrodynamic pressure is modeled by Eqn. (2.47). Thus, the forces and moments on the body surface are given by Eqn. (2.48) and (2.49), respectively.

$$MDF = \rho \int_{\sigma} \left[\frac{\left(\nabla \Phi^{(1)}\right)^2}{2} + X \cdot \nabla \Phi_t^{(1)} + \Phi_t^{(1)} R * \right] n d\sigma + \frac{\rho g}{2} \oint_{\Gamma} \eta^{(1)} (2\varrho_3 - \eta^{(1)}) n d\Gamma \tag{2.48}$$

$$MDM = \rho \int_{\sigma} \left[\left(\frac{\left(\nabla \Phi^{(1)}\right)^2}{2} + X \cdot \nabla \Phi_t^{(1)} + \Phi_t^{(1)} R * \right) (r * n) + \Phi_t^{(1)} T * n \right] d\sigma + \frac{\rho g}{2} \oint_{\Gamma} \eta^{(1)} (2\varrho_3 - \eta^{(1)}) (r * n) d\Gamma \tag{2.49}$$

where $\Phi_t^{(1)} = \partial \Phi^{(1)} / \partial \mathrm{t}$; $T = (\xi_1, \xi_2, \xi_3)$ and $R = (\theta_1, \theta_2, \theta_3)$ are the translational and rotational movements of the body, respectively; n is the normal vector to the body surface; Γ is the waterline of the body; $\eta^{(1)}$ is the wave elevation; $r = (x - x_0, y - y_0, z - z_0)$ is the position vector with respect to the reference point $r = (x_0, y_0, z_0)$ for rotation and; and finally

$$X = T + R * r = (\varrho_1, \varrho_2, \varrho_3). \tag{2.50}$$

Note that the first term in Eqns. (2.48) and (2.49) corresponds to the convective term of Bernoulli's equation, while the second term is the correction of the first-order dynamic pressure on the displacement. As in the previous case, the mean drift loads in regular waves are obtained by taking the mean value during one wave period.

2.3.3 *Middle-Field Formulation*

Introduced by Chen [16], the middle-field formulation defines a reduced domain D enclosed by the body surface σ, a fictitious surface C surrounding the body and the mean free surface F limited by the curves Γ_C and Γ which are the intersection of D and σ with the plane $z = 0$. Thus, by applying Gauss' theorem to Eqns. (2.48) and (2.49), it is possible to demonstrate that the mean drift loads correspond to

$$MDF = -\frac{\rho g}{2}\oint_{\Gamma} \Xi k d\Gamma + \rho\int_{F}\left[\left(\eta^{(1)}\Phi_{zt}^{(1)} + \frac{\nabla\Phi^{(1)^2}}{2}\right)k\right]dF + \frac{\rho g}{2}\oint_{\Gamma_C}\eta^{(1)^2} n d\Gamma + \frac{\rho}{2}\int_{C}\left[2\Phi_n^{(1)}\nabla\Phi^{(1)} - \nabla\Phi^{(1)^2} n\right]dC \quad 2.51$$

$$MDM = -\frac{\rho g}{2}\oint_{\Gamma} \Xi(\mathrm{r} * k) d\Gamma + \rho\int_{F}\left[\left(\eta^{(1)}\Phi_{zt}^{(1)} + \frac{\nabla\Phi^{(1)^2}}{2}\right)(r * k)\right]dF + \frac{\rho g}{2}\oint_{\Gamma_C}\eta^{(1)^2}(r * n) d\Gamma + \frac{\rho}{2}\int_{C}\left[2\Phi_n^{(1)}\left(\mathrm{r} * \nabla\Phi^{(1)}\right) - \nabla\Phi^{(1)^2}(r * n)\right]dC \quad 2.52$$

$$\Xi = \left(\eta^{(1)^2} - 2\eta^{(1)} \cdot \xi_3\right) n_3 - 2\eta^{(1)}(X \cdot n) \quad 2.53$$

Therefore, Eqns. (2.52) and (2.53) are used to calculate the mean drift loads in six degrees of freedom. As in the previous cases, the mean drift loads in regular waves are obtained by taking the mean value during one wave period. Note that, the shape of the control surface was not defined. Thus it can be defined arbitrarily. Moreover, in the case of multi-body analysis, each control surface can be defined by each body individually.

Another important consequence of these formulations is that if the fictitious surface C is extended to infinity, the formulation obtained is equivalent to the far-field method of section 2.3.1, while if the surface C is shifted back to the body surface, the near-field method of section 2.3.2 is obtained. Consequently, with the middle-field formulation it is possible to state that the near-field and far-field approaches are also equivalent.

2.4 SECOND-ORDER LOADS

The second-order loads are proportional to the wave amplitude and are associated with wave-wave and wave-body interactions [11]. Thus, these forces contain terms corresponding to frequencies that are equal to sums and differences of the elementary wave frequencies, i.e., wave drift loads (low-frequency effects) and sum frequency loads (high-frequency effects) [57].

Second-order wave loads are usually represented by the quadratic transfer function (QTF) [41]. The QTF can be decomposed into the contributions of two parts, as shown in Eqn. (2.54). The first part F_1 contains quadratic terms due to the products of first-order

quantities; consequently, it depends only on the first-order wave potential. The second part F_2 is a consequence of the solutions of the second-order wave potential [60].

$$F(f_1, f_2) = F_1(f_1, f_2) + F_2(f_1, f_2) \quad 2.54$$

where F is the second-order load and f_1 and f_2 are two elementary wave frequencies of an irregular sea.

The first term F_1 is equivalent to the mean drift force, and there are three formulations to calculate this term, as mentioned in Section 2.3. The second term can be formulated as shown in Eqn. (2.55) [60].

$$F_2(f_1, f_2) = \frac{-i\rho}{g}(\omega_2 - \omega_1)\int_S \left(\phi_I^{(2)} + \phi_D^{(2)}\right)\bar{\eta}\, dS \quad 2.55$$

where ω_1=2πf_1, ρ is the water density, g is gravitational acceleration, S is the body surface, $\phi_I^{(2)}$ is the second-order wave incident potential, $\phi_D^{(2)}$ is the second-order wave diffracted potential, and $\bar{\eta}$ is the normal vector to the body surface. Since $\phi_I^{(2)}$ is well described by an analytical expression [72], the next step is to calculate the second-order wave diffracted potential. The following approaches have been proposed to determine this integral.

2.4.1 Direct Method

In this method, proposed by [46] and [67] the full second-order problem is solved directly from Eqn. (2.55). Thus, the second-order wave loads are obtained by direct pressure integration over the body surface.

2.4.2 Indirect Method

In this method, proposed by [60], the second-order wave diffracted potential is calculated in an indirect manner using first-order quantities by introducing an assisting velocity potential ψ which is the solution of the first-order radiation problem at the sum or difference frequency as shown in Eqn. (2.56). This approach is similar to the Haskind relation used to determine the first-order wave diffracted potential.

$$\int_H \phi_D^{(2)}\eta dS = -\int_H \left(\frac{\partial \phi_I}{\partial n} - \aleph_H\right)\psi\, dS - \frac{1}{g}\int_{FS} \aleph_F \psi dS \quad 2.56$$

where $\aleph_H$ represents the linear and rotational body motions and $\aleph_F$ is an integrand over the free surface, as shown in Eqns. (2.57) and (2.58). The first term of Eqn. (2.56)

is an integral over the body surface, and the second term involves an integration over the free surface.

$$\aleph_H = \frac{1}{2}\left[(i\omega_2 X_2^* - \nabla\emptyset_2^*)(R_1 \times n) - \left(i\omega_1 X_1 \ - \nabla\emptyset_1\ \right)(R_2^* \times n) - \left(X_1\ \nabla\right)\nabla\emptyset_2^* n - (X_2^* \nabla)\nabla\emptyset_1\ n\right] \quad 2.57$$

$$\begin{aligned}\aleph_F = {} & i(\omega_1 - \omega_2)\left[\nabla\emptyset_{I1}\nabla\emptyset_{D2}^* + \nabla\emptyset_{D1}\nabla\emptyset_{I2}^* + \nabla\emptyset_{D1}\nabla\emptyset_{D2}^*\right] \\ & -\frac{i\omega_1}{2g}\left[\left(\emptyset_{I1} + \emptyset_{D1}\right)\left(-\omega_2^2\frac{\partial}{\partial z} + g\frac{\partial^2}{\partial z^2}\right)\emptyset_{D2}^* + \emptyset_{D1}\left(-\omega_2^2\frac{\partial}{\partial z} + g\frac{\partial^2}{\partial z^2}\right)\emptyset_{I2}^*\right] \\ & -\frac{i\omega_2}{2g}\left[\left(\emptyset_{I2} + \emptyset_{D2}^*\right)\left(-\omega_1^2\frac{\partial}{\partial z} + g\frac{\partial^2}{\partial z^2}\right)\emptyset_{D1} + \emptyset_{D2}^*\left(-\omega_1^2\frac{\partial}{\partial z} + g\frac{\partial^2}{\partial z^2}\right)\emptyset_{I1}\right]\end{aligned} \quad 2.58$$

where X and R are the linear and rotational motions of the floating body, respectively.

The convergence of the free surface integral (FSI) is slow and requires a relatively long processing time [75]. The contribution of the FSI to the wave drift loads on large volumes is not significant and can be neglected [63]. In contrast, this integral is predominant in the sum-frequency component and is unavoidable [63]. Thus, this term requires careful evaluation.

2.4.3 Newman Approximation

The calculation of QTFs involves many numerical challenges and a large number of numerical unknowns; consequently, it is expensive in terms of processing time [75]. Thus, several approximate methods have been developed with the aim of simplifying the associated computational effort. The most widely used is the Newman approximation (NA) [66]. With this approach, the term F_2 of Eqn. (2.54) is estimated using the term F_1 as shown in Eqn. (2.59).

$$F_2(f_1, f_2) = sgn\left(F_1(f_1, f_1)\right)\sqrt{\left(F_1(f_1, f_1) \times F_1(f_2, f_2)\right)} \quad 2.59$$

Note that, this method was developed for the estimation of wave drift loads on large structures such as barges or FPSOs operating in deep water with low natural frequencies [62]. Several works [41], [63], and [75] have discussed the limitations of this method. Consequently, its accuracy needs to be evaluated for each situation.

Finally, note that there is no approximation to the QTF sum-frequency term.

2.5 COUPLED ANALYSIS OF MOORED STRUCTURES

This section presents a brief review of the equations that characterize the time domain (TD) simulations performed in Orcaflex software [70]. The interaction between mooring lines and floating bodies is addressed with a so-called coupled analysis. This method consists of the solution of two groups of equations.

For the first equation, the floating body is considered to be a rigid body subject to the action of external loads such as waves and currents; the mooring line forces are applied to the connection points (fairlead) as shown in Eqn. (2.60).

$$[A + M]\ddot{x} + B\dot{x} + Cx = F_{WAVE} + F_{CURRENT} + F_{ML} \quad 2.60$$

where A is the added mass; M is the mass of the system; B is the damping; C is the hydrostatic restoration, F_{WAVE} includes the linear diffraction forces, mean drift forces and second-order forces on the floating body; $F_{CURRENT}$ is the average current force on the structure; and F_{ML} is the forces exerted by the mooring lines on the floating body. Note that Eqn. (2.60) represents only one degree of freedom; and the complete formulations involve similar equations for the other degrees of freedom.

Thus, after defining the initial conditions of the system (position, velocities, and acceleration), Eqn. (2.60) is solved for each time step, and the new position of the body is obtained. Consequently, the new positions of the fairleads are obtained as well.

The second group of equations consists of a FEM model for the mooring lines. This group of equations includes the effects of the weight and buoyancy of the lines, added mass and drag forces. The forces applied by the floating body on the lines and the information provided by the solution of Eqn. (2.61), i.e., the new position of the far end of the lines as shown in Eqn. (2.61) are considered at each time step of the simulation.

$$M_{ML}\ddot{x}_{ML} + B_{ML}\dot{x}_{ML} + C_{ML}x_{ML} = F_{EXT} + F_{ML} \quad 2.61$$

where M_{ML} is the mass matrix of the mooring lines, B_{ML} is the structural damping, C_{ML} is the restoring forces on the lines, F_{EXT} is a group of forces which includes drag forces and added mass and F_{ML} are the forces applied by the floating body on the mooring line. The force that the lines apply to the floating body is obtained from Eqn. (2.60).

The interaction between both groups of equations occurs at each time step, transmitting the motions of the floating body to the mooring lines; subsequently, the forces exerted on the mooring lines are applied to the floating body, as shown in Fig. 2.2

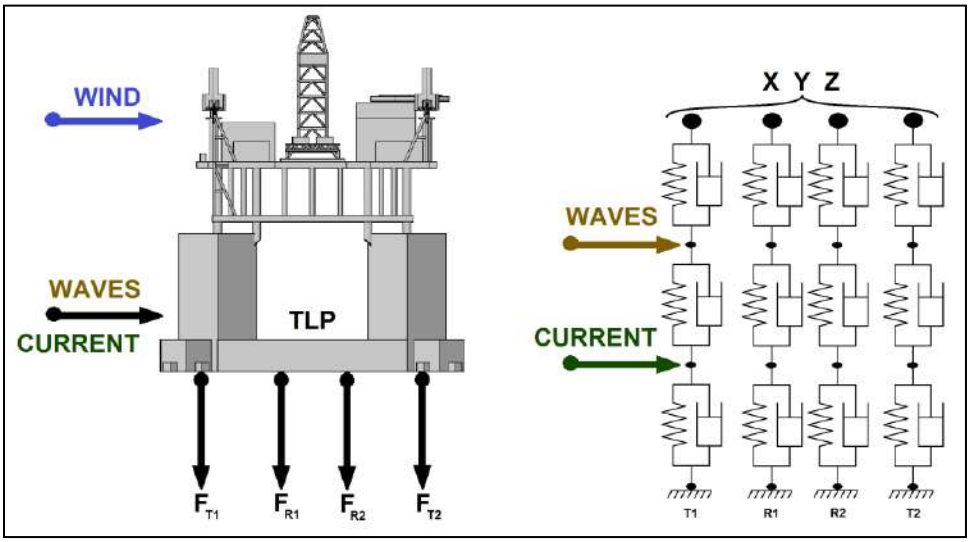

Figure 2.2 Coupled model of the floating body – mooring line interaction.

2.6 VORTEX INDUCED MOTIONS

Vortex induced motions (VIM) refers to resonant movements as a consequence of fluid-structure interaction [33]. Due to the characteristics of the vortex shedding, the pressure distribution around the body varies at a defined frequency, the so-called vortex shedding frequency f_s [9]. Thus, when f_s is approximately equal to the natural frequency of the structure f_n, the structure undergoes oscillatory movements with an amplitude of the same order of magnitude as the characteristic length L_C of its transversal section [52]. Note that, the "equality" between f_s and f_n occurs for a fixed range of current velocities, i.e., far from this range of velocities, there are no resonant motions [6].

In addition, experimental tests have shown that cylinders in a tandem arrangement, as in the case of multi-column floaters, can suffer from the phenomenon known as Galloping [89]. Fluid forces generated by relative motions between a structure and fluid cause that the body motion descends, and body remains stable, or ascends and motion becomes unstable. Both scenarios depend on the current speed. When the current speed exceeds a specific threshold, known as critical velocity, the structure becomes unstable, and galloping occurs [4]. In other words, the structure can be seen a dynamical system that undergoes a super-critical Hopf Bifurcation, as the current speed exceeds the critical velocity [5].

Galloping is known as dynamic instability that is induced due to the internal turbulence of the fluid. Thus, Galloping enhances any initial small motion of the structure and turns it to an oscillation [8]. Dynamically speaking, Galloping is damping-controlled phenomena, since its occurrence involves zero damping. Thus, the amplitude of oscillation is preserved, and an isolated limit cycle is formed. This limit cycle follows nonlinear chaotic equations such as the van der Pol-Duffing equation [30], and [31].

Therefore, Galloping is physically different from VIM. While VIM is a resonance motion, i.e., the frequency of the exciting forces coincides with the natural frequency of the body, Galloping is a low-frequency motion, i.e., the vortex shedding frequency f_s is larger than the natural frequency of the structure. Furthermore, drag forces do not limit the Galloping; thus, the amplitude of motions increases steadily with the current velocity [95].

Figure 2.3 presents the dynamic behavior of different arrangements of cylinders subject to currents. Depending on the distribution of the cylinders, flow induced vibration regimes caused by both VIM and galloping were observed. VIM and galloping can occur singly, in combination or separately.

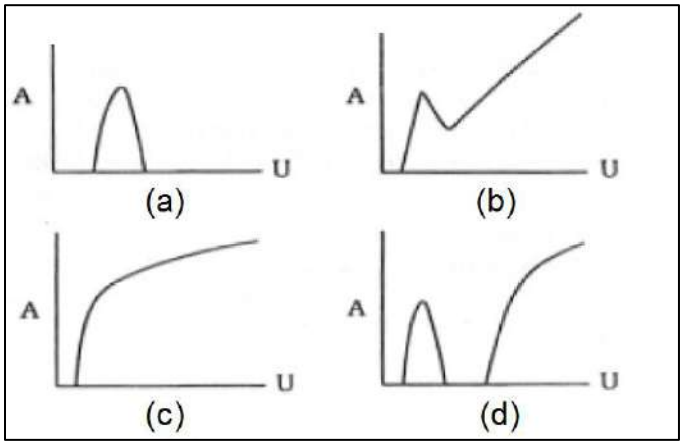

Figure 2.3 Flow-induced motions on cylinders in tandem configuration (a) VIM alone, (b) VIM and Galloping combined, (c) Galloping Alone and (d) VIM and Galloping separated [89].

In the offshore industry, this phenomenon has been observed and studied mainly in the context of one-column structures, such as Spar platforms [79], [93], and [98]; and mono-columns [34]. However, recent studies have demonstrated that deep draft TLPs and Semi-submersibles are also susceptible to these motions [95]. Figure 2.4 presents experimental

results for a deep draft semi-submersible with VIM behavior for transversal movements. Moreover, Figure 2.5 shows Yaw motions of four floaters, all of them exhibiting galloping instabilities.

To aid in understanding such a complex phenomenon several nondimensional parameters have been defined. For instance, reduced velocity V_R establish a relationship between the flow velocity V_C and the natural frequency of the structure f_n as shown in Eqn. (2.62).

$$V_R = \frac{V_C}{L_c \cdot f_n} \tag{2.62}$$

where L_c is a characteristic length of the body. The Strouhal number St is defined as the ratio of inertial forces due to the unsteadiness of the flow to inertial forces due to changes in velocity from one point to another in the flow field [25], it is formulated in Eqn. (2.63).

$$St = \frac{L_c \cdot f_S}{V_C} \tag{2.63}$$

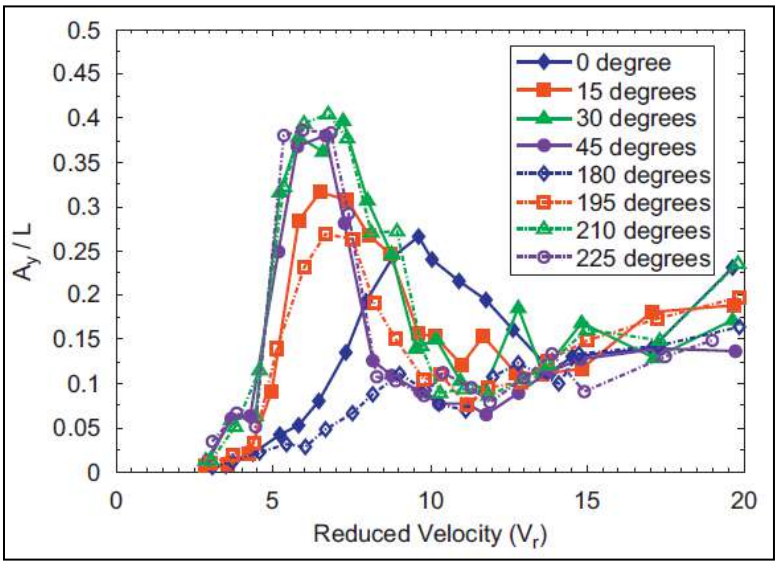

Figure 2.4 VIM of a semi-submersible in transversal motion [35].

The Strouhal number for circular cylinders is approximately constant and equal to 0.2 for the transitional Reynolds number regime in cylinders with high aspect ratio (L/D), as shown in Fig. 2.6 [9]. This observation implies that the frequency of vortex shedding f_S is approximately linearly dependent on the current velocity.

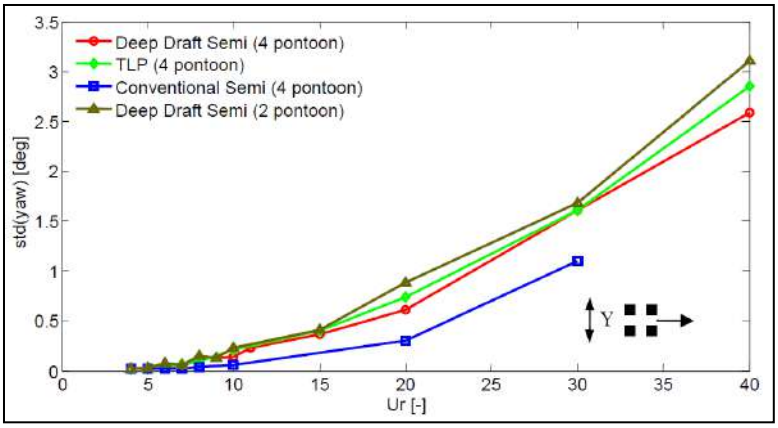

Figure 2.5 Galloping instabilities for Yaw motion of four floaters [95].

The Reynolds number is defined as the ratio of inertial forces to viscous forces, as shown in Eqn. (2.64).

$$\mathrm{Re} = \frac{V_C L_c}{\nu} \qquad 2.64$$

where ν is the kinematic viscosity of the fluid. Typically, on offshore platforms, the Reynolds number takes values on the order of 1.0E7 corresponding to the transcritical flow regime. Consequently, the boundary layer is turbulent upstream of the separation point [28], which represents an enormous technical challenge for the experimental tests using reduced or even ultra-reduced scale modes.

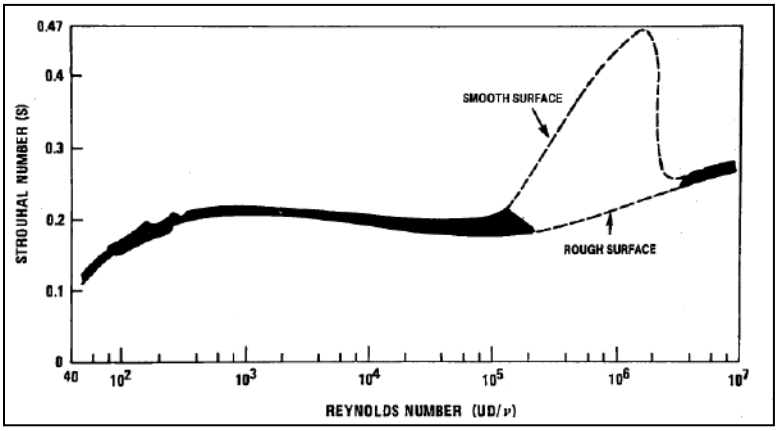

Figure 2.6 Strouhal number vs. Reynolds number relationship [9].

Hydrodynamic scaling laws require geometric, kinematic and dynamic similarity between the model and prototype [84]. However, due to technical and physical limitations,

it is impossible to satisfy all of these laws simultaneously [12]. [93] shows that experiments that satisfy only the Froude model law have lower Reynolds numbers as shown in Eqn. (2.65)

$$\mathrm{Re}_{MODEL} = \frac{\mathrm{Re}_{PROTOTYPE}}{\sqrt{\lambda^3}} \qquad 2.65$$

where λ is the scale factor. Thus, when using scale factors between 50 and 200, the model Reynolds numbers are in the range of 1.0E3 to 1.0E5 which correspond to the subcritical flow regime in which the boundary layer is always laminar [28].

Recent studies on this issue [23], [79], and [98] have considered different flow regimes. The authors have concluded that VIM results in the subcritical flow regime are acceptable and slightly conservative.

Full-scale data presented in [77] showed that the amplitude of induced movements was significantly higher than that predicted in experimental tests. Although these differences can be attributed to Reynolds number differences, [77] also considered interactions between waves, current, and wind to be a possible reason for such differences. Therefore, it is still too early to reach a conclusion on this point. Furthermore, the experimental tests with reduced scale models involve other relevant aspects such as the following:

- *Blockage effects in the current channel*

  Although [99], states that blockage effects from walls are negligible when the ratio between characteristic length L_C and the width of current channel is less than 0.1, it is not clear if this ratio applies to a complex geometry such as a multi-floater column. Note that, [3] establishes that VIM response in deep water is not a function of the water depth; however, it is not clear what effect the bottom has in terms of the amplitude of the current induced motions.

- *Faithful representation of the floaters*

  Several works, [35] and [88], have demonstrated that the amplitude of the motions developed by the unit depends on the details of the geometry of the hull. Consequently, details such as fairlead and cathodic anodes could play a major role in experimental tests. Based on this fact, it is possible to develop mitigation devices with the correct dimensions to introduce modifications in the motion pattern developed by the floater and reduce the order of magnitude of the VIM.

- *Surface tension and rugosity of the floater hull*

  Scale effects include not only Reynolds effects but also the correct representation of the floater geometry in terms of rugosity; moreover, due to the reduced scale, the effects of the surface tension could play a major role.

  No references were found on this topic. Consequently, it is not clear if these effects play a relevant role in VIM and Galloping phenomena, particularly in ultra-reduced scale models.

- *Mooring lines and risers*

  Typically mooring lines, risers and even tendons of a TLP are not considered in experimental tests. Equivalent systems normally consider the contribution of the mooring lines in the restoration of the motions of the floater. However, it is not clear how the damping associated with these elements could modify the motions of the offshore unit. Recent studies [36] and [49] have demonstrated that damping plays a major role in the mitigation of the motions developed by the units.

  In addition, these elements are susceptible to resonance motions as well. As shown in Appendix A, TLP tendons are vulnerable to VIV resonance motions. Therefore, it is not clear if these vibrations could induce higher movements of the unit.

- *Combined effects of waves and currents*

  Recent works [89] have presented experimental evidence that the effects of waves and currents combined induce larger motions on the floater. However, the experimental results presented in [36] suggest the opposite trend. Consequently, it is not clear if it is possible to determine a general rule regarding the combined effects of current and waves.

- *Column Length*

  Several works, for instance [36] and [95], have demonstrated that the primary geometrical parameter of the floaters in the development of VIM is the length of the columns; as a general rule, it is clear that longer columns are susceptible to larger induced movements.

CHAPTER III. TLP-TAD SYSTEM CASE STUDY

In this chapter, the main properties of the TLP-TAD system are presented. Geometrical and physical properties of the floaters considered in this work are reported. Moreover, the mooring systems of the TLP, the TAD and the mechanical connection between both floaters are described. Finally, important properties such as natural periods and the linear stiffness matrix are calculated and presented.

3.1 TENSION LEG PLATFORM

The Tension Leg Platform (TLP) is one of the most important floating production systems for deepwater operations in the oil and gas industry. TLPs units are particularly suitable for water depths between 300 and 1600 meters, the industry has used them since the 1980s in diverse scenarios such as the North Sea (Hutton, Snorre and Heidrun), Gulf of Mexico (Jolliet, Typhoon, Neptune and Bigfoot), Africa (Kizomba A, Kizomba B, Oveng), Southeast Asia (West Seno and Malakai) and Brazil Offshore (Papaterra).

Fundamentally, the TLP consists of a hull moored by rigid tendons to the seabed. These tendons are designed to restrain the vertical motions of the TLP due to waves. The hull of the TLP has an excess of buoyancy to provide adequate pre-tension in the tendons. For the TLP hull, several configurations can be found; the conventional TLP presented in Fig. 3.1, comprises a pontoon in a closed configuration with four columns; and tendon porches attach to the column base. In contrast, the concept of the extended TLP or ETLP has the tendon porches attached to the ends of extended pontoons, as shown in Fig. 3.1.

The hull considered in the present work corresponds to the ETLP concept and consists of four rectangular pontoons in a closed configuration and four columns with square sections. Note that the columns are rotated 45° about the vertical axis. Figure 3.2 presents a 3D view of the TLP and the main dimensions of the hull. The main particulars of the TLP are listed in Table 3.1.

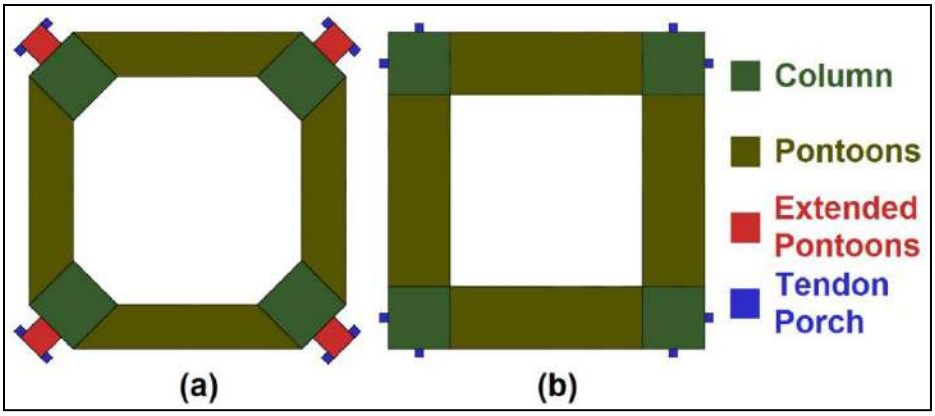

Figure 3.1 TLP hull configuration (a) E-TLP and (b) conventional TLP.

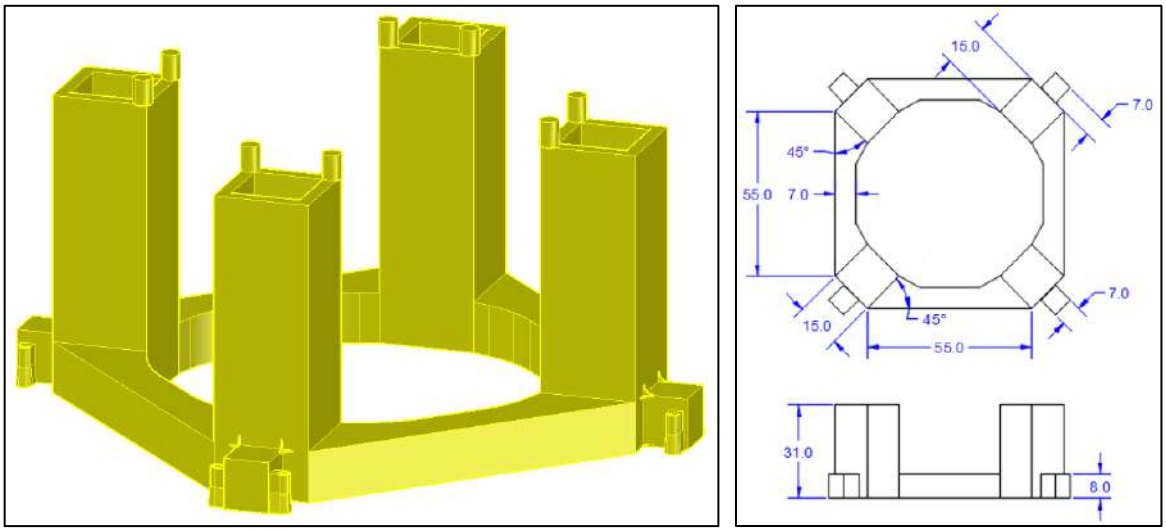

(A) (B)

Figure 3.2 Extended Tension Leg Platform (E-TLP) hull.

Table 3.1 Main characteristics of the TLP.

Description	Value	Units
Water depth	1200	[m]
TLP overall breadth	80.0	[m]
Draft	31.0	[m]
Mass	32897	[mT]
Vertical position of center of gravity	31.1	[m]
Radius of gyration (Rxx)	33.6	[m]
Radius of gyration (Ryy)	33.4	[m]
Radius of gyration (Rzz)	37.0	[m]

The hull of the TLP is moored to the seabed by eight tendons with a length of 1155 meters and a pre-tension of 11 500 kN. The tendons are circular pipes with a mass per unit length equal to 0.635 mT/m, axial stiffness equal to 1.71E7 kN and an outer diameter equal to 0.81 m.

3.2 TENDER ASSISTED DRILLING

The TAD unit is a semi-submersible platform composed of two rectangular pontoons connected by three circular beams and six columns, as shown in Fig. 3.3. The main characteristics of the TAD are listed in Table 3.2.

The main advantages of the use of semi-submersible platforms as TAD platforms are the low motions developed by this unit relative to barges, excellent stability, large deck area and relatively fast tow speeds.

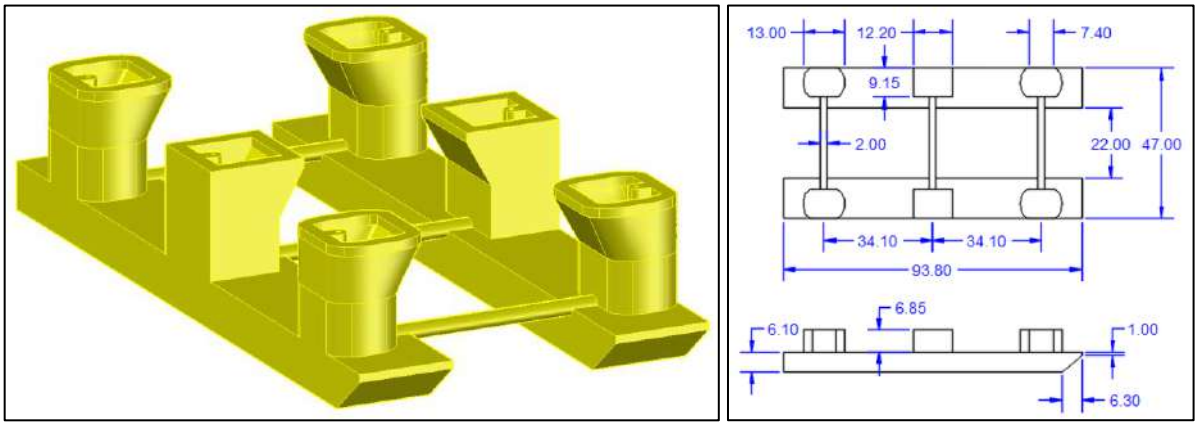

(A) (B)

Figure 3.3 Tender Assisted Drilling (TAD) hull.

Table 3.2 Main characteristics of the TAD.

Description	Value	Units
TAD overall length	93.8	[m]
TAD overall breadth	47.0	[m]
Draft	13.0	[m]
Mass	18122	[mT]
Longitudinal position of center of gravity	-0.9	[m]
Vertical position of center of gravity	14.3	[m]
Radius of gyration (Rxx)	16.8	[m]
Radius of gyration (Ryy)	29.0	[m]
Radius of gyration (Rzz)	31.2	[m]

The TAD unit is moored to the seabed with a semi-taut leg system of eight lines composed of a combination of: steel chain with a nominal diameter of 0.12 m and mass per unit length of 0.26 mT/m; and polyester ropes with a nominal diameter of 0.15 m and mass per unit length of 0.018 mT/m. The values of the pre-tension of the mooring lines vary in the range of [1200 – 2300] mT.

3.3 HAWSER SYSTEM

The hawser system is designed to control the relative motions between the TLP and the TAD unit in horizontal modes. It contains 12 lines of polyester ropes, as shown in Fig. 3.4, with a nominal diameter equal to 0.2 m and mass per unit length equal to 0.026 mT/m. Figure 3.5 presents the nonlinear axial stiffness of the polyester ropes.

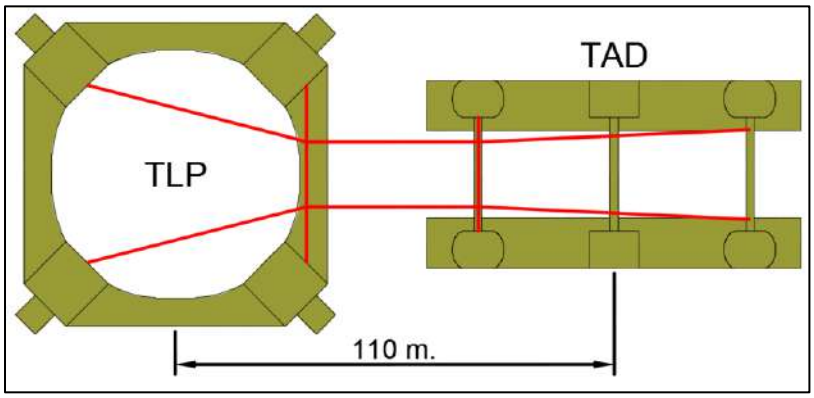

Figure 3.4 Hawser line system for the TLP-TAD connection.

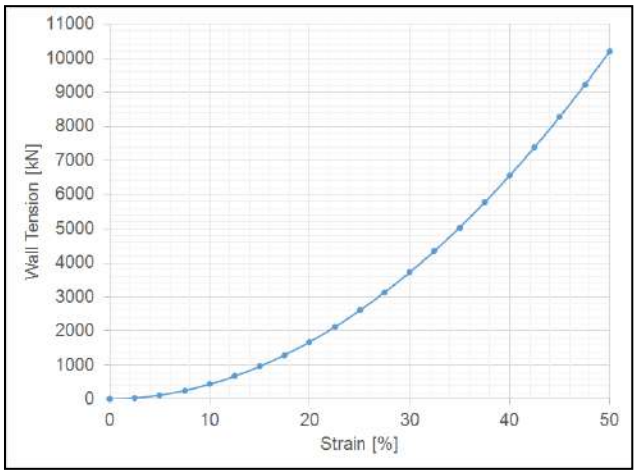

Figure 3.5 Axial stiffness of polyester ropes in hawser lines.

3.4 STIFFNESS AND NATURAL PERIODS

With the information provided in the previous sections, numerical models were developed in Orcaflex [70] to calculate the stiffness curves and matrixes, and the natural periods of the floaters. Three cases are considered: TLP alone, TAD alone and TLP connected with TAD by a hawser system. Figure 3.6 presents the numerical models. In addition, for the case TLP alone, stiffness curves calculated with the Orcaflex FEM model are compared with the analytical formulations presented in Section 2.1.

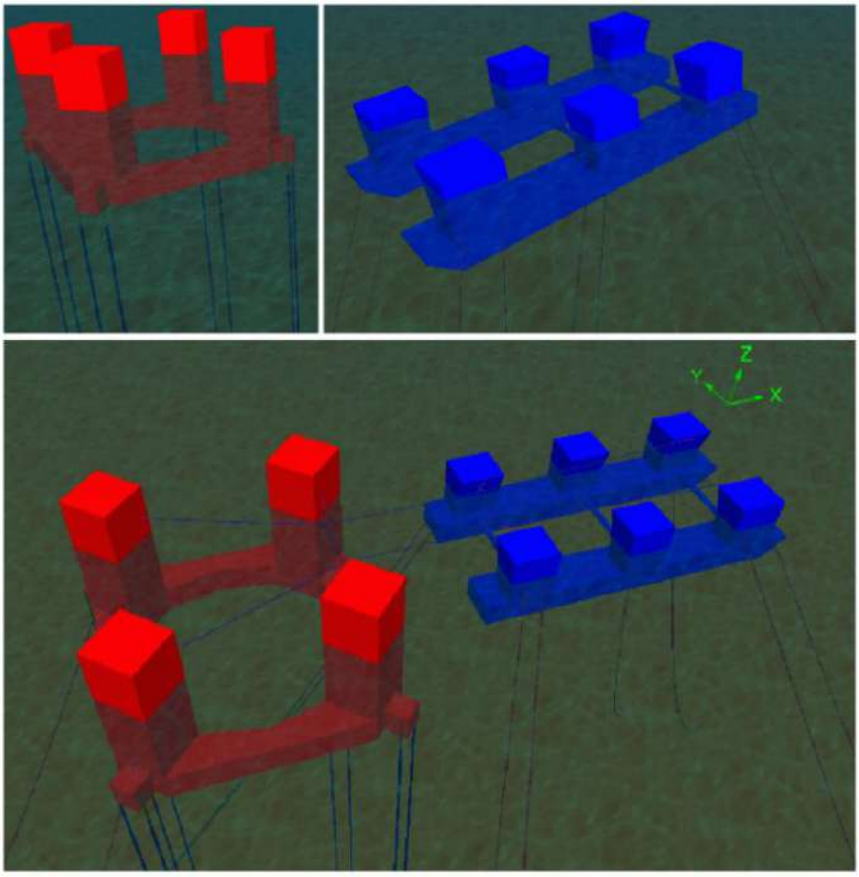

Figure 3.6 Numerical models of TLP alone, TAD alone and TLP-TAD multi-body system.

The stiffness curves and matrix are obtained by numerical offset tests, i.e., by applying a known constant load to the system and reporting the response. In addition, the natural periods were estimated by numerical decay tests, i.e., given an initial displacement, the system is

released to move freely; then, the time domain movements are analyzed by the Fast Fourier Transform (FFT).

As mentioned in Section 2.1, the linear stiffness constants due to the TLP tendons are given by Eqns. (3.1) to (3.4)

$$C_{11} = C_{22} = \sum_{i=1}^{N} \frac{Tt_n}{L_n} \tag{3.1}$$

$$C_{33} = \sum_{i=1}^{N} \frac{E_n A_n}{L_n} \tag{3.2}$$

$$C_{44} = C_{55} = \sum_{i=1}^{N} \frac{E_n A_n}{L_n} {y_n}^2 \tag{3.3}$$

$$C_{66} = \sum_{i=1}^{N} \frac{Tt_n}{L_n} \left({X_n}^2 + {Y_n}^2\right) \tag{3.4}$$

where C_{jj} are the linear stiffness coefficients, N is the number of tendons, L_n is the tendon length, Tt_n is the pre-traction in the tendon, E_n is the elastic modulus, A_n is the cross-sectional area of the tendon, and X_n *and* Y_n are the tendon coordinates. Note that, j=1, 2, 3...6 correspond to Surge, Sway, Heave, Roll, Pitch and Yaw, respectively.

Figure 3.7 shows the stiffness curve for surge comparing the analytical and numerical formulations. The analytical formulation presents excellent agreement for offsets in the range of [0 – 40] m. However, for larger offsets, the nonlinear effects become larger, and significant differences are observed.

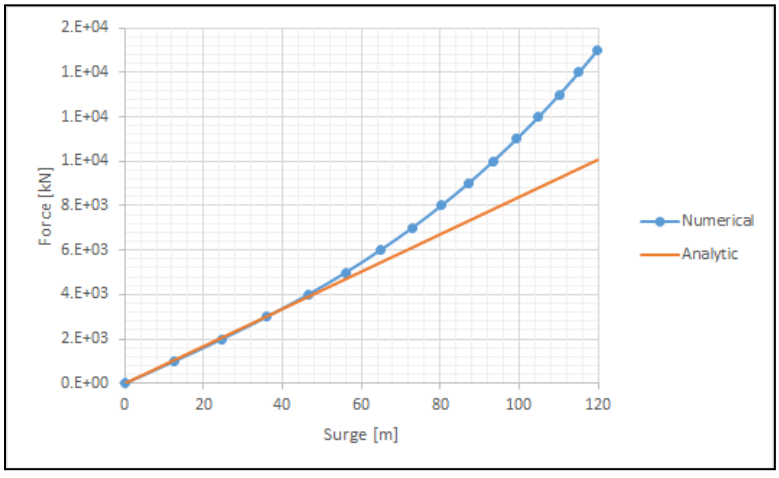

Figure 3.7 Stiffness curve for Surge of the TLP alone from analytical and numerical formulae.

Figure 3.8 presents the results for the stiffness curves for the six degrees of freedom of the TLP, comparing the analytical formulations for the TLP alone with numerical results for the TLP alone and the TLP coupled with the TAD. Figure 3.9 shows the results for the stiffness curves for the six degrees of freedom of the TAD, comparing the numerical results for the cases of the TAD alone and the TAD coupled with the TLP. Finally, Table 3.3 presents the results of the numerical decay tests, comparing the single-body and multi-body cases.

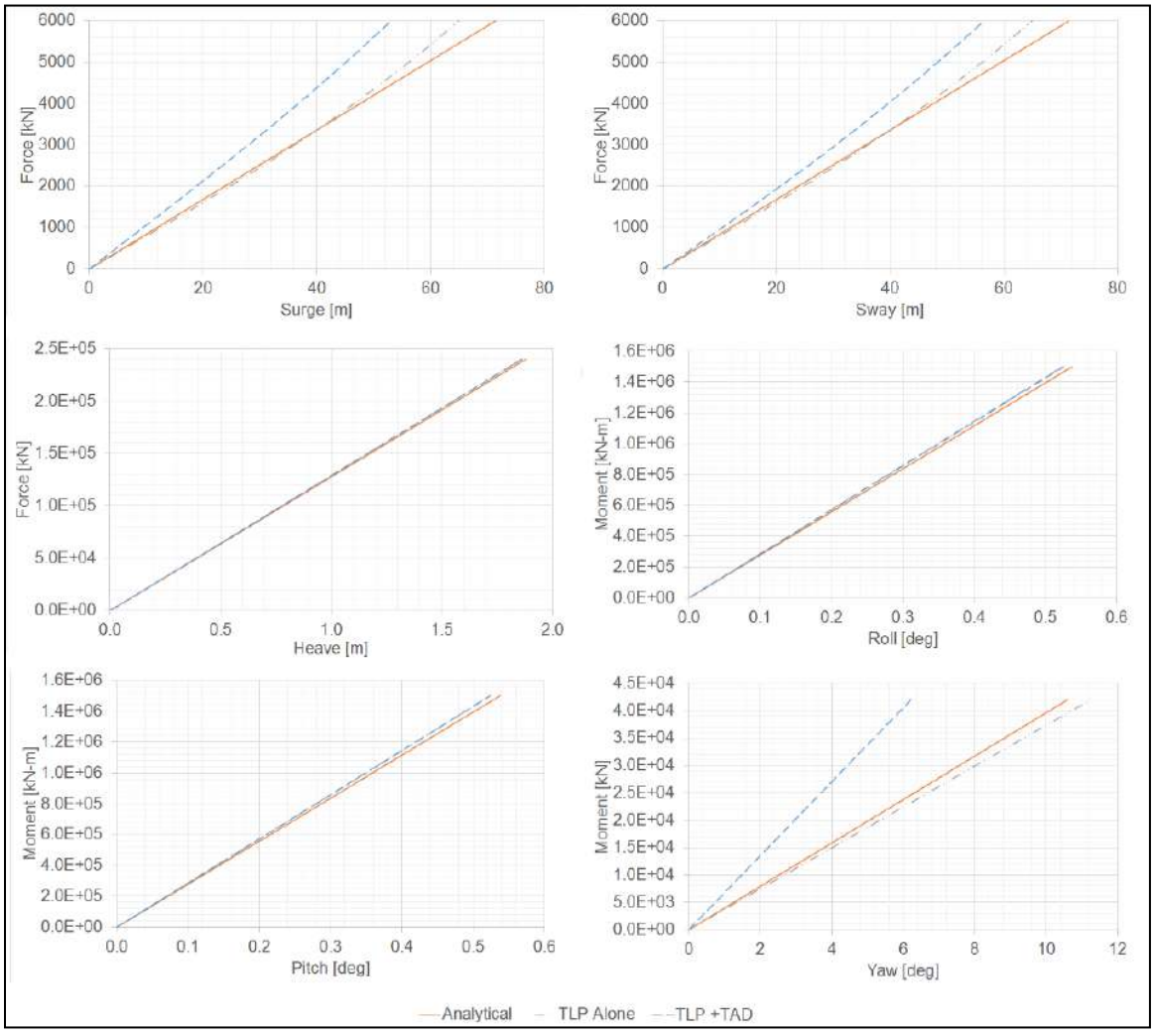

Figure 3.8 TLP stiffness for six degrees of freedom. The orange and black lines represent the results for the TLP alone using analytical and numerical approaches, respectively. The blue lines present the results for the TLP coupled with the TAD using the numerical approach.

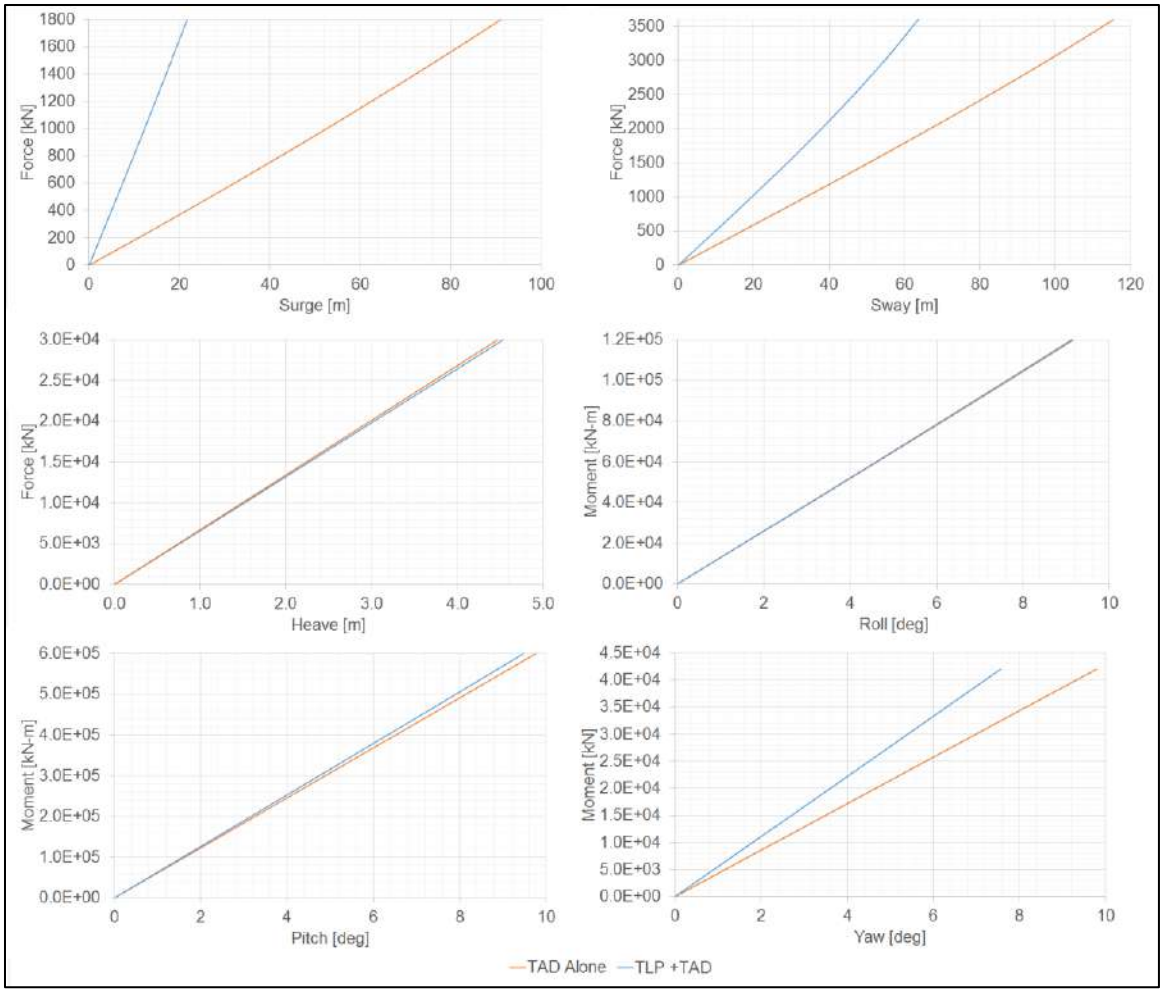

Figure 3.9 TAD stiffness for six degrees of freedom. The orange lines represent the results for the TAD alone. The blue lines present the results for the TAD coupled with TLP. Both sets of results were produced using the numerical approach.

Table 3.3 Natural periods of the TLP and TAD for the single-body and multi-body cases.

Mode	TLP		TAD	
	Alone	Connected to TAD	Alone	Connected to TLP
Surge	201	183	224	183
Sway	201	199	221	199
Heave	4.40	4.40	16.4	16.3
Roll	3.93	3.93	25.9	25.6
Pitch	3.93	3.93	18.3	18.6
Yaw	134	95.7	68.9	57.4

Based on these results, the following conclusions are drawn.

- Despite some differences at larger offsets, the analytical and numerical approaches present reasonable agreement. Consequently, the analytical formulation provides accurate results for the TLP alone case.
- The comparison between the single-body and multi-body cases for the TLP and TAD reveals relevant differences in horizontal modes; it is evident that these are a consequence of the hawser system. No significant differences were found in terms of the vertical motions.
- The values of the natural periods of the TLP and TAD confirm the influence of the hawser system in the behavior of the floaters for horizontal modes. Note that the natural periods of Surge, Sway and Yaw change significantly. Notably, the natural periods of Surge and Sway are the same for the TLP and TAD.

Finally, the same procedure used to obtain the stiffness curves for the six degrees of freedom of each floater was used to calculate the complete stiffness matrices. Note that these matrices present the linear approximation of the nonlinear stiffness calculated with the numerical formulation for all cases. Tables 3.4, 3.5, and 3.6 present the stiffness matrices for the TLP alone, TAD alone and TLP-TAD multi-body system, note that the units for lengths, forces, and angles are meters, kN, and radians, respectively.

Table 3.4 Stiffness matrix of TLP alone.

Modes	Surge	Sway	Heave	Roll	Pitch	Yaw
Surge	79	0	0	0	-1881	0
Sway	0	79	0	1881	0	0
Heave	0	0	120056	0	0	0
Roll	0	1881	0	165131634	0	0
Pitch	-1881	0	0	0	165131634	0
Yaw	0	0	0	0	0	214368

Table 3.5 Stiffness matrix of TAD alone.

Modes	Surge	Sway	Heave	Roll	Pitch	Yaw
Surge	18	0	14	0	976	0
Sway	0	32	0	-1084	0	-452
Heave	14	0	106	0	2429	0
Roll	0	-1081	0	187783	0	-55164
Pitch	980	0	2429	0	254768	0
Yaw	0	-449	0	15077	0	252593

Table 3.6 Coupled stiffness matrix of TLP and TAD.

		TLP						TAD					
	Modes	Surge	Sway	Heave	Roll	Pitch	Yaw	Surge	Sway	Heave	Roll	Pitch	Yaw
TLP	Surge	108	0	-370	0	-1625	0	-94	0	2	0	2745	0
	Sway	0	96	0	1647	0	622	0	-31	0	296	0	656
	Heave	-370	0	120102	0	6873	0	2	0	-38	0	-1290	0
	Roll	0	1646	0	165156387	0	460738	0	293	0	-4036	0	-9308
	Pitch	-1625	0	6873	0	165279702	0	2808	0	1183	0	10579	0
	Yaw	0	622	0	460293	0	405718	0	-588	0	8188	0	6380
TAD	Surge	-93	0	1	0	-1245	0	97	0	-1	0	1510	0
	Sway	0	-31	0	249	0	-887	0	57	0	-1340	0	-1322
	Heave	1	0	-38	0	1181	0	-1	0	148	0	3196	0
	Roll	0	252	0	-4021	0	7577	0	-1340	0	186382	0	40915
	Pitch	-1217	0	-1288	0	9913	0	1510	0	3196	0	366694	0
	Yaw	0	992	0	-8620	0	6453	0	-1322	0	41418	0	372138

CHAPTER IV. WAVE-INDUCED LOADS AND MOTIONS

This chapter presents a numerical study of linear and second-order wave loads on the TLP-TAD multi-body system. An extensive hydrodynamic analysis focuses on the hydrodynamic interactions between the floaters and how these effects modify the wave loads on the platforms. Time and frequency domain approaches were applied in this study. Using TD simulations, the simplifications adopted in the FD analysis, the accuracy of the Newman approximation, and the contribution of nonlinear wave loads are evaluated.

4.1 INTRODUCTION

First-order wave loads, which are proportional to the wave amplitude and associated with the wave frequency, affect the motions of floating moored structures [28]. The second-order wave loads are proportional to the square of the wave amplitude and related to the sum or difference of a pair of frequencies of the irregular sea [11].

The first-order wave loads provide the dominant wave loading on floating bodies [28] and include added mass, potential damping, diffraction forces and mean drift forces. The second-order loads are usually smaller than the first-order loads. However, these loads can excite resonance motions in frequencies at which the system has low damping [28]. Therefore, the second-order wave loads have particular importance in the design of mooring systems.

The multi-body system composed of a Tension Leg Platform (TLP) and a Tender Assisted Drilling (TAD) unit involves the complex scenario of two floaters moored in close proximity. This complexity requires an extensive and careful hydrodynamic analysis to guarantee the successful execution of such a challenging project.

In the present study, the 3D diffraction-radiation code Wamit [59] was used to calculate the wave loads. In addition, time domain simulations were conducted using the fully 3D nonlinear time domain finite element software Orcaflex [70]. Thus, the study is divided into two parts: the first-order analysis, and the second-order studies.

The first part includes the analysis of the hydrodynamic coefficients in the frequency domain; here the floaters are analyzed in three cases: TLP alone, TAD alone, and TLP connected to TAD with a hawser system. For the multi-body analysis, several relative positions were studied to analyze the hydrodynamic coupling effects between the floaters. The properties of the floaters, the mooring lines of the TLP and TAD, and the hawser system are presented in Chapter III. Note that, in the frequency domain, the mooring systems are modeled by linear stiffness matrixes. Subsequently, time domain simulations have conducted to analyze the simplifications adopted in the frequency domain studies; this study in time domain includes an extensive analysis of regular and irregular waves in three cases, TLP alone, TAD alone, and the multi-body cases.

The second part of this study involves the analysis of the second-order loads on the system. Low-frequency second-order loads on the TLP and TAD and high-frequency loads for vertical motions of the TLP were analyzed. This study includes computation of the second-order loads using the direct and indirect methods presented in Section 2.4. Additionally, the importance of the free surface integral (FSI) on the computation of the second-order loads and the accuracy of the Newman approximation (NA) for low-frequency loads are examined in frequency domains. Finally, fully nonlinear time domain simulations were conducted to verify the accuracy of the Newman approximation (NA) and the relevance of high-frequency second-order loads to the TLP-TAD multi-body system.

4.2 LINEAR WAVE-INDUCED MOTIONS

In this section, the linear wave induced motions and loads on the TLP-TAD multi-body system were examined. This study includes an analysis of coupling effects on the multi-body system. The first-order diffraction loads, mean drift loads, and the Response Amplitude Operator (RAO) were reviewed considering the floaters in single-body and multi-body cases. Subsequently, time domain simulations were conducted in regular and irregular seas to verify the accuracy of the frequency domain predictions.

4.2.1 Geometry Discretization

The computation of the wave loads requires discretization of the body surfaces. [59] provides two methods to represent the geometry of the bodies, the low-order, and the higher-order methods.

The low-order approach represents the geometry of the floater with a set of flat four-sided panels. The potential velocity and the physical quantities derived from it are considered to be constant in each panel area. Consequently, the accuracy of the calculations depends on the complexity of the geometry and the number of panels used to represent it. In contrast, the higher-order method characterizes the geometry of the body with continuous b-spline surfaces. Thus, physical quantities are calculated as continuous functions on each surface. In the present study, both methods were used to verify their accuracy for the calculations of wave hydrodynamic loads on the TLP-TAD system. Figure 4.1 shows the 3-D meshes for the TLP and TAD represented with the low-order and higher-order methods, note that due to the symmetry of the bodies, only one quadrant of the TLP and two quadrants of the TAD, in green color, were modeled. The main geometrical characteristics of both floaters were presented in Chapter II.

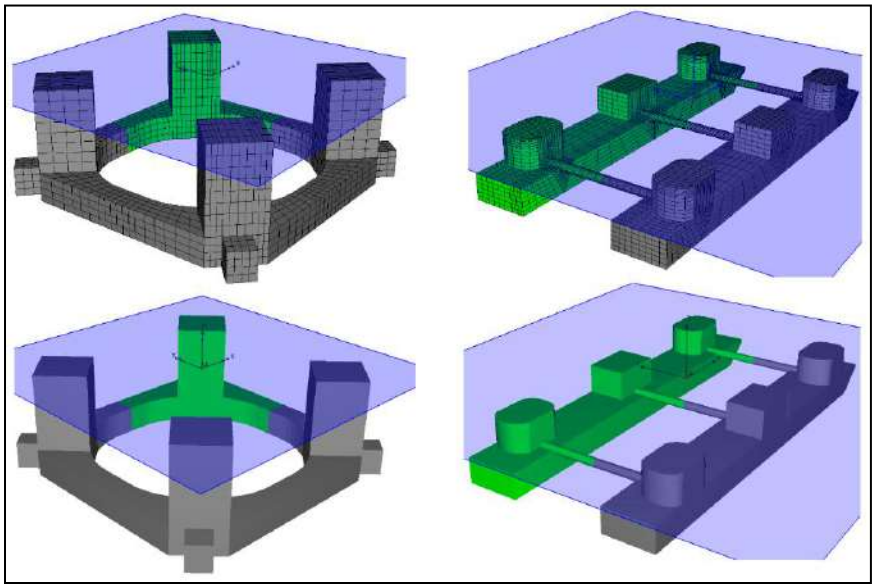

Figure 4.1 Computational grids of TLP (left) and TAD (right) using the low-order method (above) and the higher-order method (below).

The mean drift loads were computed using the middle-field method described in Section 2.3.3. This step required the discretization of a control surface involving the bodies. According to [99], the use of control surfaces in the middle-field method improves the accuracy of the results in the integration of the momentum flux when

one analyzes bodies with sharp corners. As in the case of body surfaces, the control surfaces can be modeled using the low-order and the higher-order methods. Figure 4.2 presents the control surfaces of the TLP and TAD, due to the symmetry of the control surfaces, only one quadrant for the TLP and two quadrants for the TAD, in green color, are used in the calculations. Note that, the higher-order method was used with the aim of increasing accuracy.

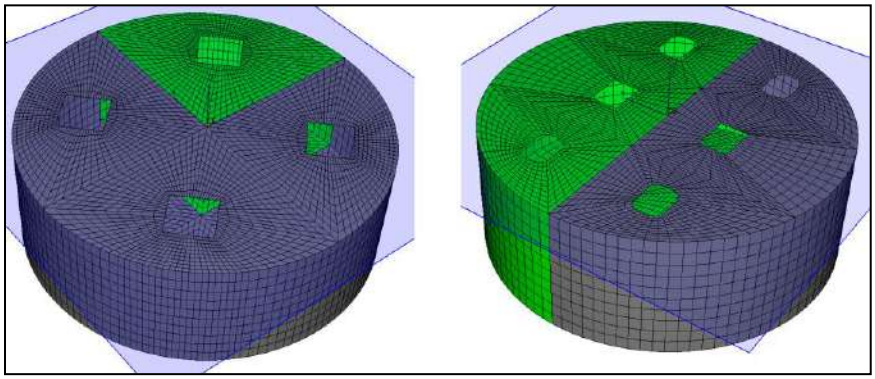

Figure 4.2 Control surfaces for the calculation of mean drift loads: TLP (left) and TAD (right)

4.2.2 Sensitivity Analysis

The sensitivity analysis was performed with the aim of verifying the influence of the computational grids on the first-order wave loads. This analysis included six grids divided into two groups: low-order grids and higher-order grids. Thus, three levels of refinement were considered in each group: coarse, medium and fine.

In the low-order method, the grids were refined by increasing the number of panels used to represent the geometry of the bodies [59]. In the higher-order method, the maximum size of the panels into which the body surfaces are divided determines the refinement [59].

Tables 4.1 and 4.2 present the main characteristics of the computational grids. Note that, due to the symmetry of the bodies, the number of panels in the low-order grids represents only one quadrant of the TLP hull and two quadrants of the TAD hull.

The sensitivity analysis is focused on the Response Amplitude Operator (RAO) of the TLP alone and the TAD alone. The range of wave periods considered is [2 - 40]

sec. The range of wave headings is [0° - 180°] in steps of 15°. Note that, the wave heading indicates the direction in which the waves are progressing. Figure 4.3 presents the main wave headings and the coordinate systems adopted in the present analysis.

Table 4.1 Number of panels in the TLP and TAD low-order grids

Grid code	Refinement	Floater	
		TLP	TAD
LO1	Coarse	768	1712
LO2	Medium	1728	2675
LO3	Fine	3072	3924

Table 4.2 Maximum panel sizes of the TLP and TAD higher-order grids

Grid code	Refinement	Floater	
		TLP	TAD
HO1	Coarse	20	20
HO2	Medium	10	10
HO3	Fine	5	5

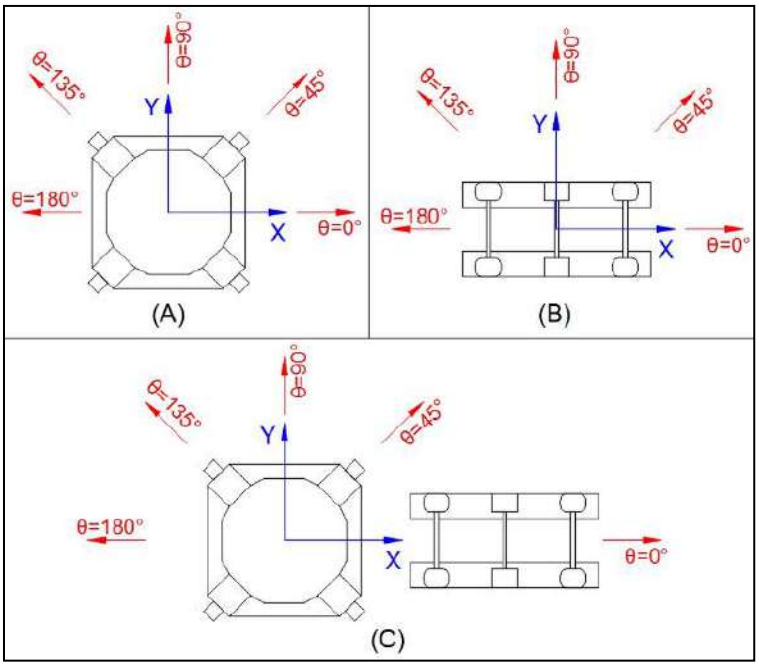

Figure 4.3 Global coordinate system used in the analysis.

The linear stiffness matrixes from the mooring systems calculated in Section 3.4 and viscous damping coefficients reported in Appendix B were incorporated into the numerical simulations. The physical properties of the floaters were presented in Chapter III.

Figures 4.4 and 4.5 present a comparison of the RAOs for the TLP and TAD respectively. Selected results are presented only. As noted above, six grids for both floaters were tested, three using the low-order panel method (LO1, LO2, and LO3) and three using the higher-order panel method (HO1, HO2, and HO3).

Despite small differences, the results were strongly consistent between the low and higher-order methods. Moreover, the results seem to be independent on the grid refinements for both floaters.

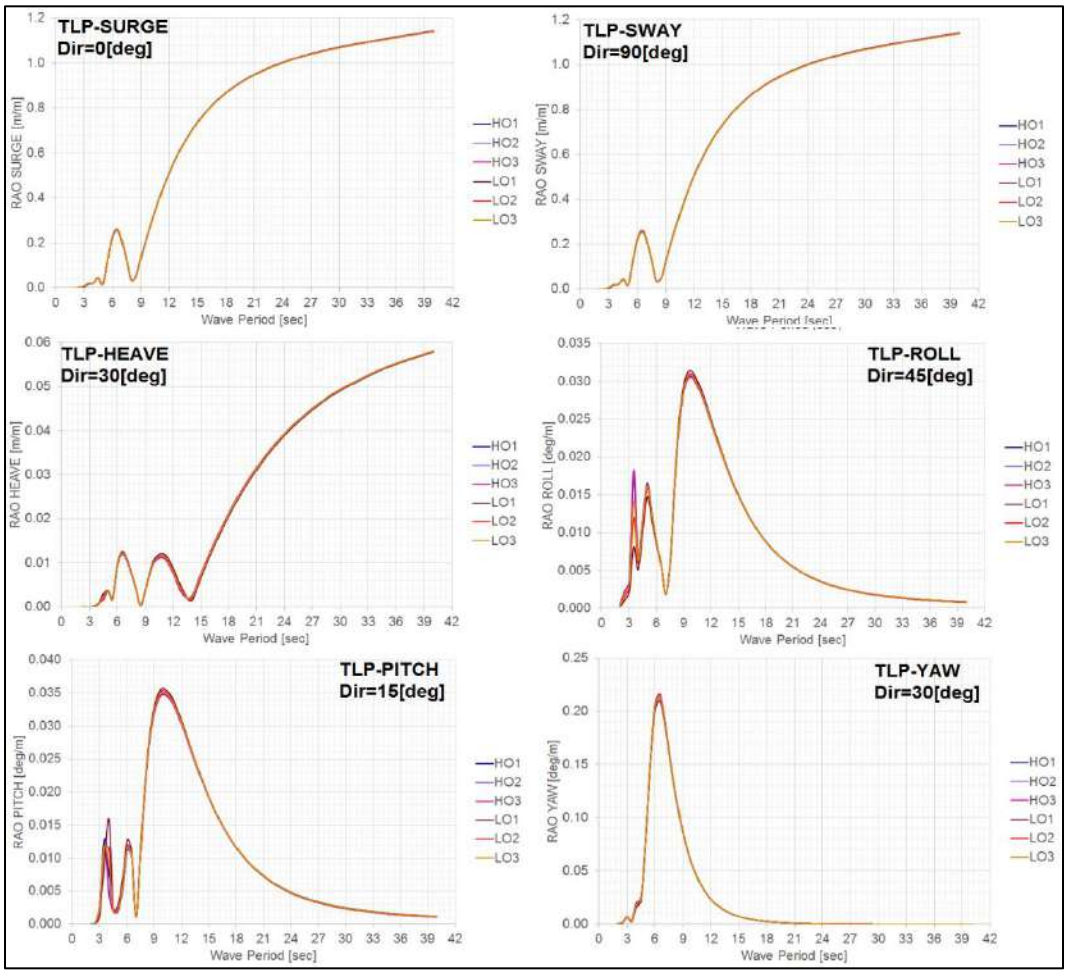

Figure 4.4 Analysis of the RAO of the TLP for different computational grids

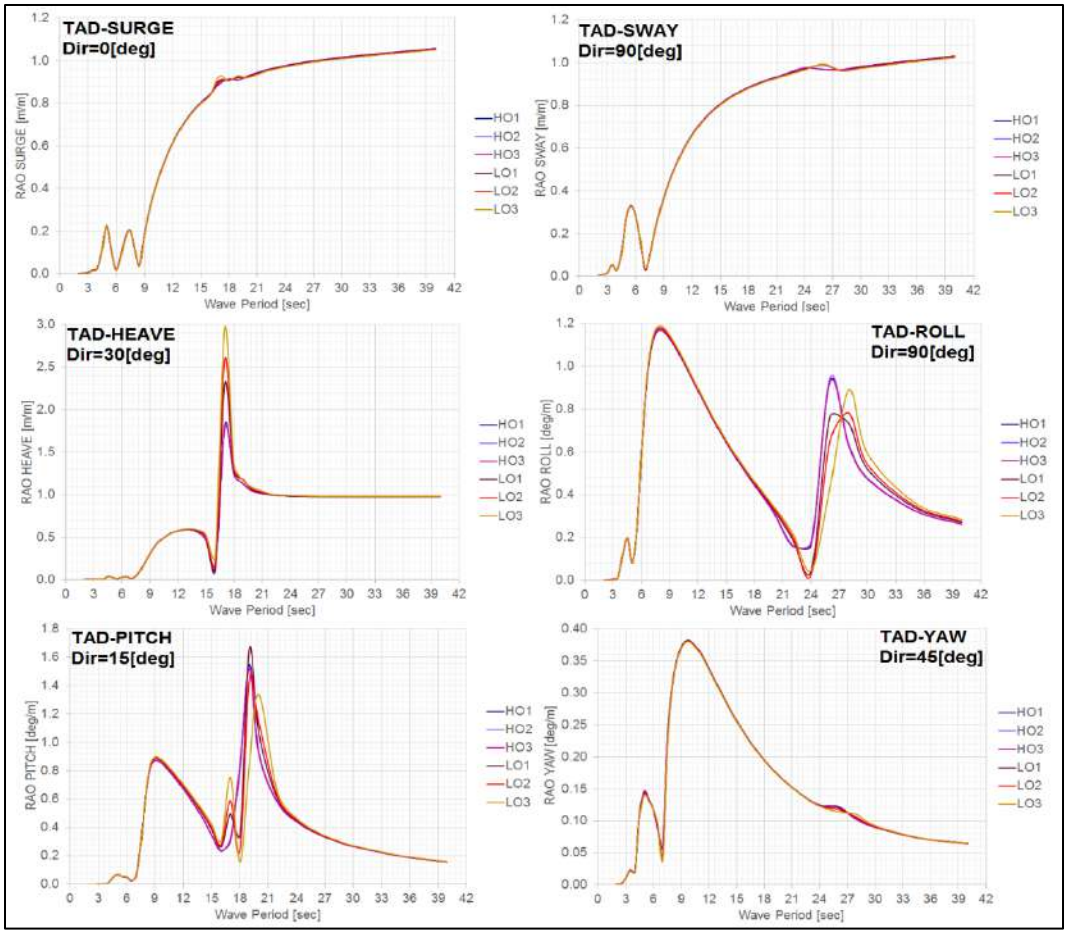

F***igure 4.5*** Analysis of the RAO of the TAD for various computational grids

In the case of the TLP, the largest differences for Roll and Pitch correspond to wave periods in the range of [3-6] sec. For TAD, the maximum differences are observed for Heave, Roll and Pitch for wave periods in the range of [15-18] sec., [21-36] sec. and [15-22] sec. respectively. Another important observation is that the differences between low-order grids are considerably larger than the discrepancies between higher-order grids, i.e., the results for the higher-order grids are independent on refinement, while the low-order grids present a slight dependence on refinement.

Thus, both methods are adequate for the calculations of wave loads. Because the dependence on the higher-order method on grid refinement is smaller and almost negligible, the higher-order grids with the finest refinement HO3 were used for both floaters in the following sections.

4.2.3 Hydrodynamic Coefficients

After defining the computational grids to represents the geometry of the bodies, the first-order wave potential for the multi-body system was calculated to investigate the interactions between the floating bodies. Thus, this extensive study includes the analysis of two single-body cases (TLP alone and TAD alone) and the nine multi-body cases shown in Fig. 4.6.

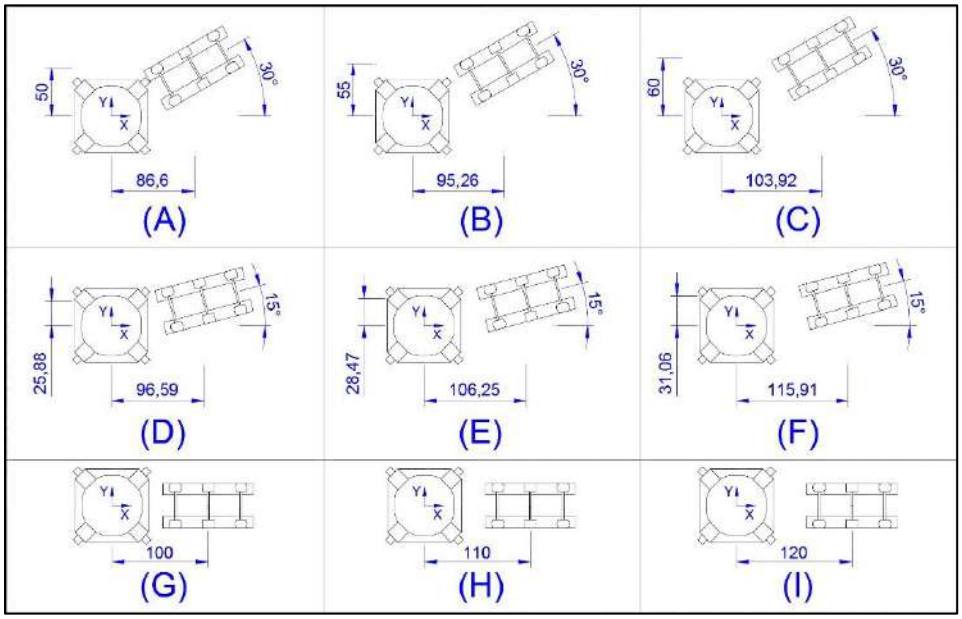

Figure 4.6 Positions of TLP and TAD for multi-body analysis (units are meters).

The analysis is focused on the diffraction forces, RAOs and mean drift forces. The range of wave periods considered is [2 - 40] sec. The range of wave headings is [0° - 345°] in steps of 15°. Note that, the mooring systems in the single-body and multi-body cases are represented by the linear stiffness matrixes presented in Section 3.4. Moreover, viscous damping coefficients, reported in Appendix B, were incorporated into the numerical simulations.

Figures 4.7 and 4.8 present a comparison of the linear diffraction loads on the TLP and TAD respectively. For a better comparison of the hydrodynamic interactions, results for the single-body and multi-body cases are depicted together. Selected results were presented only.

The diffraction loads on the TLP present little variations between the single-body and multi-body cases. In general, the maximum variations occur in the wave period range of [0 - 9] sec. For Surge, the discrepancies are slightly higher for the range of wave periods of [4 – 8] sec. Sway and Heave do not present significant variations, and for Roll, Pitch, and Yaw the largest differences are observed in the vicinity of the peak forces.

Finally, in the range of wave periods of [15 – 40] sec., no differences exist between the single-body and multi-body cases.

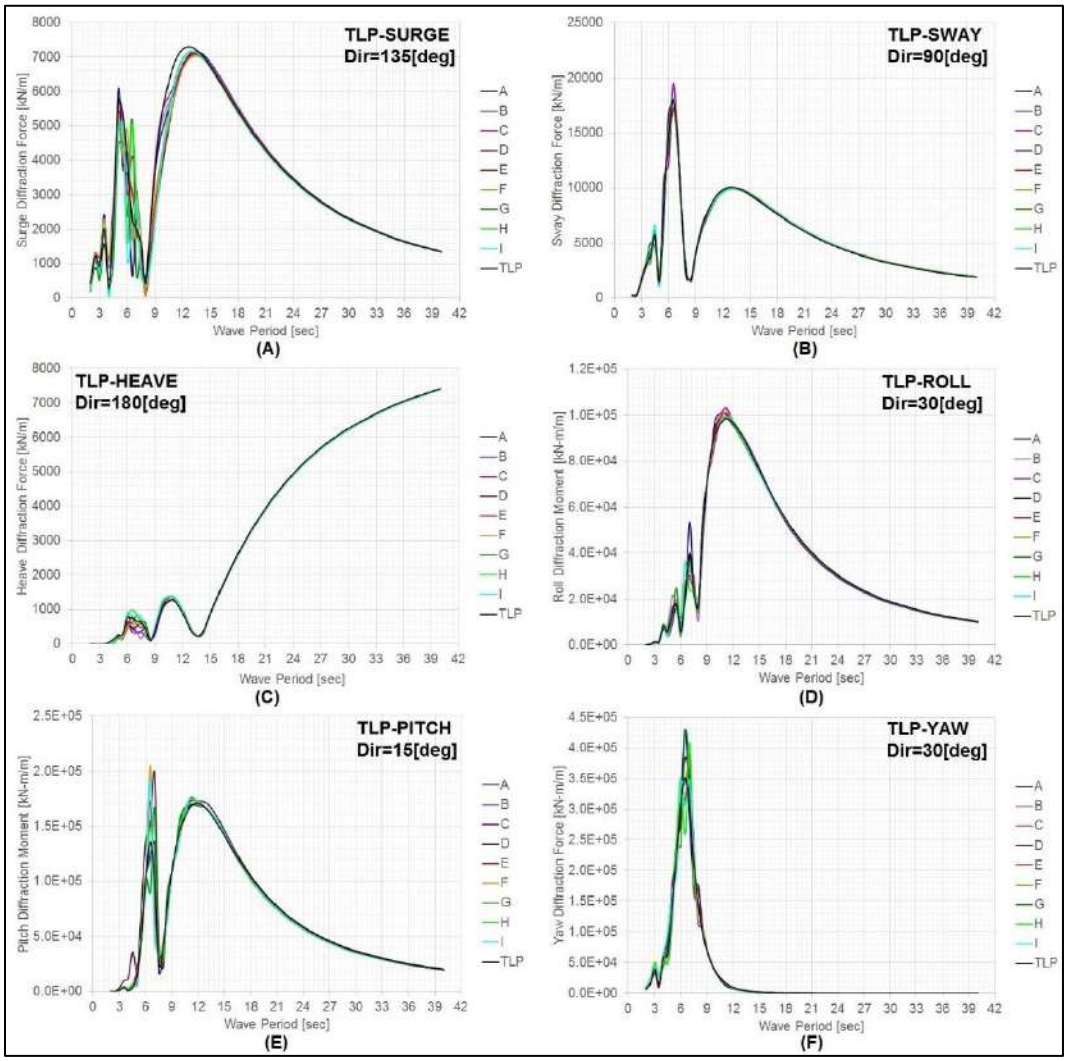

Figure 4.7 Diffraction loads on the TLP for single-body and multi-body cases.

The diffraction loads on the TAD present higher differences than the observed on the TLP between the single-body and multi-body cases. The larger variations occur in the vicinity of the peak forces and for wave periods in the range of [2 – 12] sec. No significant differences are observed between the single-body and multi-body cases for larger periods.

In general, despite some small variations, the differences between the single-body and multi-body cases, for both floaters, are relatively small. Thus, the presence of one body does not modify the wave diffraction loads significantly on the other one, i.e., the hydrodynamic interaction between the floaters is weak.

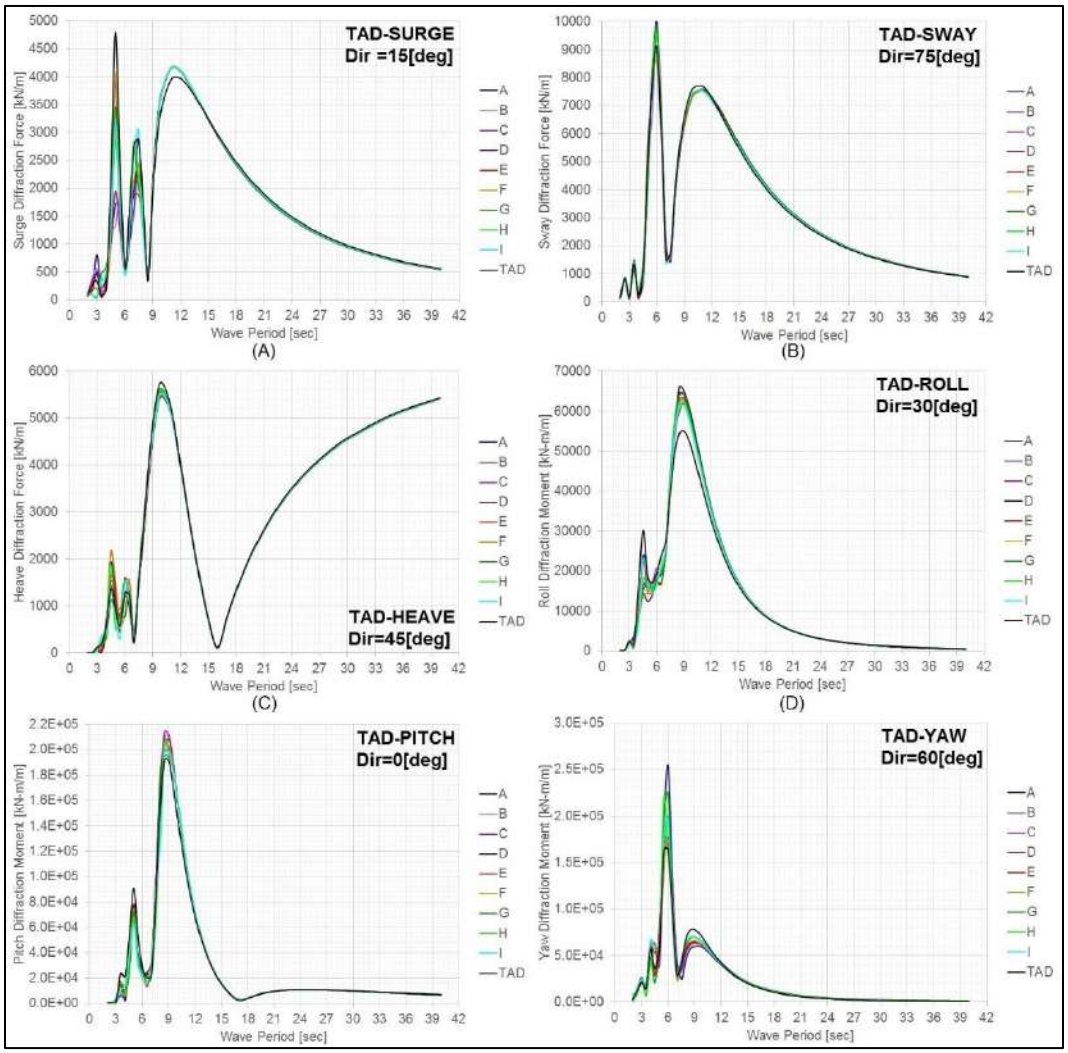

Figure 4.8 Diffraction loads on the TAD for single-body and multi-body cases.

The mean drift loads on the TLP and TAD are presented in Figs. 4.9 and 4.10, respectively. The results for the single-body and multi-body cases are shown together. The mean drift loads on the TLP present small differences for periods greater than 12 sec. However, for shorter periods, the trends depend on the mode. For instance, Surge presents significant variations for wave periods in the range of [5 -12] sec. Sway and Heave present relatively small differences over the entire range of wave periods. Roll and Pitch present the largest variations in the range of [2 – 10] sec. Finally, Yaw motion presents the largest discrepancies over the entire wave period range.

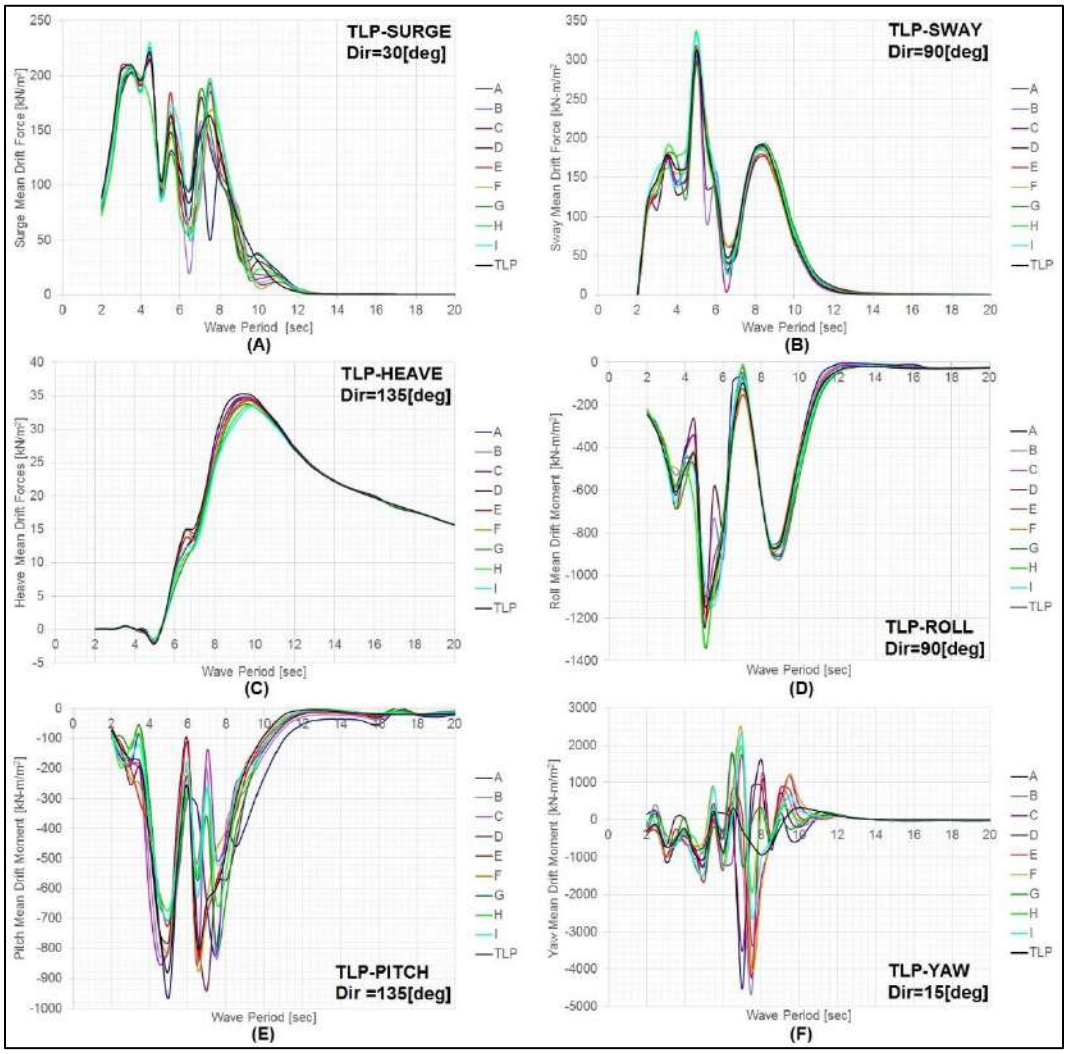

Figure 4.9 Mean drift loads on the TLP for single-body and multi-body cases.

The mean drift loads on the TAD unit present significant differences for periods in the range of [2 – 8] sec. That is, the variations are concentrated in a smaller range of wave periods than in the case of the TLP. Surge, Sway and Heave motions present minor variations between the single-body and multi-body cases. However, it is evident that the trends are approximately the same for all of these cases in each mode. Roll and Pitch present small variations around the peak loads, particularly in the range of [6 - 8] sec. Finally, the mean drift moment for Yaw present the largest discrepancies in terms of trends and order of magnitude for the entire wave period range.

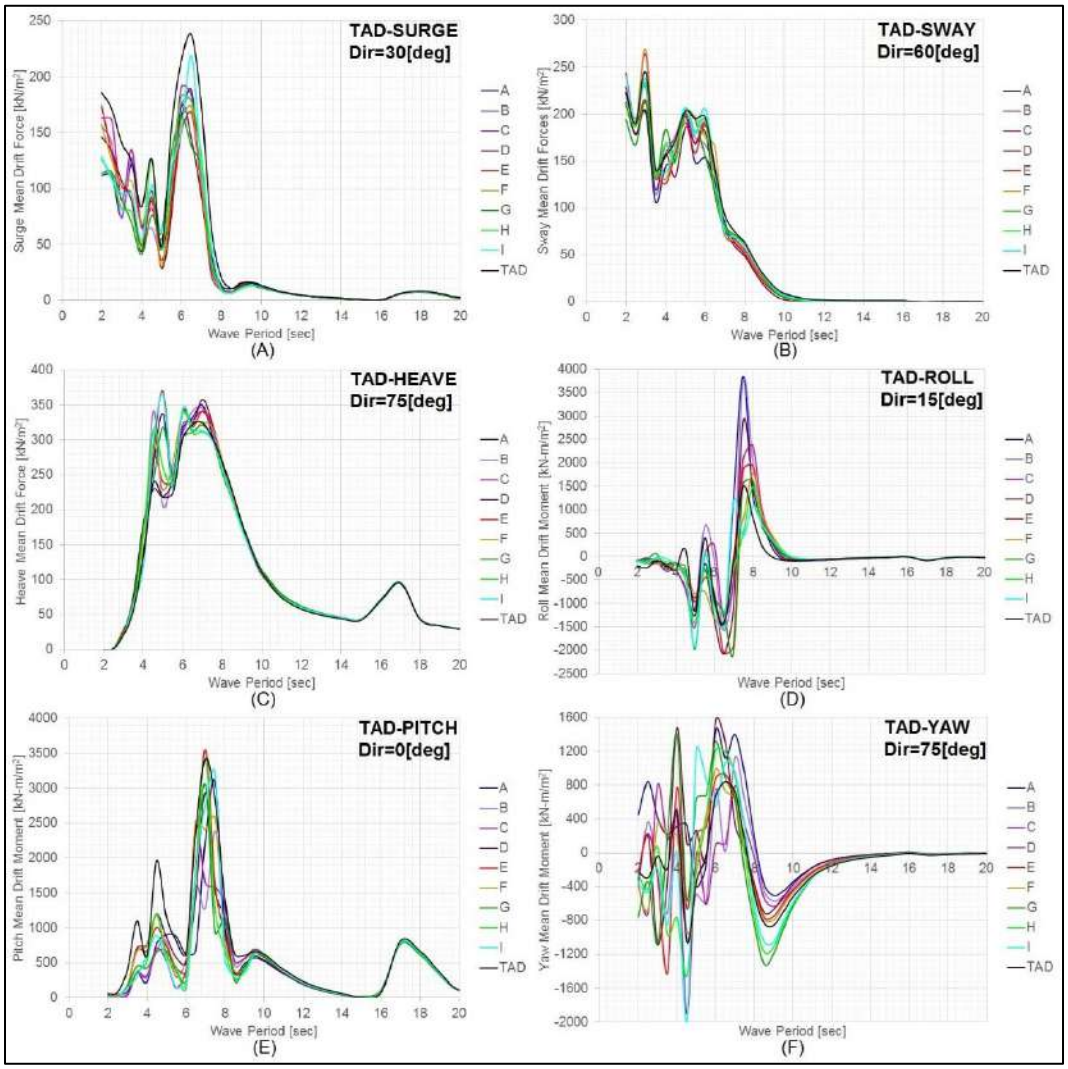

Figure 4.10 Mean drift loads on the TAD for single-body and multi-body cases.

In general, the variations in mean drift loads were considerably higher than those observed for linear diffraction loads. The linear motions (Surge, Sway, and Heave) present smaller differences, while the rotational motions (Roll, Pitch, and Yaw) present higher variations, particularly for Yaw.

Figures 4.11 and 4.12 present a comparison of the RAOs of the TLP and TAD, respectively. In the case of the TLP, the RAOs do not present relevant differences between the single-body and multi-body cases. Only Yaw motion presents significant variations over the wave period range of [5-8] sec.

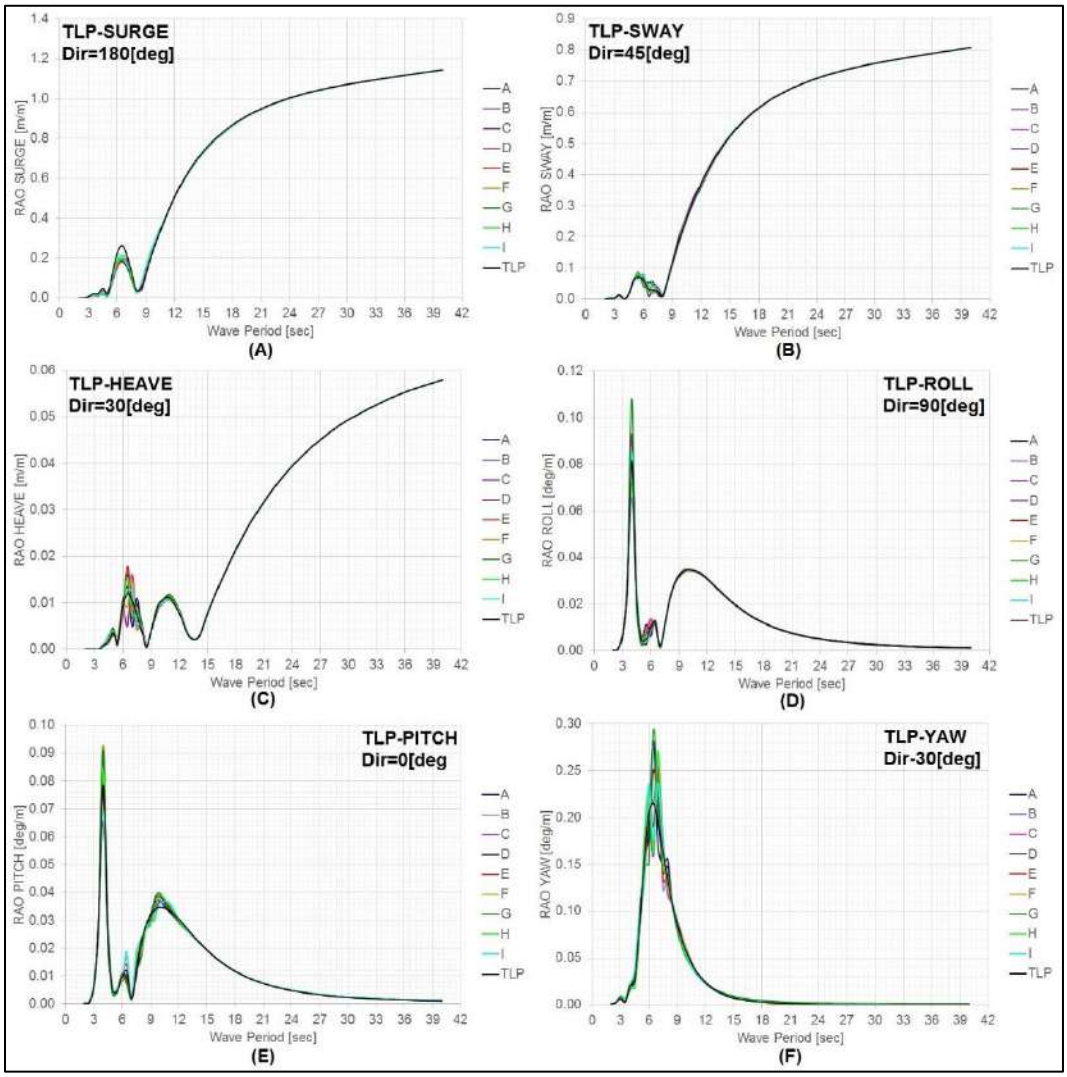

Figure 4.11 RAOs of the TLP for the single-body and multi-body cases.

The trend observed in the RAOs of the TLP is reported in the TAD unit as well, i.e., small differences exist in all modes except for Yaw, which presents significant variations for wave periods over the range of [5-12] sec.

In general, neither units presented any major modifications in the RAOs due to the presence of the other floater. Consequently, it is possible to conclude that the hydrodynamic coefficients present a relatively weak coupling effect. The behavior of one body in the multi-system can be approximated by its behavior alone.

An interesting aspect of this analysis is related to the CPU time consumed by the two approaches. In general, no significant differences were found with similar grades of mesh refinement.

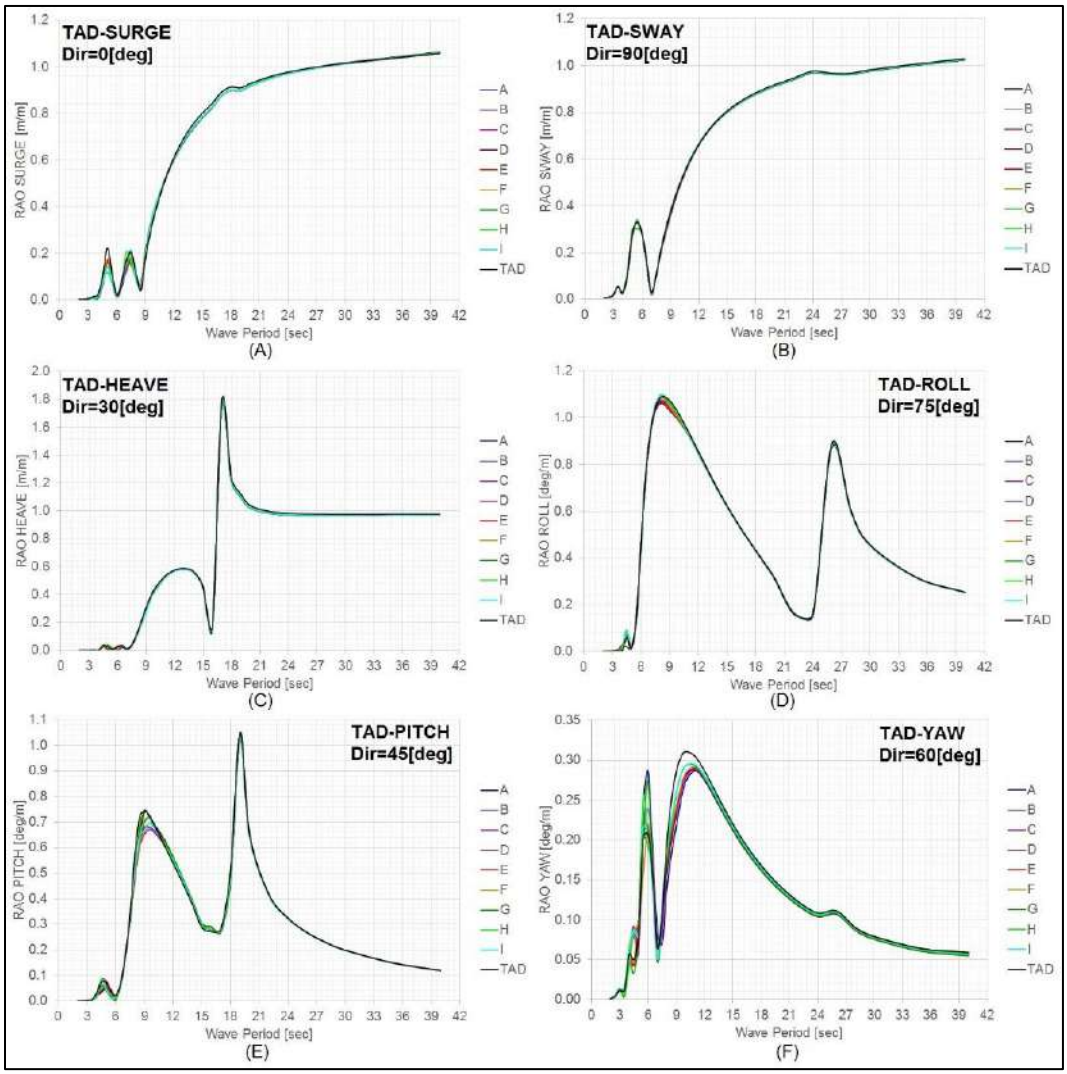

Figure 4.12 RAOs of the TAD unit for single-body and multi-body cases.

Another important conclusion of this analysis corresponds to the variation of the hydrodynamic coefficients with the relative position of the bodies. Normally, in time domain simulations, these coefficients are considered to be constant. This study has proved that this approximation is reasonable due to the relatively small variation in these coefficients with the position of the floaters.

4.2.4 Response in Regular Sea

In this section, the behavior of the multi-body system is analyzed using regular waves. The RAOs of the TLP and TAD reported in the previous section are compared with time domain simulations performed in Orcaflex [70].

As mentioned above, the frequency domain omits the nonlinear properties of the mooring lines, the interaction between floating bodies and mooring lines, the drag forces and the added mass of mooring. In addition, the RAOs are considered to be linear, i.e., these coefficients do not depend on the wave amplitude. In contrast, time domain simulations include all of these aspects that were omitted in the frequency domain. Therefore, here is examined the accuracy of the frequency domain predictions relative to those of the more realistic study performed with the time domain approach.

Table 4.3 presents the wave periods and the wave amplitudes considered in this analysis. Note that, to investigate possible nonlinear effects in the RAOs, two wave amplitudes were taken into account for each wave period. The wave headings considered in the study ranged from 0° to 180° in steps of 45°. As in the frequency domain analysis, the damping ratios presented in Appendix B were included in the time domain simulations.

Table 4.3 Regular wave characteristics used in the time domains simulations

Wave No.	1	2	3	4	5	6	7	8	9	10	11	12	13	14	15	16	17	18	19	20	21
Period [sec]	2.0	2.5	3.0	3.5	4.0	4.5	5.0	5.5	6.0	6.5	7.0	8.0	9.0	10	12	14	16	18	20	25	30
H1 [m]	0.5	0.5	0.5	0.5	0.5	0.5	0.5	0.5	0.5	0.5	0.5	0.5	0.5	0.5	0.5	0.5	0.5	0.5	0.5	0.5	0.5
H2 [m]	0.9	1.4	2.0	2.7	3.5	4.4	5.5	6.0	6.0	6.0	6.0	6.0	6.0	6.0	6.0	6.0	6.0	6.0	6.0	6.0	6.0

Figure 4.13 presents the time domain RAOs of the TLP and TAD for the single-body cases considering the wave heights H1 and H2 of Tab. 4.3. Despite small

differences observed for wave periods higher than 15 sec., the RAOs present the same behavior for both wave heights.

Figure 4.14 shows the results of the time domain simulations considering the multi-body cases. In this case, the RAOs show more dependence on the wave height. The differences are slightly higher than for the single-body cases. Note that, for the single-body and multi-body cases, the highest values of the RAOs do not necessarily correspond to the highest wave amplitude, i.e., in some wave periods, the maximum response amplitude corresponds to the lowest wave amplitude.

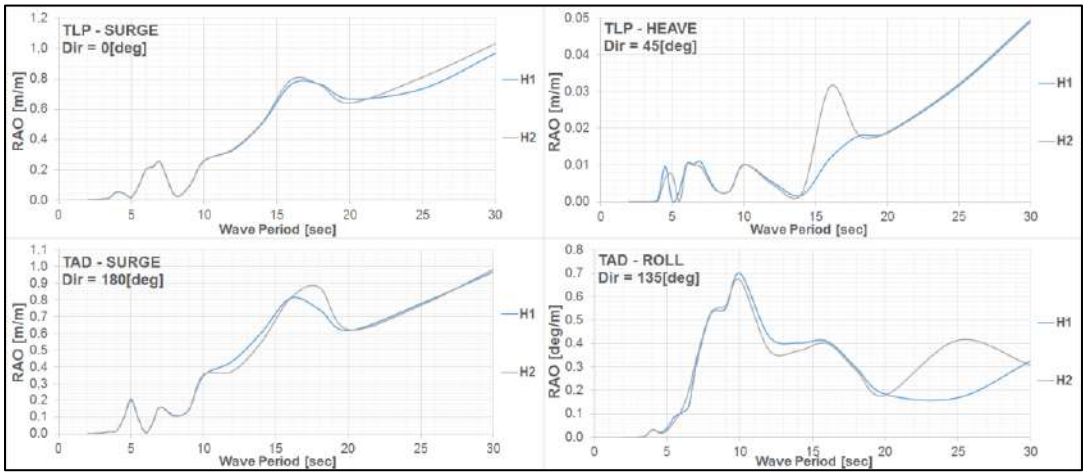

Figure 4.13 Time domain RAOs of the TLP and TAD for the single-body cases.

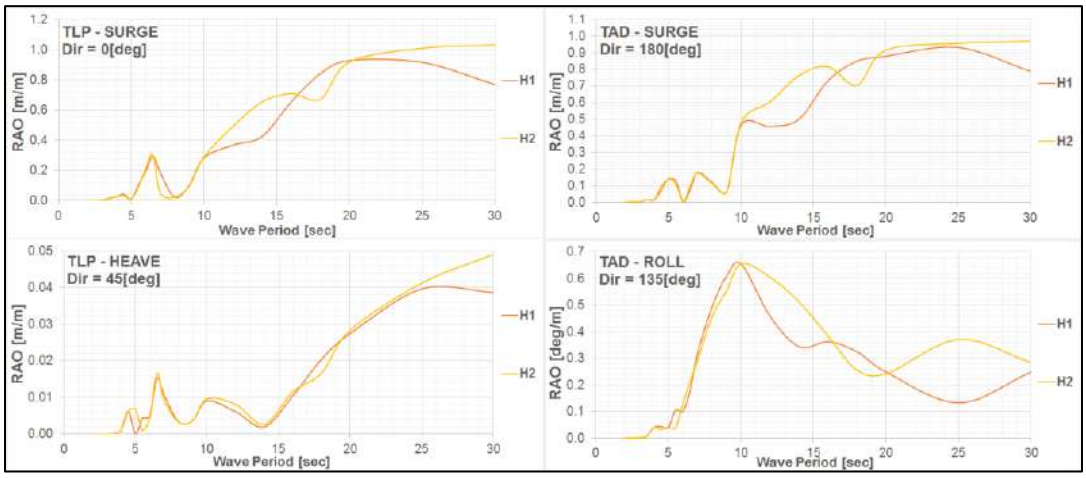

Figure 4.14 Time domain RAOs of the TLP and TAD for the multi-body cases.

Figure 4.15 presents a comparison between the single-body and multi-body cases for wave height H1. The largest differences occur at the larger wave periods.

Moreover, these disparities are considerably higher than those predicted by the frequency domain predictions. In general, significant differences arise for periods greater than 10 sec.

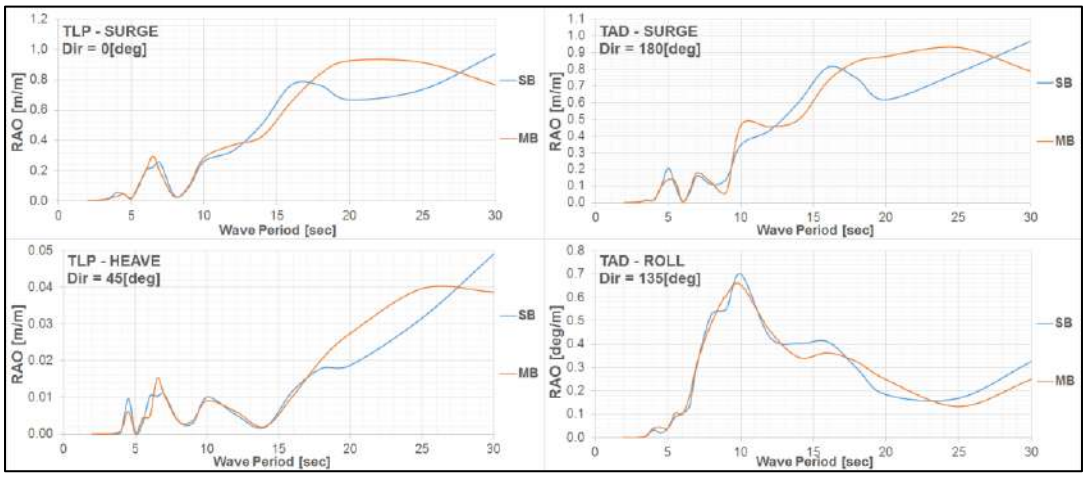

Figure 4.15 Time domain RAOs of the TLP and TAD. Single-body (SB) vs. Multi-body (MB).

Finally, a comparison between the frequency domain (FD) and time domain (TD) predictions is presented below. Figure 4.16 presents a comparison of the response amplitude operator (RAOs) of the TLP for the following cases: TLP alone in the frequency domain (FD_AL); TLP coupled with TAD in the frequency domain (FD_CO); TLP alone in the time domain with wave height H1 (A1_TD_AL); TLP coupled with TAD in the time domain with wave height H1 (A1_TD_CO); TLP alone in the time domain with wave height H2 (A2_TD_AL); and TLP coupled with TAD in the time domain with wave height H2 (A2_TD_CO).

This analysis reveals relevant differences for wave periods in the range of [10 - 30] sec. Note that, for Surge and Yaw, the frequency domain predictions are the most conservatives. For Heave, Roll, and Pitch, peaks that the frequency domain approach does not predict are observed in the time domain simulations for wave periods of 16.0, 4.0, and 4.0 sec., respectively. Finally, for Yaw motion, at some wave headings, no motions are observed in the frequency domain. However, the time domain simulations reveal small motions in the range of wave periods of [5 – 10] sec.

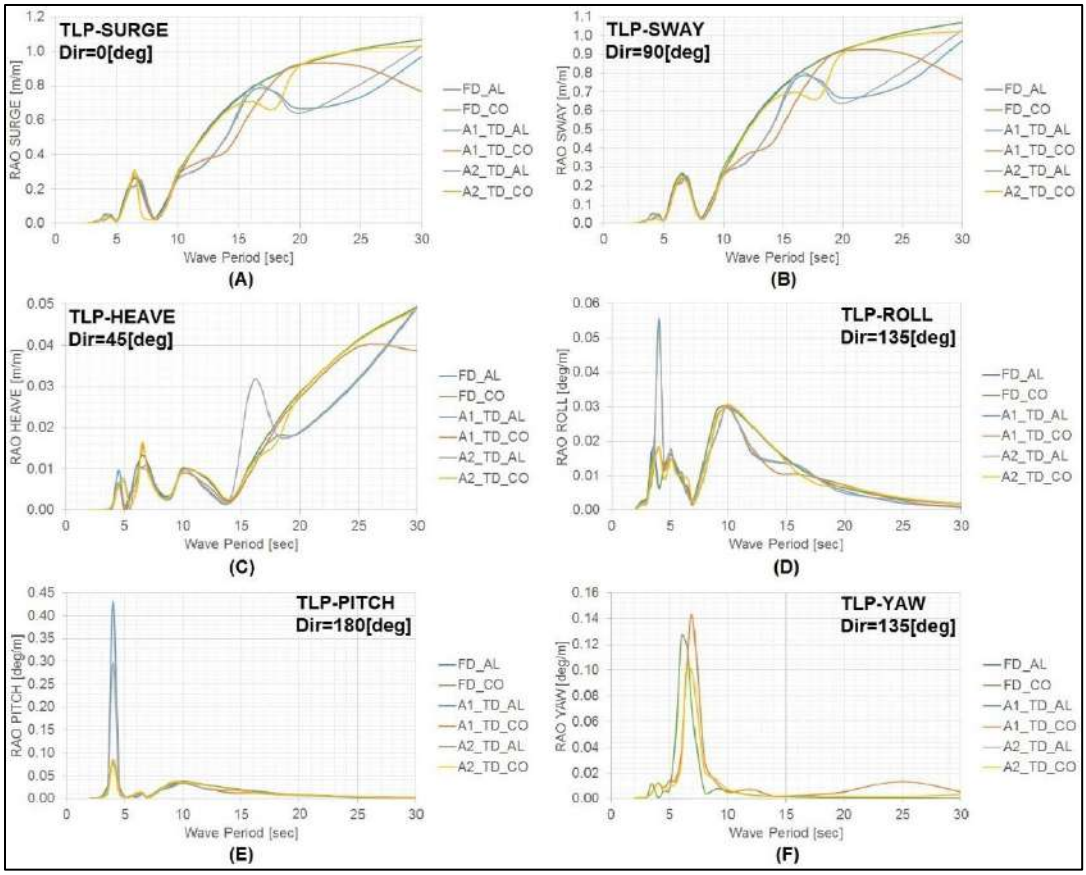

Figure 4.16 – RAO of the TLP for the single-body and multi-body cases analyzed by frequency and time domain.

Similarly, Figure 4.17 presents a comparison of response amplitude operator (RAOs) of the TAD for the following cases: TAD alone in the frequency domain (FD_AL); TAD coupled with TLP in the frequency domain (FD_CO); TAD alone in the time domain with wave height H1 (A1_TD_AL); TAD coupled with TLP in the time domain with wave height H1 (A2_TD_AL); TAD alone in the time domain with wave height H2 (A1_TD_CO); and TAD coupled with TLP in the time domain with wave height H2 (A2_TD_CO).

For the TAD, the highest variations occur in the range of wave periods of [10 - 30] sec. However, the frequency domain predictions were the more conservative ones for all modes, with some exceptions for certain wave headings for Roll and Pitch as shown in Fig. 4.17.

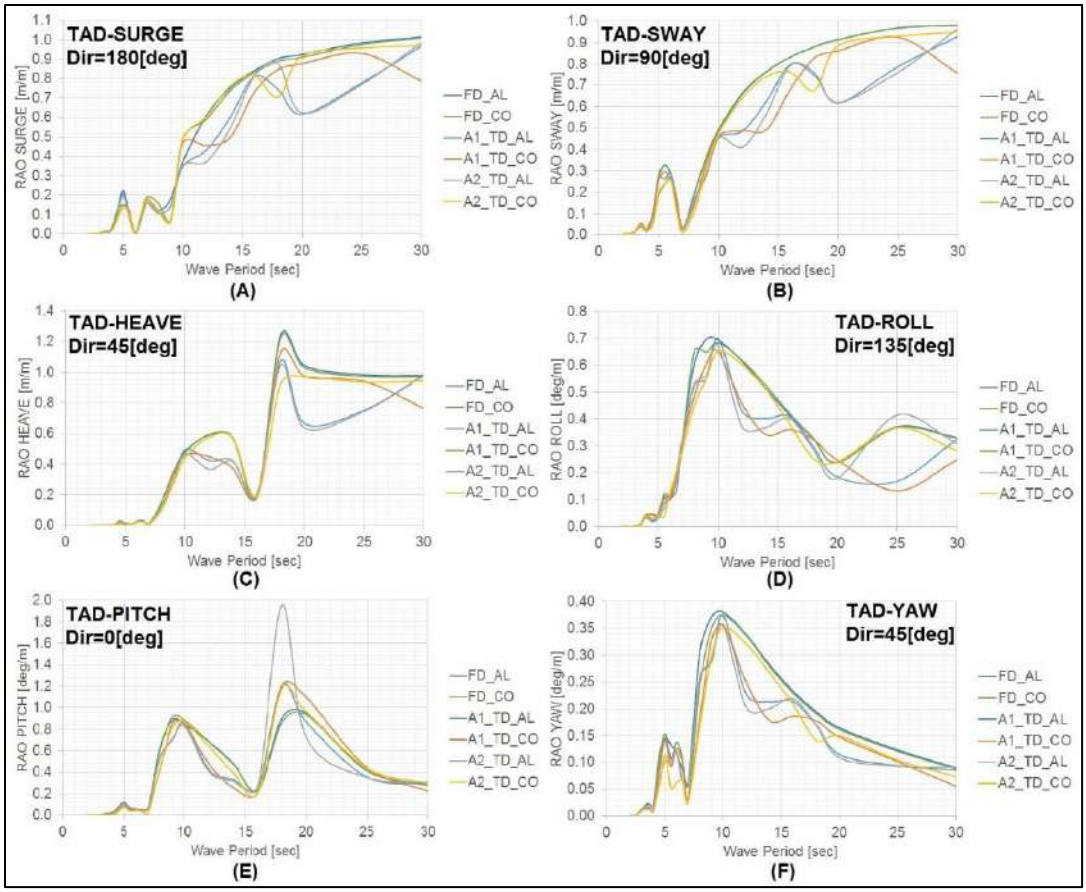

Figure 4.17 – RAO of the TAD for the single-body and multi-body cases analyzed in the frequency and time domain.

In general, major differences between the time domain and the frequency domain predictions were observed, particularly for periods in the range of [10 – 30] sec. In addition, the variations between the cases analyzed with the time domain approach are significantly larger than the differences between cases examined with the frequency domain approach. Therefore, these differences can be explained for the more realistic representation of mooring lines in the time domain simulations.

Furthermore, the horizontal modes present the most significant differences between the single-body and multi-body cases. It confirms the influence of the hawser system; note that, as shown in Section 3.4 the hawser system primarily modifies the behavior of the horizontal modes of the floaters.

For most of the cases, the frequency domain predictions were the most conservative. Therefore, the frequency domain approach can be used as a useful and quick tool in the analysis of the system in the initial design stages.

4.2.5 Response in Irregular Sea

In this section, the behavior of the multi-body system is analyzed in seas with irregular waves. Table 4.4 presents the combinations of significant wave height (Hs), peak period (Tp) and Gamma parameter (Ga) considered in this analysis. The JONSWAP spectrum with three parameters (Hs, Tp, Ga) [43] was used to represent the energy distribution of the irregular sea, as shown in Fig. 4.18. The range of wave headings considered in this analysis is from 0° to 180° with steps of 45°.

In the frequency domain, the response of the floating structures S_{xx} corresponds to the power spectral density (PSD) calculated by the Eqn. (4.1).

$$S_{xx} = S_{\omega} * RAO^2 \tag{4.1}$$

where S_{ω} is the sea spectrum, and RAO is the Response Amplitude Operator of the body. The RAOs take into account the hydrodynamic coefficients of added mass, potential damping and diffraction loads. Note that, the mooring lines are modeled by linear stiffness matrixes.

Table 4.4 Wave conditions for the irregular sea analysis

Wave code	Hs [m]	Tp [sec]	Ga [-]
J1	0.5	5.0	2.8
J2	2.5	7.5	2.2
J3	4.5	10.0	2.0
J4	6.0	12.0	1.6
J5	7.5	13.5	1.4

In the time domain, in addition to the hydrodynamic coefficients mentioned above, both the mean drift loads and low-frequency QTFs approximated with the Newman method described in Section 2.4.3 were included into the Orcaflex runs. As discusses in Section 2.5, the time domain simulations model the mooring lines using the Finite Element Method (FEM), which provides a more realistic representation of these structural elements and considers drag forces and added mass on mooring lines. Consequently, the nonlinear properties of the mooring system and the interaction between the lines and floating bodies are taken into account.

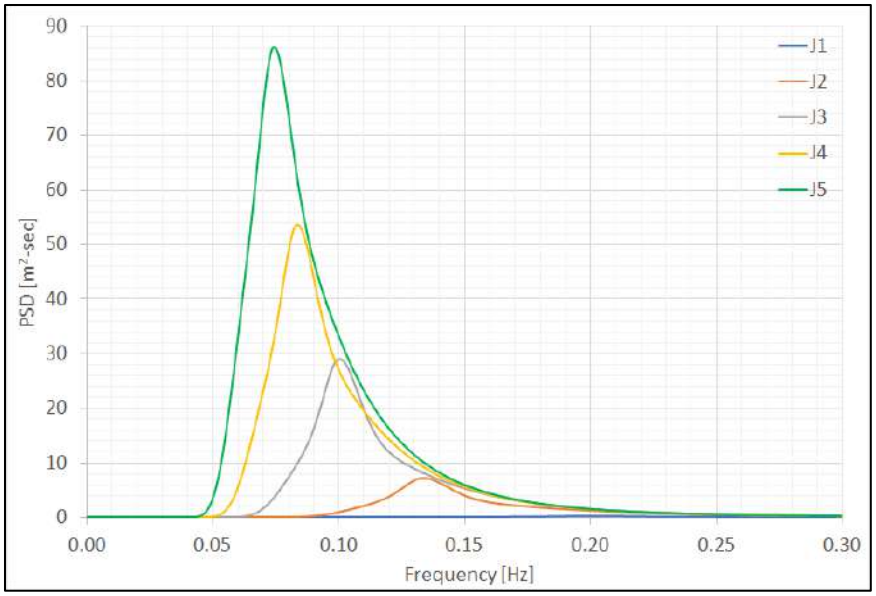

Figure 4.18 JONSWAP wave spectrum considered in the irregular sea analysis

As recommended in [24], the time domain simulations with irregular waves are performed considering storms of 3-hours duration. Finally, the comparison between the frequency domain (FD) and time domain (TD) predictions is made using the power spectral density (PSD) calculated by the Fast Fourier Transform (FFT) applied to the time series of the floater response.

Figure 4.19 presents the comparison between the frequency domain and time domain responses of the TLP alone in irregular waves. For Surge and Sway motions, the FD presents excellent agreement for the range of wave frequencies of [0.05 – 0.10] Hz. However, the low-frequency response shows higher energy that the FD do not include.

Heave presents reasonable agreement, particularly for frequencies in the range of [0.04 – 0.16] Hz. The peak energy at 0.227Hz does not appear in FD results, note that the TD simulations do not consider high-frequency second-order loads, consequently, the peak of energy at the natural frequency of the TLP for Heave correspond to the response of the tendons, which are represented accurately using FEM.

Roll and Pitch motions present reasonable agreement between the FD and TD predictions, even in the high-frequency range. Finally, Yaw presents the worst

agreement. Although it is a low-frequency motion, the FD does not represent this range of wave frequencies.

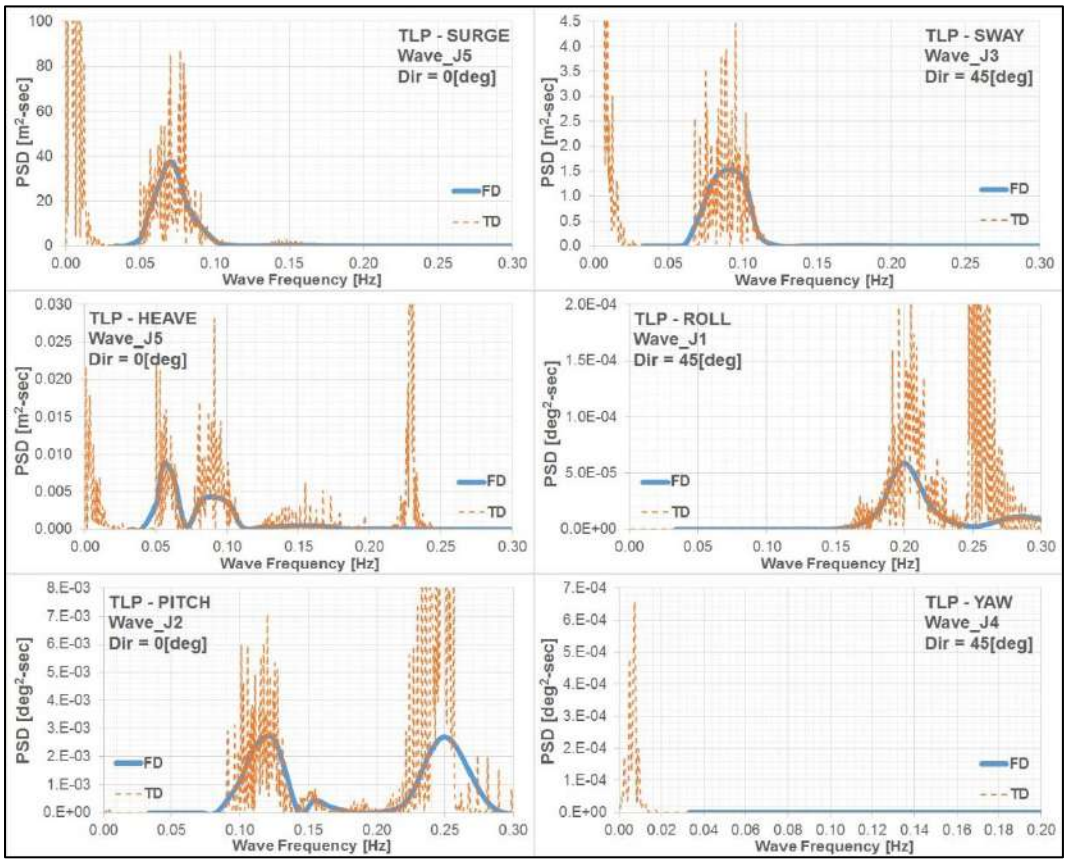

Figure 4.19 – Response of the TLP alone analyzed by the FD and TD.

Figure 4.20 presents the comparison between the frequency and time domain responses of the coupled TLP in random waves. The differences between the FD and TD predictions were essentially the same as in the case of the TLP alone. FD presents reasonable agreement for the main wave frequency ranges; however, FD does not represent the low-frequency and high-frequency responses. As in the case of TLP alone, Yaw motion presents the worst agreement, the low-frequency range is not properly represented, and even some peaks in high-frequency are observed in the FD predictions.

Figure 4.21 compares the frequency and time domain response of the TAD alone in random waves. In general, the predictions of the FD approach present excellent results for frequencies in the range of [0.05 – 0.30] Hz. for all degrees of freedom.

However, the FD approach fails to represent the low-frequency responses, and for some modes (namely, Surge, Sway, and Yaw) this part of the energy distribution presents the highest peaks in the TD results.

Finally, Figure 4.22 presents the comparison between the frequency and time domain response of the TAD coupled in irregular waves. In general, the same observations from the TAD alone case can be applied to the multi-body cases.

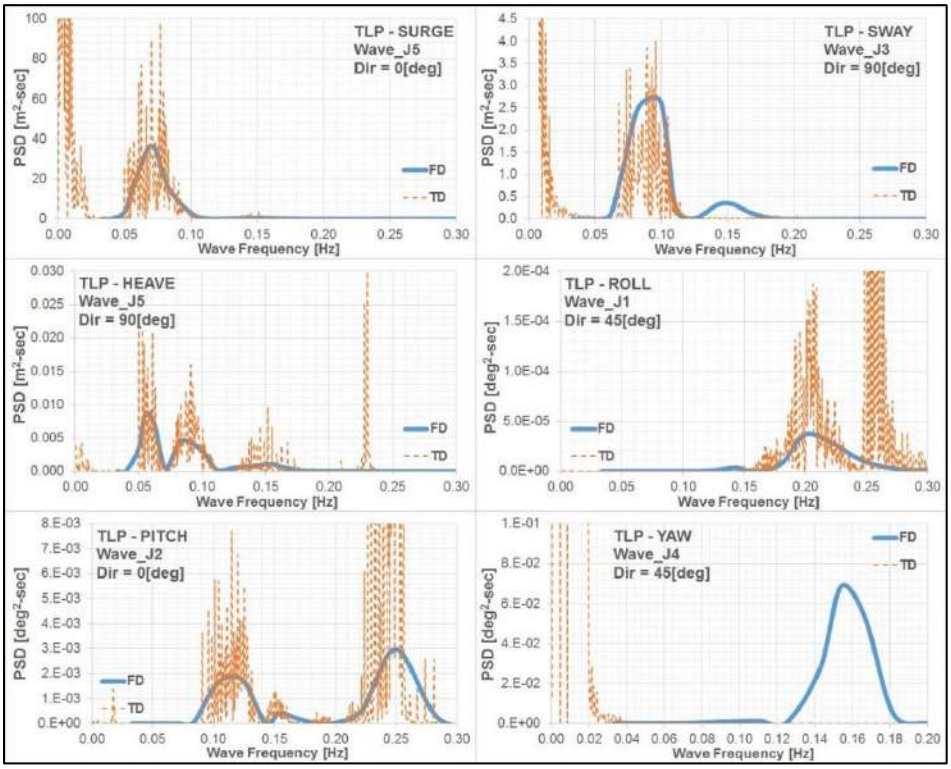

Figure 4.20 – Response of coupled TLP analyzed in the frequency and time domain.

In general, the FD predictions present favorable results relative to the TD results for the main wave frequency range. The FD approach did not consider low-frequency and high-frequency loads, consequently, the predictions of this method fails to represent these frequency regions.

Unfortunately, in some cases, the low-frequency and high-frequency contributions represent, in terms of energy, the strongest part of the responses. Thus, in the analysis of the TLP-TAD multi-body system subject to irregular waves, the FD approach must be applied with extreme care and with knowledge of its significant limitations.

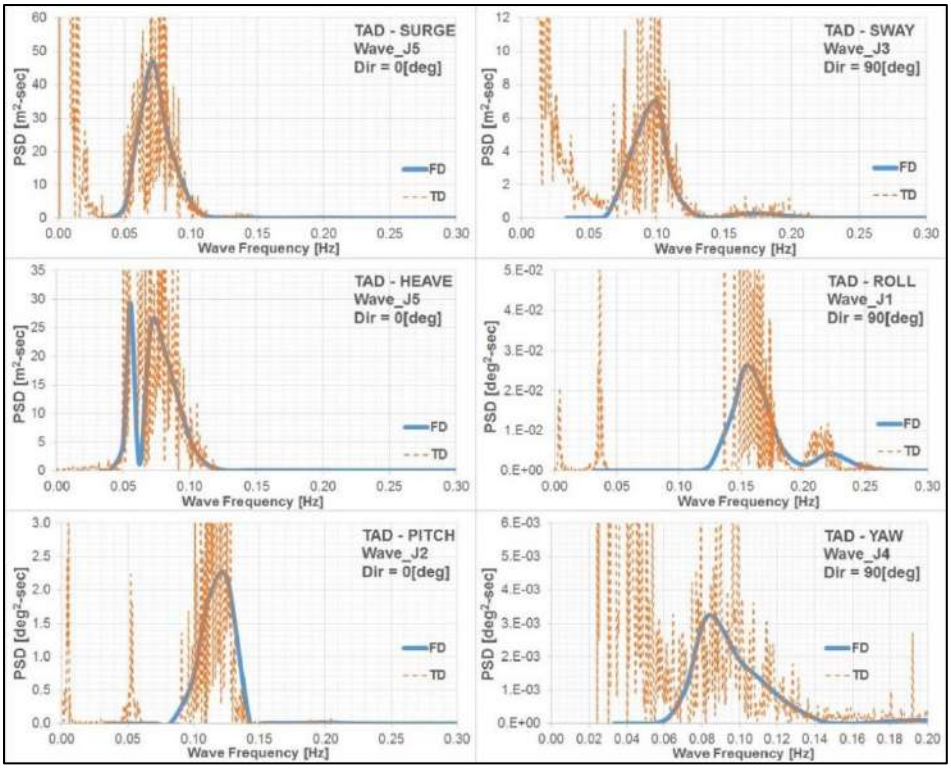

Figure 4.21 – Response of the TAD alone analyzed in the FD and TD.

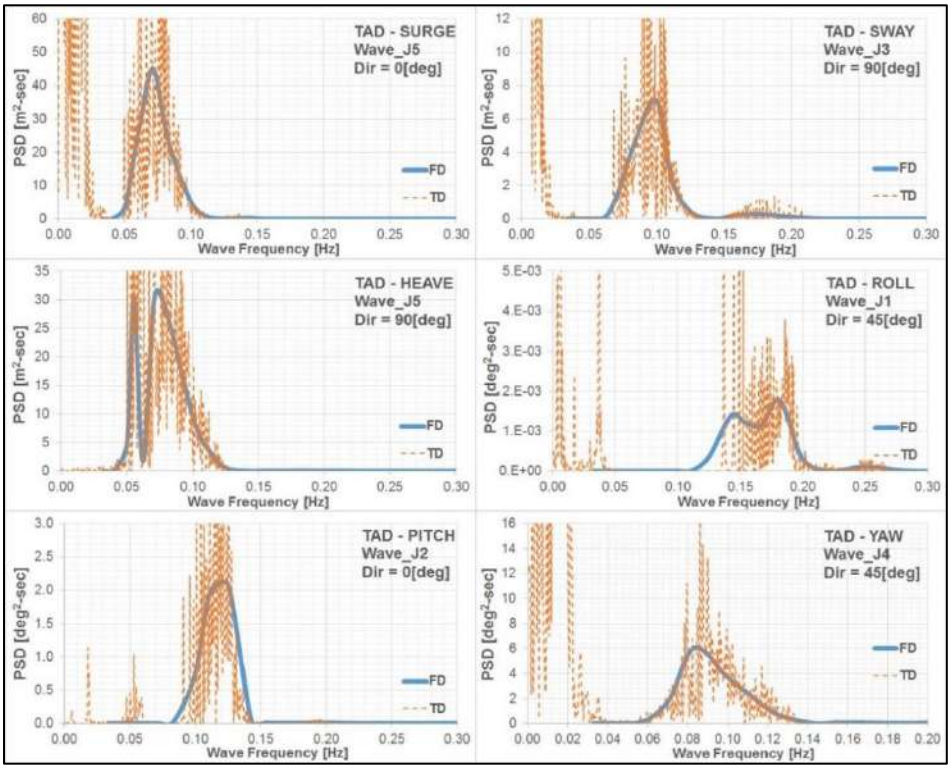

Figure 4.22 – Response of the coupled TAD analyzed in the FD and TD.

4.3 SECOND-ORDER WAVE LOADS

The second-order loads are proportional to the square wave amplitude and correspond to the wave-wave and wave-body interactions [11]. Thus, these forces contain terms corresponding to frequencies equal to sums and differences of the elementary wave frequencies, i.e., wave drift loads (low-frequency effects) and sum frequency loads (high-frequency effects) [57].

Figure 4.23 presents a typical distribution of the energy of the irregular waves in the frequency domain. Vertical lines represent the natural frequencies of the TLP and TAD. The TLP has low natural frequencies in the horizontal modes (i.e., Surge, Sway, and Yaw) and high natural frequencies in the vertical modes (i.e., Heave, Roll, and Pitch). In contrast, the TAD presents low natural frequencies in horizontal and vertical modes.

Note that, the natural frequencies of the TLP and TAD are out of the high-energy region where the first-order loads are predominant. However, these are located in areas where the second-order loads of low and high frequencies are predominant. Furthermore, possible resonant motions due to the second-order loads must be investigated and considered in the moored system design of the TLP-TAD system.

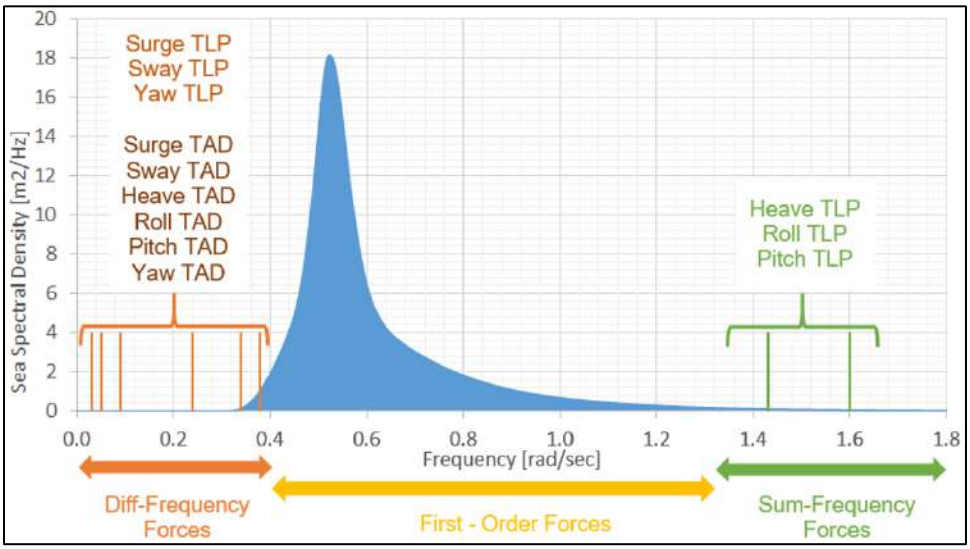

Figure 4.23 Typical wave energy spectrum and natural frequencies of TLP-TAD system.

This section presents a numerical study of the second-order wave loads on the TLP-TAD multi-body system. Second-order wave loads are represented by the quadratic transfer

function (QTF). An extensive hydrodynamic analysis focusing on the hydrodynamic interactions between the floaters and how these effects modify the second-order loads on the platforms was performed.

The second-order Quadratic Transfer Functions (QTFs) were evaluated using the indirect and direct methods presented in Section 2.4. The importance of the free surface integral (FSI) shown in Section 2.4.2 in the estimation of the second-order QTFs was checked. In addition, the accuracy of the Newman approximation (NA) presented in Section 2.4.3 for the low-frequency QTF was evaluated. Finally, time domain simulations were conducted to complete the analysis of the NA accuracy and the importance of sum-frequency loads on the behavior of the TLP-TAD multi-body system.

4.3.1 Free Surface Discretization

The computation of the second-order wave loads requires the discretization of the hull and the free surface around the bodies. The computational grids of the floaters are presented in Section 4.2.1. The free surfaces were modeled using the computational grids presented in Fig. 4.24. Note that, the low-order panel method described above was used to represent these surfaces. Table 4.5 presents the number of panels used in the discretization of the free surface for three cases: TLP alone, TAD alone and TLP-TAD multi-body.

Chapter III contains the physical and geometrical properties of the floaters, and the linear stiffness matrixes considered in this analysis. Finally, as in the case of the first-order analysis, the damping ratios presented in Appendix B were included in the numerical simulations.

Table 4.5 Number of panels in the free surface.

Case	Number of panels	Reference
TLP alone	7680	Fig. 4.24 (A)
TAD alone	14680	Fig. 4.24 (B)
TLP+TAD	15740	Fig. 4.24 (C)

Note that, the number of panels presented in Table 4.5 represents one quadrant of the free surface in the case of the TLP alone and two quadrants for TAD alone and coupled TLP - TAD cases.

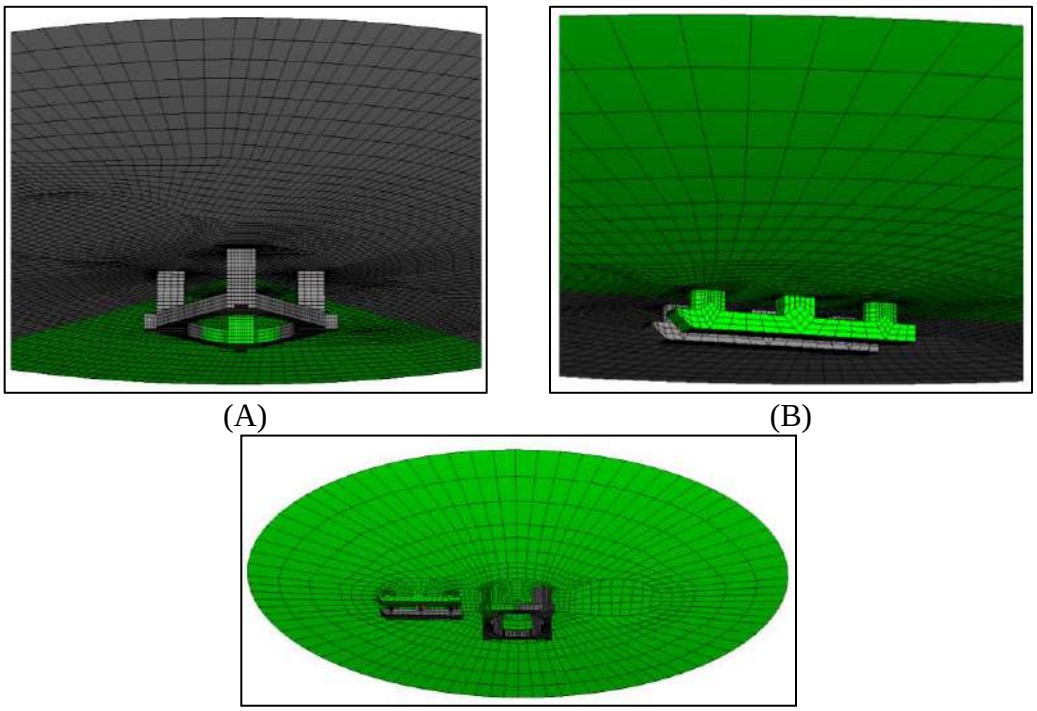

(A) (B)

(C)

Figure 4.24 – Free surface discretization (A) TLP alone, (B) TAD alone and (C) TLP-TAD multi-body case.

4.3.2 Direct Method vs. Indirect Method

As shown in Section 4.2.2, the representation of the hull of the floating bodies by a set of flat panels requires an analysis of the influence of the computational grids on the hydrodynamic coefficients. This observation can be extended to the second-order loads. Thus, the results presented in [55] indicate the dependence on second-order loads on the discretization of the free surface. In this work is also noted that the agreement between the results estimated by the direct and indirect methods indicates that the computational grids have appropriate refinement and, consequently, a satisfactory numerical convergence was achieved. Because, although the methods

were developed using different numerical formulations, the methods are physically equivalent. Hence, the results obtained from these methods must be the same.

Thus, with the aim of verifying the influence of the computational grid on the calculation of the second-order loads, a sensitivity analysis has been performed. This study included the calculations of the second-order wave loads using the direct and indirect methods presented in Section 2.4. The numerical analysis consisted of three cases: TLP alone, TAD alone and TLP connected with TAD. For all of the cases, five wave headings were considered: 0°, 45°, 90°, 135° and 180°. The range of wave frequencies considered was from 0.05 to 0.25 Hz in steps of 0.001Hz, i.e., 201 wave frequencies. The second-order wave loads were calculated for all of the frequency combinations, i.e., 20301 pair of frequencies for each wave heading.

Figure 4.25 presents the high-frequency QTF of the TLP alone based on the direct method for three cases: (namely, (A) Heave and θ = 0°, (B) Pitch and θ = 0°, and (C) Roll and θ = 45°) and the indirect method for three cases (namely, (D) Heave and θ = 0°, (E) Pitch and θ = 0°, and (F) Roll and θ = 45°).

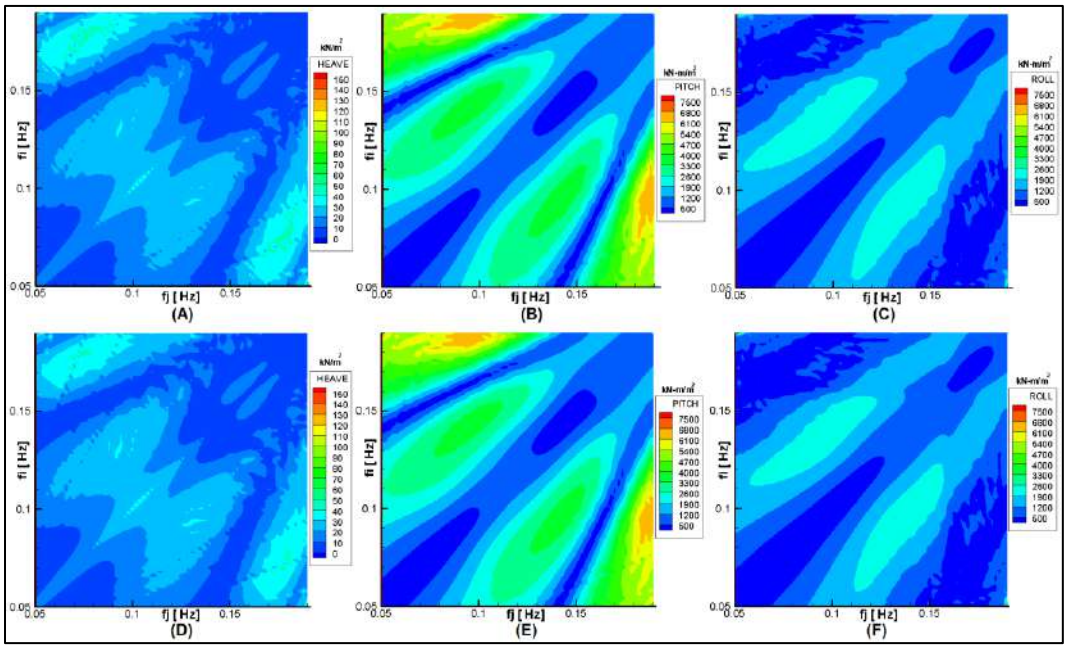

Figure 4.25 –High-frequency QTFs of TLP alone. Direct method: (A) Heave and θ=0°, (B) Pitch and θ=0°, and (C) Roll and θ=45°. Indirect method: (D) Heave and θ=0°, (E) Pitch and θ=0°, and (F) Roll and θ=45°.

Figure 4.26 presents the low-frequency QTF of the TLP for Surge for the following cases: (A) TLP alone using the direct method, (B) TLP alone using the indirect method, (C) TLP coupled with TAD using the direct method, and (D) TLP coupled with TAD using the indirect method. The wave heading for all cases is 45°.

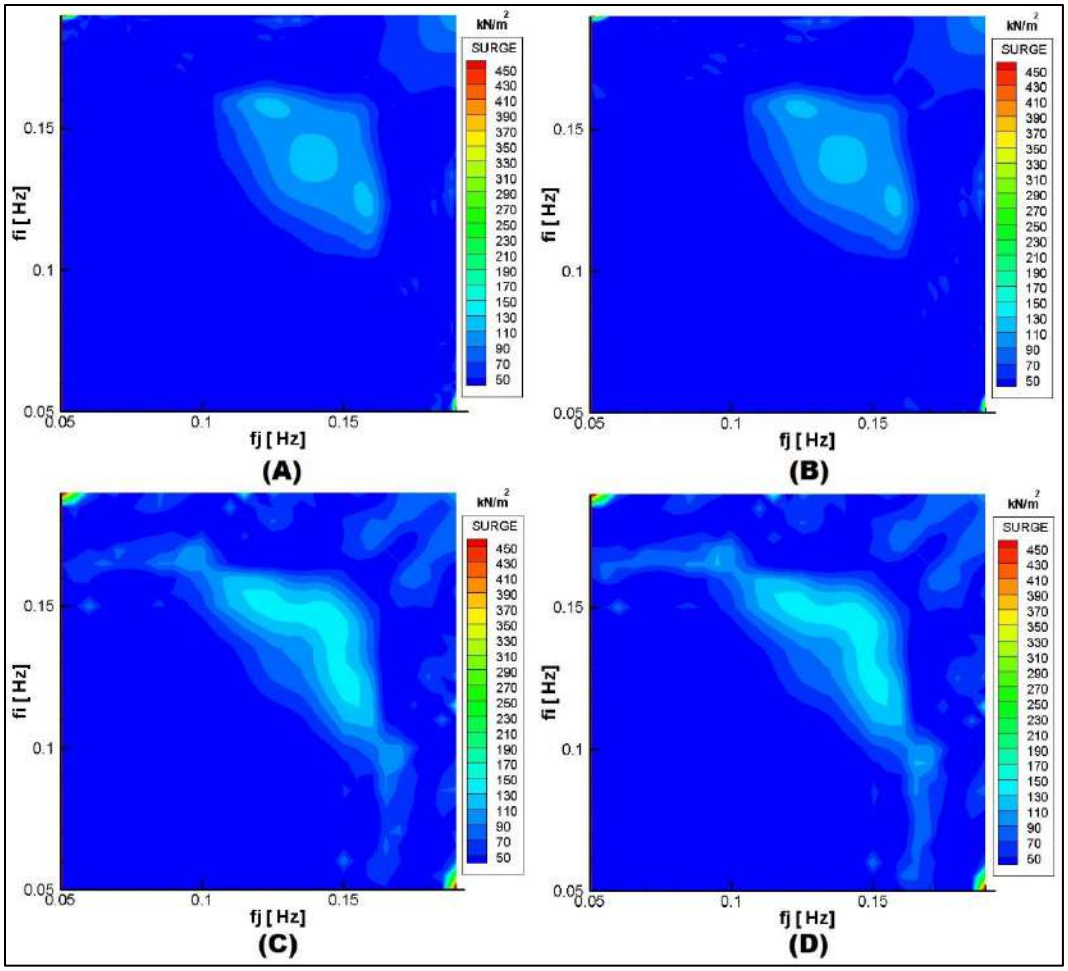

Figure 4.26 – Low-frequency QTFs for Surge and θ=45°. (A) TLP alone and direct method (B) TLP alone and indirect method (C) TLP coupled and direct method (D) TLP coupled and indirect Method

Figure 4.27 presents the low-frequency QTF of the TAD considering the following cases: (A) TAD alone using the direct method, (B) TAD alone using the indirect method, (C) TAD coupled with TLP using the direct method, and (D) TAD coupled with TLP using the indirect method. The wave heading for all cases is 45°.

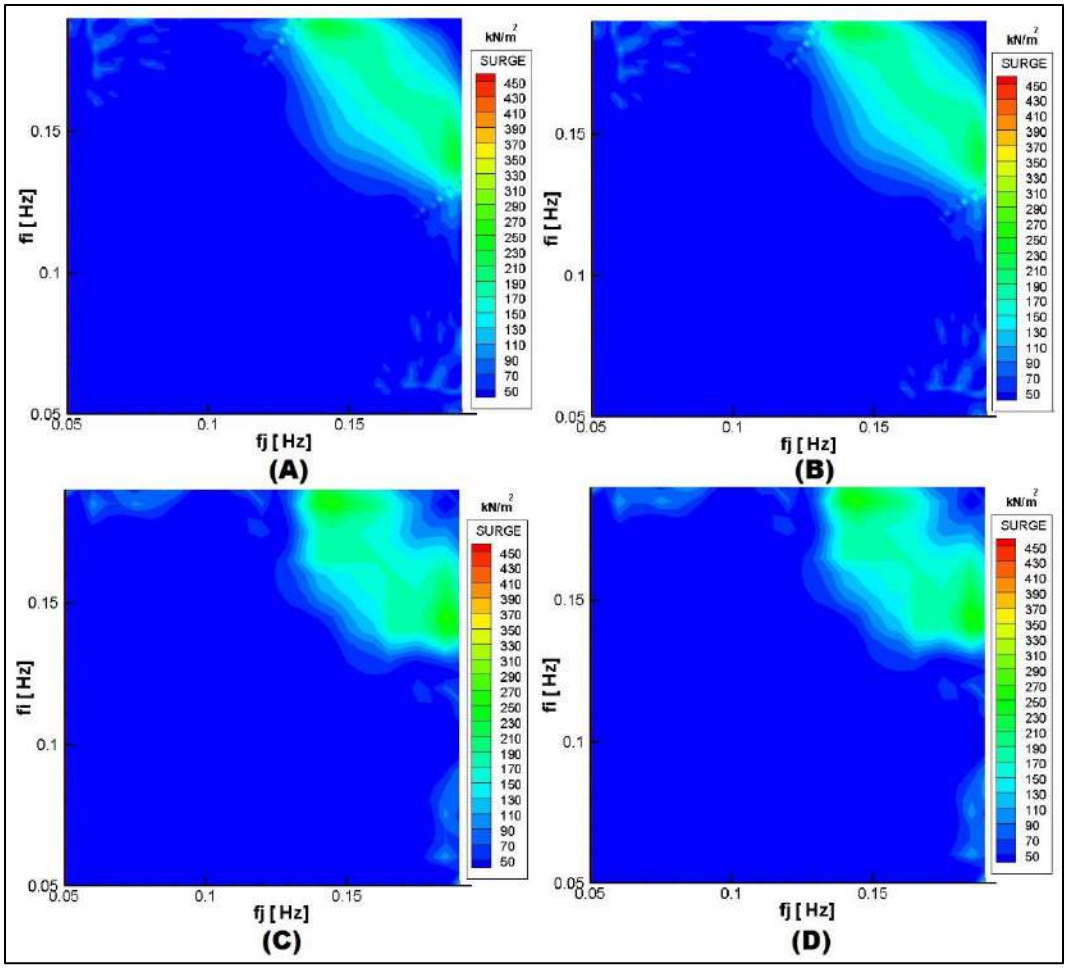

Figure 4.27 – Low-frequency QTFs for Surge and θ=45°. (A) TAD alone and direct method, (B) TAD alone and indirect method, (C) TAD coupled and direct method, and (D) TAD coupled and indirect method

In general, the direct and indirect methods present similar results, not only in the single-body cases but also for the multi-body case, and for the sum-frequency and difference-frequency QTFs. Therefore, it is possible to conclude that the mesh refinement is sufficient to achieve accurate results. In addition, it is important to note that convergence of the direct and indirect methods for low-frequency QTFs is easier than the convergence of high-frequency QTFs. The high-frequency QTFs require fine refinement in the free surface to achieve the same results with both methods. Therefore, the convergence of high-frequency QTFs must take priority in the analysis of the TLP-TAD multi-body system.

Furthermore, the differences observed between the alone and coupled cases in Figs. 4.26 and 4.27 present evidence of hydrodynamic coupling effects on the second-order loads. The results of Section 4.2.3 proved that hydrodynamic coupling effects are weak in linear wave loads. However, the second-order loads appear not to follow the same trend.

4.3.3 Importance of The Free Surface Integral

As noted in Section 2.4, computation of the free surface integral (FSI) requires an enormous amount of time. Thus, several studies have discussed the relevance of this term in the calculation of low and high-frequency QTFs, for instance [63] and [75]. Although most of these studies have concluded that the free surface integral has no significant impact on the computation of low-frequency second-order loads, these conclusions are limited to ship-shaped floaters. Consequently, the importance of the free surface integral needs to be evaluated for geometries with pontoons and columns as is the case for the geometry of the TLP and TAD.

Furthermore, [60] demonstrated that the free surface integral is a relevant term in the calculation of high-frequency second-order loads. However, that conclusion is also assessed for the TLP-TAD multi-body system by the analysis described below.

Using the computational grids validated in the previous section, the analysis of the influence of the free surface integral was performed using the direct method and comparing the results obtained with and without the Free Surface Integral (FSI).

Figure 4.28 presents the low-frequency QTFs of the TLP alone for Surge motion and the high-frequency QTFs of the TLP alone for Heave. The comparison of QTFs for Surge reveals differences in the regions $(f_i \cong f_j)$ and $(f_i > 0.15\,Hz \cap f_j < 0.10\,Hz)$; some peaks forces estimated by the direct method consider the FSI are not reproduced in the results that do not consider the FSI. The differences become more significant in the case of Heave, in which the high-frequency QTFs calculated without the FSI present substantially different results over the entire range of frequencies.

Figure 4.29 presents the low-frequency QTFs of the TAD alone for Surge and Heave motion. In the case of TAD, the analysis of QTFs for Surge reveals significant differences, relatively high forces are observed in the regions $(f_i > 0.15\,Hz \cap f_j <$

$0.10\ Hz)$ and $f_i \cong f_j$ in the results with the FSI that are not present in the calculation without the FSI. Similar results are found in the QTFs for Heave motions.

In general, the differences between QTFs computed with and without the FSI were significant at low and high-frequencies. In the case of low-frequency QTFs, the differences were higher in regions away from the diagonal $f_i \cong f_j$. Thus, if the natural frequency of the floating body is close to the diagonal $f_i \cong f_j$, these differences may not be relevant, while if the natural frequency is far from the diagonal, the QTFs without the FSI may provide inaccurate results.

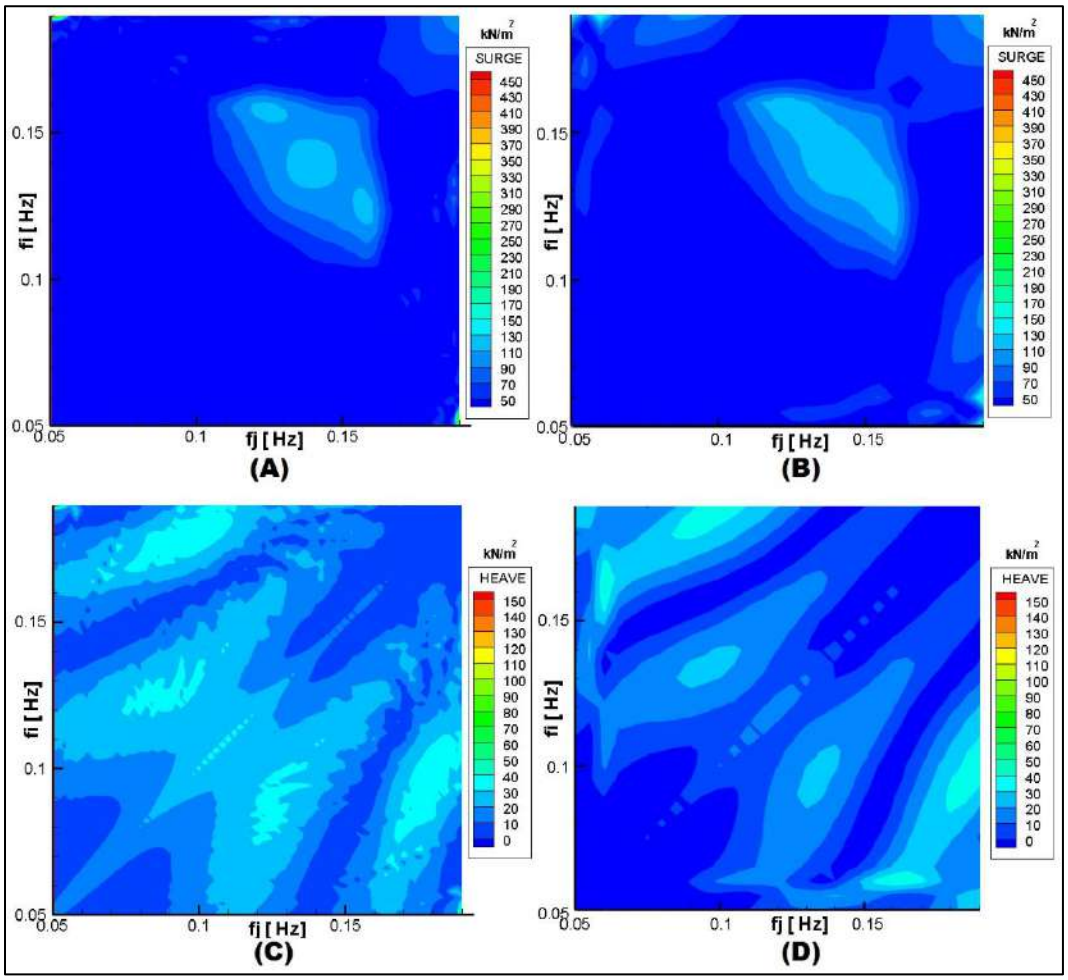

Figure 4.28 – QTFs of the TLP and θ=135° (A) Surge with the F.S.I. (B) Surge without the F.S.I (C) Heave with the F.S.I. (B) Heave without the F.S.I

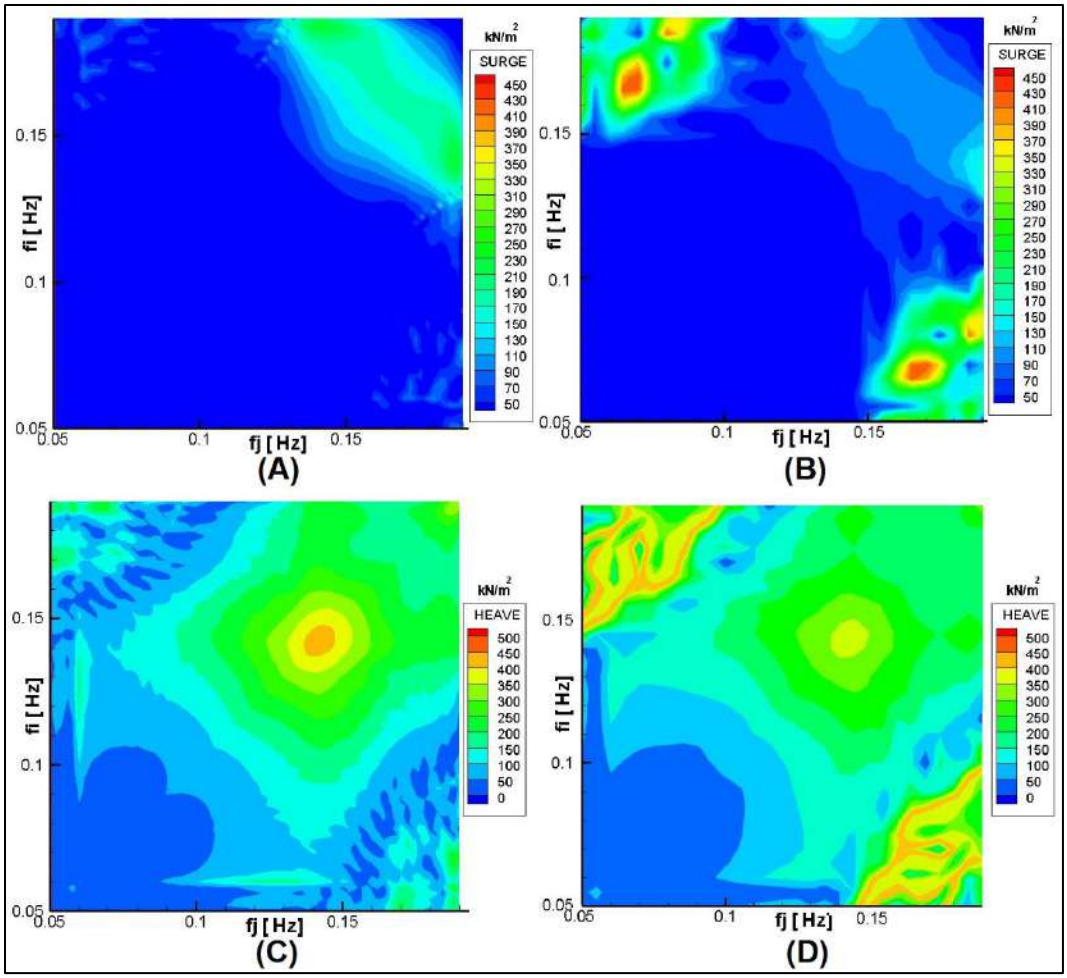

Figure 4.29 – QTFs of the TAD and θ=135° (A) Surge with the F.S.I. (B) Surge without the F.S.I (C) Heave with the F.S.I. (B) Heave without the F.S.I

For the high-frequency QTFs of the TLP, the differences were relatively large in terms of trends and order of magnitude. Consequently, the computing of these loads without considering the Free Surface Integral (FSI) it is not recommended.

Another interesting aspect of this analysis is related to the CPU time consumed by the different methods, i.e., the direct method, indirect method and direct method without the free surface integral. Table 4.6 presents a comparison of the CPU time required by these methods for the three cases analyzed: TLP alone, TAD alone and TLP-TAD. Note that, for a simple comparison, the CPU time for the direct method was used as a reference value (100%). Notably, on average, the indirect method consumes 35% less time than the direct method. The direct method without the free

surface integral takes, on average, 70% less CPU time. Therefore, considering these results and the conclusions of Section 4.3.2, the indirect method considering the FSI has shown to be the more efficient and accurate method for the estimation of second-order loads on the TLP-TAD multibody-system.

Table 4.6 – Summary of CPU time

Component	Case	Method	CPU Time
Diff-frequency	TLP alone	Direct w FS	100%
		Indirect w FS	72.5%
		Direct w/o FS	18.3%
	TAD alone	Direct w FS	100%
		Indirect w FS	67.7%
		Direct w/o FS	23.3%
	TLP-TAD	Direct w FS	100%
		Indirect w FS	60.8%
		Direct w/o FS	34.6%
Sum-frequency	TLP alone	Direct w FS	100%
		Indirect w FS	77.2%
		Direct w/o FS	18.6%
	TLP-TAD	Direct w FS	100%
		Indirect w FS	67.3%
		Direct w/o FS	37.4%

4.3.4 Difference-Frequency Loads

In this section, the low-frequency QTFs for the TLP alone, TAD alone and coupled TLP-TAD cases are presented and discussed. Comparison between the single-body and multi-body cases are shown with the aim of investigating the hydrodynamic interactions between the floaters and their influence on the QTFs of the TLP and TAD.

In addition, the performance of the Newman approximation (NA) is evaluated by comparing its predictions with the QTFs calculated with the direct method (full-QTF). Note that, as mentioned in Section 2.4.3, the QTFs can be estimated based on the mean drift loads in an approximated manner using the Newman method. Thus, the complete low-frequency QTF matrix can be deduced by Eqn. (2.59).

Figure 4.30 compares the low-frequency QTFs of the TLP for Surge motion, considering the following cases: (A) TLP alone and θ = 0°, (B) TLP coupled with TAD and θ = 0°, (C) TLP coupled with TAD and θ = 180°, (D) Newman approximation for TLP alone and θ = 0°, (E) Newman approximation for TLP coupled with TAD and θ = 0° and (F) Newman approximation for TLP coupled with TAD and θ = 180°. Note that, θ is the wave heading.

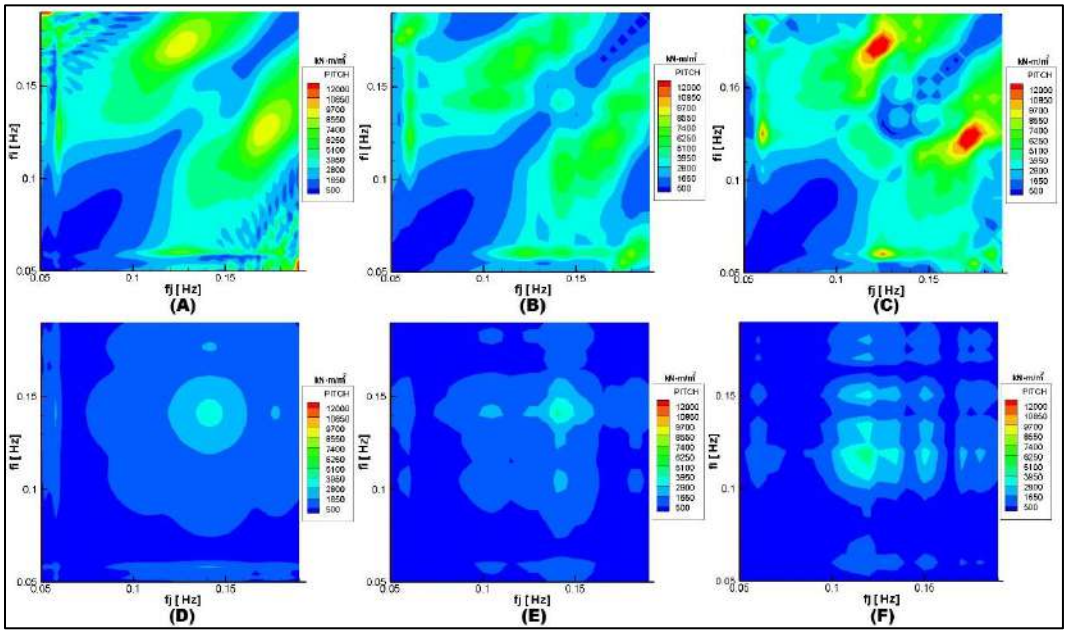

Figure 4.30 – QTFs of the TLP for Surge (A) Alone and θ=0°, (B) Coupled and θ=0°, and (C) Coupled and θ=180°. Newman approximation for QTF (D) Alone and θ=0°, (E) Coupled and θ=0°, and (F) Coupled and θ=180°

A comparison between cases (A), (B) and (C) in Fig. 4.30 reveals strong hydrodynamic coupling effects, particularly in the region where $f_i \cong f_j$. Additionally, significant differences between the forces are found in the region where $f_i > 0.15\ Hz$. A comparison of the full-QTFs with the Newman approximation for the three cases, reveals poor global agreement, particularly for regions far from the condition of $f_i \cong f_j$.

Figure 4.31 compares the low-frequency QTF of the TLP for Yaw in the following cases: (A) TLP alone and θ = 45°, (B) TLP coupled with TAD and θ = 45°,

(C) TLP coupled with TAD and θ = 135°, (D) Newman approximation for TLP alone and θ = 45°, (E) Newman approximation for TLP coupled with TAD and θ = 45°, and (F) Newman approximation for TLP coupled with TAD and θ = 135°

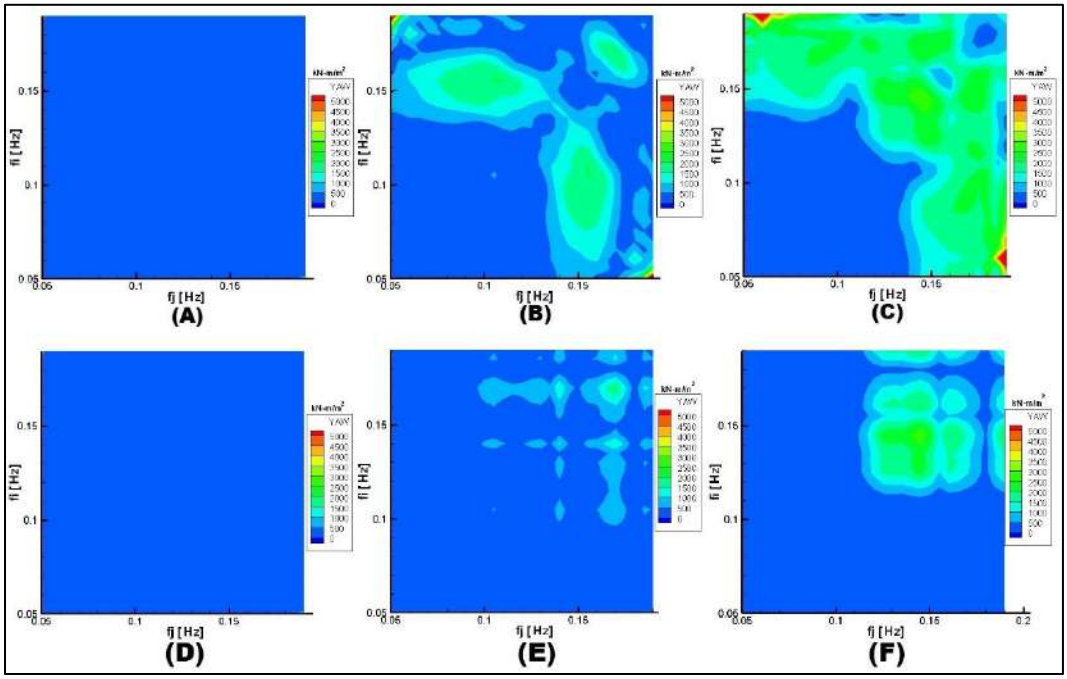

Figure 4.31 – QTFs of the TLP for Yaw (A) Alone and θ=45°, (B) Coupled and θ=45°, and (C) Coupled and θ=135°. Newman approximation for QTF (D) Alone and θ=45°, (E) Coupled and θ=45°, and (F) Coupled and θ=135°

As in the results obtained for the case of Surge motion, strong influence between the floaters are observed. For instance, the TLP alone case with θ = 45° presents small second-order moment; however, the multi-body cases with θ = 45° and in particular for θ = 135° present large values of the second-order moment. In addition, the Newman approximation provides a poor global agreement with the full-QTFs. In order to compare the full-QTFs with the predictions given by the Newman approximation in more detail, curves were defined for which the values of the QTFs correspond to the pair of frequencies (f_i, f_j) with constant difference df, as shown in Eqn. (4.2). This constant is defined to be equal to the natural frequency of the analyzed mode.

$$df = f_i - f_j = constant \tag{4.2}$$

Figure 4.32 compares the full-QTFs with their respective the Newman approximation for Surge in these cases: alone with θ = 0°, coupled with θ = 0° and coupled with θ = 180°. Note that, the difference frequency df was set to 0.005 Hz, which is the Surge natural frequency of the TLP.

Figure 4.33 compares the full-QTFs with their respective the Newman approximation for Yaw for the following cases: alone with θ = 45°, coupled with θ = 45° and coupled with θ = 135°. In this case, df =0.007 is the Yaw natural frequency of the TLP.

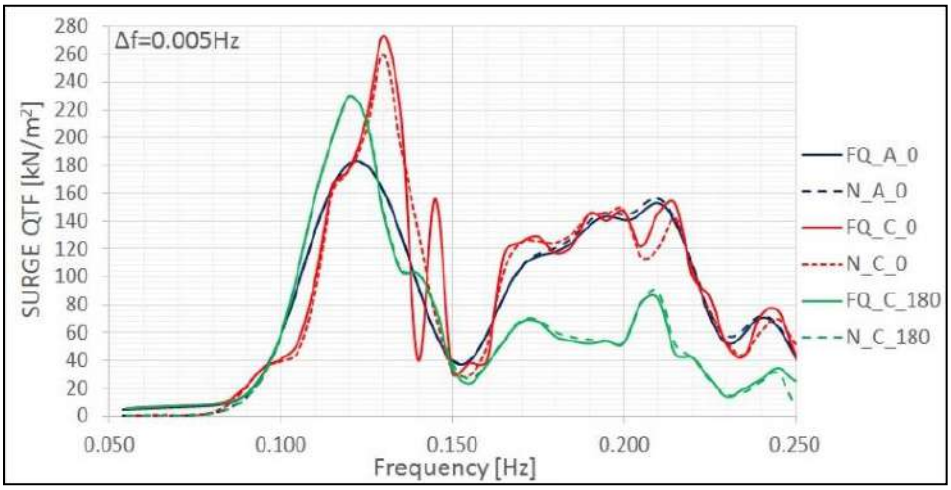

Figure 4.32 Full-QTF (FQ) vs. Newman approximation (N) for the TLP for Surge. A and C denote alone and coupled with TAD, respectively. θ = 0° and 180°.

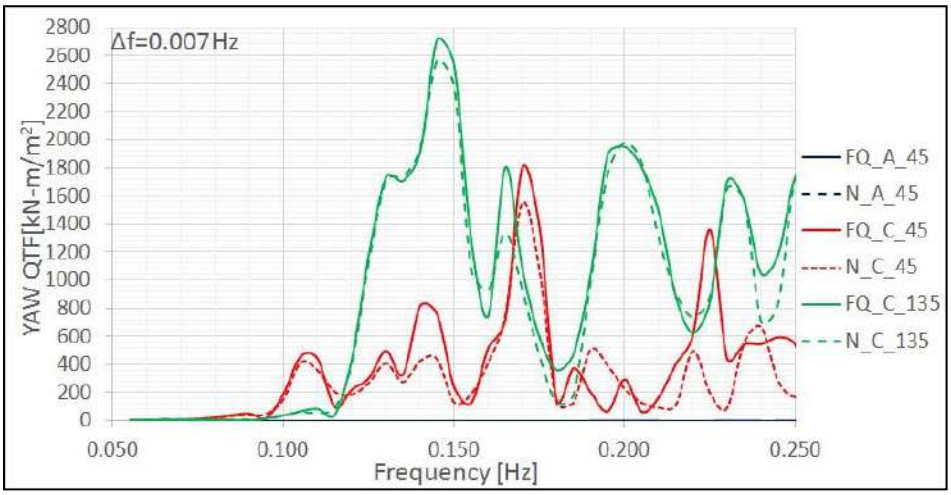

Figure 4.33 – Full-QTF (FQ) vs. Newman approximation (N) for the TLP for Yaw. A and C denote alone and coupled with TAD, respectively. θ = 45° and 135°.

Figures 4.32 and 4.33 confirm that the hydrodynamic coupling effects are stronger when the wave headings are equal to 135° and 180°. That is, the variations in QTFs between the single-body and multi-body cases are relatively high for these wave headings.

Although, the Newman approximation presents poor global agreement with the full-QTF as shown in Figs. 4.30 and 4.31, it presents excellent agreement for a difference frequency df equal to the natural frequencies of Surge and Yaw. This result could be a consequence of the relatively small values of these natural frequencies of the TLP.

Figure 4.34 presents the QTFs of the TAD for Surge motion. This figure compares the following cases: (A) TAD alone and θ = 0°, (B) TAD coupled with TLP and θ = 0°, (C) TAD coupled with TLP and θ = 180°, (D) Newman approximation for TAD alone and θ = 0°, (E) Newman approximation for TAD coupled with TLP and θ = 0° and (F) Newman approximation for TAD coupled with TLP and θ = 180°.

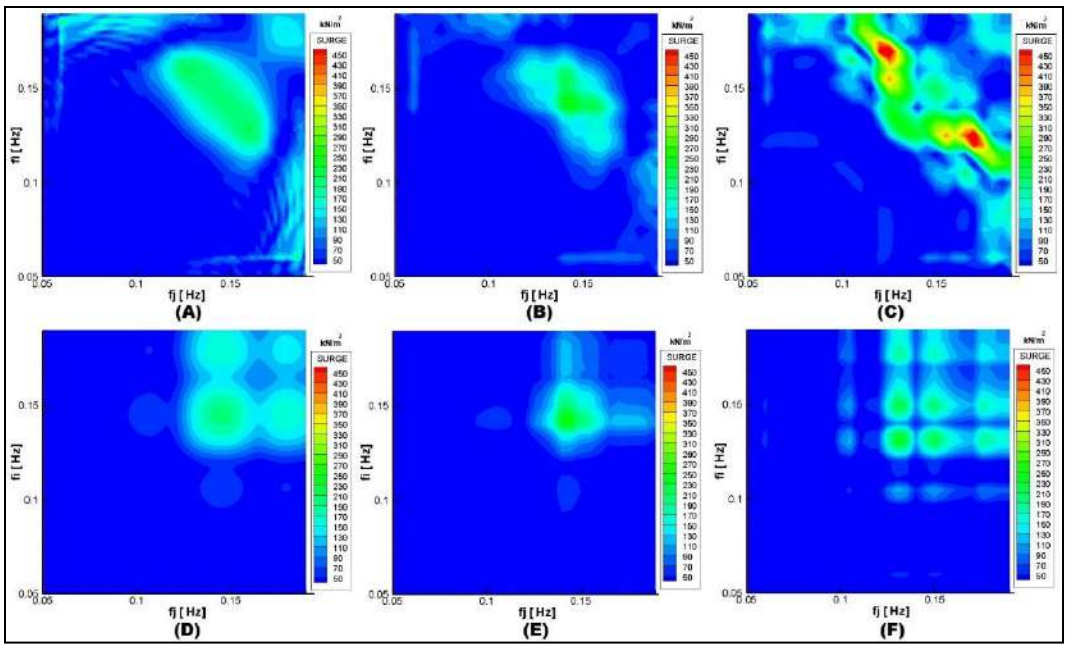

Figure 4.34 – QTFs of the TAD for Surge (A) Alone and θ=0°, (B) Coupled and θ=0°, and (C) Coupled and θ=180°. Newman approximation for QTF (D) Alone and θ=0°, (E) Coupled and θ=0°, and (F) Coupled and θ=180°

Figure 4.35 presents the comparison between the full-QTFs and the Newman approximation for Surge in the following cases: alone with θ = 0°, coupled with θ = 0° and coupled with θ = 180° using a difference frequency $df = 0.004Hz$, which corresponds to the values of the natural frequency of Surge for the TAD.

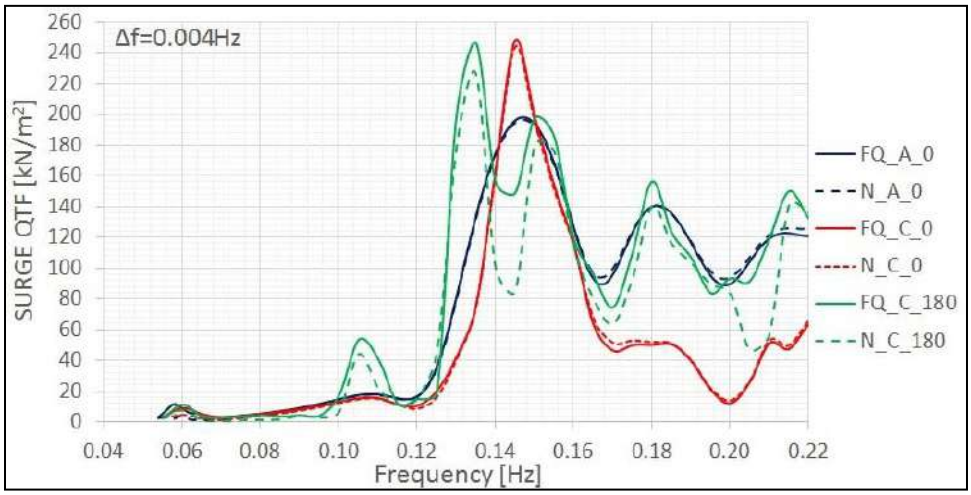

Figure 4.35 – Full QTF (FQ) vs. Newman approximation (N) of the TAD for Surge. A and C denote alone and coupled with TLP, respectively. θ = 0° and 180°.

The differences between the single-body and the multi-body cases are significant, particularly in the case of θ = 180° (see parts (A) and (C) of Fig. 4.34). Moreover, it is evident that the Newman approximation presents poor global agreement with the full-QTF. However, for the QTF analyzed at the natural frequency of Surge in Fig. 4.35, there is relatively strong agreement. As in the case of the TLP, this result could be a consequence of the relatively small natural frequency of the TAD for Surge.

Fig. 4.36 compares the low-frequency QTFs of the TAD for Heave motion between the following cases: (A) TAD alone and θ = 0°, (B) TAD coupled with TLP and θ = 0°, (C) TAD coupled with TLP and θ = 180°, (D) Newman approximation for TAD alone and θ = 0°, (E) Newman approximation for TAD coupled with TLP and θ = 0° and (F) Newman approximation for TAD coupled with TLP and θ = 180°.

Figure 4.37 compares the full-QTFs with their respective Newman approximation for the TAD for Heave motion for the following cases: alone with θ = 0°, coupled with θ = 0° and coupled with θ = 180°. The natural frequency for Heave 0.061Hz is set as the difference frequency df.

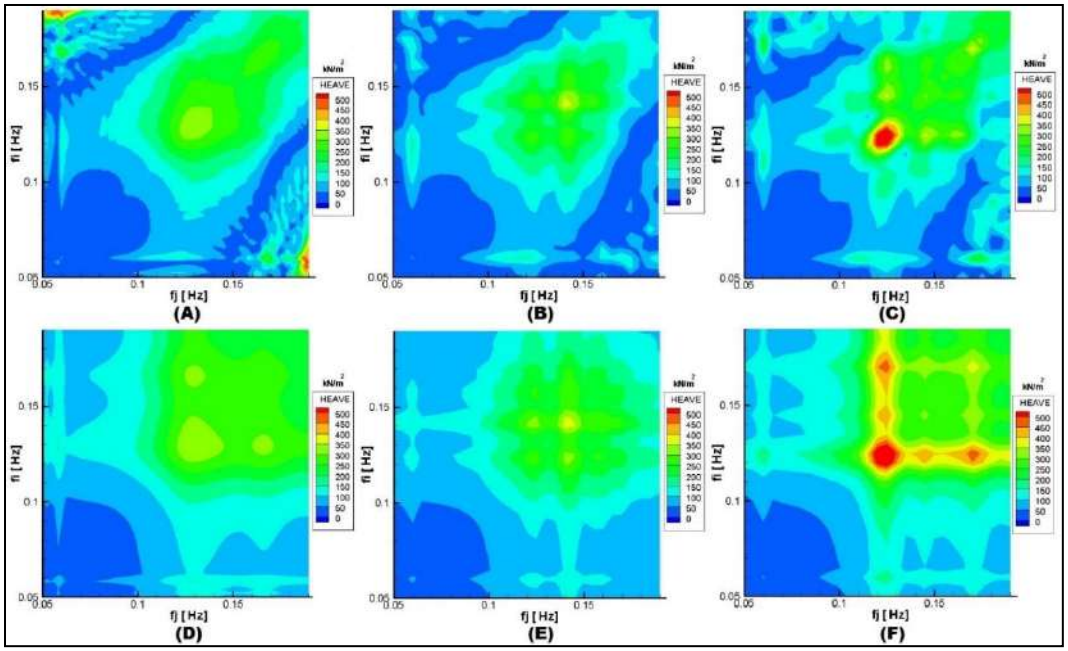

Figure 4.36 – Low-frequency QTFs of the TAD for Heave (A) Alone and θ=0°, (B) Coupled and θ=0°, and (C) Coupled and θ=180°. Newman Approximation for QTFs (D) Alone and θ=0°, (E) Coupled and θ=0°, and (F) Coupled and θ=180°

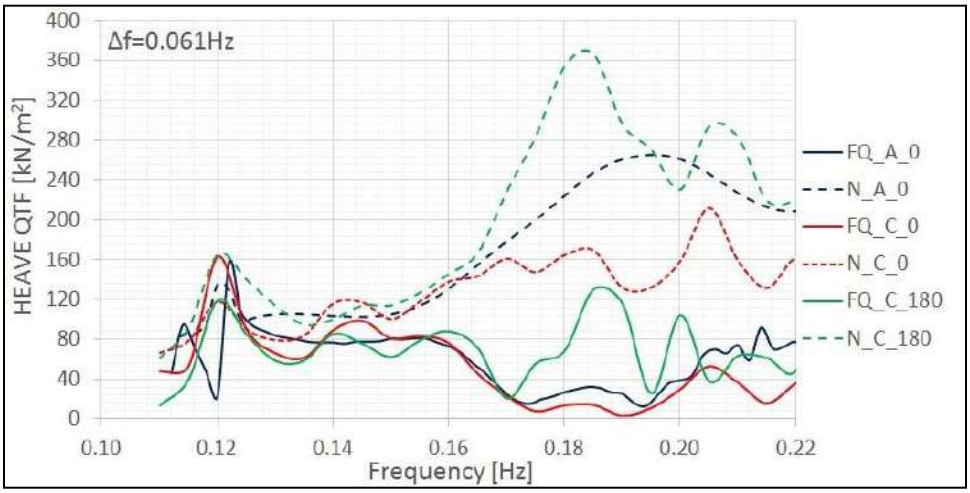

Figure 4.37 – Full QTF (FQ) vs. Newman approximation (N) of the TAD for Heave. A and C denote alone and coupled with TLP, respectively. θ = 0° and 180°.

An analysis of the QTFs of the TAD for Heave motions reveals relevant variations between the single-body and multi-body cases, particularly for multi-body case with θ=180° in the region where $f_i \cong f_j \cong 1.25Hz$, where a huge force peak is

observed. In general, the variations are higher in the region where $f_i \cong f_j$. A comparison of the full-QTF with their respective Newman approximation maps reveals poor global agreement. An analysis of the curves with a difference frequency equal to the heave natural frequency reveals poor local agreement as well, it is clear that the Newman approximation overestimates the second-order force for heave on the TAD unit.

Figure 4.38 compares the low-frequency QTFs of the TAD for Pitch motion in the following cases: (A) TAD alone and θ = 0°, (B) TAD coupled with TLP and θ = 0°, (C) TAD coupled with TLP and θ = 180°, (D) Newman approximation for TAD alone and θ = 0°, (E) Newman approximation for TAD coupled with TLP and θ = 0° and (F) Newman approximation for TAD coupled with TLP and θ = 180°.

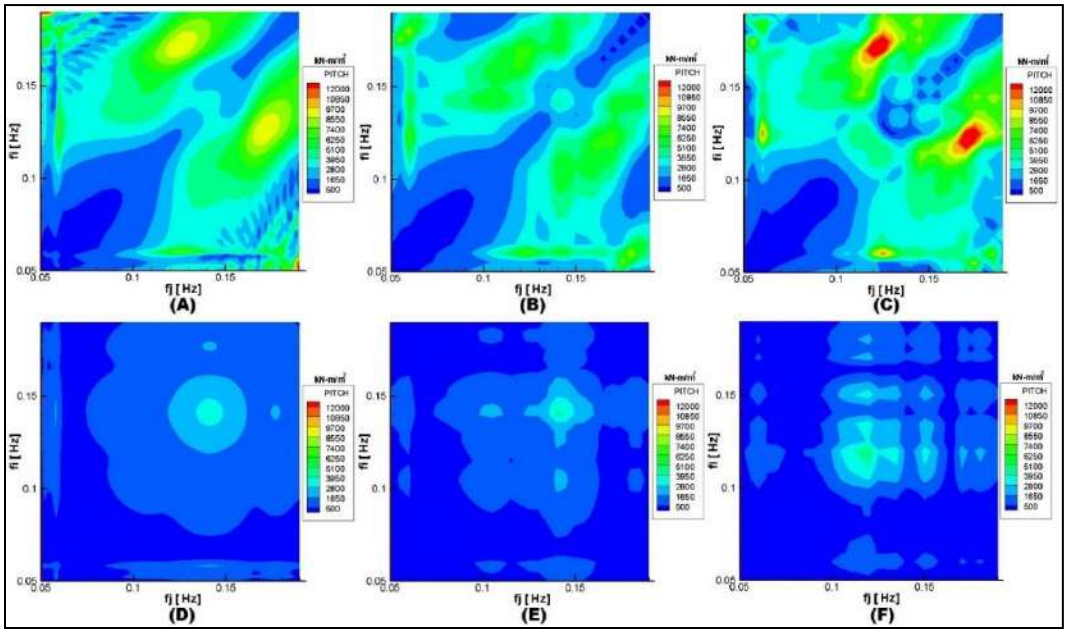

Figure 4.38 – Low-frequency QTFs of the TAD for Pitch (A) Alone and θ=0°, (B) Coupled and θ=0°, and (C) Coupled and θ=180°. Newman Approximation for QTFs (D) Alone and θ=0°, (E) Coupled and θ=0°, and (F) Coupled and θ=180°

In addition, a local analysis considering a difference frequency $df = 0.055Hz$, which is the natural frequency of the TAD for Pitch is presented in Fig. 4.39 for the following cases: alone with θ = 0°, coupled with θ = 0° and coupled with θ = 180°.

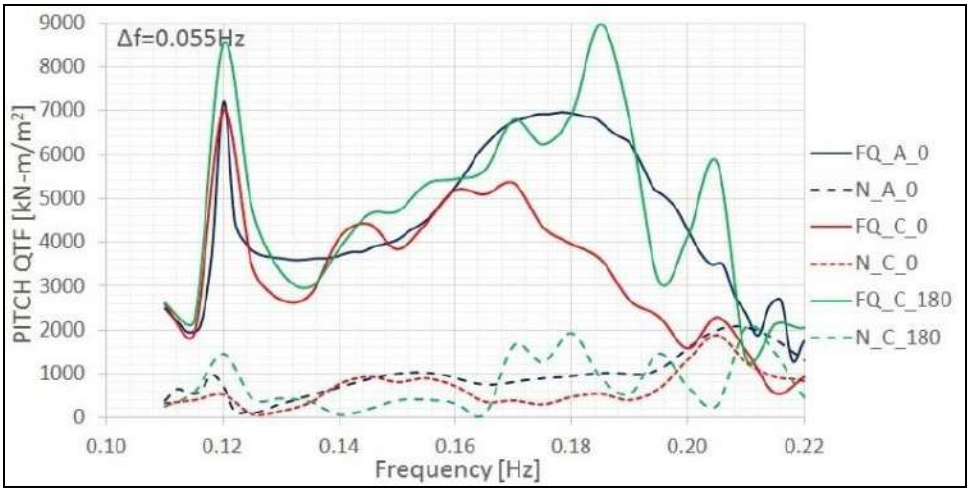

Figure 4.39 – Full QTF (FQ) vs. Newman Approximation (N) of the TAD for Heave. A and C denote alone and coupled with TLP. θ = are 0° and 180°.

An analysis of the QTFs of the TAD for Pitch motions reveals significant variations between the single-body and multi-body cases that appear in nearly all of the degrees of freedom, particularly in the multi-body case with θ=180° in the regions under the condition $\left(f_i \cong 0.125\ Hz \cap f_j \cong 0.175\ Hz\right)$ where a huge moment peak is observed. In general, the variations are higher in the region where $f_i \cong f_j$. The comparison of the full-QTFs with their respective Newman approximation reveals poor global agreement. Finally, an analysis of the curves with a difference frequency df equals to the Pitch natural frequency reveals poor local agreement as well; it is clear that the Newman approximation underestimates the Pitch moments on the TAD unit.

4.3.5 Sum-Frequency Loads

The analysis of the QTFs concludes with the study of high-frequency loads on the TLP for the single-body and multi-body cases when the TLP is connected to the TAD.

Note that, in the case of high-frequency QTFs, no approximate method exists to estimate the values of the second-order high-frequency loads.

Figure 4.40 presents the high-frequency QTF of the TLP for Heave in the following situations: (A) Alone and θ = 0°, (B) Coupled with TAD and θ = 0°, and

(C) Coupled with TAD and θ = 180°. In addition, the high-frequency QTF of the TLP for Pitch is presented for the cases of (D) Alone and θ = 0°, (E) Coupled with TAD and θ = 0°, and (F) Coupled with TAD and θ = 180°.

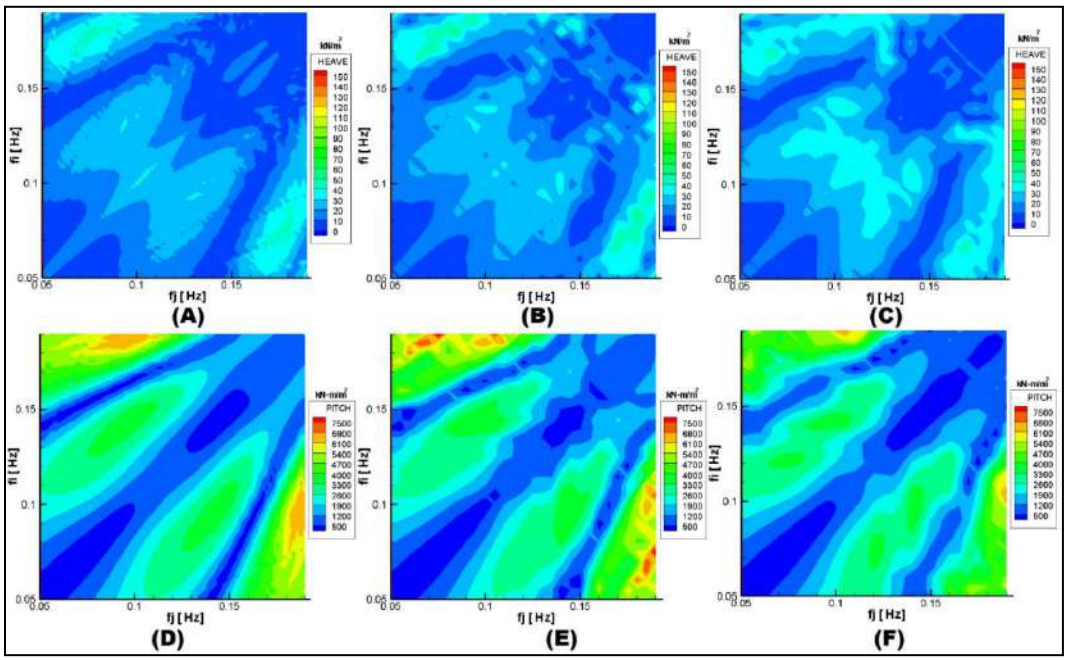

Figure 4.40 – High-frequency QTFs of the TLP for Heave (A) Alone and θ=0°, (B) Coupled and θ=0°, and (C) Coupled and θ=180°. High-frequency QTFs of the TLP for Pitch (D) Alone and θ=0°, (E) Coupled and θ=0°, and (F) Coupled and θ=180°.

The high-frequency QTFs of the TLP for Heave and Pitch present small variations between the single-body and multi-body cases. In general, when the TAD is present, these loads undergo slight amplifications. The highest variations are observed in the multi-body case and θ = 180° and for regions with ($f_i \cong 0.15\ Hz$) for both degrees of freedom. Based on this extensive analysis of the second-order loads on the TLP-TAD multi-body system, the following conclusions are drawn:

- Numerical grids of the floaters and the discretization of the free surface were validated. Calculations using the indirect and direct methods present similar results. Thus, a reasonable numerical convergence was achieved.

- The importance of the free surface integral was tested and confirmed. The results showed that even the low-frequency QTFs of both floaters are sensitive to the free surface integral. The TAD presents the more significant variations. These results indicate that the free surface integral cannot be neglected without previous analysis in this type of geometry. In addition, the influence of this integral on the high-frequency QTFs of the TLP has been confirmed.
- Significant differences between the single-body and multi-body cases reveal that hydrodynamic coupling effects on the second-order loads of the TLP-TAD system are relevant. These effects induced significant variations in the low-frequency QTFs of both floaters, in both horizontal modes and vertical modes. Similar variations in the high-frequency QTF were observed, however, these variations are minor relative to the low-frequency results.
- The results of Section 4.2 showed that this multi-body system presents weak hydrodynamic coupling effects for first-order loads on the systems. However, such behavior was not found for the second-order loads.
- For horizontal modes, the Newman approximation presents poor global agreement with the full-QTF. However, when the QTFs were analyzed in detail with the constant difference frequency df equal to the natural frequency of the floaters, acceptable "local" agreements were found. This finding is a consequence of the relatively low natural frequencies of the floaters in these modes.
- For vertical modes, the comparison between the Newman approximation and full-QTF of the TAD reveals poor global and local agreement. The method overestimated the Heave forces and underestimated the Pitch moments.
- In general, it is possible to conclude that the Newman approximation presents satisfactory predictions when the natural frequency is lower than 0.005 Hz.

4.4 TIME DOMAIN ANALYSIS OF SECOND-ORDER LOADS

This section provides an analysis of the second-order loads on the TLP-TAD multi-body system using the time domain approach. Several numerical simulations were conducted using Orcaflex [70]. This study has three objectives. First, to confirm the predictions of frequency domain analysis regarding the accuracy of the Newman approximation. Second, to verify the

importance of high-frequency QTFs for the behavior of the system. Third, to evaluate the hydrodynamic coupling effects by comparing the behavior of the units in single-body and multi-body cases.

The numerical configuration and environmental conditions considered in the time domain simulations are presented in Section 4.2.5. Note that, the low-frequency QTFs were approximated using the Newman approximation and the high-frequency QTFs were neglected.

Figure 4.41 presents the results of time domain simulations of the TLP alone considering the wave conditions of Table 4.4. Notably, for Surge motion, slight differences exist between the results obtained with the Newman Approximation (NA) and the full-QTFs.

Similar results arise for Sway and Yaw motions. These results confirmed the predictions of the analysis in the frequency domain, i.e., although the Newman approximation presents poor global agreement with the full-QTFs, it provides results an excellent local agreement for modes with relatively low natural frequencies.

In contrast, for Heave motion, the differences between simulations with and without the sum-frequency QTFs were small. The results including the high-frequency loads were slightly larger.

Finally, the analysis of Pitch and Roll motions reveals significant differences between simulations with and without consideration of the high-frequency effects. It is evident that in this case, the sum-frequency QTFs cannot be neglected.

Figure 4.42 presents the results of time domain simulations of the coupled TLP. In general, the results from the multi-body analysis were consistent with the single-body case, Surge and Yaw present similar trends, i.e., the NA present reasonable agreement with the full-QTFs. In addition, the response for Roll and Pitch were significantly lower in TD simulations without consideration of the sum-frequency QTFs. As in the TLP single-body case, the high-frequency QTFs cannot be neglected for these modes.

For Sway response, the Newman approximation does not provide accurate predictions, notable differences are observed in Fig. 4.42 part. (B). Therefore, the NA must be applied with extreme care and with knowledge of its limitations for this mode in the multi-body cases.

For Heave, a similar trend to the single-body case was found, i.e., no significant differences are observed.

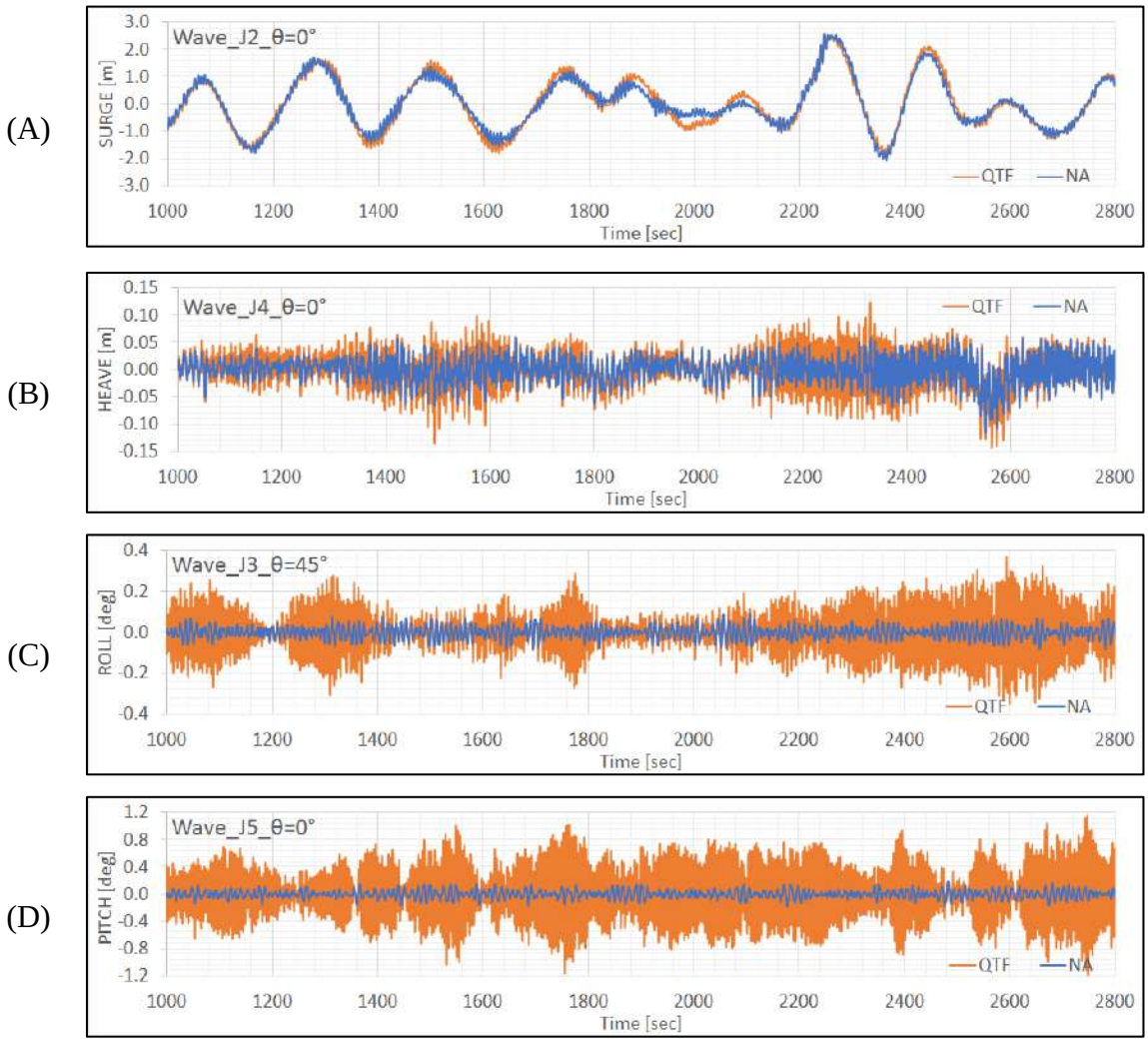

Figure 4.41 – Newman approximation vs. full-QTF for the TLP alone.

Figure 4.43 presents the results of time domain simulations of the TAD alone. Despite some small differences exist for Surge, Sway, and Yaw, the agreement between the Newman approximation and the full-QTFs is excellent.

For Heave of the TAD, in general, the Newman approximation provides reasonable predictions. However, significant differences in the time traces are observed.

For Roll and Pitch motions of the TAD, important differences are observed, the predictions provided by the full-QTFs are systematically higher than the Newman Approximation results.

(A)

(B)

(C)

(D)

(E)

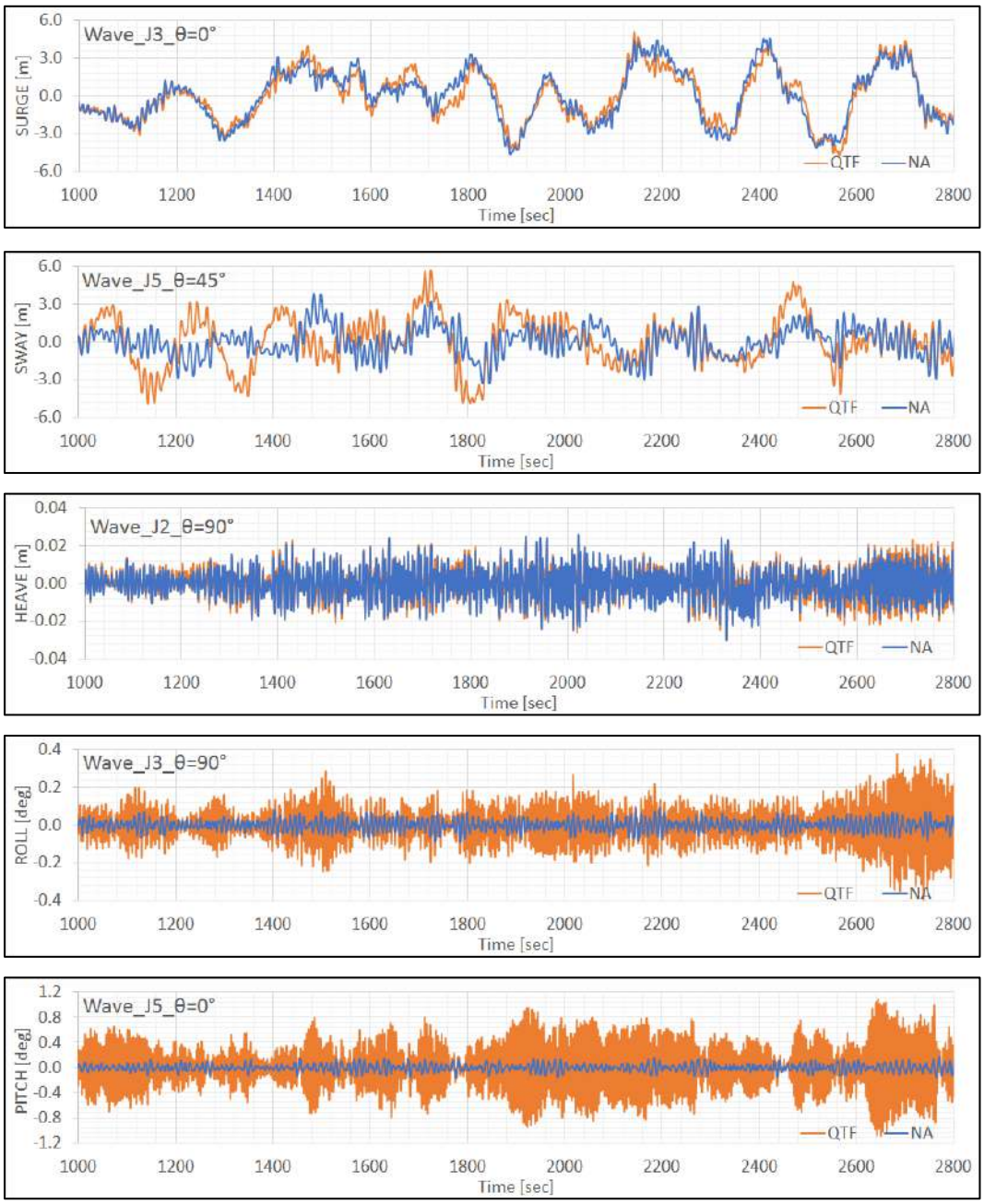

Figure 4.42 – Newman approximation vs. full-QTF for the Coupled TLP.

Figure 4.44 presents the results of time domain simulations of the coupled TAD. The differences observed for Surge are small. The differences between the prediction given by the Newman Approximation and the full-QTFs increase for Sway and Yaw. For Heave motions, no significant differences were found between the two methods. Finally, for Roll and Pitch, the predictions from the full-QTFs were systematically higher, i.e., the Newman approximation underestimates the movements in these modes.

(A)

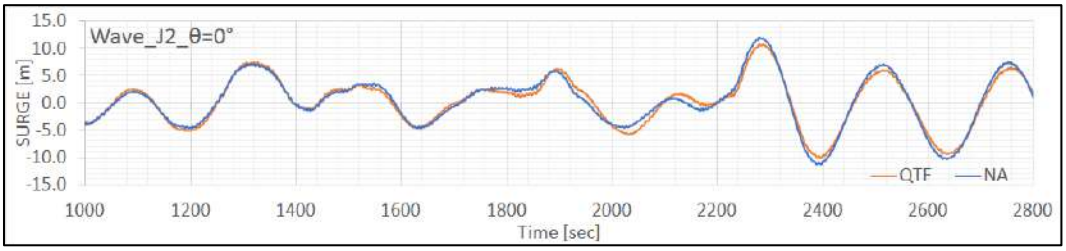

(B)

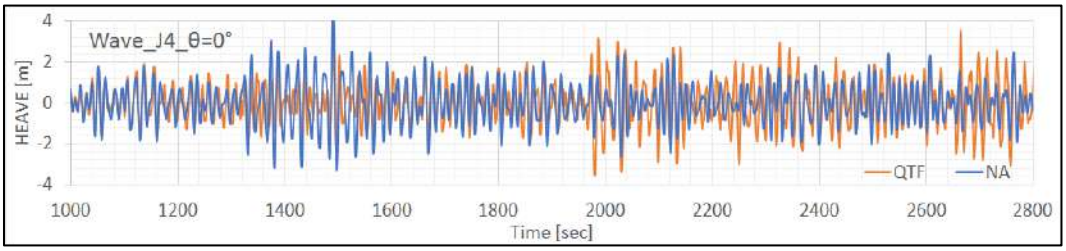

(C)

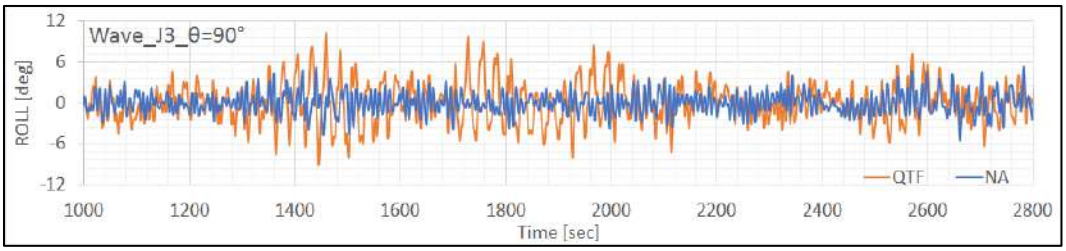

(D)

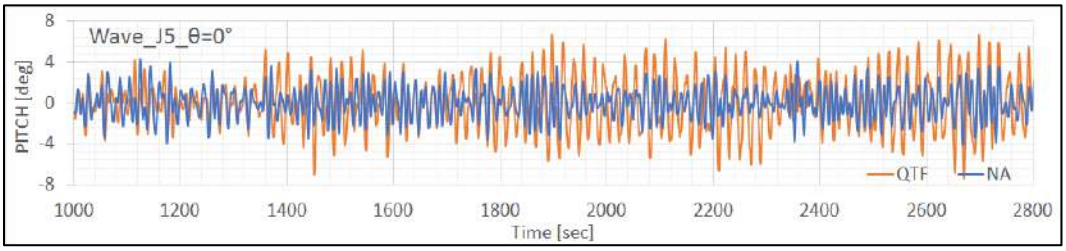

(E)

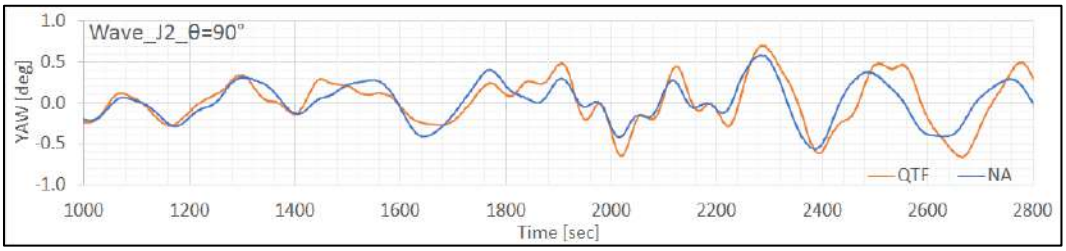

Figure 4.43 – Newman approximation vs. full-QTF for the TAD alone.

(A)

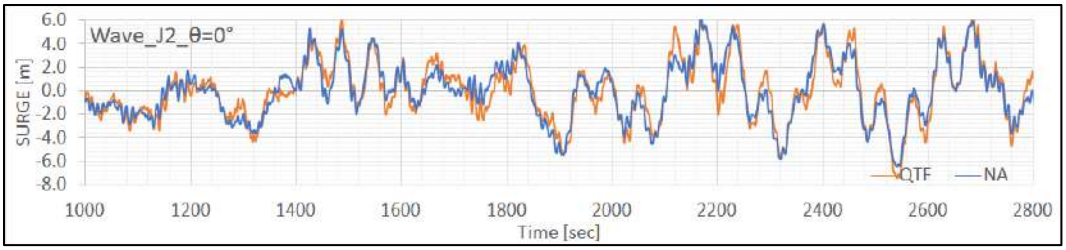

(B)

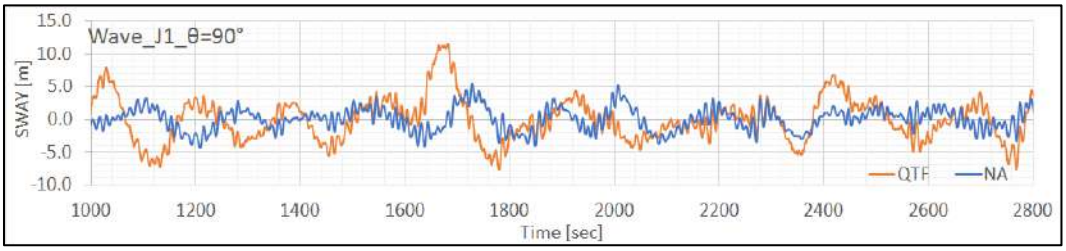

(C)

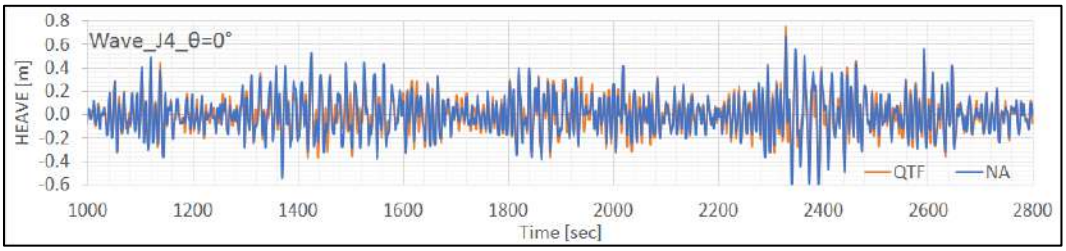

(D)

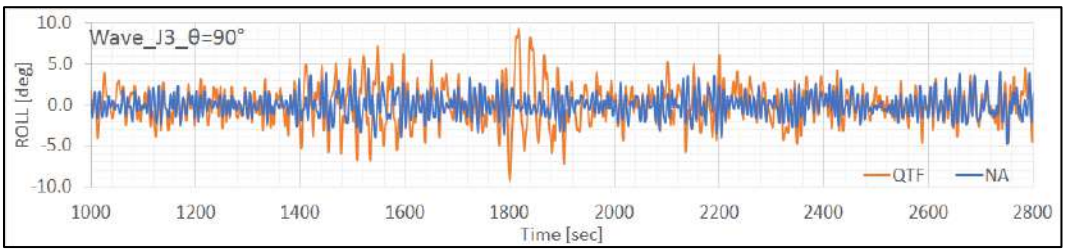

(E)

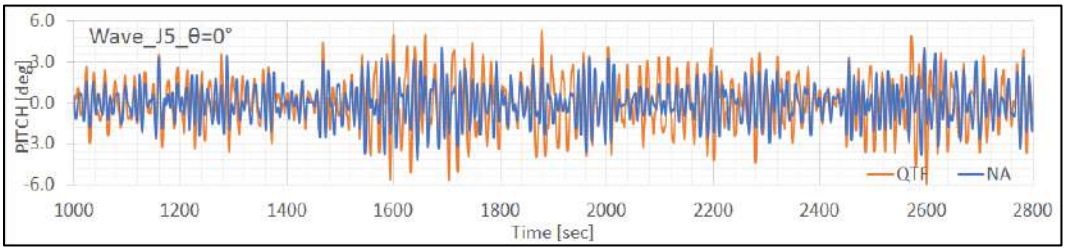

(F)

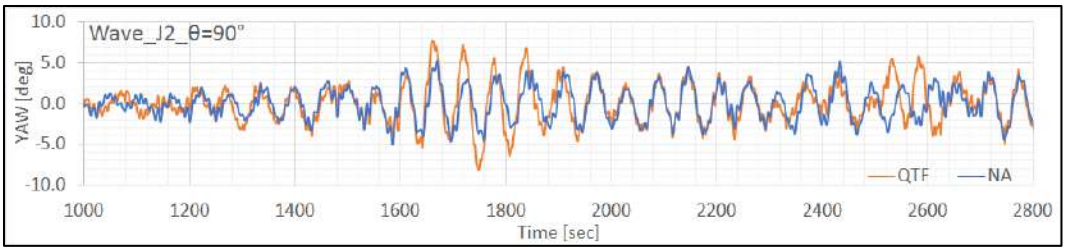

Figure 4.44 – Newman approximation vs. full-QTF for the coupled TAD.

As a conclusion, in horizontal modes, the Newman approximation presents excellent results for Surge, Sway, and Yaw for both floaters in the single-body cases. However, significant differences were found in these modes in the analysis of the multi-body cases.

Note that, the QTFs, for the single-body and multi-body cases, are approximated by the Newman method based on the mean drift loads. As shown in Section 4.2.3, the differences observed in the mean drift loads between single-body and multi-body cases are small. Consequently, no relevant differences are expected between the QTFs of the single-body and multi-body cases provided by the Newman approximation. This could be the reason why the Newman approximation presents relevant differences in the time domain simulations for the multi-body cases calculate with the full-QTFs that incorporate the coupling effects in the multi-body cases.

Therefore, the hydrodynamic interactions in the low-frequency QTFs have a significant impact on the analysis of the multi-body cases and the Newman approximation must be carefully used for horizontal modes in these cases.

The analysis of vertical modes reveals that Heave of the TAD does not present relevant differences between the Newman approximation and full-QTFs. However, Roll and Pitch present important differences. Generally, the results from full-QTFs are slightly higher than those provided by the Newman approximation.

Finally, the analysis of vertical motions of the TLP reveals that the influence of the high-frequency QTFs for Heave in the single-body cases is marginal. Consequently, the use of FEM to represent the TLP tendons seems to be sufficient to represent the high-frequency motions in this mode. However, for the multi-body cases, the differences between the simulations with and without consideration of the high-frequency QTFs were slightly larger than the single-body case. Therefore, for multi-body analysis, the use of the sum-frequency QTFs is recommended.

For Roll and Pitch, the differences between the motions computed with and without the high-frequency QTFs were significant for the single-body and multi-body cases. the predictions provided by the simulation that considered the sum-frequency effects are systematically higher. Thus, these results have been proved that high-frequency QTFs cannot be neglected in the analysis of the system.

CHAPTER V. CURRENT LOADS

This chapter presents an experimental and numerical analysis of current loads on the TLP-TAD multi-body system including an extensive study of shielding effects. The model tests consider the cases of the TLP alone, the TAD alone and the multi-body system with several relative positions between the floaters. Computational Fluid Dynamics (CFD) simulations were conducted to evaluate blockage and scale effects on the current load coefficients. Furthermore, several current velocities and angles of attack were examined.

5.1 INTRODUCTION

Current loads on offshore structures have a tremendous importance in the design of mooring systems, installation analysis, wet tow operations, and the dimensioning of dynamic positioning systems [20]. An underestimation of these loads could affect safety during operations; In contrast, an overestimation could lead to a severe impact on profitability. Consequently, accurate estimations of current loads are indispensable for an efficient design [20].

The prediction of current loads can be assessed using theoretical or empirical methods, CFD simulations, or experimental tests in a current channel, wind tunnel, or towing tanks. However, due to the complex geometries of offshore platforms, experimental tests have been used as the most trusted method. Although CFD is now an attractive alternative to model tests, it still requires further validations, and its applicability may be limited [94].

Recent studies have focused on current loads on offshore structures, for instance, [47], [90], and [94]. Only a few have investigated shielding effects on multi-body systems [48], and none was focused on the TLP-TAD system.

Note that, when two bodies are positioned close to each other and subject to currents, significant shielding or interaction effects can be observed. Thus, the presence of one body can significantly modify the current loads on other [48]. Consequently, this effect must be considered in multi-body systems.

This work presents an extensive experimental and numerical study of the current loads on the TLP-TAD multi-body system. The experimental tests are performed in the current channel of the Laboratory of Waves and Currents (LOC) of COPPE/UFRJ with the aim of investigating shielding effects on the current loads. The units are tested alone and then tested while interacting with one another. Several relative positions between the floaters are considered.

Note that, in experimental tests, current load coefficients are typically measured for a fixed floater. In [20] current loads are measured in a wind tunnel, and [48] used a towing tank. In both examples, the authors considered mass distribution and the motion of the platform to be negligible. In concordance with these previous experimental tests, the current loads are measured with the unit TLP and TAD hulls fixed.

The numerical analysis is performed with the aim of investigating possible blockage effects due to the walls of the channel and scale effects corollary to the difference in Reynolds numbers between the model-scale and full-scale. ANSYS-CFX software [2] was used in the numerical analysis. First, the influence of the computational grids was analyzed. Then, the numerical predictions are compared and validated with the experimental data. Finally, blockage and scale effects are investigated for the TLP alone and TAD alone.

5.2 SIMILITUDE AND FROUDE MODEL LAW

Model tests are intended to reproduce the behavior of full-scale systems using reduced scales with the highest possible accuracy [84]. Thus, the physical similitude between model scale and full-scale behavior is divided into three types of similarities: geometric, kinematic, and dynamic [12]. Geometric similarity requires that any equivalent dimensions of the full-scale and model-scale bodies are related by Eqn. (5.1).

$$\lambda = \frac{L_{FULL-SCALE}}{L_{MODEL-SCALE}} \tag{5.1}$$

where λ is known as the model scale factor. Kinematic similarity implies that the ratios between full-scale velocities must be equal to the equivalent velocity ratios in the model scale. Finally, dynamic similarity implies that the ratios between the full-scale forces must be equal to the equivalent force ratios in the model scale [12].

According to [84], if the geometric and dynamic similarities are ensured, then kinematic similarity follows. The geometric similarity is obtained by the faithful representation in reduced scale of the geometry of the bodies. However, limitations such as roughness of the body surfaces and the presence of walls in the laboratory facilities must be considered.

The dynamic similarity is evaluated using non-dimensional coefficients such as the Froude number, Reynolds number, Mach number, Weber number, Strouhall number and Keulegan-Carpenter number [12]. These coefficients are defined as ratios of the forces involved in the physical phenomena. In offshore hydrodynamic testing, the most significant forces are classified to be the gravitational, viscous, pressure, drag, and inertial forces.

All of the nondimensional parameters play a role in the correct representation of dynamic similarity. However, only a few are predominant. Consequently, the scaling laws are defined by the equality of only the most relevant non-dimensional numbers [84]. In offshore hydrodynamics, the most relevant non-dimensional parameters are the Froude and Reynolds numbers. These non-dimensional parameters are defined below.

The Froude number relates inertia and gravitational forces on an element of fluid in a medium by Eqn. (5.2) [12]. In systems with water flow and free surface, the gravitational effects are significant, while effects such as viscosity and surface tension are small and can be neglected [84].

$$Fr = \frac{V_C}{\sqrt{g \cdot L_C}} \tag{5.2}$$

The Reynolds number relates inertial and viscous forces by Eqn. (5.3).

$$Re = \frac{V_C \cdot L_C}{\mu} \tag{5.3}$$

Thus, to guarantee similitude between model-scale and full-scale behavior, these non-dimensional quantities must be equal for both scales. Unfortunately, in practice, it is not possible to simultaneously satisfy the scaling laws based on Froude and Reynolds numbers [84]. In addition, maintaining an equality of Reynolds number presents a practical limitation because the model scale requires relatively high velocities. Consequently, the scaling law must be chosen as a compromise between the fulfillment of dynamic similarity and the reliability of the model tests [84].

Conventional model tests of offshore structures are typically based on the Froude scaling law, i.e., the dynamic similarity is addressed by equality of the Froude numbers in the model-scale and full-scale. In addition, the geometrical similarity is represented in Eqn. (5.1). Based on these two conditions, the scale factors for the main physical parameters involved in the experimental tests are deduced as shown in Tab. 5.1.

Table 5.1 Scale factors for the main physical properties in offshore model testing.

Parameter	Scale factor
Length	λ
Area	λ^2
Volume	λ^3
Time	$\lambda^{0.5}$
Velocity	$\lambda^{0.5}$
Acceleration	1
Radius of gyration	λ
Mass	$\lambda^3(\rho_{FS}/\rho_{MS})$
Force	$\lambda^3(\rho_{FS}/\rho_{MS})$
Moment	$\lambda^4(\rho_{FS}/\rho_{MS})$
Pressure	$\lambda(\rho_{FS}/\rho_{MS})$

Note that, ρ_{FS} is the full-scale fluid density, while ρ_{MS} is the model-scale fluid density.

5.3 REGIME FLOW AND SCALE EFFECTS

The purpose of this model test campaign is to investigate the current loads on the TLP-TAD multi-body system in different current conditions (velocities and angles of attack). The range of current velocities considered in this study is presented in Tab. 5.2.

As described above, in a conventional model test of offshore structures, the physical scaling and test execution are only feasible using the Froude model law. Consequently, the scale effects due to the difference in the Reynolds number must be considered. Table 5.2 presents the Froude and Reynolds number for the full-scale and model-scale. Note that, in

the calculation of the dimensionless numbers, the characteristic length is assumed to equal the diagonal of the square profile of the TLP column (L=21.21 m). The values for the TAD are similar. See Eqns. (5.2) and (5.3).

Table 5.2 Current velocities, Froude and Reynolds numbers of the model tests.

Full scale			Model scale		
Vc [m/s]	Re [-]	Fr [-]	Vc [m/s]	Re [-]	Fr [-]
0.3	6.33E06	0.021	0.021	2.44E03	0.021
0.6	1.27E07	0.042	0.042	4.47E03	0.042
0.9	1.90E07	0.062	0.064	6.71E03	0.062
1.2	2.53E07	0.083	0.085	8.94E03	0.083
1.5	3.16E07	0.104	0.106	1.12E04	0.104

The Reynolds numbers at full-scale are on the order of [1.0E6 - 1.0E7], which corresponds to the transcritical flow regime. Consequently, the boundary layer is turbulent upstream of the separation point [28]. The Reynolds number at model scale is related to the Reynolds number at full-scale by Eqn. (5.4)

$$Re_{MODEL} = \frac{Re_{FULL}}{\sqrt{\lambda^3}} \qquad 5.4$$

where λ is the model scale factor. Thus, the Reynolds numbers at model scale are in the range of [1.0E3 – 1.0E4], which corresponds to the subcritical flow regime, in which the boundary layer is laminar [28].

As shown in Part (c) of Fig. 5.1, the Reynolds number has a strong influence on the drag forces on circular sections. The drag in the transcritical flow regime is considerably lower than the drag in the subcritical flow regime. Consequently, significant scale effects due to the Reynolds number difference can be expected in floating bodies with cylindrical elements with circular sections.

Figure 5.1 Part (C) and Fig. 5.2 present experimental evidence that drag forces on rectangular sections have a weak dependence on the Reynolds number. This finding can be related to the fact that the separation point in sharp edged structures is fixed, while for curved shapes it depends strongly on the Reynolds number. Therefore, fewer scale effects associated

with the Reynolds number can be expected in floating bodies with cylindrical elements than in those with square sections.

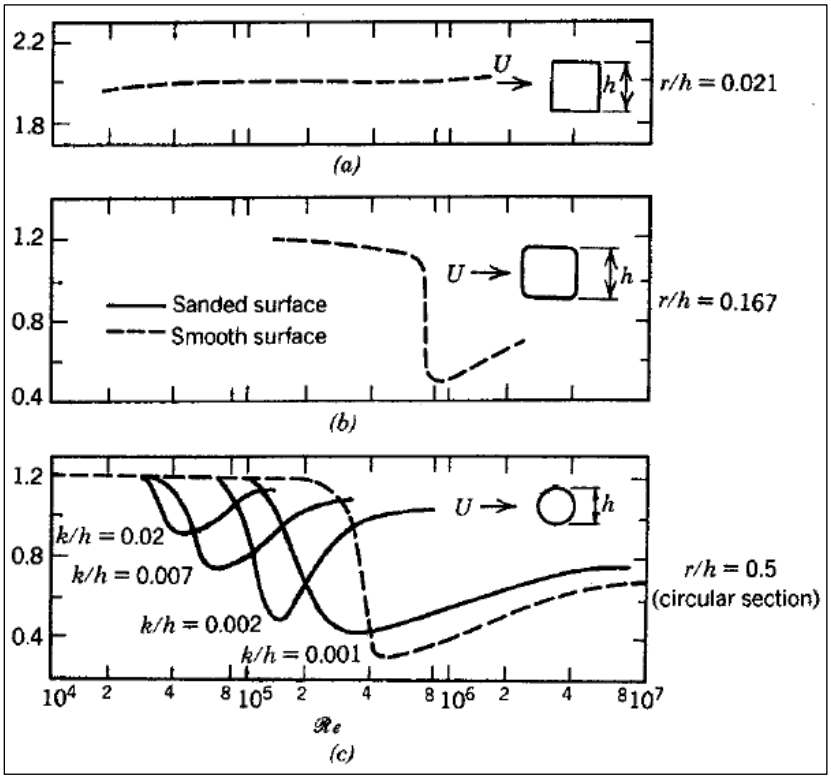

Figure 5.1 Reynolds number influence on the drag coefficients of square cylinders with different corner radii [83].

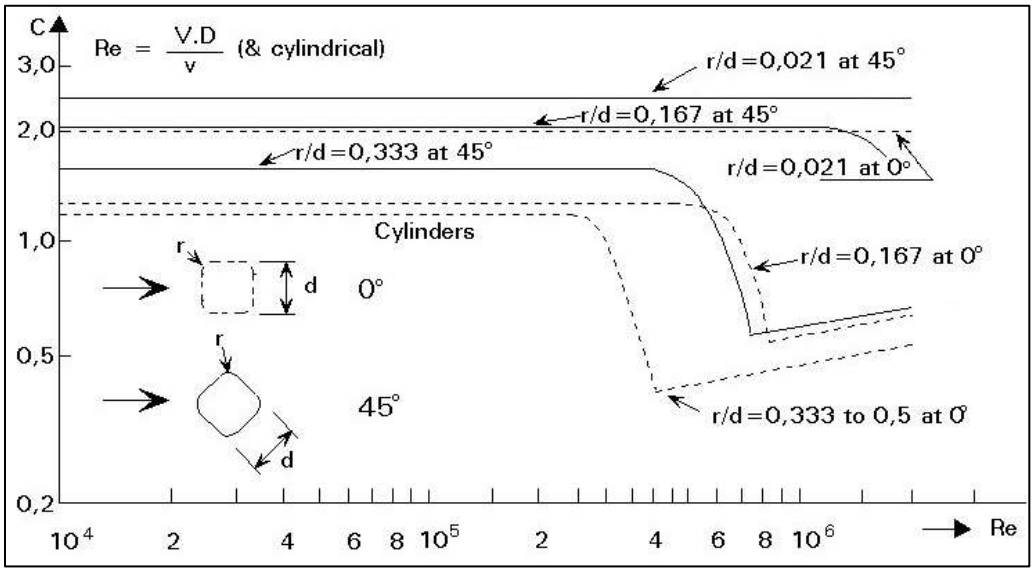

Figure 5.2 Drag coefficients for a square section with several corner radii [76].

5.4 ULTRA-REDUCED SCALE MODELS

The scale factor is probably the most important parameter in experimental tests. Depending on the physical phenomenon, models that are too small present scale effects due to viscosity and represent a substantial challenge in the correct representation of the mass distribution [84]. However, large models are expensive, difficult to handle and sensitive to blockage effects, i.e., the walls and bottom of the tank can modify the behavior of the reduced model [84].

Therefore, the scale must be defined based on the dimensions of the floater, the environmental conditions of interest and the operational limitations of the current channel. Tab. 5.3 presents the properties considered in the scale factor analysis. Figure 5.3 presents a schematic representation of the experimental setup considered in the scale factor analysis. The analysis of the scale factor focuses on the following relations:

$$C1\ [\%] = 100 \cdot \frac{T1}{k1} \tag{5.5}$$

$$C2\ [\%] = 100 \cdot \frac{L2}{k3} \tag{5.6}$$

$$C3\ [\%] = 100 \cdot \frac{A_{TLP}}{k4} \tag{5.7}$$

where $T1$ is the TLP draft, $L2$ is the total TAD length, A_{TLP} is the TLP transversal area, $k1$ is the channel depth, $k2$ is the channel breadth, and $k3$ is the channel transversal area. Note that, these parameters were selected because they are the critical dimensions of the floaters in terms of minimizing the blockage effects. For reference, see Fig. 5.3 and Tab. 5.3. These parameters ($T1$, $L2$ and A_{TLP}) are related to the full-scale values of Tab. 5.3 by the scale factors presented in Tab. 5.1. Moreover, C1 is the ratio between the maximum draft of the floaters and the depth of the channel, C2 is the ratio between the maximum horizontal dimension of the floaters and the breadth of the channel, and C3 is the ratio between the maximum transversal area of the floaters and the transversal area of the channel.

Note that, the values of the coefficients C1, C2, and C3 from Eqns. (5.5) and (5.6) depend on the scale factor. Thus, after establishing reasonable limits for these coefficients (C1 and C2 were limited to 35%, and C3 was limited to 7.5%), the most suitable scale factor was chosen as 1:200. Table 5.4 presents a summary of the scale factor analysis.

Table 5.3 Parameters included in the analysis of the scale factor.

Description		Symbol	Values	Units
TLP	Breadth overall	L1	80.5	[m]
	Draft	T1	31.0	[m]
	Transversal area	A_{TLP}	1619.5	[m^2]
TAD	Length overall	L2	93.8	[m]
	Breadth overall	L3	47.0	[m]
	Draft	T2	12.95	[m]
	Transversal area	A_{TAD}	817.8	[m^2]
Current Channel	Breadth	-	1.4	[m]
	Depth	-	0.5	[m]
	Transversal area	-	0.7	[m^2]
	Maximum current velocity	-	0.5	[m/s]

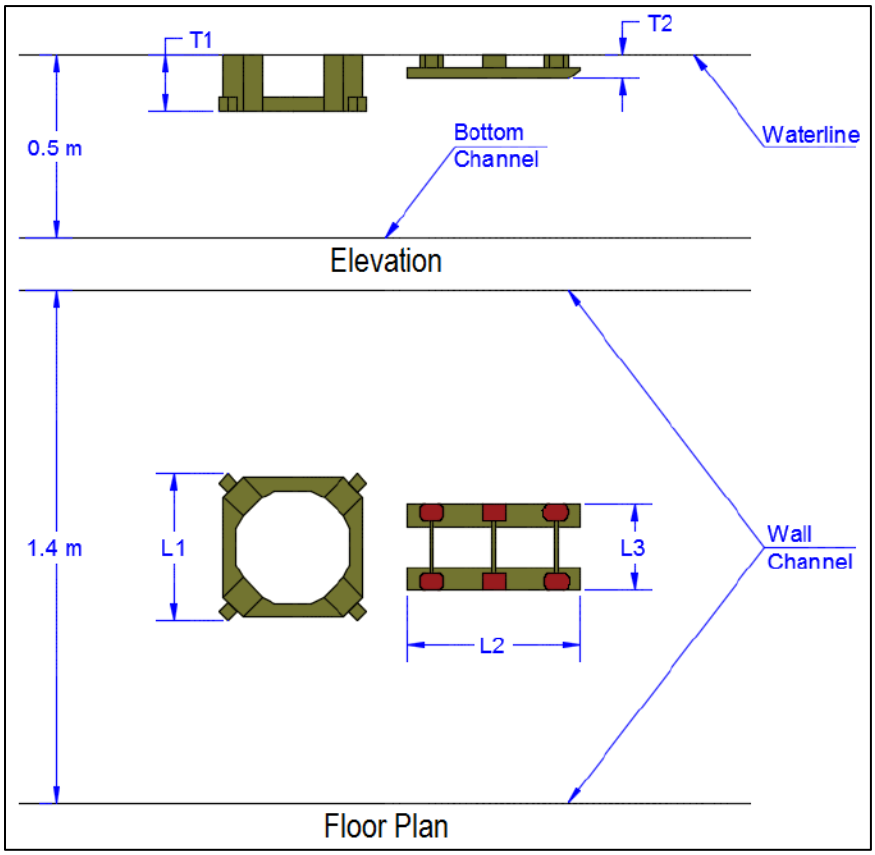

Figure 5.3 Arrangement for the scale factor analysis.

Table 5.4 Summary of scale factor analysis.

Scale factor	C1 [%]	C2 [%]	C3 [%]	Max. V_C [m/s]
120	51.7	55.8	16.1	0.14
150	41.3	44.7	10.3	0.12
175	35.4	38.3	7.6	0.11
200	31.0	33.5	5.8	0.11
220	28.2	30.5	4.8	0.10
250	24.8	26.8	3.7	0.09
300	20.7	22.3	2.6	0.09
Limits	35.0	35.0	7.5	0.50

Finally, the ultra-reduced scale models were constructed using 3D-printed blocks made of PLA filament by fused deposition modeling (FDM) technology. Figures 5.4 and 5.5 present the TLP and TAD models under construction and complete, respectively.

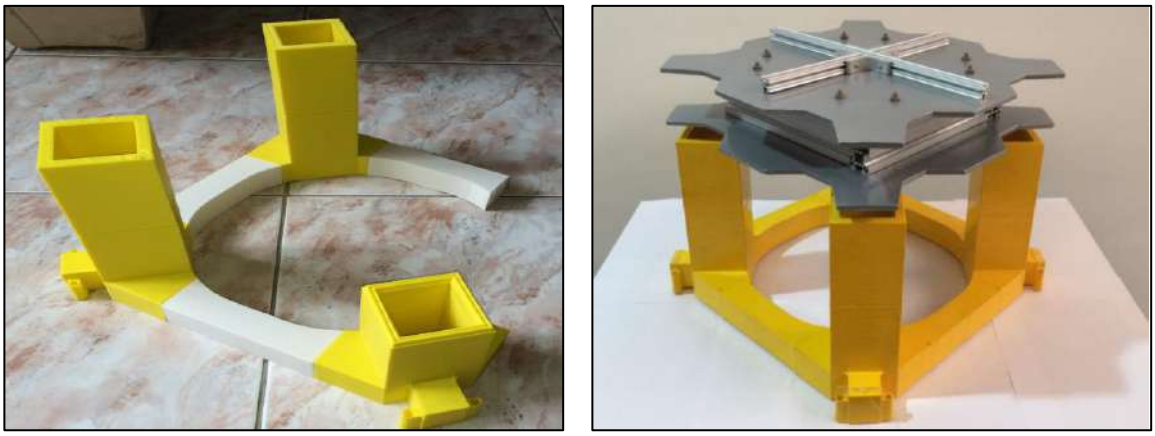

Figure 5.4 Construction of the TLP ultra-reduced model.

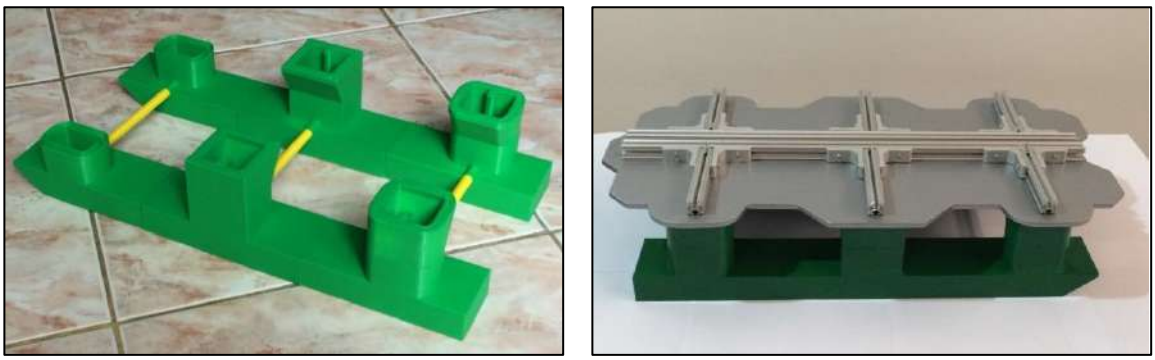

Figure 5.5 Construction of the TAD ultra-reduced model.

5.5 EXPERIMENTAL SETUP

The model tests were conducted in the current channel of the Laboratory of Waves and Currents (LOC) of COPPE/UFRJ. The current channel is 22 m in length, 1.4 m in width and 0.5 m in depth. Four electrical pumps generate the flow into the channel. An electronic module controls the RPM of the pumps and consequently the flow velocity in the channel. Finally, a propeller flowmeter measures the flow velocity.

The experimental setup was assembled to measure the current loads on the floaters, considering the five current velocities of Tab. 5.2 and current angles of incidences varying from 0° to 360° in 15° increments.

The main components of the experimental apparatus are the aluminum profile supports mounted on the walls of the current channel, the load cell to measure the forces and moment on the bodies in the horizontal plane and the rotational plate to modify the angle of attack. An HBM Quantum X MX840B unit completes the data acquisition system. This unit is an 8-channel universal amplifier that connects the load cell to a CPU computer.

Note that, the aluminum profile supports comprise four parts: the fixed part, the mobile part along the x-axis, a mobile part along the y-axis and the mobile part along the z-axis. Figure 5.6 presents these parts in silver, green, dark yellow and yellow, respectively. The movable parts guarantee the correct position and draft of the mounted platform during the tests.

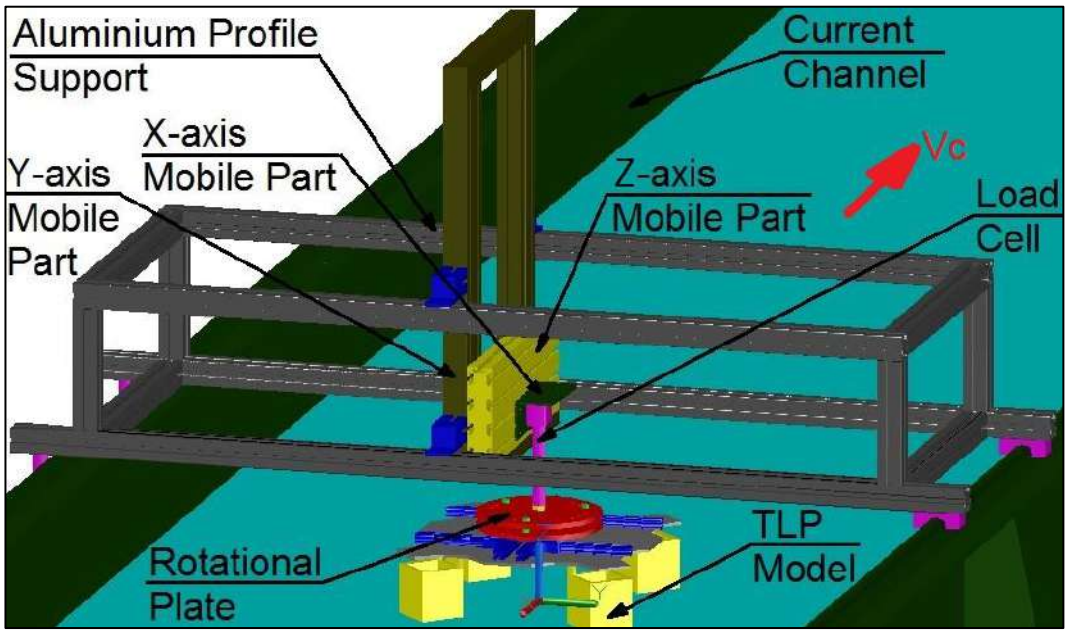

Figure 5.6 Experimental setup for the TLP alone. The current direction is shown in red.

Figures 5.6 and 5.7 present the experimental arrangement for TLP alone and TAD alone cases, respectively. The apparatus for both single-body cases is the same.

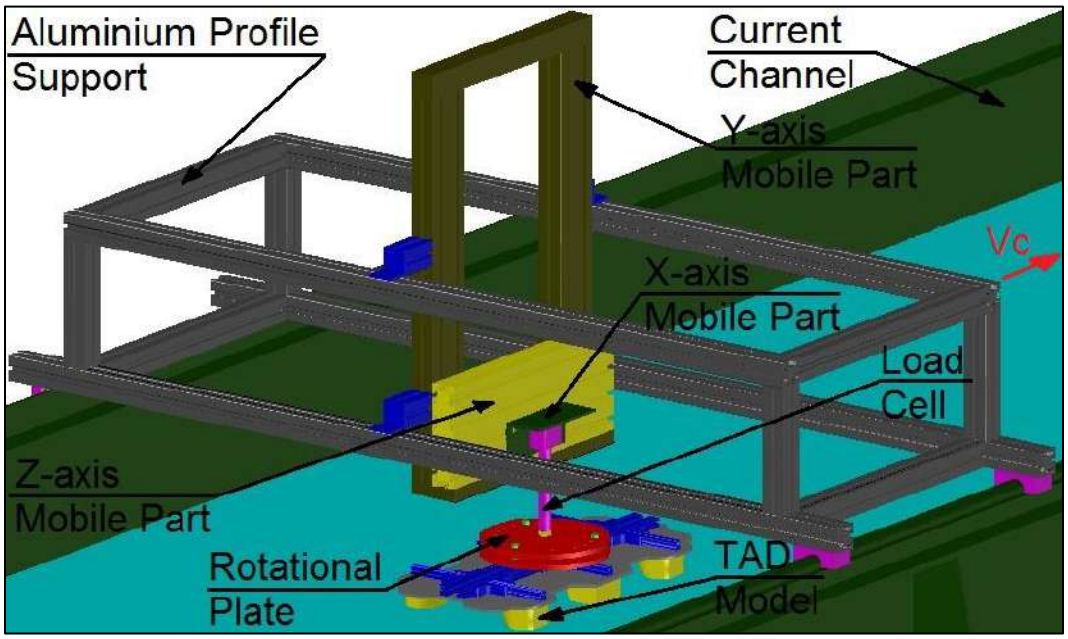

Figure 5.7 Experimental setup for the TAD alone. The load cell is shown in magenta.

The multi-body case is divided into two sub-cases. In the first, the TLP is the main unit, and the TAD is the auxiliary unit. In the second, the TAD is the main unit, and the TLP is the auxiliary unit.

For both sub-cases, the main unit is mounted on the load cell, and the auxiliary unit is fixed at a constant distance from the main unit. Thus, the main unit is analyzed for all the angles of attack and current velocities, while the auxiliary unit is fixed.

Figures 5.8 and 5.9 present the experimental setup for both multi-body sub-cases. The main unit is mounted the same manner as that described for the single-body cases. The auxiliary unit is fixed to the additional support. This support is installed on aluminum support to ensure the correct position and draft of the auxiliary unit along the x-axis, y-axis, and z-axis during the tests.

Furthermore, each sub-case considered the main unit upstream and downstream of the auxiliary unit. In addition, three relative distances between the main and auxiliary units were

considered, as shown in Figs. 5.10 and 5.11. Table 5.5 presents the relative distances between the TLP and TAD.

Table 5.5 Relative distances between main and auxiliary units

Case code	Full-scale Dx [m]	Model-scale Dx [m]
D1	100	0.50
D2	110	0.55
D3	120	0.60

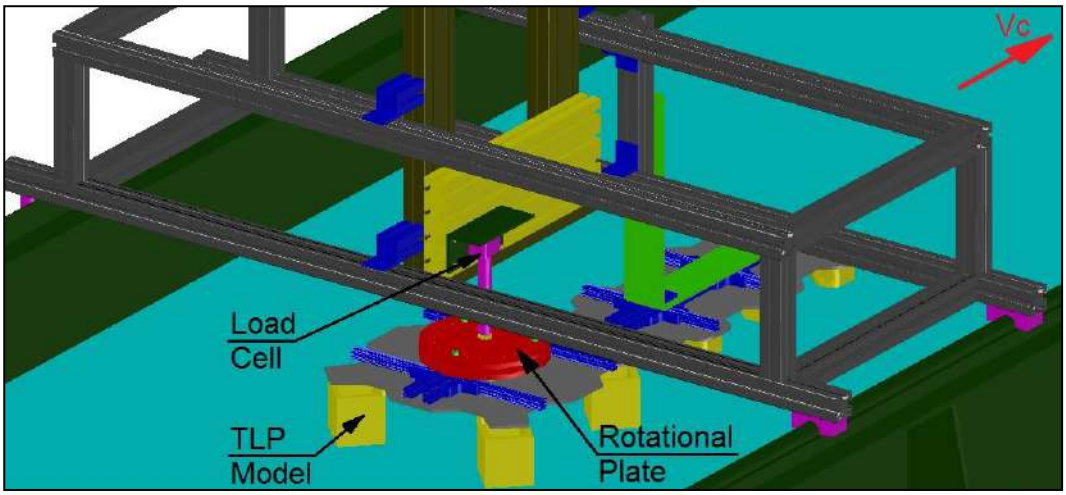

(A)

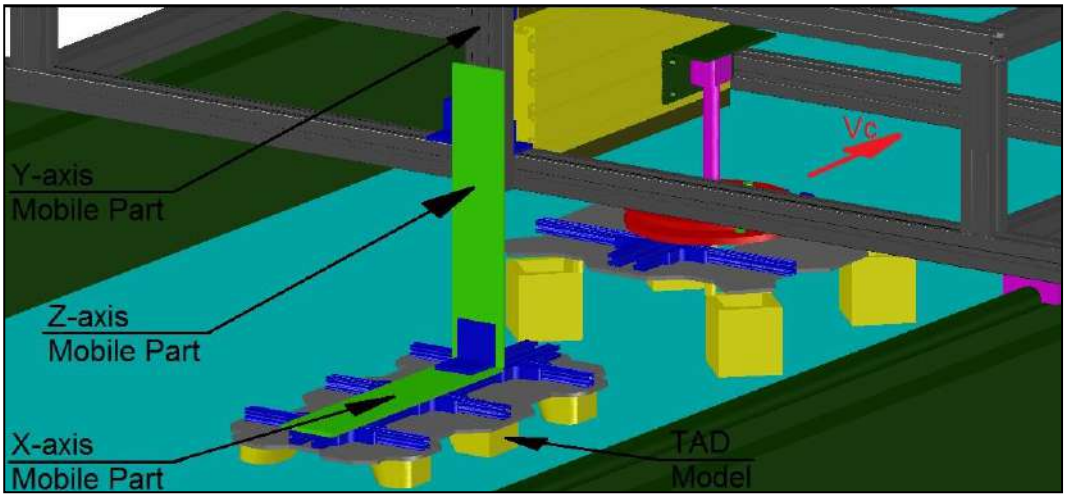

(B)

Figure 5.8 Experimental setup for the multi-body case. TLP as a main unit and TAD as an auxiliary unit: (A) TLP upstream and (B) TLP downstream.

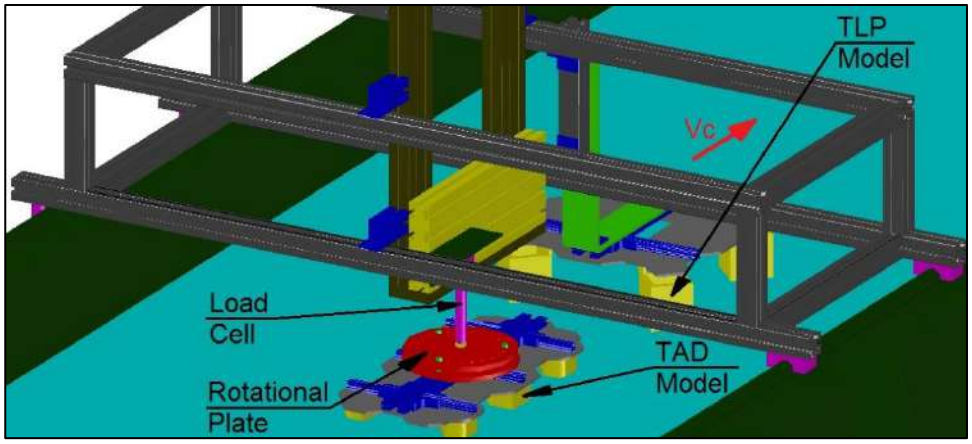

(A)

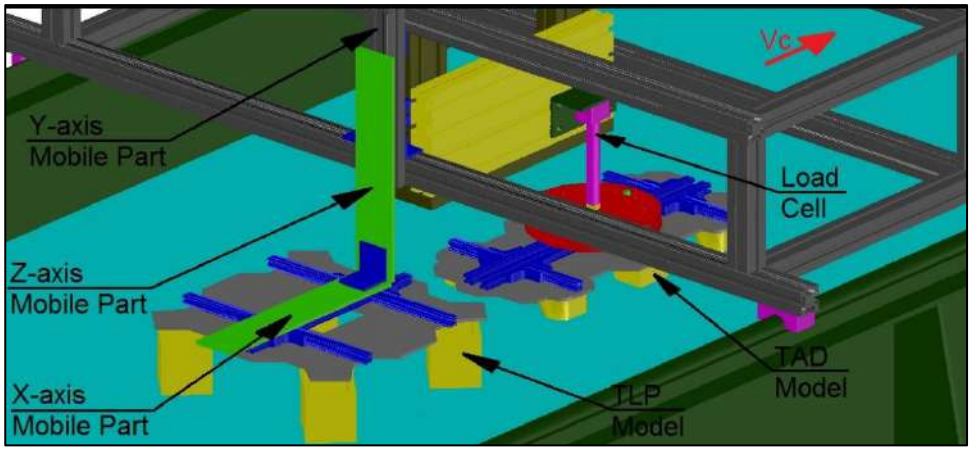

(B)

Figure 5.9 Experimental setup for the multi-body case. TAD as a main unit and TLP as an auxiliary unit: (A) TAD upstream and (B) TAD downstream.

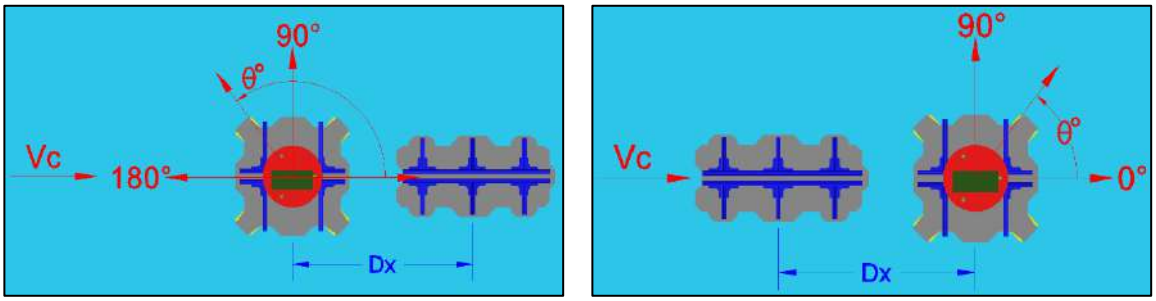

(A) (B)

Figure 5.10 Relative distances between TLP and TAD:
(A) TLP upstream and (B) TLP downstream.

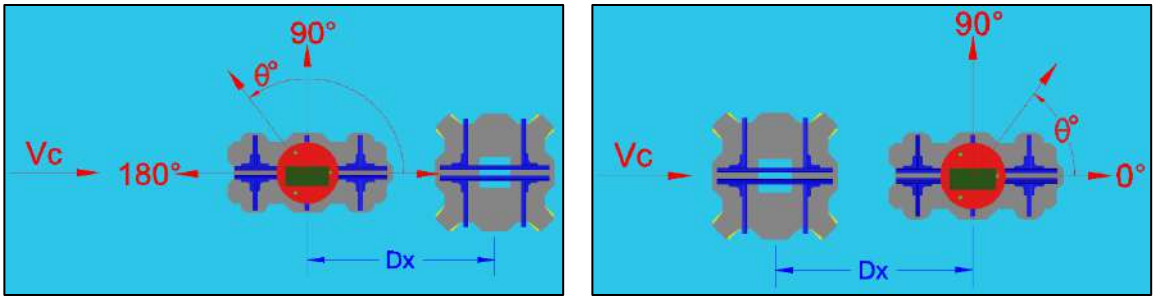

(A) (B)

Figure 5.11 Relative distances between TAD and TLP:
(A) TAD upstream and (B) TAD downstream.

The load cell was calibrated by applying known forces and moments to the systems. The current velocities were calibrated by varying the RPM of the pumps. Table 5.6 presents the mean value, standard deviation, and turbulence intensity of the current velocities. Figure 5.12 a time series of measurements of current velocities. In general, the differences between mean values and target values are reasonable, i.e., less than 10%. The turbulence intensity is relatively high, as is evident at velocity V1.

Table 5.6 Experimental and target values of the current velocities of the model tests.

	Target values		Experimental values			
	Full-scale [m/s]	Model scale [m/s]	Mean [m/s]	Error [%]	Std. Dev. [m/s]	Turbulence intensity [%]
V1	0.3	0.021	0.023	8.3	0.0030	13.0
V2	0.6	0.042	0.044	5.9	0.0039	8.9
V3	0.9	0.064	0.060	5.7	00057	9.5
V4	1.2	0.085	0.080	6.4	0.0063	7.9
V5	1.5	0.106	0.111	4.8	0.0091	8.2

Finally, Table 5.7 presents a summary of this experimental campaign. Each test has a duration of 300 sec. at model scale, which represents more than 70 minutes at full scale. Furthermore, each test was repeated three times, and the average values were reported to suppress variations. A total of 60 tests were conducted for the TLP alone; 195 tests for the

TAD alone were performed, and 144 tests have been conducted for the TLP-TAD multi-body system.

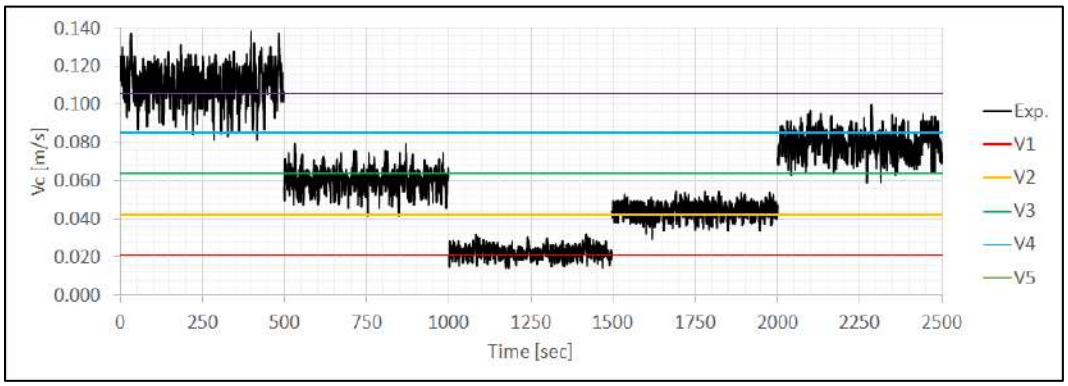

Figure 5.12 Time series of the current velocities.

Table 5.7 Summary of the experimental campaign.

Tests Description	Current velocity [m/s]	Current angle [deg.]
TLP alone	0.3 -1.5@0.3	0°-45°@15°
TAD alone	0.3 -1.5@0.3	0°-180°@15°
TLP upstream with TAD @ Dx = 100m	0.3 and 1.5	0°-345°@15°
TLP upstream with TAD @ Dx = 110m	0.3 and 1.5	0°-345°@15°
TLP upstream with TAD @ Dx = 120m	0.3 and 1.5	0°-345°@15°
TLP downstream with TAD @ Dx = 100m	0.3 and 1.5	0°-345°@15°
TLP downstream with TAD @ Dx = 110m	0.3 and 1.5	0°-345°@15°
TLP downstream with TAD @ Dx = 120m	0.3 and 1.5	0°-345°@15°
TAD upstream with TLP @ Dx = 100m	0.3 and 1.5	0°-345°@15°
TAD upstream with TLP @ Dx = 110m	0.3 and 1.5	0°-345°@15°
TAD upstream with TLP @ Dx = 120m	0.3 and 1.5	0°-345°@15°
TAD downstream with TLP @ Dx = 100m	0.3 and 1.5	0°-345°@15°
TAD downstream with TLP @ Dx = 110m	0.3 and 1.5	0°-345°@15°
TAD downstream with TLP @ Dx = 120m	0.3 and 1.5	0°-345°@15°

5.6 EXPERIMENTAL RESULTS

The outputs of the experimental tests are the current loads on the floaters in the horizontal plane. Thus, the forces F_X and F_Y on the x-axis and y-axis, and the moment M_Z about the z-axis were measured by the load cell. These forces and moments are reported in the non-dimensional form presented in Eqns. (5.8) to (5.10).

$$C_{FX} = \frac{F_X}{0.5\rho V^2 A_X} \tag{5.8}$$

$$C_{FY} = \frac{F_Y}{0.5\rho V^2 A_Y} \tag{5.9}$$

$$C_{MZ} = \frac{M_Z}{0.5\rho V^2 A_Z L_Z} \tag{5.10}$$

where C_{FX}, C_{FY} and C_{MZ} are the nondimensional coefficients, ρ is the water density of the channel, V is the current velocity, and A_X, A_Y, A_Z and L_Z are characteristic dimensions of the platforms. Table 5.8 presents these characteristic dimensions for both platforms.

Table 5.8 Characteristic dimensions of TLP and TAD.

Parameter	TLP		TAD	
	Full scale	Model scale	Full scale	Model scale
$A_X\ [m^2]$	2000	0.050	300	0.0075
$A_Y\ [m^2]$	2000	0.050	800	0.0200
$A_Z\ [m^2]$	1000	0.025	1000	0.0250
$L_Z\ [m]$	31	0.155	15	0.0750

The initial tests were conducted with the TLP and TAD alone over a current velocity range of [0.3 - 1.5] m/s to assess the dependence on current speed. Five current velocities were considered in this analysis. Due to the symmetry of the hulls, the angles of attack were respectively reduced to 4 ([0° - 45°] in steps of 15°) and 13 ([0° - 180°] in steps of 15°).

Figure 5.13 presents the coefficient C_{FX} for the TLP and TAD alone with an angle of attack equal to 0°. Although some fluctuations of C_{FX} were observed, these variations represent less than 3.4%. Similar spreading was found in the coefficients C_{FY} and C_{MZ}.

The results from the tests with different angles of attack reveal same trends. Therefore, it is possible to conclude that there were no significant effects due to current velocity in the range adopted for the tests.

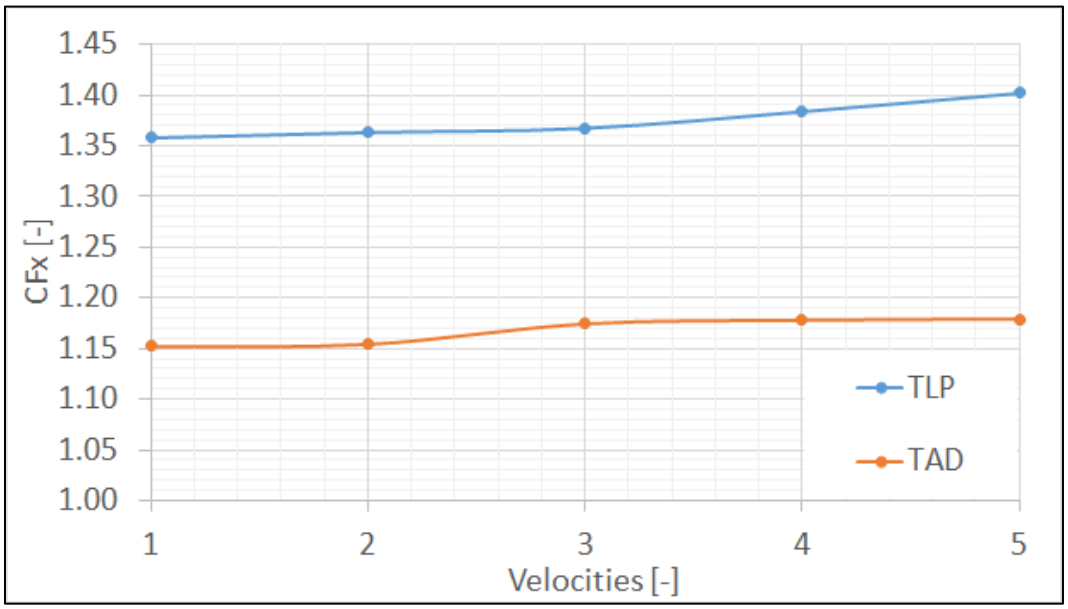

Figure 5.13 Variation of C_{FX} with the current velocity.

Based on these results, the number of current velocities of the tests was reduced from 5 to 2 in the multi-body cases. An analysis of the influence of the current velocity on the current load coefficients for the multi-body cases reveals similar trends. No significant variations were found, and the fluctuations between the values represent less than 5.1% for all multi-body cases. The variations in the repeated tests were relatively low; less than 3.9% in all cases.

The current loads on the TLP and TAD alone were assessed through an analysis of the angle of attack. Figures 5.14, 5.15 and 5.16 present, respectively, the current load coefficients C_{FX}, C_{FY} and C_{MZ} of the TLP alone. In the three figures the following are observed:

- C_{FX} presents relatively small variation over angles of attack ranging from 0° to 60°. The peak force corresponds to 30°. In the range of [60° - 120°], C_{FX} decays linearly with the angle of attack.

- C_{FY} presents constant behavior with small variation over angles of attack ranging from 30° to 150°. The force peak corresponds to 60°. Additionally, C_{FY} presents a linear behavior over the range of [150° - 210°].
- C_{MZ} presents periodical behavior with peaks in the moment for angles 30°, 60° and so on. It is important to note that the moment has a no zero value for the angles of 0° and 45°, when due to the symmetry, a zero value could be expected.

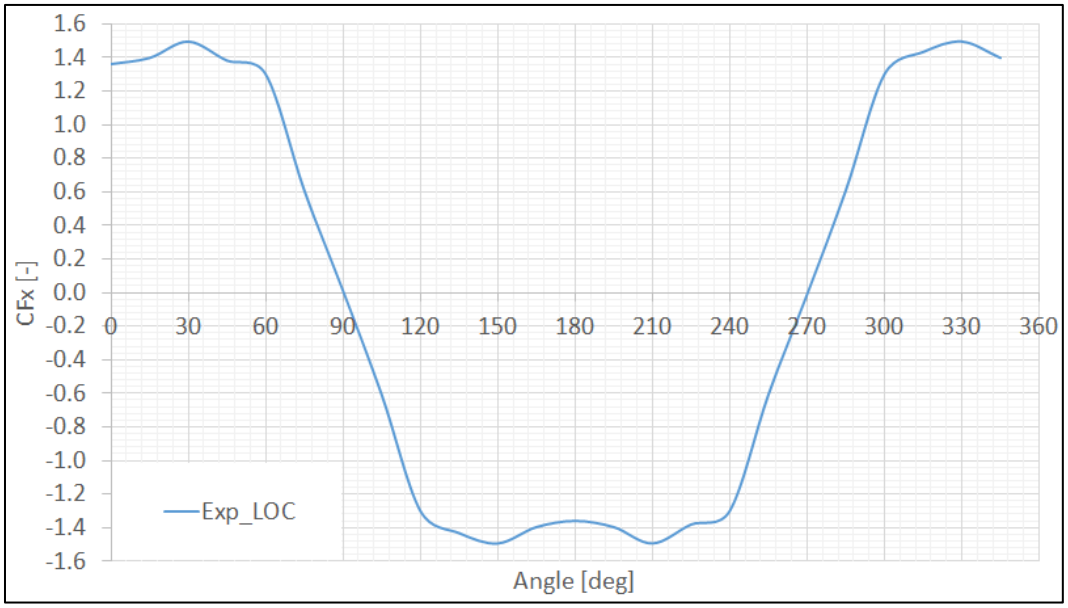

Figure 5.14 Variation of C_{FX} with angle of attack for TLP alone.

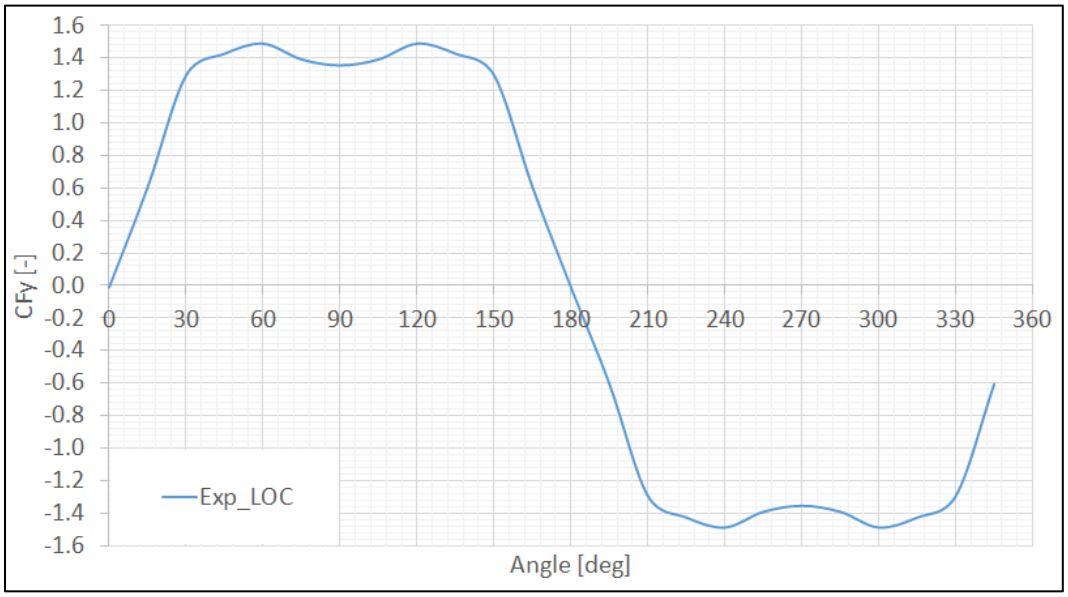

Figure 5.15 Variation of C_{FY} with angle of attack for TLP alone.

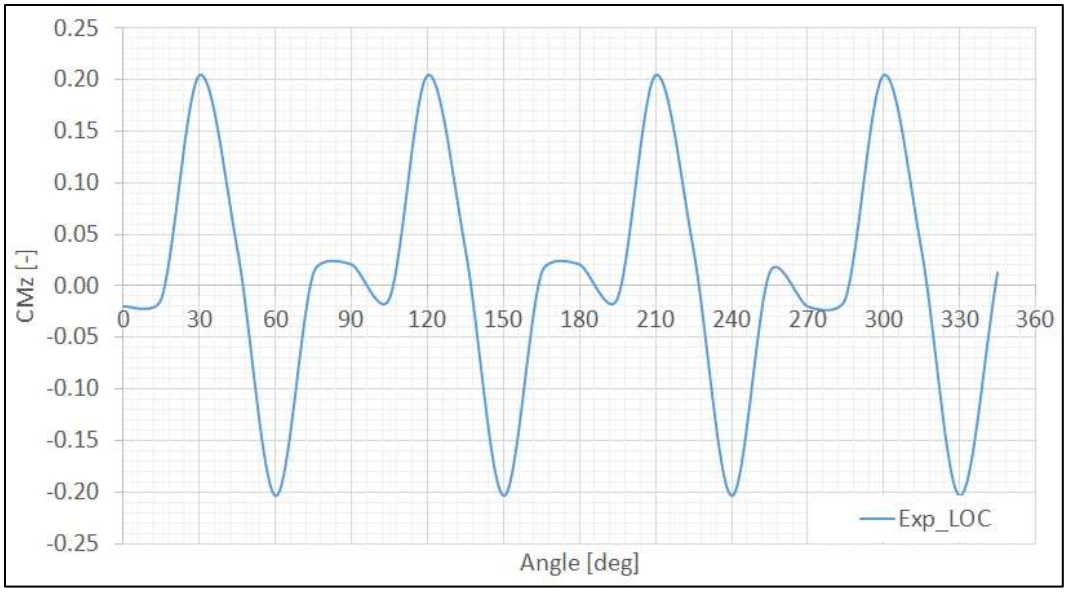

Figure 5.16 Variation of C_{MZ} with angle of attack for TLP alone.

Similarly, Figs. 5.17, 5.18 and 5.19 present, respectively, the current load coefficients C_{FX}, C_{FY} and C_{MZ} of the TAD alone. The following are observed:

- C_{FX} presents the peak force at 25°, and presents a linear trend over angle of attack ranging from 30° to 150°. In contrast to the TLP case, the TAD does not present large constant value force regions.

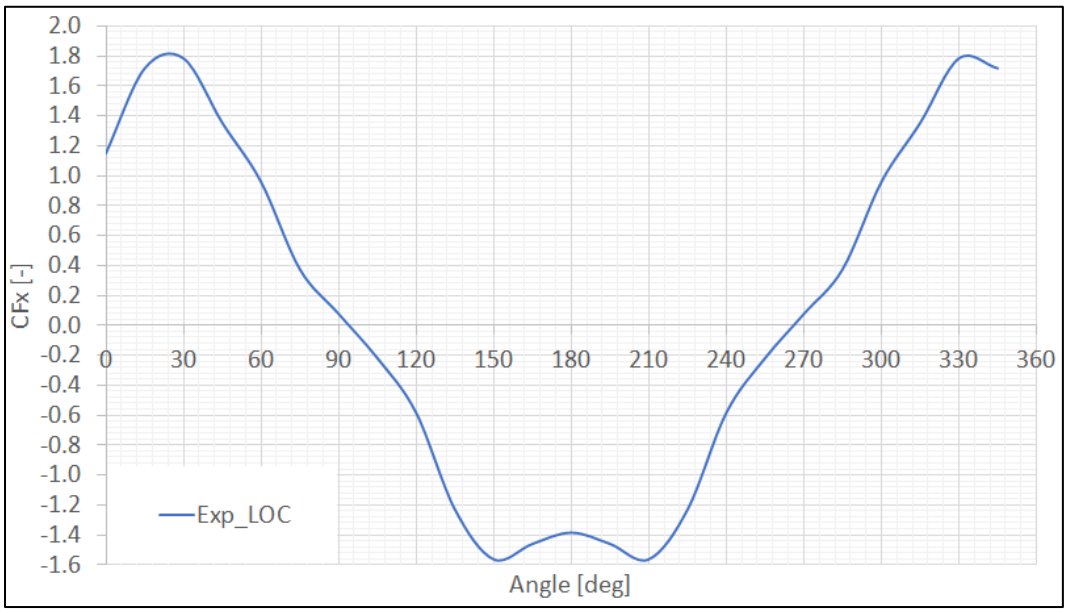

Figure 5.17 Variation of C_{FX} with angle of attack for TAD alone.

- C_{FY} presents constant behavior with little variations over angle of attack ranging from 60° to 120°. The peak force corresponds to 60°. Additionally, C_{FY} presents linear behavior over the range of [120° - 240°].
- C_{MZ} presents peaks in the moment for angles of 60° and 75°. The curve increases and decreases linearly over the ranges of [0° - 60°] and [75° - 105°], respectively.

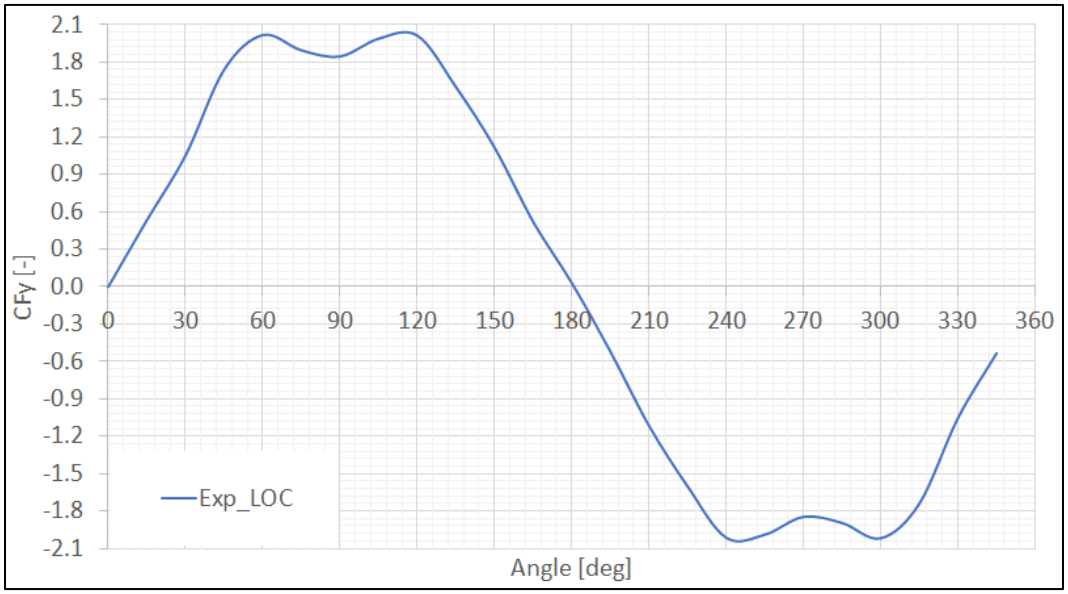

Figure 5.18 Variation of C_{FY} with angle of attack for TAD alone.

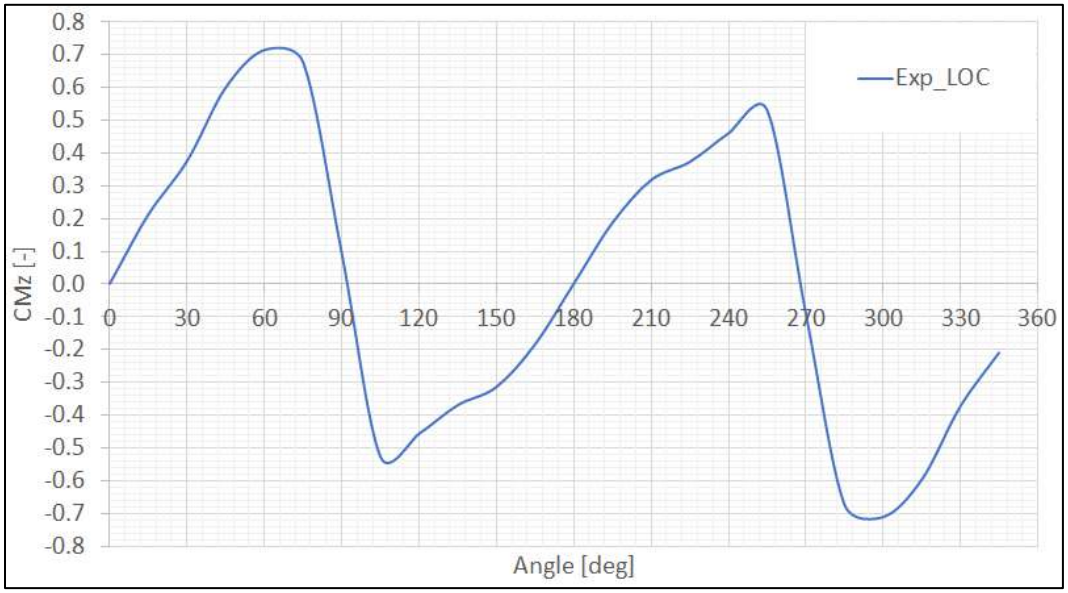

Figure 5.19 Variation of C_{MZ} with angle of attack for TAD alone.

The results of the multi-body tests with the TLP as the primary unit and the TAD as an auxiliary unit are shown and discussed below. The TLP was analyzed for the cases being upstream (UP) and downstream (DO) of the TAD. Three relative distances were considered (namely, D1, D2, and D3; see Tab. 5.5). For a better comparison of the relevance of shielding effects on the current coefficients, the results of the TLP alone are depicted together.

Figures 5.20, 5.21 and 5.22 present, respectively, the coefficients C_{FX}, C_{FY} and C_{MZ} of the TLP. In these figures, the part (A) presents the global results, while the part (B) presents only the results for one relative distance (D1).

The variations in coefficient C_{FX} of the TLP upstream range of [-7.5% to 5.3%] relative to that of the TLP alone. The highest variation occurs at an angle of attack equal to 30°. The results of the TLP downstream case present variations in the range of [-8.5% to 5.6%] relative to that of the TLP alone. The largest difference occurs for at an angle of 135°. See part (B) of Fig. 5.20 for angles of attack in the ranges of [120° – 240°] and [300° – 345°]

The coefficient C_{FY} with the TLP upstream varies in the range of [-6.4% to 5.7%] relative to that of the TLP alone. The highest variation occurs for an angle of attack equal to 30°. In contrast, the results of the case TLP downstream case present variations in the range of [-7.0% to 3.7%] relative to that of the TLP alone. The largest difference occurs for an angle of 210°. See part (B) of Fig. 5.21 for angles of attack in the ranges of [30° – 45°] and [120° – 150°].

The variations observed in the coefficient C_{MZ} were considerably higher than those in C_{FX} and C_{FY}. The differences in relation to the case TLP alone case are more evident for angles of attack of 15°, 105° and 295°. In general, the TLP upstream presents higher loads than TLP alone and TLP downstream. However, some angles deviate from this trend.

The spread in C_{MZ} for an angle of 60° was the lowest, approximately 14%.

In general, the variations in the coefficients C_{FX} and C_{FY} were higher than the fluctuations found in the repeatability tests using different current. Although, these fluctuations could represent evidence of shielding effects, they are relatively small since the maximum difference was approximately 10%.

Moreover, no significant differences were found between upstream and downstream cases. Thus, it is difficult to establish a relationship between the variations in C_{FX} and C_{FY} and

the relative distances between the floaters. Therefore, the shielding effects on these coefficients of the TLP are relatively weak.

Only C_{MZ} presents significant variations. Therefore, the shielding effects on the current moment of the TLP are relevant and cannot be neglected.

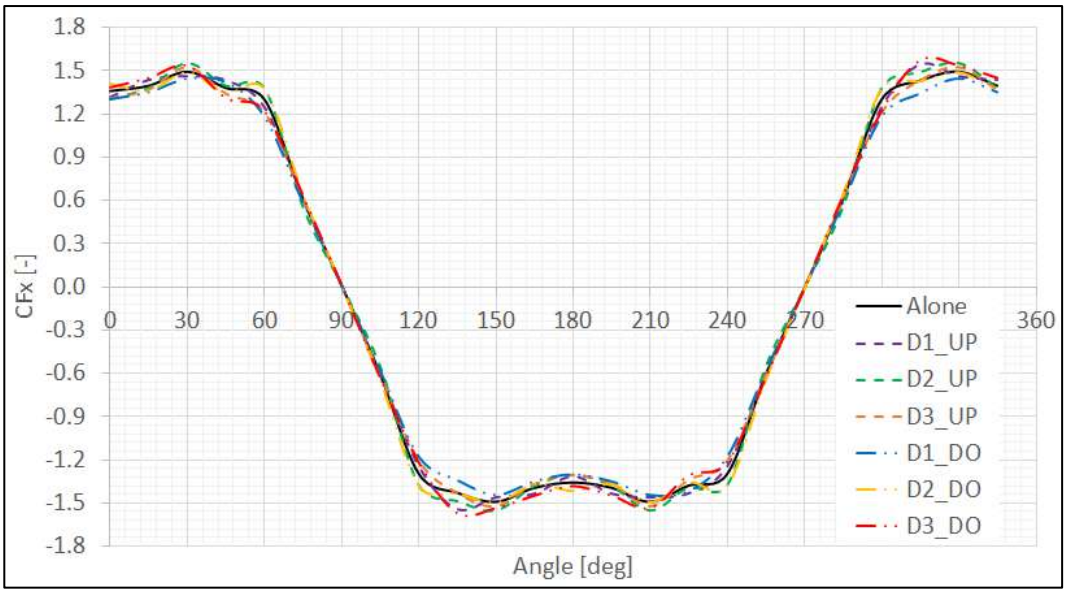

(A)

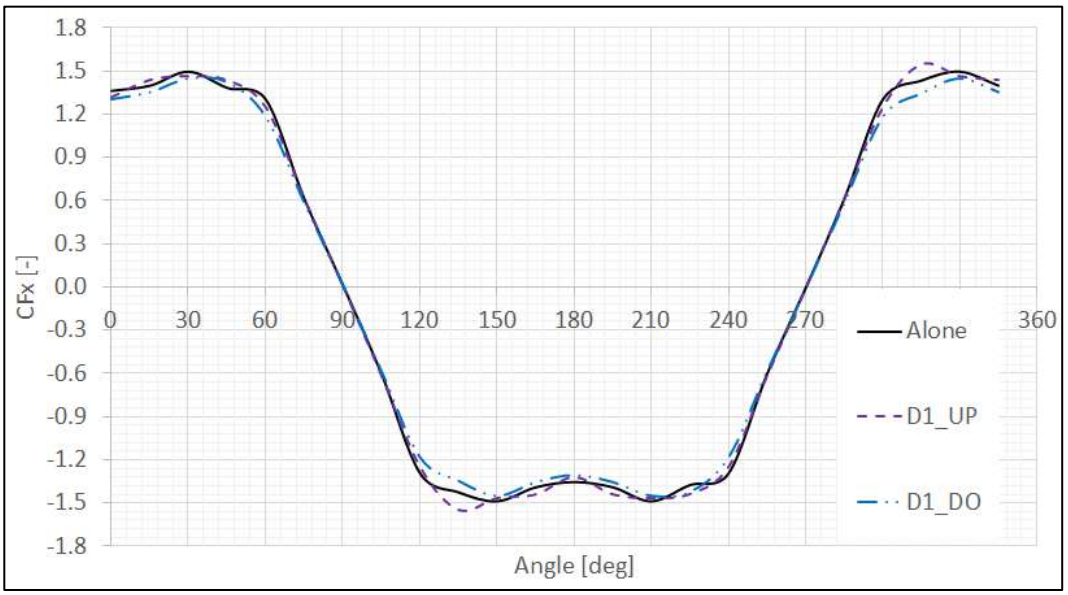

(B)

Figure 5.20 Current coefficient C_{FX} for the TLP. Single-body vs. multi-body cases with TLP upstream (UP) and TLP downstream (DO). D1= 100 m, D2= 110 m, and D3= 120 m.

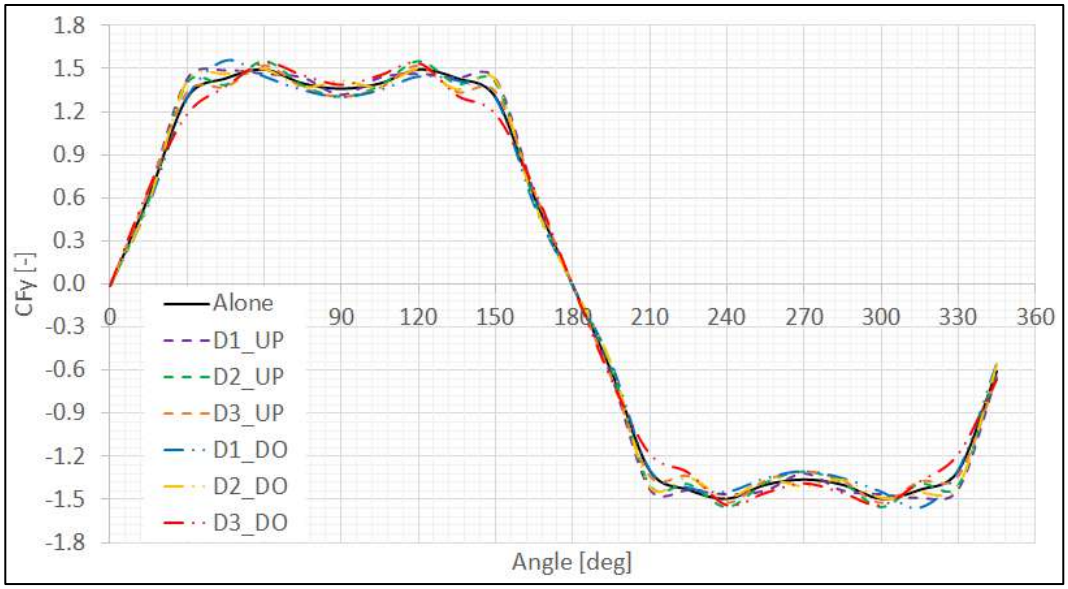

(A)

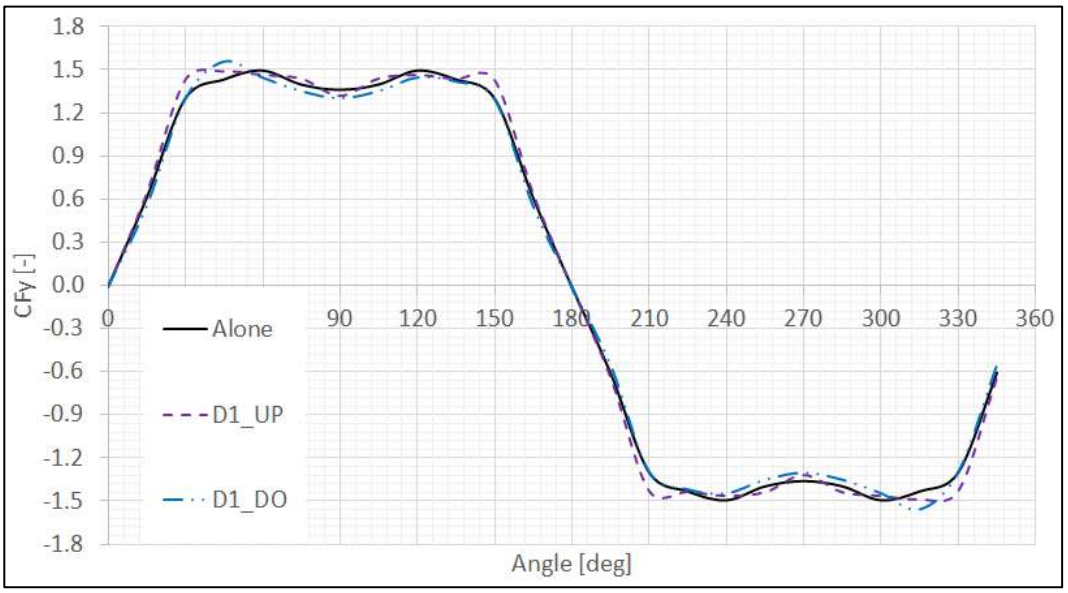

(B)

Figure 5.21 Current coefficient C_{FY} for the TLP. Single-body vs. multi-body cases with TLP upstream (UP) and TLP downstream (DO). D1= 100 m, D2= 110 m, and D3= 120 m.

Finally, the results of the multi-body tests with the TAD as the primary unit and the TLP as an auxiliary unit are presented and discussed below. The TAD was analyzed for the cases being upstream (UP) and downstream (DO) of the TLP, considering the relative distances

(namely, D1, D2, and D3) reported in Tab. 5.5. For a better understanding of the shielding effects on the current coefficients, the results of the TAD alone case are depicted together.

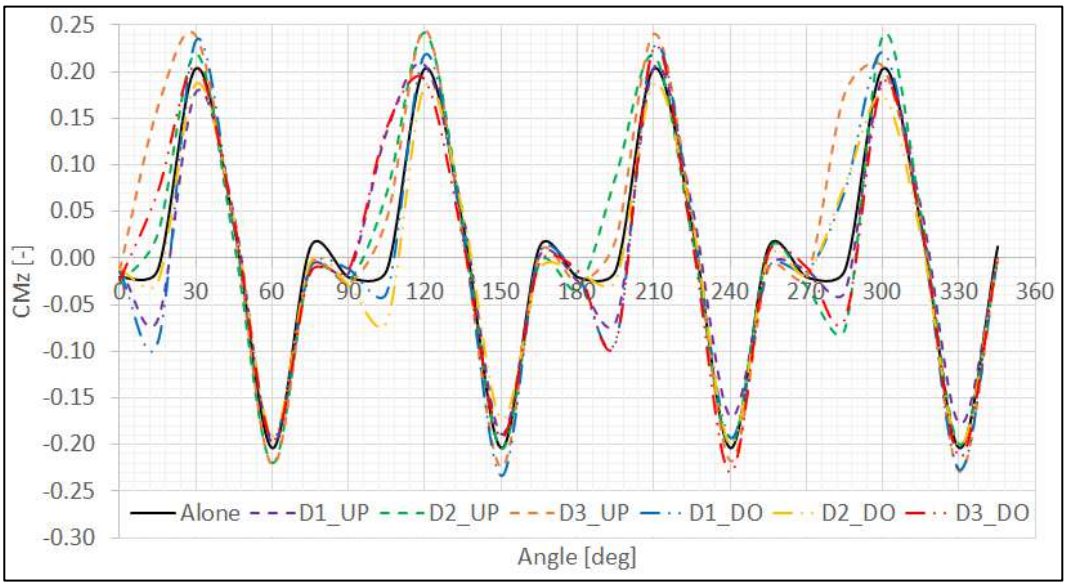

(A)

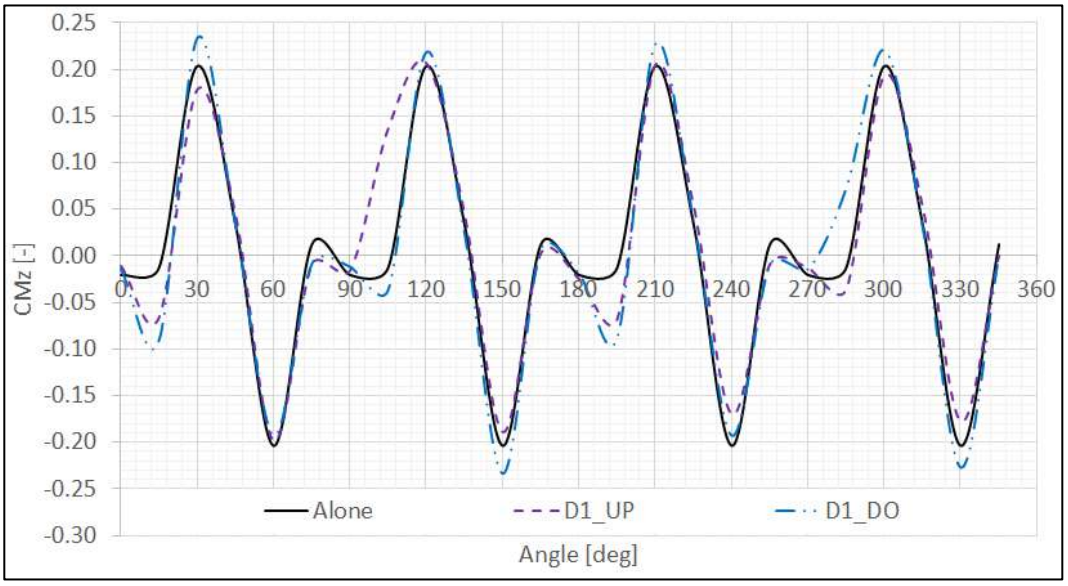

(B)

Figure 5.22 Current coefficient C_{MZ} for the TLP. Single-body vs. multi-body cases with TLP upstream (UP) and TLP downstream (DO). D1= 100 m, D2= 110 m, and D3= 120 m.

Figures 5.23, 5.24 and 5.25 present, respectively, the coefficients C_{FX}, C_{FY} and C_{MZ} for the TAD. In these figures, part (A) presents the general results, while part (B) presents only the results considering one relative distance (D1).

In contrast to the case of the TLP, where the differences between the upstream and downstream cases were not clear. The results of the TAD tests reveal a clear trend. In general, the loads on the TAD upstream were higher than those on the TAD downstream case.

Despite small differences, the loads on the TAD upstream case were similar to that of the TAD alone case. As in the case of the TLP, the relative distance between the floaters seems to have a weak influence on the current loads on the TAD.

The coefficients C_{FX} of the TAD upstream case vary in the range of [-6.3% to 4.7%] relative to that of the TAD alone case. The highest variation occurs at an angle of attack equal to 255°.

The results of the TAD downstream case present variations in the range of [-24.8% to -4.3%] relative to that of the TAD alone case. The largest differences occur for the angles 15°, 120°, and 135°.

Part (B) of Fig. 5.23 shows the differences between upstream and downstream cases (both for D1) and the alone case. Small shielding effects on TAD upstream are observed. Thus, the variations in relation to the alone case are minor.

In contrast, shielding effects on the TAD downstream were high. Consequently, the loads were minor relative to the alone case.

The C_{FY} for the TAD upstream varies in the range of [-4.9% to 3.7%] relative to that of the TAD alone case. The highest variations occur for angles of attack equal to 15° and 240°.

In contrast, the results of the TAD downstream case present variations in the range of [-26.1% to -2.0%] relative to that of the TAD alone case. The largest difference occurs at 90°. See part (B) of Fig. 5.24 for angles of attack in the range of [45° – 120°] and [240° – 315°]

Finally, the coefficients C_{MZ} of the TAD case present the same trends that are observed for C_{FX} and C_{FY}. The TAD upstream results vary in the range of [-2.7% to 4.8%] relative to that of the TAD alone case.

The highest variation occurs at an angle of attack equal to 195°. In addition, the results of the TAD downstream case present variations in the range of [-25.1% to -0.3%] relative to that of the TAD alone case.

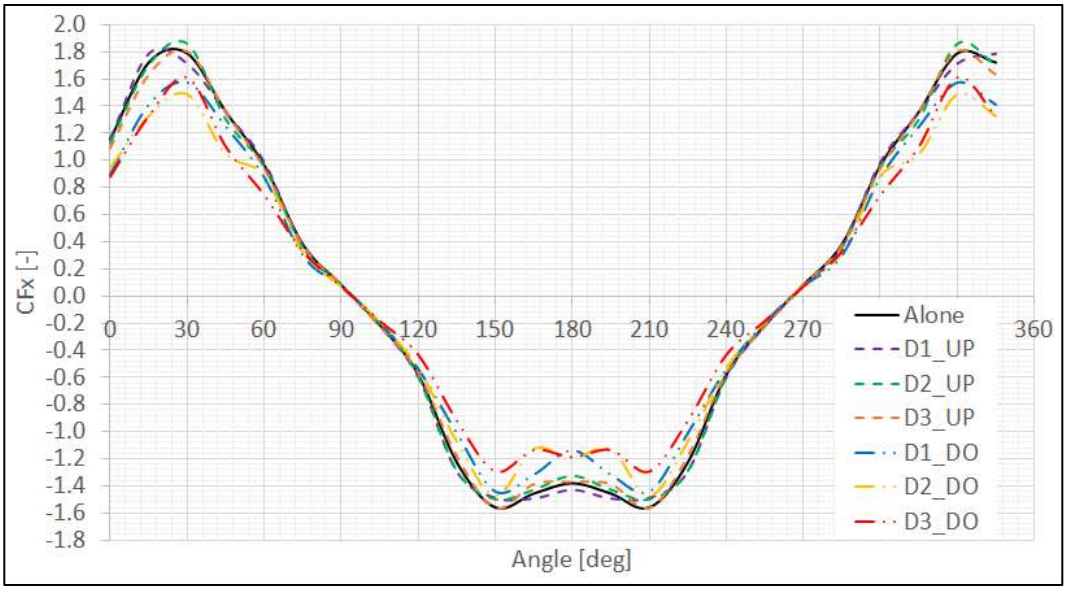

(A)

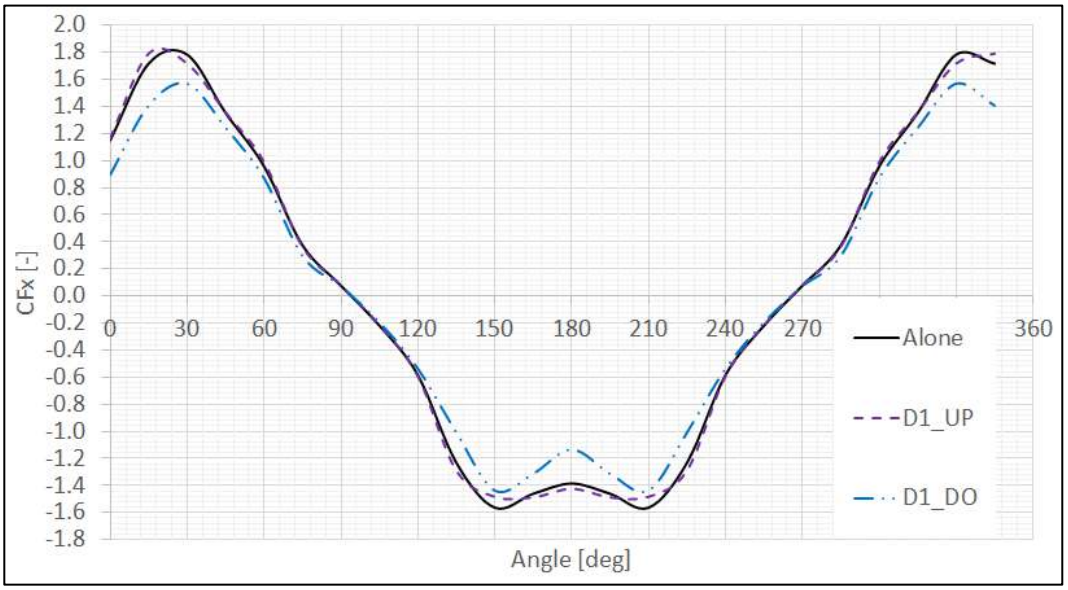

(B)

Figure 5.23 Current force coefficient C_{FX} for the TAD.

Single-body vs. Multi-body cases with TAD upstream (UP) and TAD downstream (DO).

D1 = 100 m, D2 = 110 m, and D3 = 120 m.

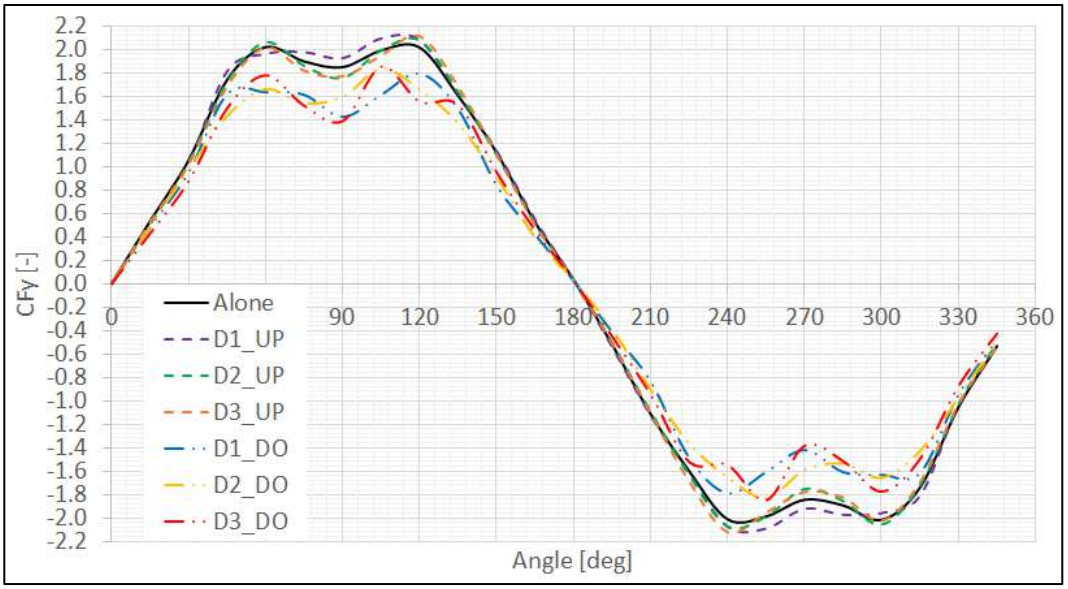

(A)

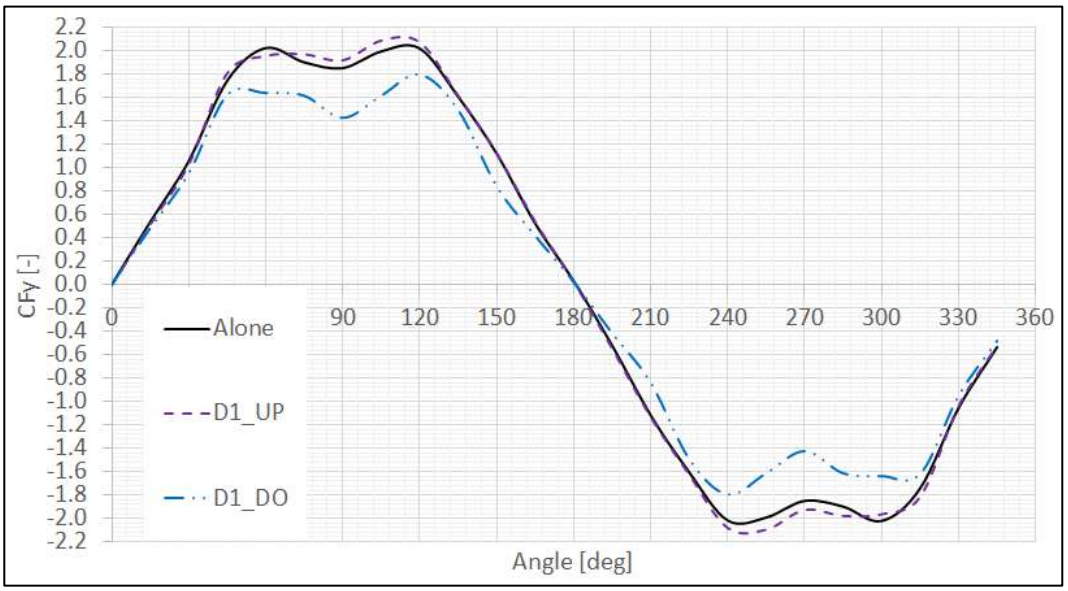

(B)

Figure 5.24 Current force coefficient C_{FY} for the TAD.

Single-body vs. Multi-body cases with TAD upstream (UP) and TAD downstream (DO).

D1 = 100 m, D2 = 110 m, and D3 = 120 m.

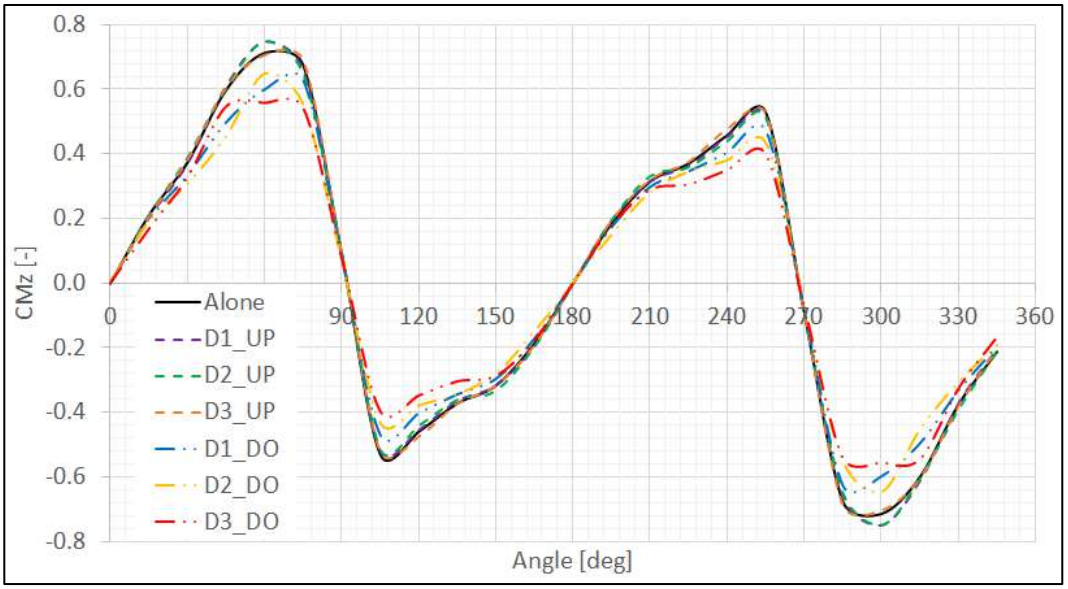

(A)

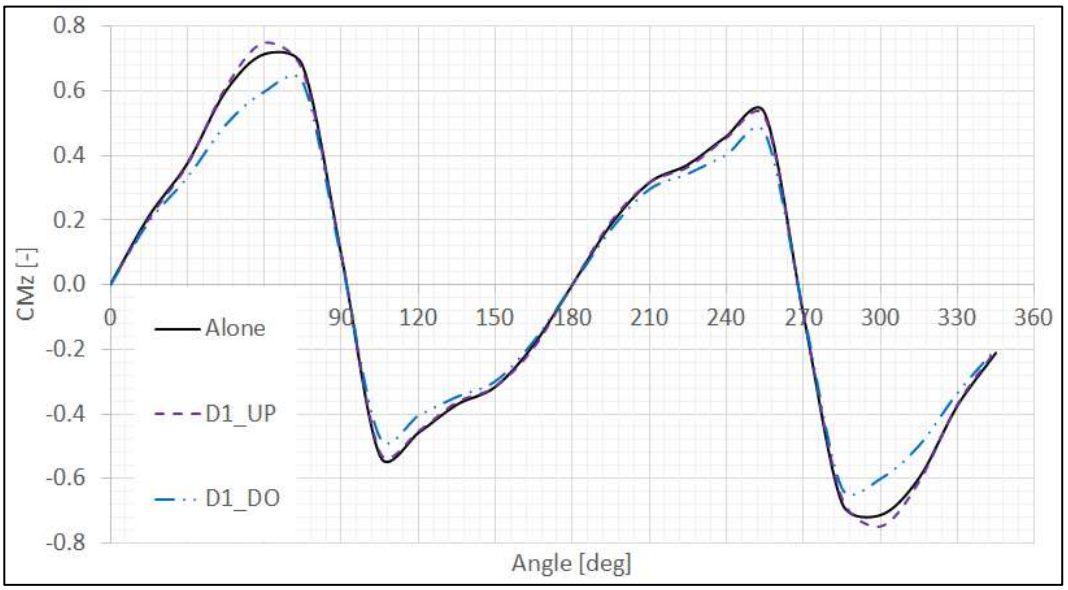

(B)

Figure 5.25 Current force coefficient C_{MZ} for the TAD.

Single-body vs. Multi-body cases with TAD upstream (UP) and TAD downstream (DO).

D1 = 100 m, D2 = 110 m, and D3 = 120 m.

5.7 FREQUENCY DOMAIN ANALYSIS

This section presents an analysis of the current loads in the frequency domain with the aim of identifying resonant frequencies that could induce VIM response in the floaters. The Power Spectral Density (PSD) is obtained by applying the Fast Fourier Transform (FFT) on the time history of the current load measurements. Note that the current velocities, frequency ranges and natural frequencies refer to the model-scale data.

The FFT was also used in the treatment of the experimental results. Fig. 5.26 compares the original time history measured in the test with the filtered signal, note that the mean values are the same for both signals.

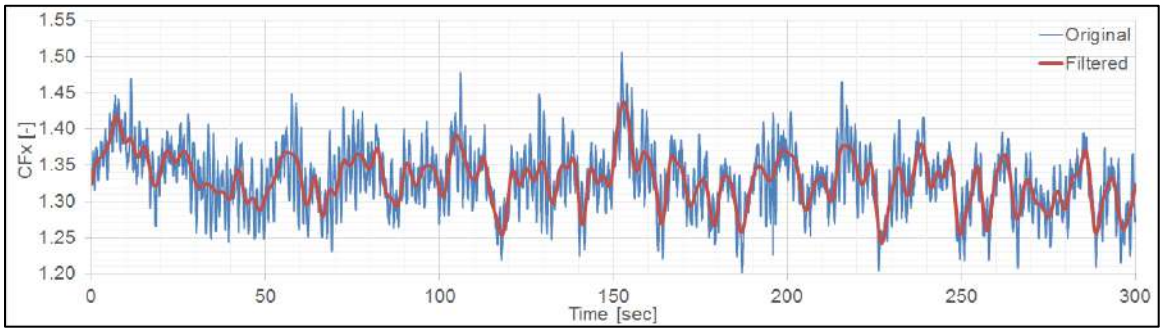

Figure 5.26 Current force coefficient C_{FX} of TLP alone with θ = 0°.

Figure 5.27 presents the power spectrum density (PSD) of the current force coefficient C_{FX} for the TLP alone considering a 0° angle of attack and the five current velocities presented in Tab. 5.6. The spectral analysis reveals an energy concentration in a short-band range of frequencies that peaks at approximately 0.05 Hz, particularly for velocities V1 and V2. As the velocity increases, the energy spreads across a wide-band range of frequencies. However, most of the energy remains concentrated in the range of [0.0 – 0.1] Hz. This fact is relevant because as mentioned in Section 3.4, the TLP has a Surge natural frequency equal to 0.070 Hz, hence, resonant motions could be expected in VIM tests.

The analysis of the coefficients C_{FX} for other angles of attack, reveals similar findings, i.e., the energy is concentrated in a low-frequency ranges of [0.0 – 0.1] Hz.

Figure 5.28 presents the PSD of the current force coefficient C_{FY} for the TLP alone at a 15° angle of attack. The PSD shows that the major of the energy is concentrated in the range of [0.0 – 0.1] Hz. However, some peaks appear at frequencies of approximately 0.15 Hz and 0.20 Hz. Note that, the Sway natural frequency is 0.07 Hz.

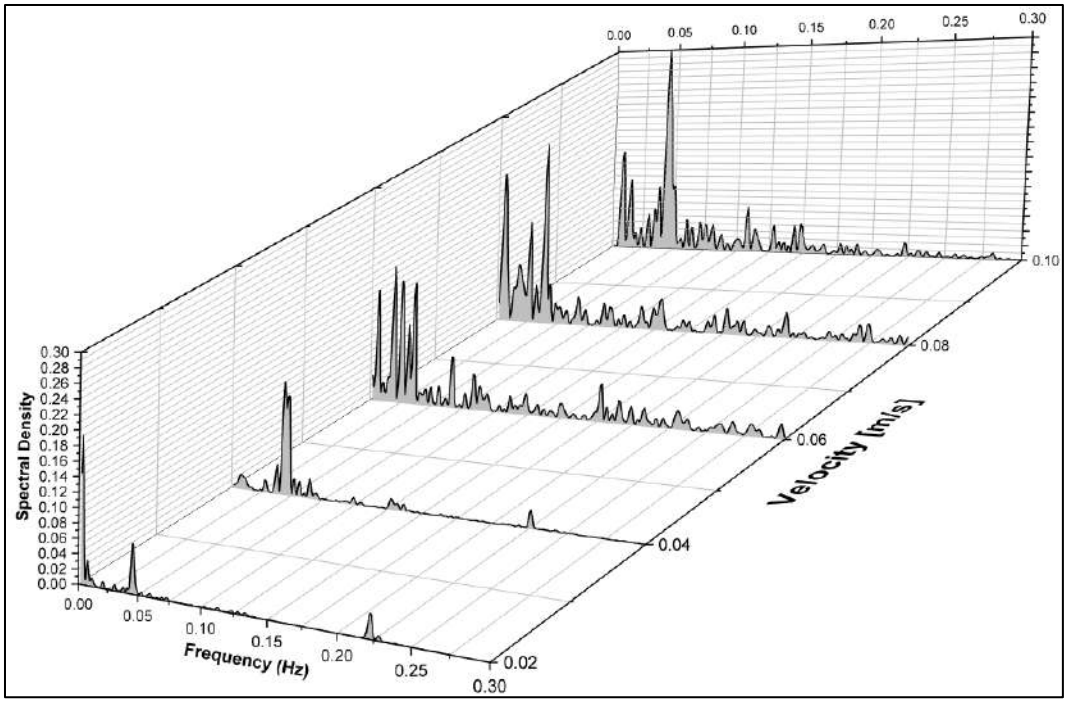

Figure 5.27 Power spectrum density from FFT of C_{FX} for TLP alone as a function of current velocity and frequency for θ = 0°.

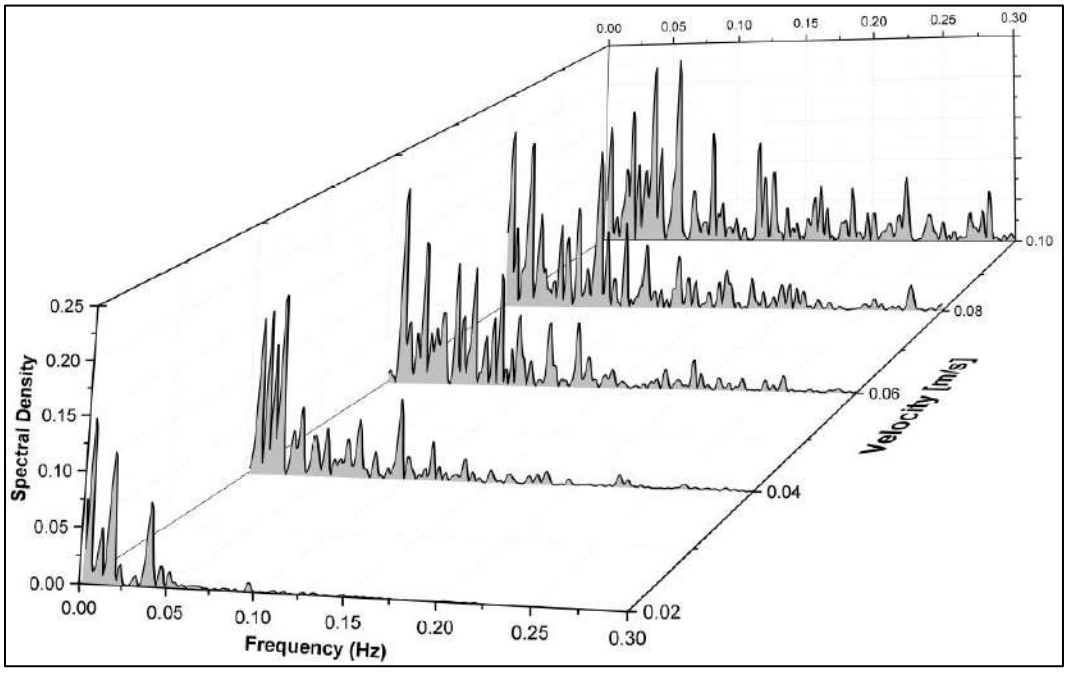

Figure 5.28 Power spectrum density from FFT of C_{FY} for TLP alone as a function of current velocity and frequency for θ = 15°.

Figure 5.29 shows the PSD of the current moment coefficient C_{MZ} for the TLP alone. Note that, in this case, the angle of attack is 30°. For velocities V1, V2 and V3, a concentration of energy is observed for frequencies in the range of [0.00 – 0.05] Hz. For velocities V4 and V5, peaks appear in the range of [0.00 – 0.15] Hz. Note that, the Yaw natural frequency is 0.106Hz.

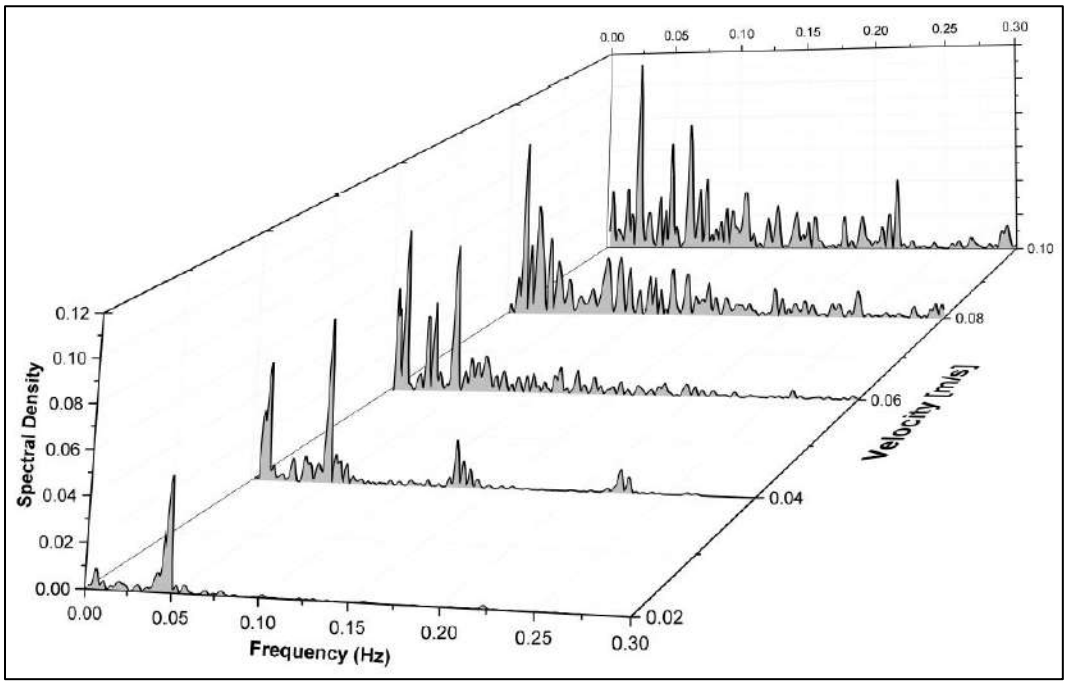

Figure 5.29 Power spectrum density from FFT of C_{MZ} for TLP alone as a function of current velocity and frequency for θ = 30°.

Figure 5.30 presents the power spectrum density of the current force coefficient C_{FX} for the TLP coupled with the TAD. Note that, the angle of attack is 0°, the distance between the floaters is D2 from Tab. 5.5, and the TLP is in the downstream position, as Fig. 5.10 – part (B) shows.

Based on the analysis presented in the previous section, no major differences between the single-body and multi-body cases were expected. However, the spectral analysis reveals small differences, particularly for velocities V3, V4, and V5. The energy peaks are observed at approximately 0.02 and 0.05 Hz, and the energy spreading is broader than that of the

single-body case, see Fig. 5.27, particularly for velocities V4 and V5, for which small peaks appear at frequencies up to 0.25Hz.

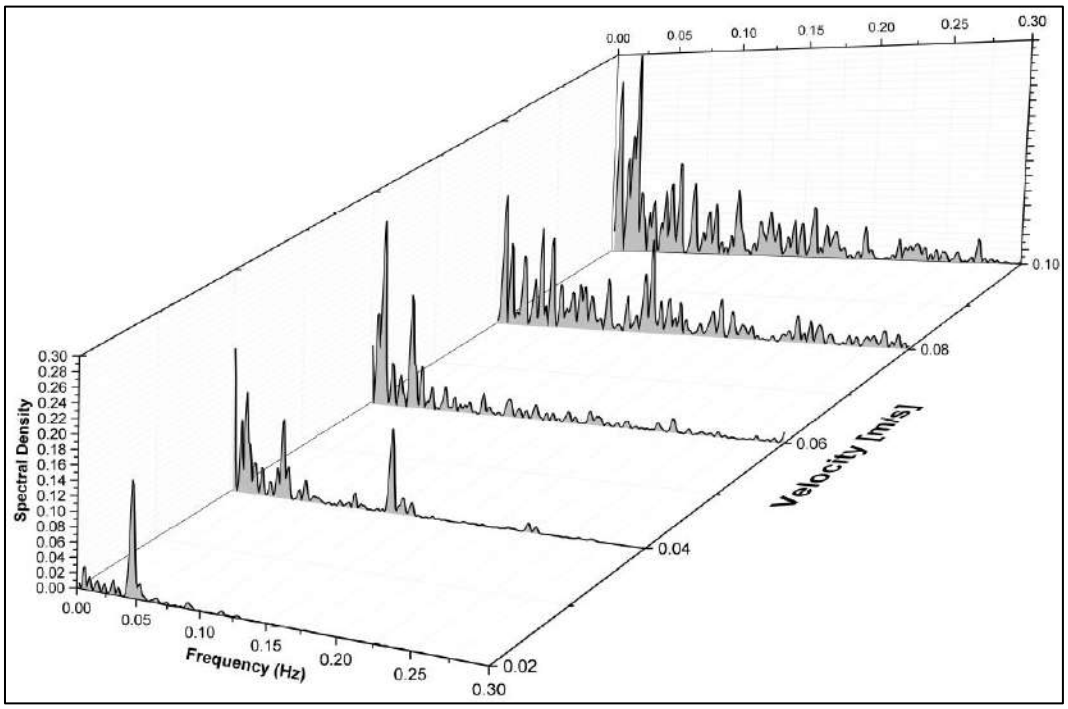

Figure 5.30 Power spectrum density from FFT of C_{FX} for TLP coupled with TAD as a function of current velocity and frequency for θ = 0°.

Figure 5.31 shows the PSD of the current force coefficient C_{FY} for the TLP coupled with the TAD at a 15° angle of attack. The distance between the floaters is D2 from Table 5.5 and the TLP is in the downstream position, as shown in Fig. 5.10 – part (B).

In this case, the spread across the frequencies is relatively broad, particularly for velocities V4 and V5. The largest peaks are in the frequency range of [0.00 - 0.15] Hz. However, additional peaks appear at frequencies of up to 0.25Hz.

Finally, Fig. 5.32 shows the PSD of the current moment coefficient C_{MZ} for the TLP coupled with the TAD. In this case, the angle of attack is 30°, the distance between the floaters is D2 from Tab. 5.5, and the TLP is in the downstream position as Fig. 5.10 – part (B) shows.

The PSD shows small differences between the single-body and multi-body cases, particularly for velocities V4 and V5. Thus, peaks of energy appear at approximately 0.2 Hz, and the spreading of the energy is slightly broader, see Fig. 5.29.

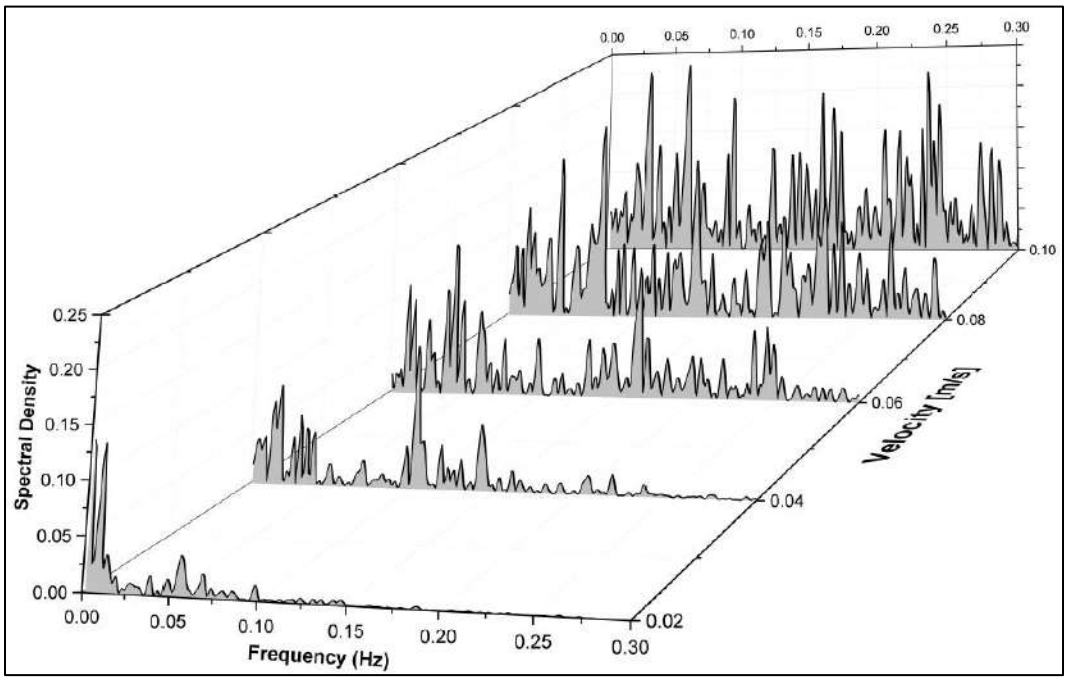

Figure 5.31 Power spectrum density from FFT of C_{FY} for TLP coupled with TAD as a function of current velocity and frequency for θ = 15°.

In general, the results reveal that for velocities V1 and V2, the energy is concentrated in the range of [0.00 – 0.05] Hz, and the variations between single-body and multi-body cases are small. For velocities V3, V4 and V5, the energy peaks are observed in the range of [0.00 – 0.15] Hz and at approximately 0.20 Hz. The spreading in the multi-body case is wider than that of the single-body case. The current coefficient C_{FY} presents the widest spread over the range of frequencies of [0.00 – 0.30] Hz.

Note that the energy peaks are observed in regions that includes the values of the natural frequencies of Surge, Sway, and Yaw. Therefore, resonance movements can be expected in the VIM tests.

The analysis of the load coefficients for other angles of attack and relative positions between the floaters presents the same general trends. In addition, the upstream TLP case presents similar results to the case of the TLP alone.

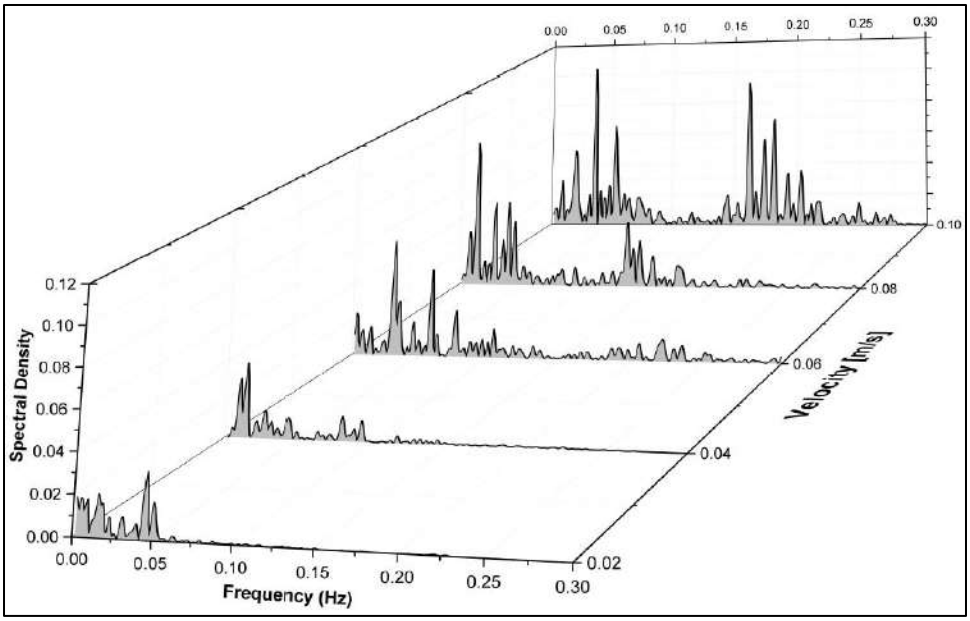

Figure 5.32 Power spectrum density from FFT of C_{MZ} for TLP coupled with TAD as a function of current velocity and frequency for θ = 30°.

The frequency domain study of the current loads on the TAD is summarized in Fig. 5.33. In this figure, the Power Spectrum Density (PSD) of C_{FX} for the TAD alone is presented. The angle of attack is 0°.

As shown in Fig. 5.33 the largest amount of energy is concentrated in the frequency range of [0.00 – 0.05] Hz, the magnitudes of the peaks outside of this range are relatively small. Note that, the differences between single-body and multi-body cases for the TAD are very small. The spreading of the energy is considerably smaller than that of the TLP.

As noted in Section 3.4, the natural frequencies of Surge, Sway and Yaw are, respectively, 0.063 Hz, 0.064 Hz, and 0.205 Hz. Therefore, the possibility of resonance movements on the TAD due to the current loads is relatively lower.

The analysis of the load coefficients C_{FX}, C_{FY} and C_{MZ} for other angles of attack and relative positions between the floaters for the multi-body cases reveals that the loads on the TAD present similar trends than that of the Fig. 5.32.

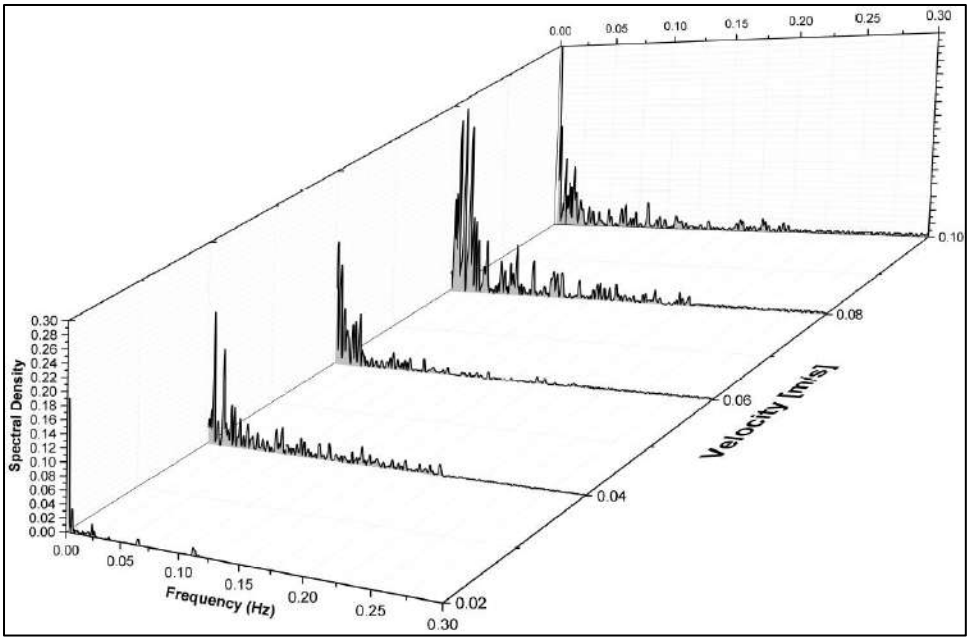

Figure 5.33 Power spectrum density from FFT of C_{FX} for TAD alone as a function of current velocity and frequency for θ = 0°.

5.8 NUMERICAL ANALYSIS

The numerical analysis using Computational Fluid Dynamics (CFD) was performed with the aim of investigating three main issues. First, to confirm the capability of CFD to reproduce the experimental results obtained in the LOC current channel. Second, to investigate blockage effects in the current load coefficients due to the walls and bottom of the channel. Third, to examine scale effects in the current load coefficients due to the tremendous difference in Reynolds number between the model-scale and full-scale. The numerical study focused on the TLP alone and the TAD alone, considering the following three cases:

- Full scale with a numerical domain to avoid the wall influences.
- Model scale with a numerical domain to avoid the wall influences.
- Model scale with a numerical domain equivalent to the current channel.

Note that, for the two first cases, the numerical domains were dimensioned to avoid the influence of the walls and bottom using the guidelines presented in [48] and [94]. Details of the numerical domains are shown in Section 5.8.1.

The interactions between currents and the 3-D body geometries were analyzed using the CFD code ANSYS CFX, which employs the Finite Volume Method (FVM) and the Reynolds-Averaged Navier-Stokes (RANS) equations complemented with turbulence models [94].

Although the interactions between the platforms and the flow are fundamentally unsteady, the computational effort required to perform unsteady simulations is prohibitive.

Therefore, due to the large number of simulations required to complete the present analysis, the study considers steady-state simulations. This simplification is not new in this kind of analysis; for instance [47], [48], and [94] used the same approach.

5.8.1 Model and Meshing

The analysis considers two main cases: TLP alone and TAD alone. The dimensions and properties of the floaters are presented in Chapter III. Each floater is analyzed in three sub-cases: full scale (FS), model scale (MS_LD) and model scale with a domain similar to the current channel (MS_SD).

For simplicity, the sub-case with the domain corresponding to the current channel dimensions is denoted as the model scale with a small domain (SD) and, the other is denoted as the model scale with a large domain (LD).

The computational domains for the three sub-cases are boxes as shown in Fig. 5.34. Table 5.9 presents the dimensions L1, L2, and H of the three computational domains for each sub-case (See Fig. 5.34). In addition, the coefficients C1 to C3 from Eqns. (5.5) to (5.7) are reported. Note that, these coefficients correspond to the dimensions of the body and the domain dimensions.

In section 5.4, the model scale factor 1:200 was selected by establishing reasonable limits for the coefficient C1, C2, and C3. The blockage effects increase with the model size. However, with smaller models, scale effects due to the Reynolds number difference and surface tension are higher. Thus, the model scale with small domain (MS_SD) sub-case has the same dimensions as the current channel and has the same coefficients C1, C2, and C3 as the experimental test. The computational domains for the full scale (FS) and model scale with large domain (MS_LD) cases were defined following the guidelines presented in [47] and [48], i.e., the dimensions

L1 and L2 of Fig. 5.34 must be at least 8Lpp, where Lpp is the maximum length of the body. For this study Lpp = 93.8 meters since it is the larger dimension of the two platforms. Finally, the parameter H must be at least 4Lpp. Note that, the dimensions of the computational domains are the same for the TLP alone and TAD alone.

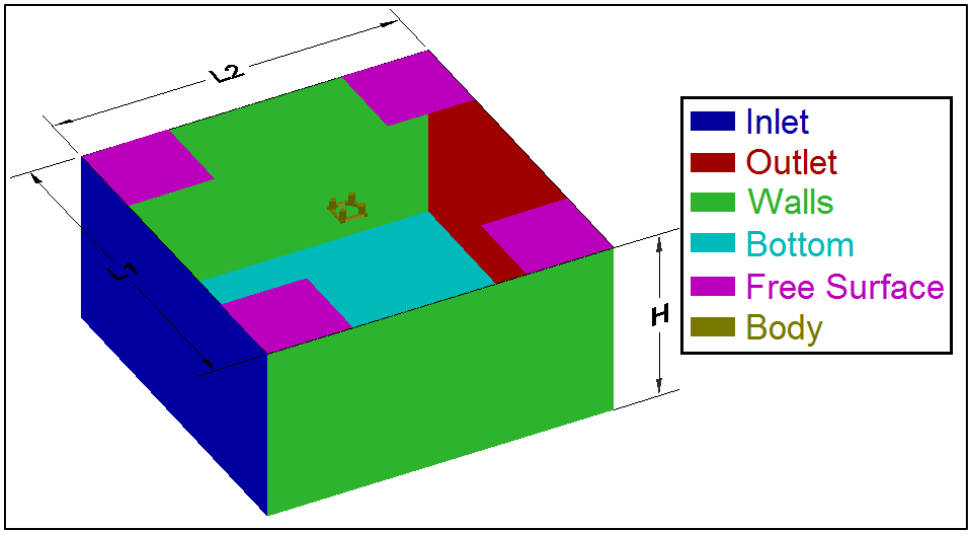

Figure 5.34 Computational domain for the CFD simulations.

Table 5.9 Computational domain for the CFD simulations.

Parameter	Full-scale	Model-scale LD	Model-scale SD
Scale	1:1	1:200	1:200
L1 [m]	800	4.0	10
L2 [m]	800	4.0	1.4
H [m]	400	2.0	0.5
C1 [%]	7.8	7.8	31.0
C2 [%]	11.7	11.7	33.5
C3 [%]	0.5	0.5	5.8

Figures 5.35 and 5.36 present the computational domains for the three sub-cases for the TLP alone and TAD alone, respectively. Note that the direction of the current velocity is always the same. Thus, for each angle of attack, the platform geometry was introduced with the appropriate orientation.

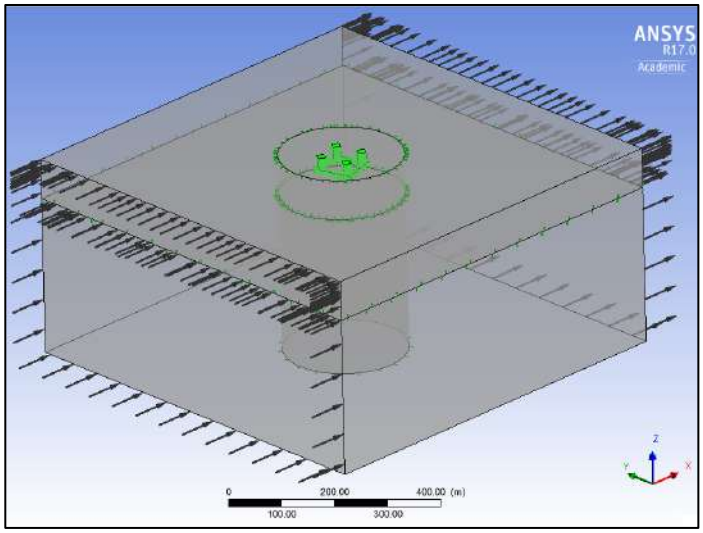

(A)

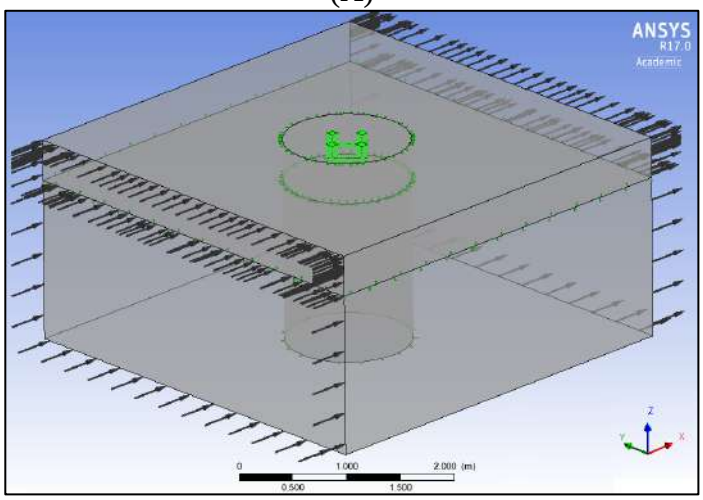

(B)

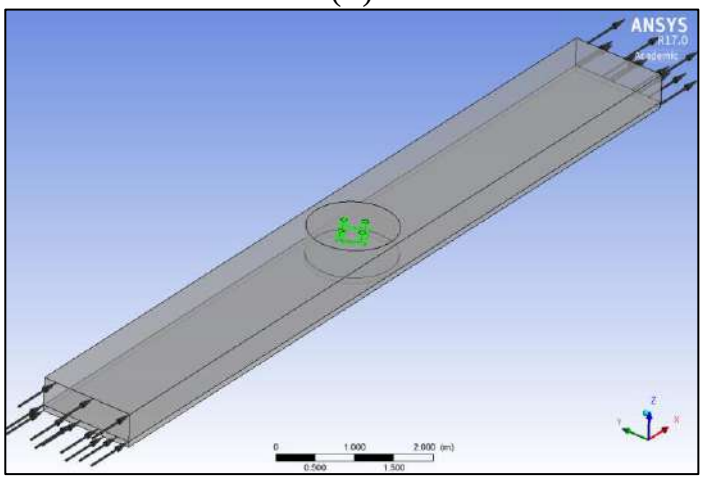

(C)

Figure 5.35 Computational domain for the TLP alone (A) Full-scale θ = 0°, (B) Model-scale LD θ = 45°, and (C) Model-scale SD θ = 30°.

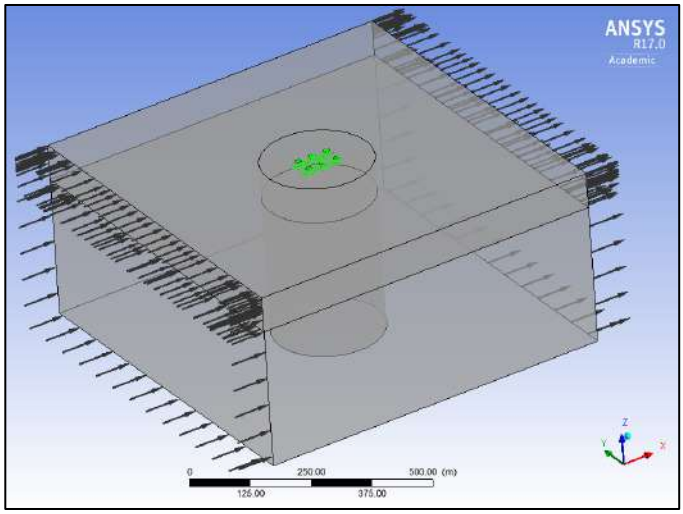

(A)

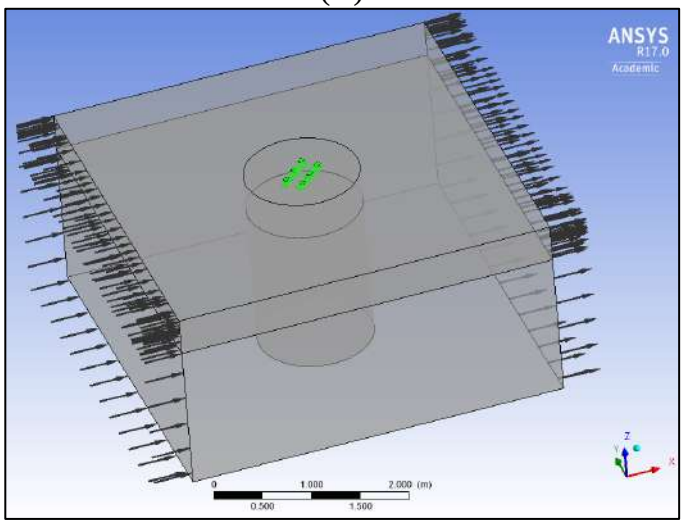

(B)

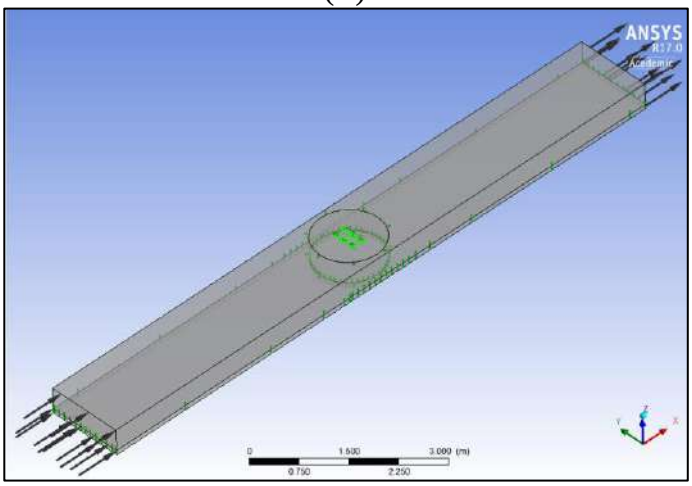

(C)

Figure 5.36 Computational domain for the TAD alone (A) Full-scale θ = 0°, (B) Model-scale LD θ = 45°, and (C) Model-scale SD θ = 90°.

The computational grids were modeled using a grid generator software which allows for building block-structured hexahedral grids.

For each sub-case three different refined grids were used. The grids are refined on the hull of the platforms to property represent the boundary layer and a maximum value of y+ below 1.

Table 5.10 presents the number of cells in the different grids for all of the cases and sub-cases. Figures 5.37 and 5.38 present the computational grids of the TLP alone and TAD alone, respectively.

Table 5.10 Number of cells, in millions, in the computational grids.

Platform	TLP alone			TAD alone		
	G1	G2	G3	G1	G2	G3
Full scale (FS)	3.45	5.93	7.56	3.19	6.90	9.27
Model scale (MS_LD)	3.85	5.46	7.36	3.34	6.29	8.97
Model scale (MS_SD)	3.70	5.90	7.40	3.28	6.65	9.00

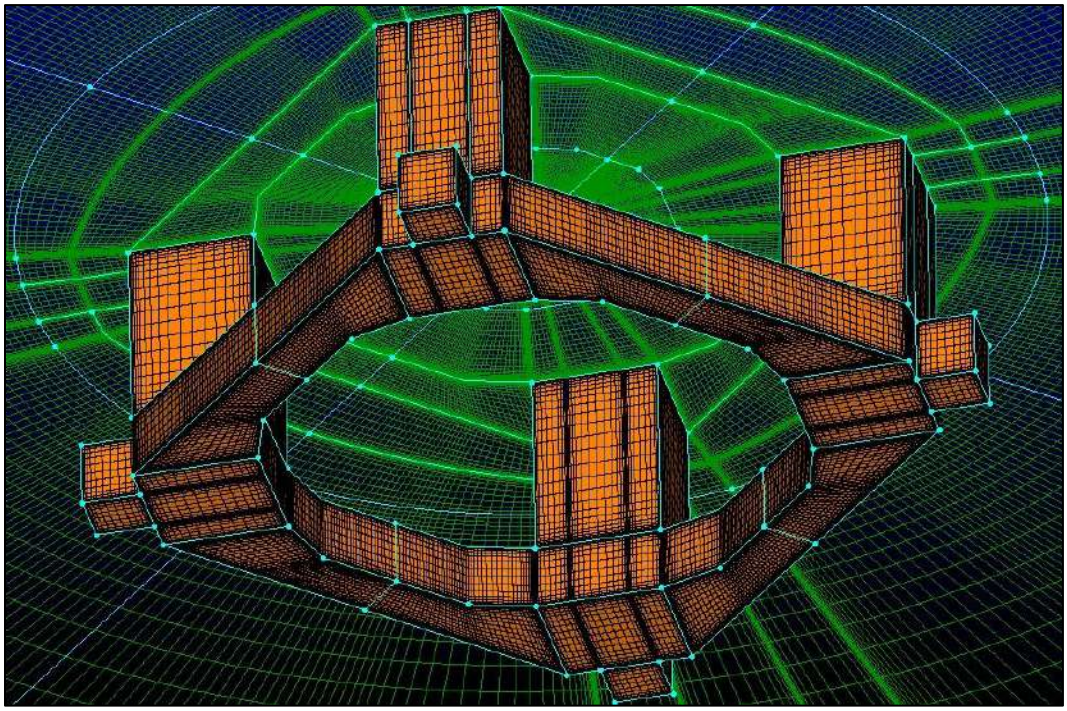

Figure 5.37 Full-scale (FS) computational grid G3 for the TLP.

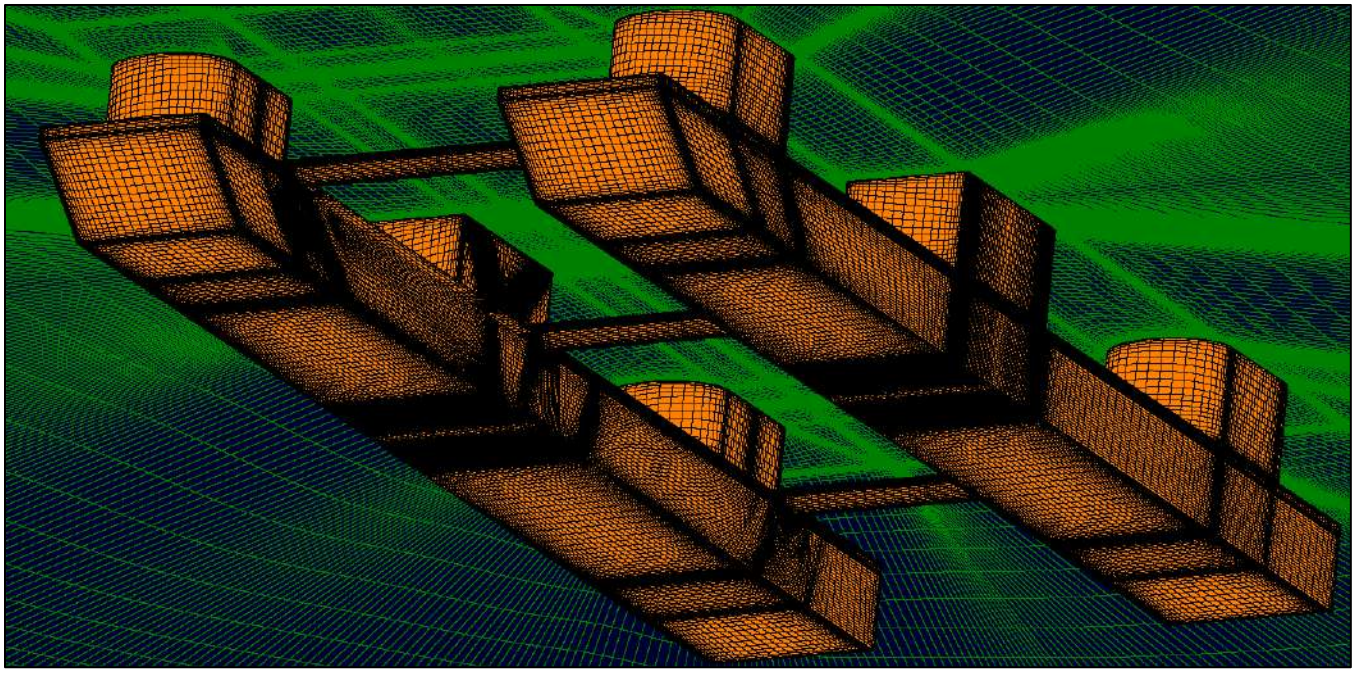

Figure 5.38 Full-scale (FS) Computational grid G3 for the TAD.

5.8.2 Numerical Settings

The numerical simulations were conducted considering the following assumptions.

- Similar to the experimental tests, the platforms are fixed.
- The flow and loads are stationary. Thus, unsteady effects from the flow and wake of the platforms are neglected.
- The flow at the inlet surface is uniform, constant and has a specific value of turbulence intensity.
- The effects of the free water surface on the current loads are negligible.

The boundary conditions considered in the numerical simulations are described below.

- On the inlet surface, the boundary condition is defined with the values for the uniform velocity and turbulence intensity reported in Tab. 5.6. Note that, for the full-scale simulations, the turbulence intensity is constant and equal to 10% for all of the current velocities.
- On the outlet surface, a constant average static pressure is imposed.

- In the full-scale (FS) and model-scale with large domain (MS_LD) cases, the walls and bottom were defined as free-slip surfaces, i.e., the normal velocity on these surfaces is equal to zero. In contrast, for the model-scale with small domain (MS_SD) case, these surfaces are considered to be no-slip surfaces. Consequently, the computational grids for these cases have adequate spatial discretization to achieve values of y+ near 1.0.
- The boundary corresponding to the mean free surface was considered to be a free-slip surface.
- The platform surfaces are defined as nonslip surfaces. Note that the computational grids for these cases have adequate spatial discretization near platform surfaces to achieve values of y+ near 1.0.

The initial condition for the simulations was defined by setting the current velocity for the full computational domain equal to the current velocity of the inlet surface. Table 5.11 presents relevant information of the setup used in the numerical simulations.

Table 5.11 Setup of the numerical simulations

Parameter	Description
Analysis type	Steady state
Grid Element type	Hex dominant
Turbulence model	Shear Stress Transport (SST) k-ω
Advection scheme	High-resolution
Minimum number of iterations	90
Maximum number of iterations	1000
Convergence Criteria	RMS < 1E-5
Maximum y+ on no slip surfaces	1.0

5.8.3 Sensitivity Analysis of The Grids

The sensitivity analysis of the grids in terms of the current load coefficients was performed for the TLP alone and TAD alone considering the three domains described above. One single current velocity of 1.5 m/s for the full-scale and 0.106 m/s for the

model-scale, was considered. In addition, four angles of attack 0°, 15°, 30° and 45° were included in the analysis.

Figure 5.39 presents the variation of the coefficient C_{FX} for the TLP alone, where three different computational grids were analyzed. In the full-scale results, differences appear in the range of [1.5% – 5.6%] between the G1 and G3 grids. However, the differences between G2 and G3 are in the range of [0.9% – 1.3%]. Note that G1 is the coarsest grid; G3 is the finest grid. The maximum differences appear for the angle of attack equal to 30°. The results for the model scale present smaller differences. For the large domain (MS_LD) case, the variations between G1 and G3 are in the range of [0.13% – 1.8%], and those between G2 and G3 are [0.04% – 0.55%]. Finally, for the model-scale with small domain (MS_SD) case, the differences between G1 and G3 are [0.69% – 1.21%] and [0.13% – 0.34%]. In general, the differences are higher for angles of attack of 15° and 30°. The results at 0° present smallest variations.

Figure 5.40 presents the variation of the coefficient C_{FX} for the TAD alone, three different computational grids were analyzed.

In the case of TAD alone, similar trends were found. At full-scale (FS), the differences are in the range of [2.5% – 6.7%] between the G1 and G3 grids and [0.85% – 1.72%] between the G2 and G3 grids. The maximum differences are for the angle of attack equal to 45°.

For the model scale with large domain (MS_LD) case, variations between the G1 and G3 are in the range of [0.98% – 1.47%], and those between the G2 and G3 are [0.11%-0.69%]. Finally, for the model-scale with small domain (MS_SD) case, the differences between the G1 and G3 were in the range of [0.18% case 2.18%] and [0.28% – 0.52%]. In general, the differences are higher for the angles of attack of 15° and 30°.

Based on the results presented, it is possible to conclude that the current load coefficients are not strongly dependent on the computational grids, particularly for the model-scale simulations. The largest differences found are less than 7%, and these correspond to the full-scale (FS). In general, mesh independence was obtained. The differences between the two finest refinements G2 and G3 in the current load coefficients are slight.

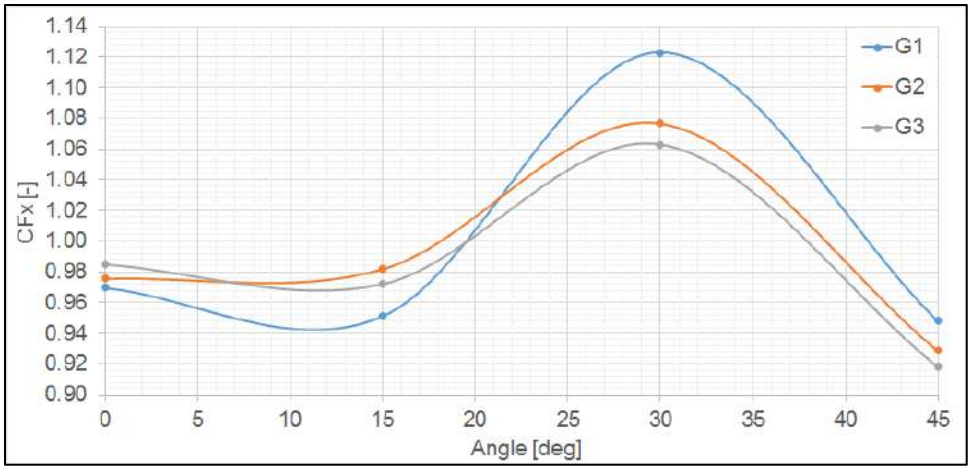

(A)

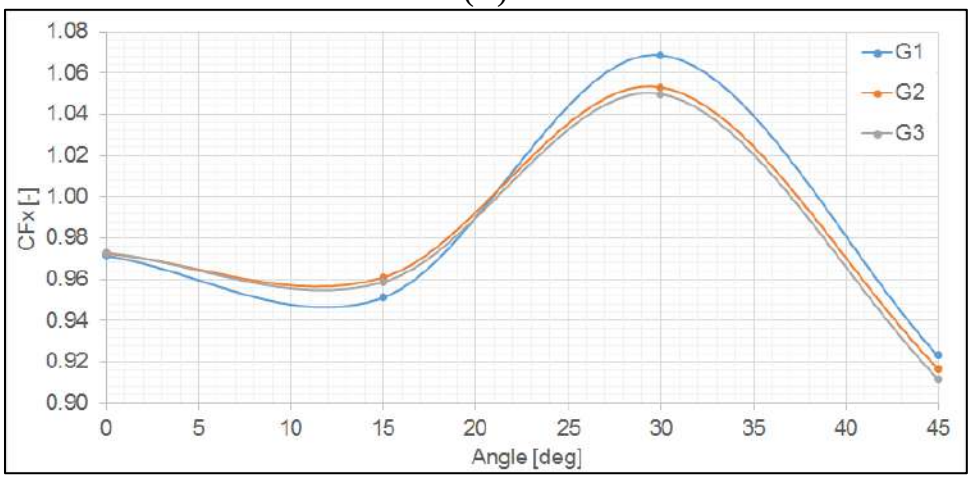

(B)

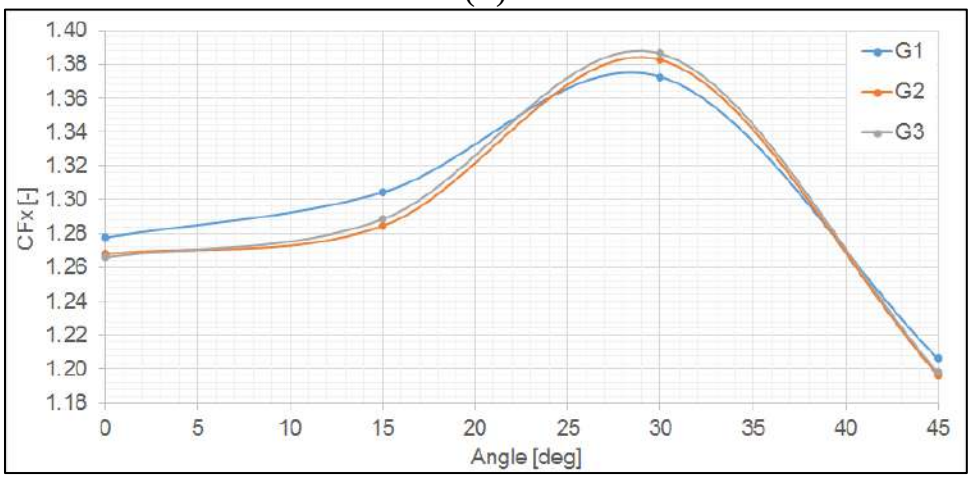

(C)

Figure 5.39 Grid convergence analysis for C_{FX} of the TLP alone.

(A) Full-scale (B) Model-scale LD (C) Model-scale SD.

Grid G1 is the coarsest, and G3 is the finest.

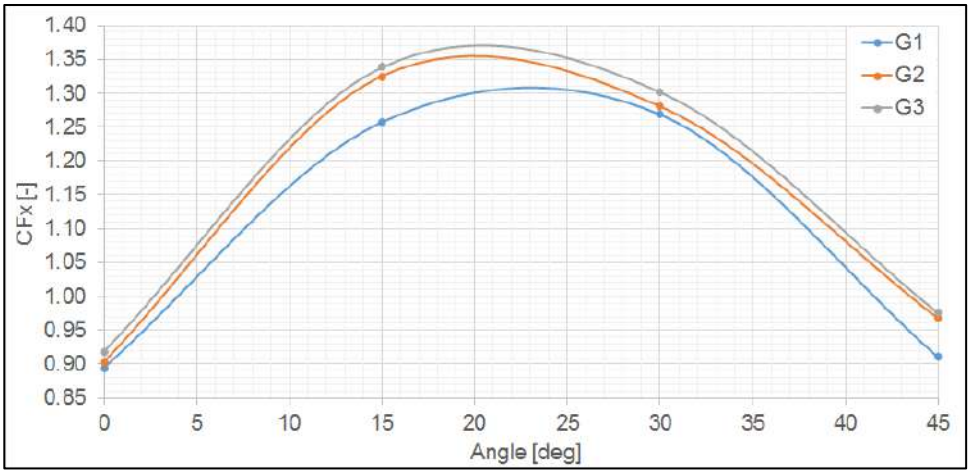

(A)

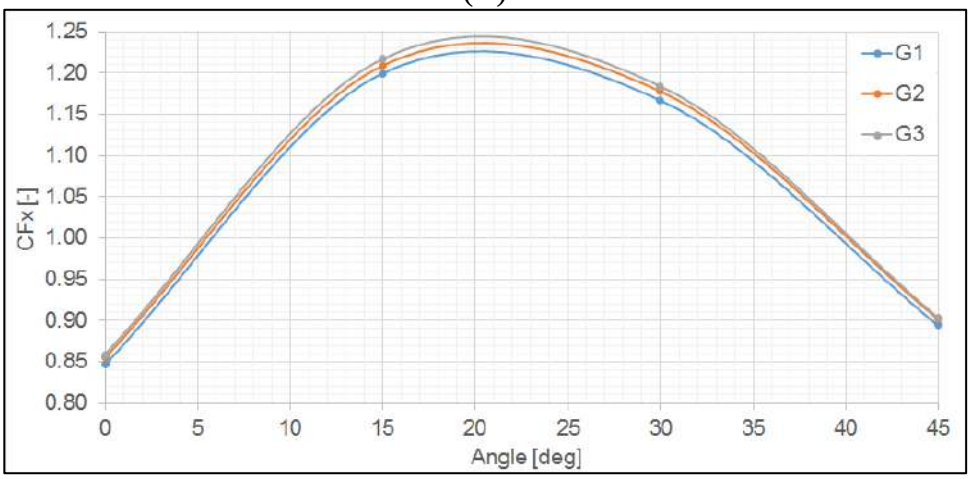

(B)

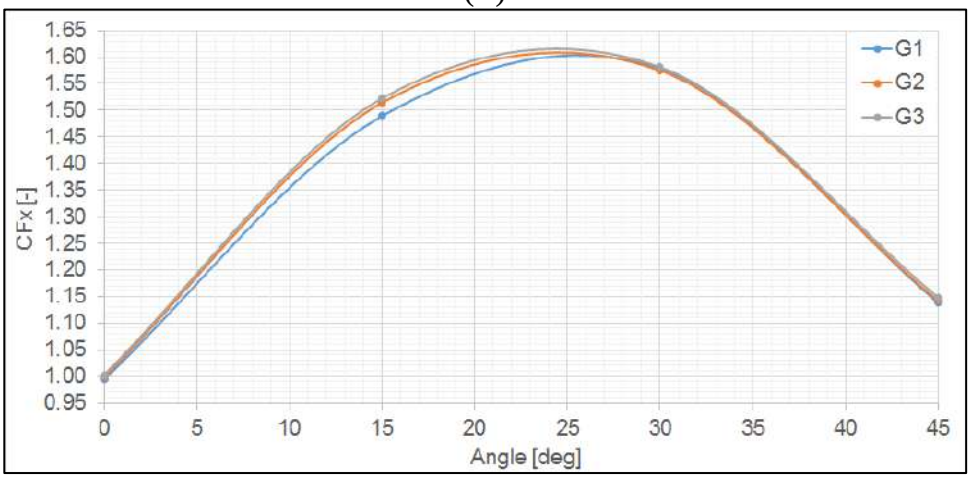

(C)

Figure 5.40 Grid convergence analysis for C_{FX} of the TAD alone.

(A) Full-scale (B) Model-scale LD (C) Model-scale SD.

Grid G1 is the coarsest, and G3 is the finest.

Tables 5.12, 5.13 and 5.14 present the value of the maximum y+ for all of the simulations mentioned above. Although, the first part of these analysis indicates that grids G2 and G3 are sufficient to achieve independence on the computational grids. The second part shows that the maximum values for y+ require the grid refinement G3. Consequently, these grids were used for the further analysis.

Table 5.12 Maximum y+ on nonslip surfaces for full-scale (FS) calculations.

Angle of Attack	TLP			TAD		
	G1	G2	G3	G1	G2	G3
0°	3.296	2.810	0.859	4.122	1.883	0.933
15°	3.295	2.836	0.849	3.984	2.137	0.979
30°	3.249	2.846	0.847	3.896	2.026	0.978
45°	3.192	2.706	0.832	4.139	2.433	0.991

Table 5.13 Maximum y+ on nonslip surfaces for model-scale with LD calculations.

Angle of Attack	TLP			TAD		
	G1	G2	G3	G1	G2	G3
0°	3.982	1.495	0.880	4.228	2.232	0.930
15°	3.902	1.397	0.875	4.182	2.151	0.905
30°	3.694	1.384	0.851	3.946	2.041	0.902
45°	3.689	1.322	0.839	4.185	2.193	0.920

Table 5.14 Maximum y+ on nonslip surfaces for model-scale with SD calculations.

Angle of Attack	TLP			TAD		
	G1	G2	G3	G1	G2	G3
0°	4.218	1.886	0.949	4.372	2.370	0.966
15°	4.198	1.871	0.949	4.197	2.359	0.923
30°	4.076	1.856	0.948	4.154	2.210	0.912
45°	3.998	1.810	0.935	4.201	2.363	0.924

5.8.4 Convergence Criteria

As shown in Section 5.8.3, iterative convergence depends on the analysis type, angle of attack and grid refinement. Thus, the following convergence criterion were adopted for the further numerical simulations.

- The number of the iterations was limited to the range of [90 – 1000].
- The maximum RMS was limited to 1.E-5.
- The highest value for y+ was limited to 1.0.

If the maximum number of iterations is reached with the residuals stagnating at orders higher than 1.E-5, the current loads are estimated by the average of the last 500 iterations. However, if the limit for the maximum RMS is reached, then the load values that are reported corresponds to the values of the last iteration.

These analyses reveal that most of the cases present excellent convergence. In the worst cases, the residuals stagnate at 1.0E-4, as shown in Fig. 5.41. However, the loads in such situations never present variations larger than 8.0%.

In contrast, in the best cases, the residual reaches 1.0E-5 at 100 iterations, as shown in Fig. 5.42.

Figure 5.41 Iterative convergence on the TLP alone – Full scale, V = 1.5 m/s, and θ = 30° corresponding to the worst iterative convergence.

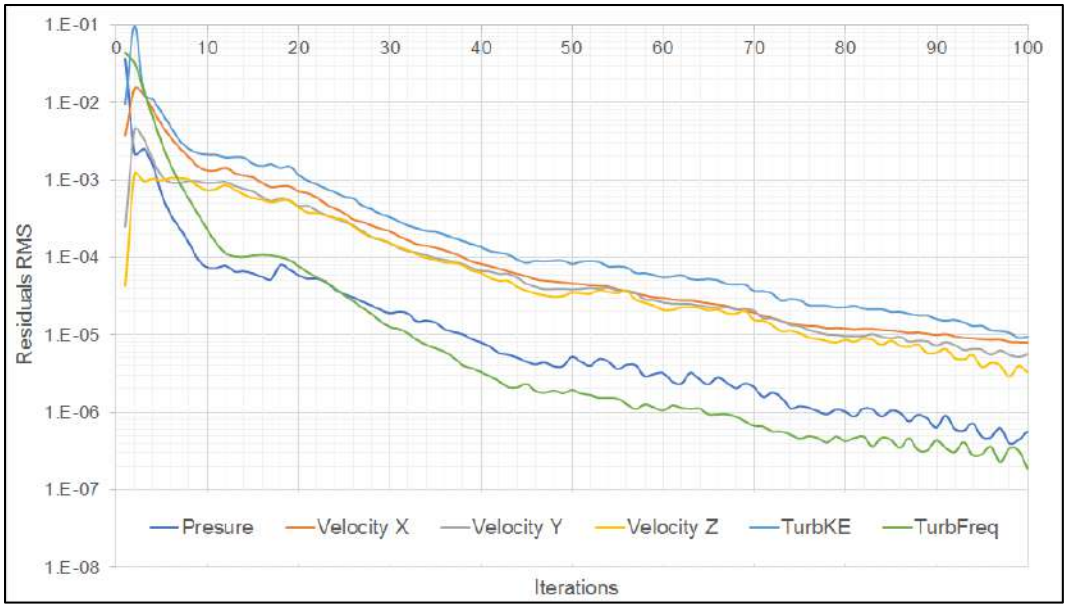

Figure 5.42 Iterative convergence on the TAD alone – Model scale LD, V = 0.021 m/s and θ = 90°, corresponding to the best iterative convergence.

5.8.5 Test Matrix

An extensive numerical analysis has been conducted considering TLP alone and TAD alone. As mentioned above, three cases were analyzed. The first was at model scale in a numerical domain with the dimensions of the current channel. The second was at model scale with a large domain. The third was at full scale with a large domain.

The simulations at model-scale with a domain with the dimensions of the current channel were performed with the aim of validating the numerical predictions. Moreover, the simulations at model-scale with a large domain were conducted to calculate the possible blockage effects on the current channel results. Finally, the simulation at full-scale with a large domain has been performed in order to evaluate the influence of Reynolds number on the current channel results.

For all cases, a range of current velocities from 0.3 to 1.5 m/s in steps of 0.3 m/s were considered. Note that, these corresponding values correspond to the full-scale values and equivalent values from the Froude scaling law were applied in the model-scale simulations. The symmetry of the hulls allows a reduction in the number of simulations. Thus, for the TLP, a range of angles of attack from 0° to 45° in steps of 15° was considered. In addition, for the TAD, angles of attack from 0° to 180° in steps

of 15° were analyzed. Table 5.15 presents the CFD simulations matrix considered in this study. A total of 60 steady-state simulations were conducted for the TLP alone. For the TAD alone, 195 steady-state simulations were performed.

Table 5.15 CFD simulations matrix.

Simulation description	Current velocity [m/s]	Current angle [deg.]
TLP alone – Full scale	0.3 -1.5@0.3	0°-45°@15°
TLP alone – Model scale – Large domain	0.3 -1.5@0.3	0°-45°@15°
TLP alone – Model scale – Small domain	0.3 -1.5@0.3	0°-45°@15°
TAD alone – Full scale	0.3 -1.5@0.3	0°-180°@15°
TAD alone – Model scale – Large domain	0.3 -1.5@0.3	0°-180°@15°
TAD alone – Model scale – Small domain	0.3 -1.5@0.3	0°-180°@15°

5.8.6 Comparison with Experimental Results

This section presents a comparison between the model-scale CFD results and the model test results for the TLP and TAD alone. Note that in this comparison, the domain of the CFD simulations corresponds to the small domain case (MS_SD), i. e. the domain for the CFD calculations has the dimensions of the current channel of LOC. The objective of this comparison is to investigate the capability and accuracy of CFD to calculate the current loads on both floaters.

Figures 5.43 and 5.44 present the comparison of experimental and numerical results for the current force coefficient C_{FX} and C_{FY}, respectively, of the TLP alone.

A good agreement between the numerical and experimental results is found, not only in trends but also in order of magnitude of the loads.

In the case of C_{FX}, the differences are less than 10% for most of the angles of attack. The maximum differences of 15% and 19% are observed at 45° and 135°, respectively. The minimum difference, approximately 7%, occurs at 0°. In the case of C_{FY}, the differences are less than 8.5% for most angles of attack. The maximum differences of 12% and 19% at 30° and 45°, respectively. The minimum difference, approximately 7%, occurs at 90° degrees.

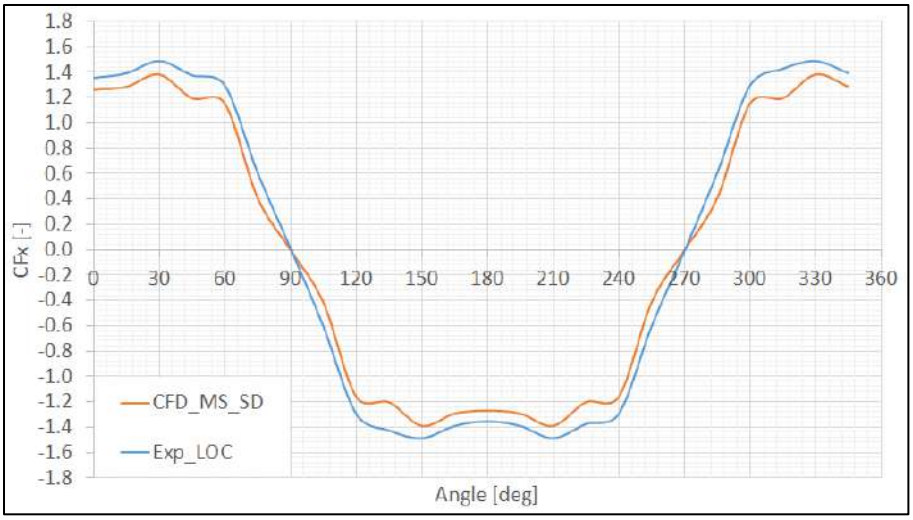

Figure 5.43 Comparison between numerical and experimental results for C_{FX} for the TLP.

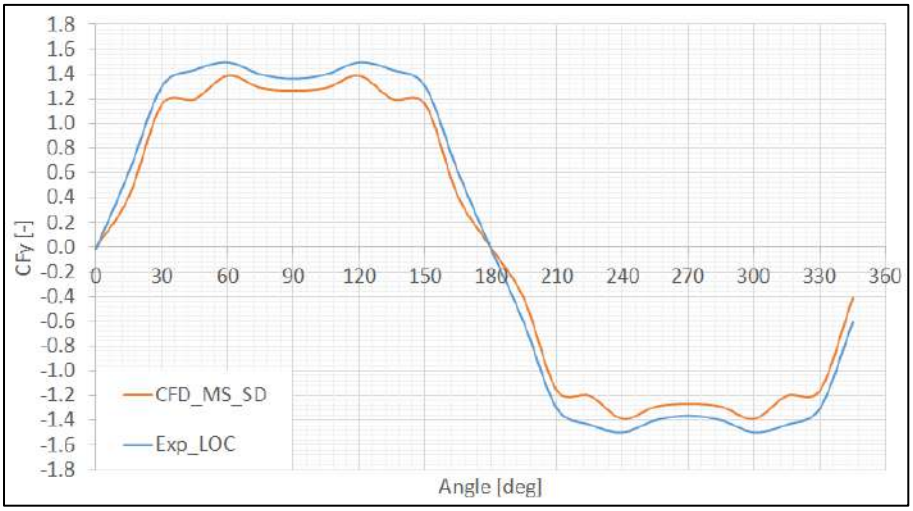

Figure 5.44 Comparison between numerical and experimental results for C_{FY} for the TLP.

Figure 5.45 presents the comparison of experimental and numerical results for the current moment coefficient C_{MZ} of the TLP alone. For this case, major differences arise, particularly for 0° and 15°. The minimum difference of 24% occurs at 30°.

Figures 5.46 and 5.47 compares the experimental and numerical results for the current force coefficients C_{FX} and C_{FY}, respectively of the TAD alone. In general, reasonable correlation is observed and the trends and order of magnitude are consistent. Both coefficients show differences around of approximately 10% between

the experimental and numerical results. For C_{FX}, the largest difference occurs at 180°, approximately 70%, while the largest difference in C_{FY} is 40% at a 90° angle of attack.

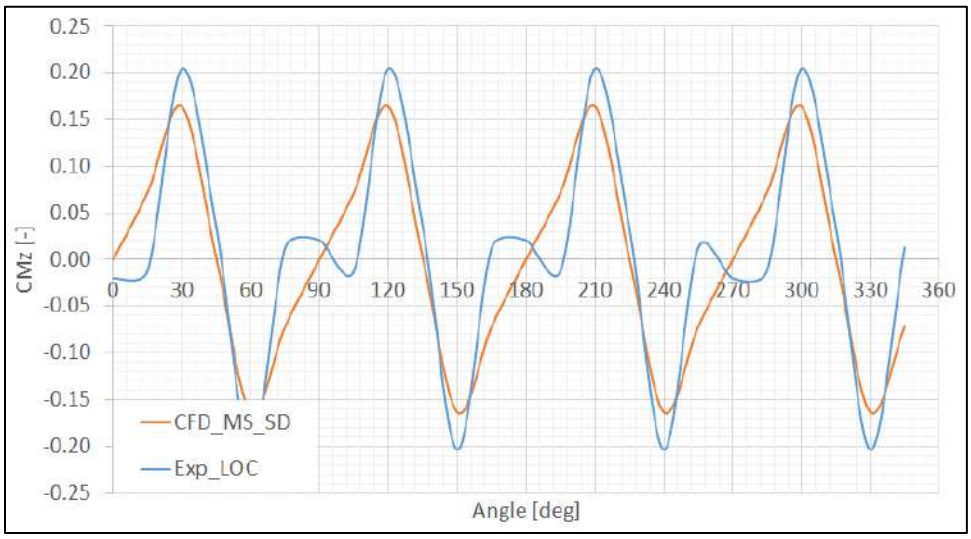

Figure 5.45 Comparison between numerical and experimental results for C_{MZ} for the TLP.

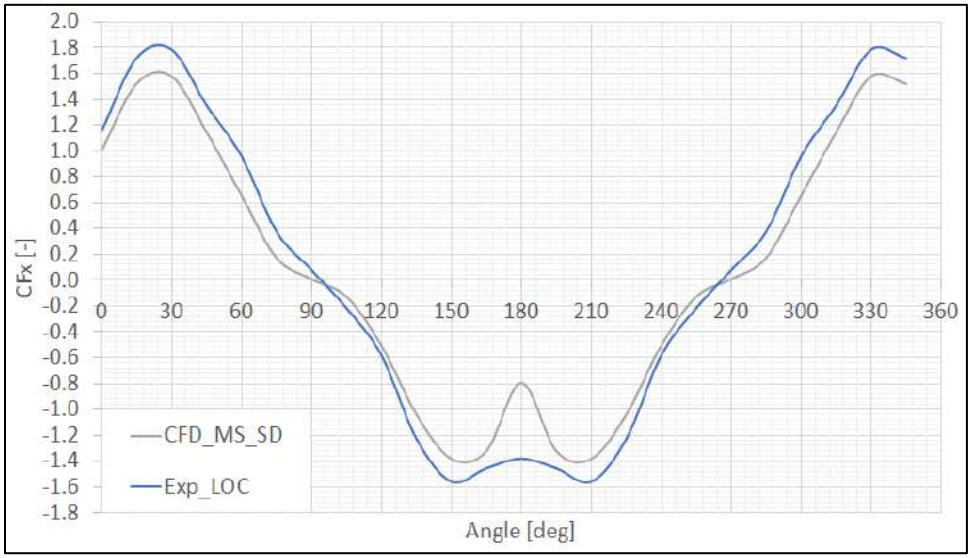

Figure 5.46 Comparison between numerical and experimental results for C_{FX} for the TAD.

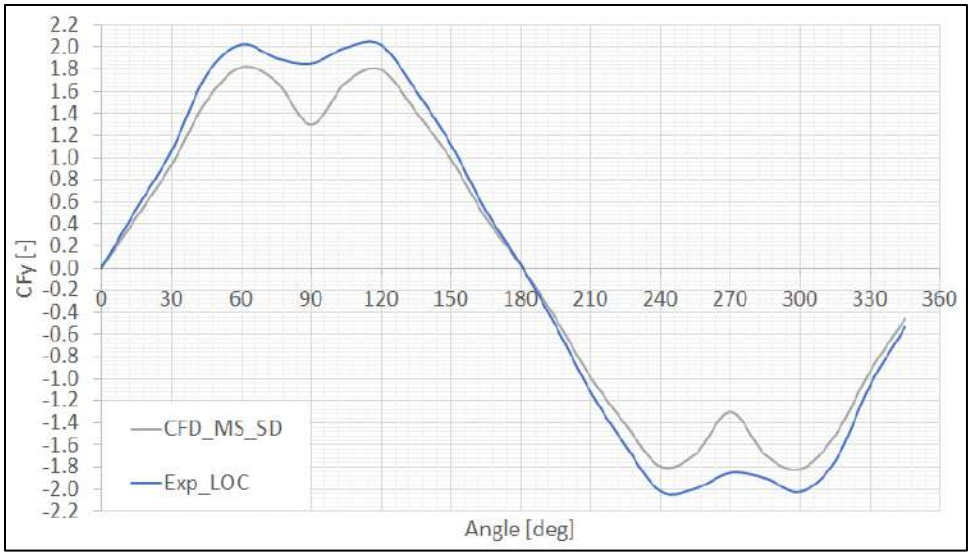

Figure 5.47 Comparison between numerical and experimental results for C_{FY} for the TAD.

Figure 5.48 presents the comparison of experimental and numerical results for the current moment coefficient C_{MZ} of the TAD alone. In this case, the differences are surprisingly low. The variations are less than 9% for angles in the range of [0° – 45°] and [150° – 180°]. The maximum difference occurs at 105°, where it is 34%.

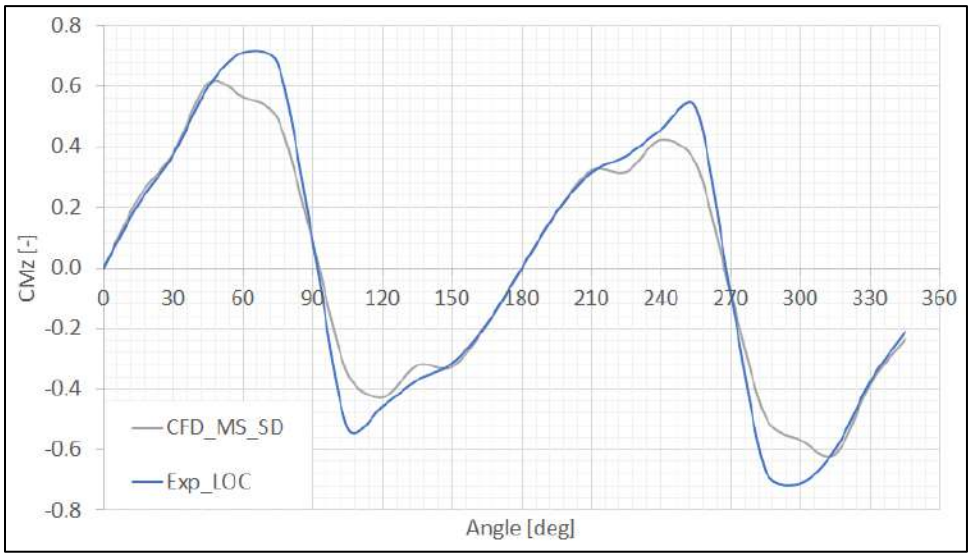

Figure 5.48 Comparison between numerical and experimental results for C_{MZ} for the TAD.

The numerical coefficients C_{FX} and C_{FY} of the TLP and TAD are systematically below the experimental results. This trend is small for most angles of attack; however, it is significant for 45°, 90° and 180°. There are several possible explanations for the small differences between experimental and numerical results, the most important are summarized below.

- Due to the ultra-reduced scale factor, the loads measured by the transducers are small. Consequently, they could be a source of error.
- In the numerical simulations, the flow was considered to be uniform; however, in the experimental tests, the flow presents spatial variations that are challenging to address.
- The massive flow separation around the floaters increases the unsteadiness in the flow. However, due to the long processing time, only steady-state simulations were performed.
- The results from the numerical simulations consider the average of the oscillating steady-state results.
- The results from the experimental tests consider only the average loads.
- Differences exist between the average transient loads from experiments and the average of the oscillating steady-state, constituting a topic recommended for further investigations.

In general, despite some differences at specific angles of attack, reasonable agreement between numerical and experimental results is observed, not only in trends but also in order of magnitude. Therefore, the results demonstrate the capability of the CFD code to predict the current loads on the TLP-TAD multi-body system.

5.9 NUMERICAL RESULTS

The numerical study was performed to investigate the blockage and scale effects on the current loads of the TLP and TAD units. Three general cases have been considered: Full-scale (FS), model scale with the large domain (MS_LD) and model scale with the small domain (MS_SD). Details of each case were shown in the previous section. The forces and moments calculated with the steady-state simulations are reported in the non-dimensional form presented in Eqns. (5.8) to (5.10).

As in the experimental analysis, the first step is to study the dependence on the current loads on current velocity. Thus, Fig. 5.49 presents the coefficient C_{FX} for the TLP for the three cases explained above. The fluctuations on the coefficients achieve values of 0.44%, 1.00%, and 1.92% for the full-scale, model-scale with large domain, and model-scale with small domain cases respectively. Similarly, Fig. 5.50 presents the coefficient C_{FX} for the TAD, where the fluctuations on the coefficients achieve values of 1.87%, 2.89%, and 2.23% for full-scale, model-scale with the large domain, and model-scale with small domain cases, respectively. Note that, the results from the simulations with different angles of attack also presented similar trends. The fluctuations between the values represent less than 3.0% for all of the numerical simulations. Note that, the spread in numerical simulations is lower than in the experimental results.

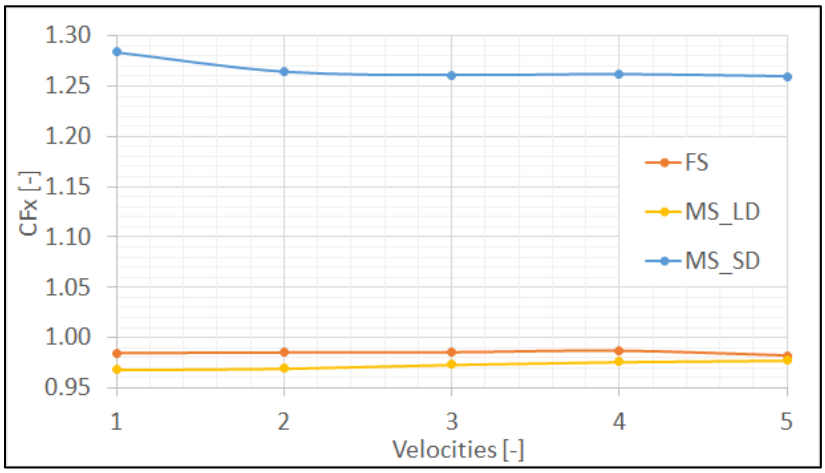

Figure 5.49 Variation of C_{FX} with current velocity for the TLP.

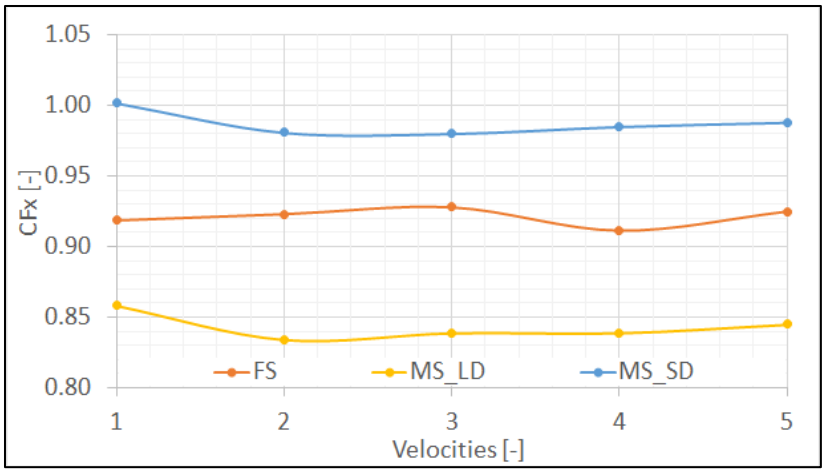

Figure 5.50 Variation of C_{FX} with current velocity for the TAD.

The next step in the numerical analysis of the TLP and TAD involves studying the angle of attack dependence. Figures 5.51, 5.52 and 5.53 present, respectively, the current load coefficients C_{FX}, C_{FY} and C_{MZ} of the TLP. In the three figures the following are observed:

- The differences in C_{FX} between the full-scale and model-scale with large domain cases are relatively low; these are in the range of [-2.7% to 2.6%]. The angle with the largest difference is 75°. The differences between the model-scale with large domain and model-scale with small domain cases are in the range of [-29.8% to 27.6%]. In this case, the largest difference corresponds to 45°.
- In the case of C_{FY}, the variations between the full-scale and model-scale with large domain cases are in the range of [-2.6% to 2.8%]. The angle with the largest difference is 15°. The differences between the model-scale with large domain and model-scale with small domain cases are in the range of [-28.5% to 29.3%]. In this case, the largest difference corresponds to 75°.
- An analysis of C_{MZ} reveals the largest variations between the full-scale and model-scale with large domain cases, these variations are in the range of [-18.4% to 17.5%], with the largest difference reported at 30°. The differences between the model-scale with large domain and model-scale with small domain cases are up to 45% for angles of 30° and 60°.

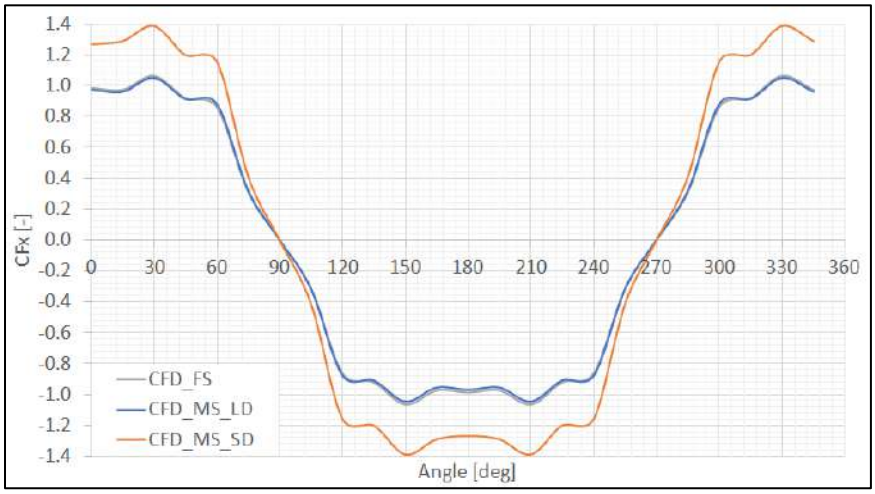

Figure 5.51 Variation of C_{FX} with angle of attack for the TLP.

In general, a comparison between the full-scale and model-scale with large domain results reveals that the coefficients C_{FX} and C_{FY} present relatively small differences, less than 3% for the angles of attack examined. Consequently, it is possible to conclude that scale effects in these cases could be negligible. In contrast, the moment coefficient C_{MZ} presents significant differences, particularly, at 15°, 30°, and 60°.

From the results of the comparison between the model-scale with large domain and model-scale with small domain cases, it is possible to conclude that blockage effects are relevant for the coefficients C_{FX}, C_{FY} and C_{MZ}. On average the differences were approximately 30%, reaching 45% for the moment coefficient.

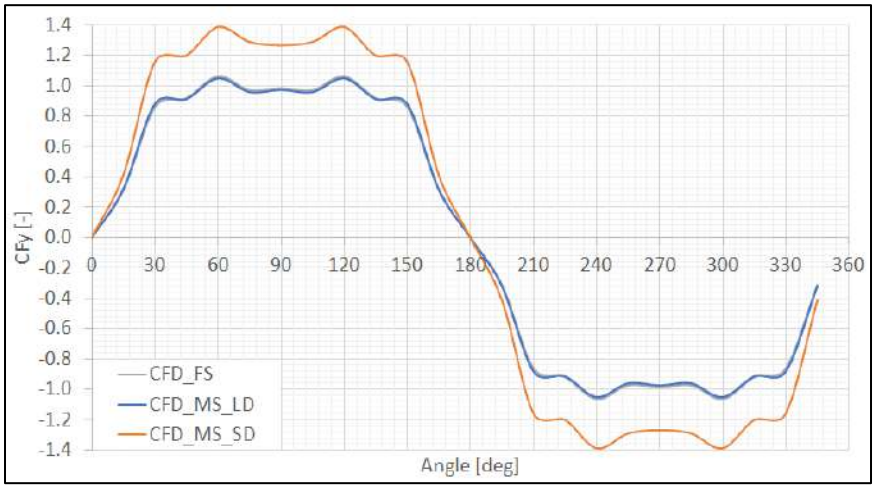

Figure 5.52 Variation of C_{FY} with angle of attack for the TLP.

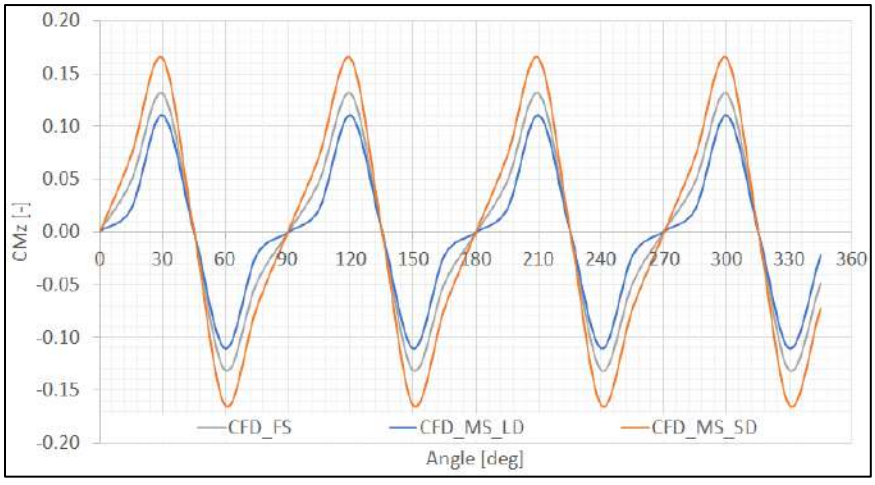

Figure 5.53 Variation of C_{MZ} with angle of attack for the TLP.

Figures 5.54, 5.55 and 5.56 present, respectively, the current load coefficients C_{FX}, C_{FY} and C_{MZ} of the TAD. In the three figures the following are observed:

- The differences in C_{FX} between the full-scale and model-scale with large domain cases are relatively low, are in the range of [-8.7% to 6.7%]. The angle with the largest difference is 15°. The differences between the model-scale with large domain and model-scale with small domain cases are in the range of [-32.8% to 29.6%]. In this case, the largest differences correspond to 15° and 45°.

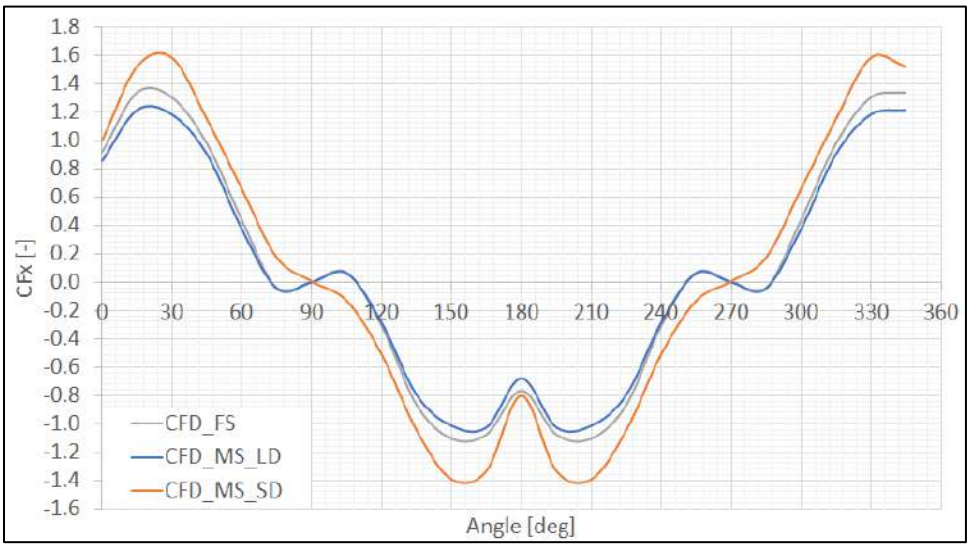

Figure 5.54 Variation of C_{FX} with angle of attack for the TAD.

- In the case of C_{FY}, the variations between the full-scale and model-scale with large domain cases are over the range of [-7.9% to 7.7%]. The angle with the largest difference is 30°. The differences between the model-scale with large domain and model-scale with small domain cases are in the range of [-32.5% to 31.3%]. In this case, the largest difference corresponds to 30°.
- An analysis of C_{MZ} reveals the largest variations between the full-scale and model-scale with large domain cases are in the range of [-13.6% to 19.5%], with the largest difference reported at 15°. The differences between the model-scale with large domain and model-scale with small domain cases are as high as 34% at 15°.

In general, a comparison of the full-scale and model-scale with large domain results reveals that coefficients C_{FX} and C_{FY} present small differences, approximately 8%. Note that

for most of cases, the variation on the TAD is considerably higher than for the TLP case. In addition, the moment coefficient C_{MZ} presents significant differences at 45°, it is as high as 26.7%.

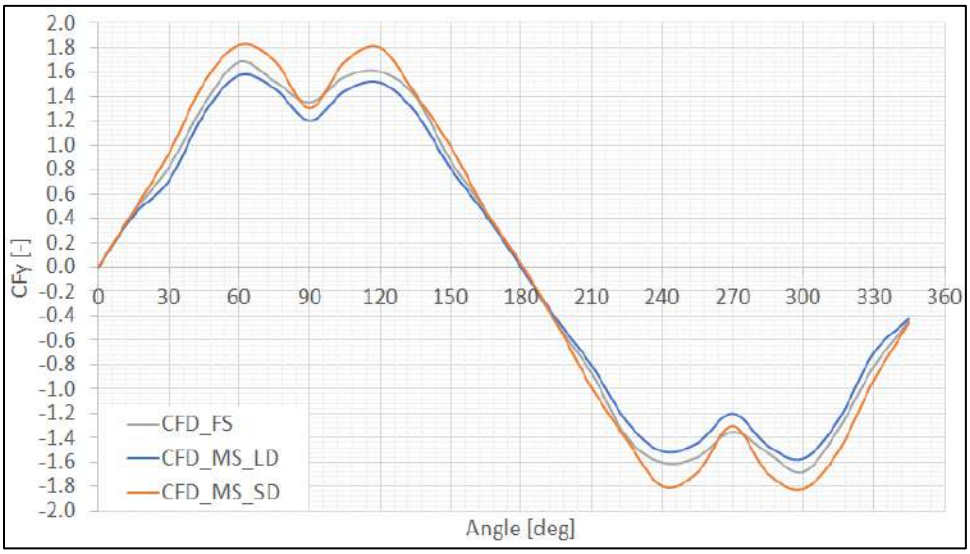

Figure 5.55 Variation of C_{FY} with angle of attack for the TAD.

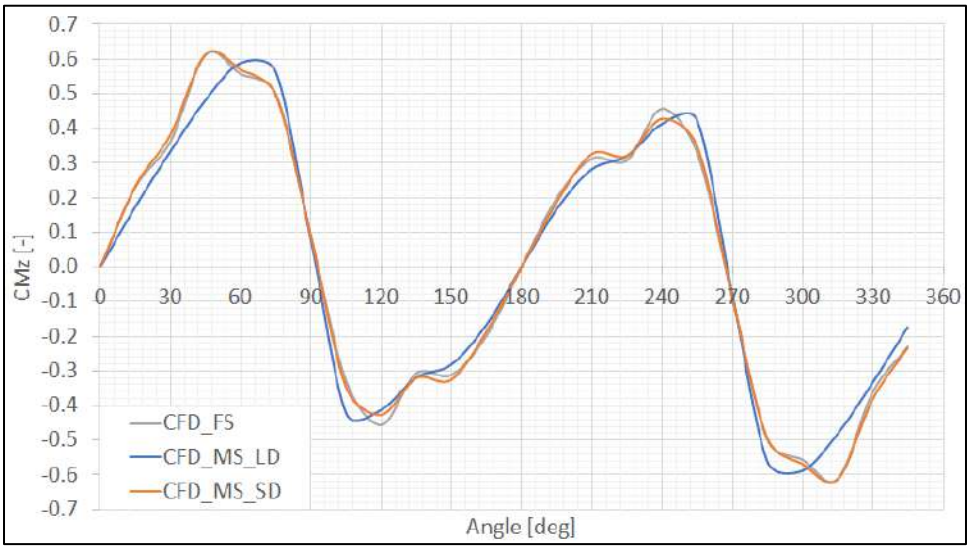

Figure 5.56 Variation of C_{MZ} with angle of attack for the TAD.

CHAPTER VI. CURRENT INDUCED MOTIONS

An extensive model tests campaign was performed to investigate the motions induced by the current on the TLP-TAD multi-body system. This study includes the analysis of the TLP alone, TAD alone, TLP coupled with the TAD without mechanical connection and TLP coupled with TAD connected by a hawser system. The model tests were conducted in the fKN@LOC Laboratory facilities at COPPE/UFRJ. The ultra-reduced model scale was 200.

6.1 INTRODUCTION

Recently, interest regarding vortex-induced motions (VIM) of offshore units has grown. These induced motions are significant for the design of mooring systems and risers for offshore platforms.

Of the multiple studies in the literature, most have focused on Spars, e.g., [7], [19], [40], [42], and [98]. Recently, some studies have presented interesting results for TLPs [51] and [95], semi-submersibles [35] and [36], and mono-columns [32]. These studies have shown that VIM is a complex topic that is dependent on several factors, including the current velocity, heading, current profile, hull geometry and appurtenances [3].

The study of VIM in offshore structures is usually conducted with experimental tests. However, experiments in ocean basins are expensive, which hinders the optimization of platform geometry to reduce the VIM response. In addition, CFD is useful and relatively efficient. However, experimental validations are still required to ensure reliable results [87] and [88]. Finally, [50] proposed a set of analytical method, however, this approach requires further investigation and validation.

In this context, experimental tests in the current channel of LOC/COPPE-UFRJ seems as the best alternative to performing VIM tests in terms of cost, time and accuracy. Consequently, the scope of this work is to investigate current induced motions on the TLP-TAD multi-body system using the facilities of the LOC. For that, a novel experimental setup for use in analyzing a deep draft TLP in a shallow current channel using ultra-reduced scales

is proposed. As mentioned in Chapter V, the model scale factor for this model tests campaign is 1:200. Due to its simplicity, this innovative experimental setup could enable future researchers to optimize the platform geometries and to develop devices to mitigate the VIM response.

In addition, a horizontal soft mooring with the appropriate stiffness is implemented to represent the mooring system of the TAD unit. Finally, four different configurations of hawser system were tested to study the influence of the mooring lines between the floaters.

Consideration of the differences in the Reynolds number and possible scale effects can be found in Section 5.3. Moreover, possible wall effects are discussed in Section 5.4.

The experimental campaign presented and discussed below focuses on the dynamic behavior of the TLP alone, TAD alone and the interaction of both floaters in proximity while connected by the hawser systems and without mechanical connections.

6.2 ULTRA-REDUCED SCALE MODELS

Details of the selection of the model scale factor and the construction of the scale models can be found in Sections 5.2 to 5.4. In addition to these factors, the VIM tests require a calibration of the physical properties of the platform such as the mass, position of the center of gravity and moment of inertia. All these parameters were defined with respect to the full-scale data presented in Chapter III.

Thus, the masses of models were measured with a digital scale, and moments of inertia about three axes were measured indirectly by the pendulum arrangement shown in the sketch of Fig. 6.1 using the Eqn. (6.1).

$$T_0 = 2\pi \sqrt{\frac{I}{Mgh}} \qquad 6.1$$

where T_0 is the period of the system in free oscillation, M is the mass of the model, g is the acceleration of gravity and I is the moment of inertia of the model in relation to the fixed point.

Note that the pendulum procedure can provide the moment of inertia and position of the center of gravity through additional measurements while varying the parameter h. However,

more accurate results for the position of the center of gravity require the arrangement shown schematically in Fig. 6.2, which is based on static equilibrium, as shown in Eqn. (6.2).

$$T \cdot d_2 - m \cdot g \cdot d_1 = 0 \qquad 6.2$$

where T is the tension of the line, d_2 is the distance from a known point to the connection between the model and support line, m is the model mass, g is the acceleration of gravity, and d_1 is the distance from the known point to the center of gravity of the platform.

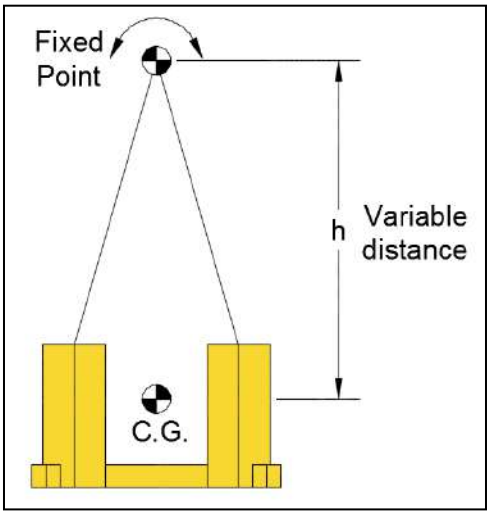

Figure 6.1 Pendulum configuration for the determination of the moment of inertia of the TLP.

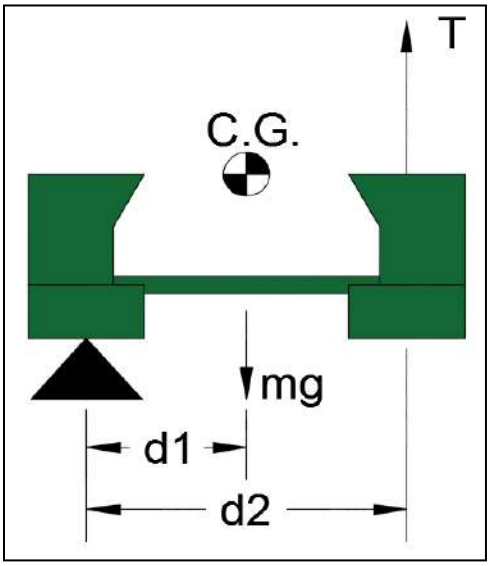

Figure 6.2 Experimental arrangement for estimating the position of the center of gravity of the TAD.

Figure 6.3 shows the two models during the inertia measurement. Tables 6.1 and 6.2 present the values of the physical properties and the margins of error about the target values of the TLP and TAD, respectively. Ballast was carefully selected to achieve the target mass values. Consequently, the radius of gyration and the center of gravity positions present slightly higher error values, however, none in any case, were greater than 5%.

For the longitudinal position of the center of gravity of the TAD, a larger error was obtained. However, in absolute terms, the target and experimental values are relatively close. Note that, these values were measured using the coordinate system presented in Chapter III.

Table 6.1 Experimental and target values of the physical properties of the TLP

Properties	Target values		Experimental values	Error [%]
	Full scale	Model scale		
Mass	32897 [mT]	4.01 [kg]	4.05 [kg]	0.97
Radius of gyration Rxx	33.58 [m]	16.79 [cm]	17.58 [cm]	4.72
Radius of gyration Ryy	33.43 [m]	16.72 [cm]	16.05 [cm]	3.95
Radius of gyration Rzz	37.04 [m]	18.52 [cm]	19.43 [cm]	4.89
Center of gravity LCG	0 [m]	0 [cm]	0.05 [cm]	-
Center of gravity TCG	0 [m]	0 [cm]	0.08 [cm]	-
Center of gravity VCG	31.10 [m]	15.55 [cm]	16.15 [cm]	3.85

Table 6.2 Experimental and target values of the physical properties of the TAD

Properties	Target values		Experimental values	Error [%]
	Full scale	Model scale		
Mass	18122 [mT]	2.21 [kg]	2.18 [kg]	1.52
Radius of gyration Rxx	16.76 [m]	8.38 [cm]	7.97 [cm]	4.95
Radius of gyration Ryy	28.98 [m]	14.49 [cm]	13.94 [cm]	3.78
Radius of gyration Rzz	31.22 [m]	15.61 [cm]	16.15 [cm]	3.49
Center of gravity LCG	-0.97 [m]	-0.49 [cm]	-0.30 [cm]	38.7
Center of gravity TCG	0 [m]	0 [cm]	-0.04 [cm]	-
Center of gravity VCG	14.34 [m]	7.17 [cm]	7.44 [cm]	3.74

(A) (B)

Figure 6.3 Inertia calibration tests: (A) Moment of inertia of the TLP (B) Position of the center of gravity of the TAD

6.3 MOORING SYSTEMS

The experimental setup includes an equivalent representation of the mooring system of both platforms and the mechanical connections for the coupled tests. Due to the complexity of the system, the design of the equivalent mooring systems was focused on horizontal stiffness, natural periods, and the set-down of the TLP. Thus, the vertical stiffness, added mass and drag forces on the mooring lines or risers and high-frequency movements due to the TLP tendons were neglected.

6.3.1 TLP

The linear stiffness of the TLP K_{SWAY} depends on the length L_n and the pre-tension Tt_n of the tendons as shown in Eqn. (6.3). Moreover, for hydrostatic equilibrium, the tendon pre-tension is given by Eqn. (6.4).

$$K_{SWAY} = \sum_{i=1}^{n} \frac{Tt_n}{L_n} \tag{6.3}$$

$$\text{Buoyancy} = \text{Weight} + \sum_{i=1}^{n} Tt_n \tag{6.4}$$

If the draft and the mass of the TLP are considered to be constant values, consequently, the pre-tensions on the tendons become constants of the system. Thus, to obtain the stiffness K_{SWAY} and, consequently, the correct natural period, the tendon must be represented with the correct scaled length.

Furthermore, the tendon length governs the set-down (the coupling effect between Heave and Surge movements), i.e., a horizontal offset produces draft variations on the TLP. As shown in Fig. 6.4, an arbitrary horizontal offset D produces a positive draft variation equal to A for a length tendon H, however, if the tendon length is reduced to H/2 the resulting draft variation is 2.65A. Therefore, a reduction in the tendon length introduces significant variations in the set-down of the TLP.

Considering these relevant aspects of TLP dynamics, three alternatives were examined to represent the TLP tendons. The first concept uses four vertical springs connected to each corner of the TLP hull, as shown in Fig. 6.5. Despite its simplicity, this concept requires relatively long tendons, which are unreliable under the conditions of the current channel. However, if the tendon length decreases, the stiffness, natural period and set-down are far from the target values, as shown in Table 6.3.

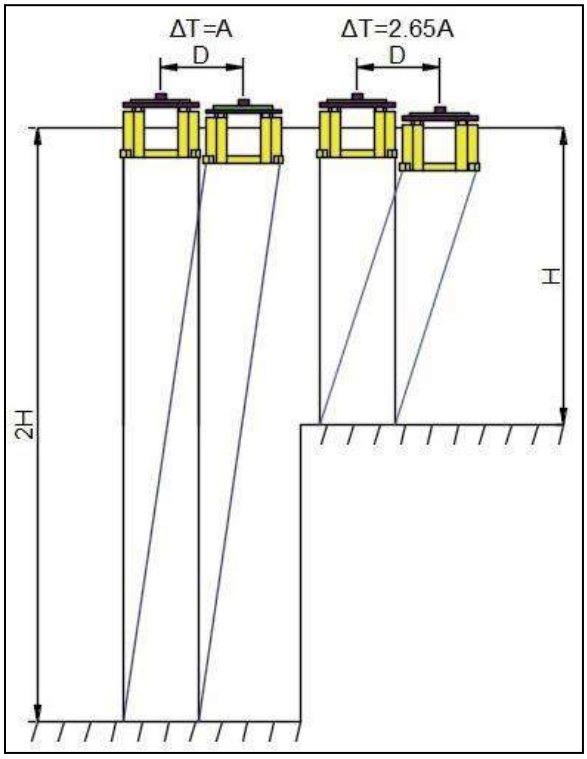

Figure 6.4 Set-down comparison for different water depths.

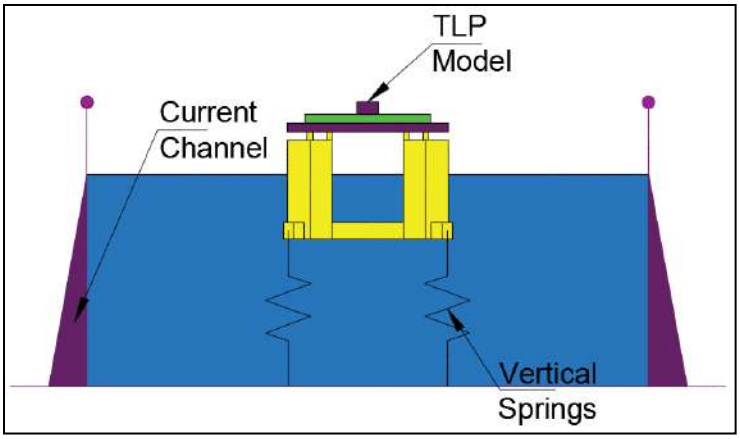

Figure 6.5 First arrangement with vertical springs.

Table 6.3 Properties if equivalent concept no. 1(Full-scale data).

Parameter	TLP properties	Concept no. 1
Tendon length [m]	1155	77
Sway stiffness [kN/m]	79.02	1194
Sway natural period [sec]	201	52
Draft variation due to the set-down [m]	A	12.5A

The second arrangement uses vertical lines composed of springs and ropes, mounted on a metal pipe tower. Four pulleys change the lines direction from horizontal to vertical as shown in Fig. 6.6. In this system, it is possible to calibrate the spring constant and the pre-tension line to achieve the target values of stiffness and natural period. Moreover, the set-down could be considered to be zero. However, in concept no. 2 is difficult to mount and to maintain the correct draft; additionally, the pulleys introduce strong mechanical damping into the system. As shown in Fig. 6.7 a decay test on Sway reveals an overdamped system.

Finally, the third arrangement uses four horizontal springs to provide restoring forces in the horizontal plane; the spring constants are calibrated to achieve the correct values of stiffness and natural period. A vertical carbon fiber pipe is connected to the far end of a metal pipe tower with a joint rod, and the pipe is attached to the TLP deck with a bearing connection as shown in Fig. 6.8. Moreover, the carbon fiber pipe provides the necessary strength to keep the proper TLP draft and mass ratio, and the

joint rod and bearing connection allow free movements of the TLP for Surge, Sway, and Yaw.

This arrangement, based on the pendulum concept, induces a negative set-down, here called s*et-up*. The horizontal offsets induce negative draft variations. However, as shown in Tab. 6.4 for a long bar, the *set-up* is low and can be neglected.

Table 6.4 Draft variations due to *set-down* and *set-up*.

Description	Draft variation ΔT [m]
TLP with tendons	A
Concept no. 01	12.5A
Concept no. 03	-1.15A

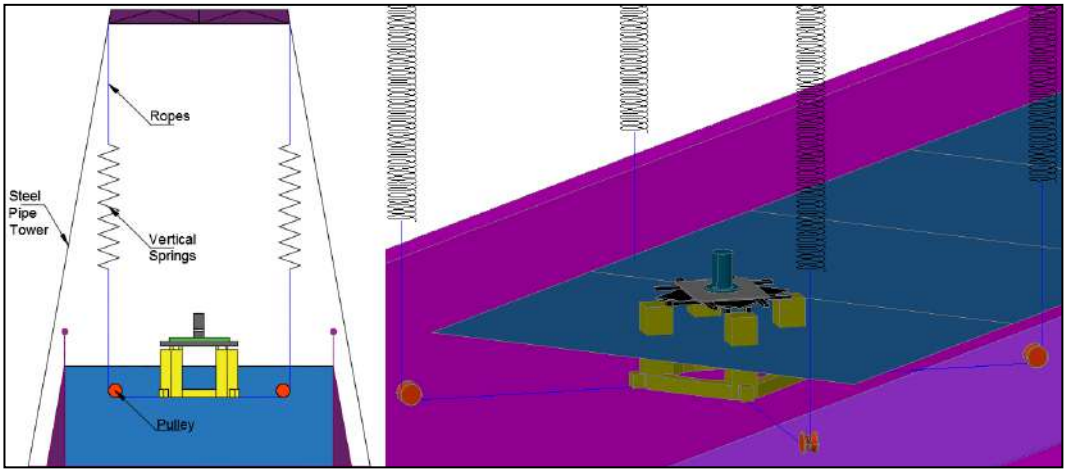

Figure 6.6 Second arrangement with vertical springs.

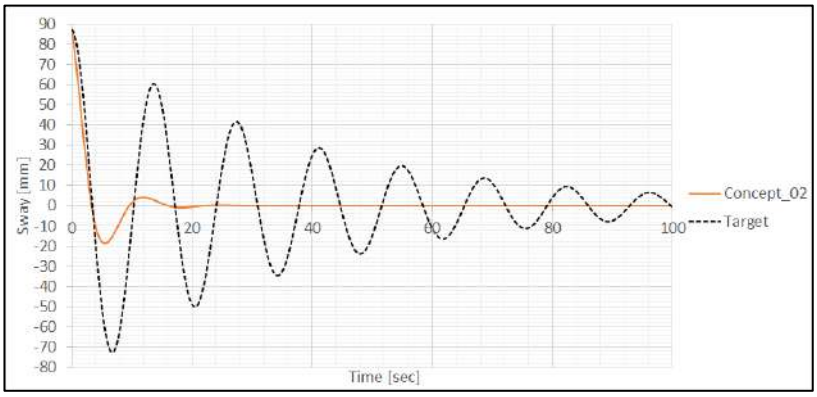

Figure 6.7 Sway decay test using the second arrangement (Data in model scale)

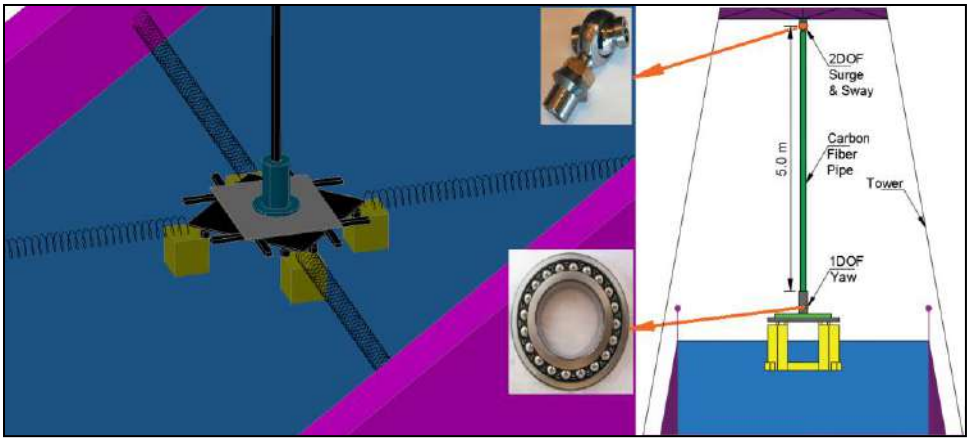

Figure 6.8 Third arrangement with horizontal springs and carbon fiber pipe.

Therefore, based on this brief analysis of these three concepts to represent the TLP tendon, the last arrangement was selected because it allows for the correct representation of stiffness and consequently of the natural periods for Sway and Yaw. In addition, the draft did not present significant variations, and there is no additional damping due to the mechanical connections.

6.3.2 TAD

As mentioned in Section 3.2, The TAD is moored using a semi-taut leg system. Thus, by linearizing the stiffness curve for Surge, Sway and Yaw, an equivalent horizontal soft mooring composed for four springs to represent the semi-taut leg system for the horizontal modes of the TAD is proposed, as shown in Fig. 6.9.

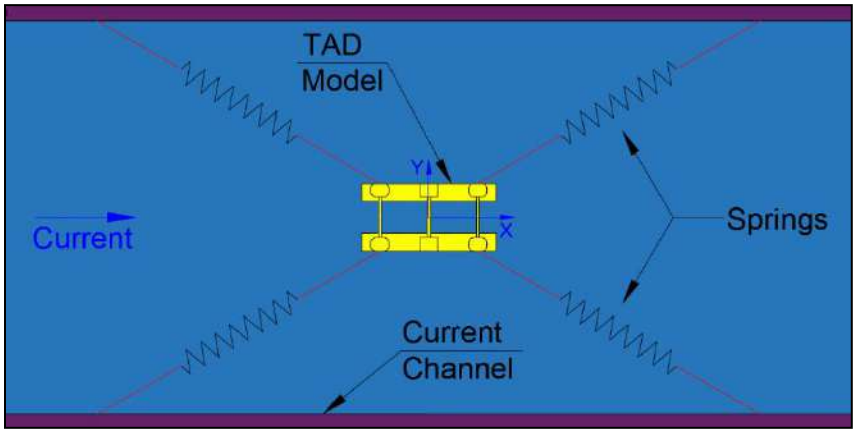

Figure 6.9 Soft mooring arrangement for the TAD platform.

6.3.3 Hawser System

As mentioned in Section 3.3, the TLP and TAD are connected by a hawser system, which is composed of a group of lines of polyester ropes. In the VIM test, the stiffness of the hawser system has been linearized.

With the aim of verifying the influence of the hawser arrangement configuration on the VIM response of the multi-body system, four different hawser configurations were tested as shown in Fig. 6.10. Note that, the first arrangement is the hawser system presented in Section 3.3. The other three arrangements were defined as modifications of the first one. In the model tests, the hawser lines were modeled by linear springs, and properties of each hawser line are presented in the next section.

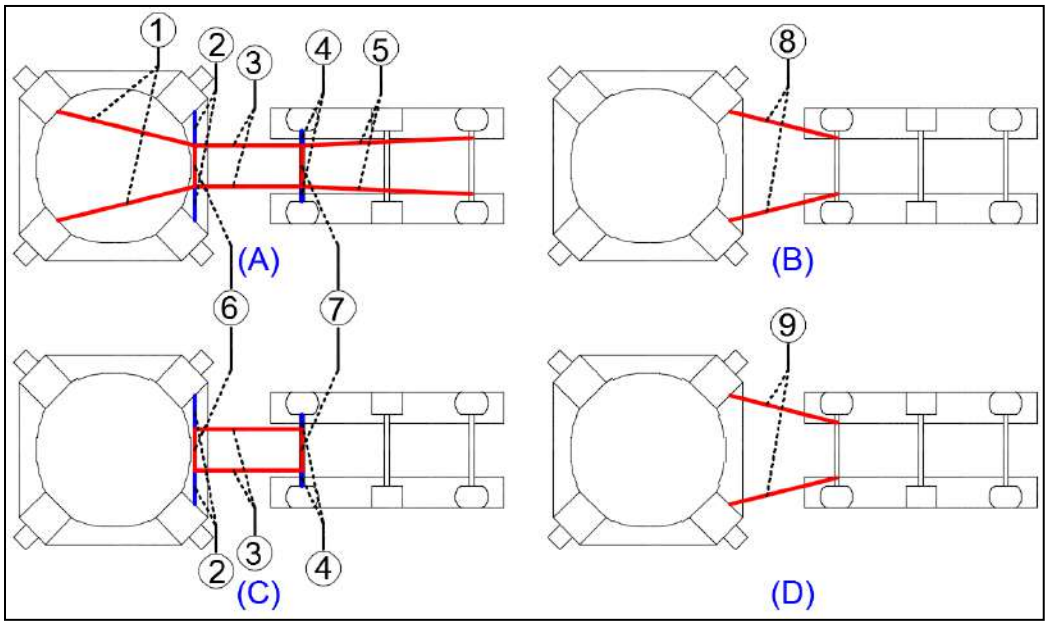

Figure 6.10 Four hawser system configurations (A) HW1, (B) HW2, (C) HW3, and (D) HW4. Indexes from 1 to 9 indicate the line types with different values of initial length, pre-tension, and axial stiffness. (See Table 6.5)

6.4 OFFSET AND DECAY TESTS

The springs used on the equivalent mooring systems of the TLP, TAD and the hawser systems were calibrated based on the theoretical values of Section 3.4. Note that, the values of Sway and Surge stiffness depend primarily on the spring constants, spring lengths, spring pre-tension, Euler angles of the springs, and positions of the floaters. In addition, Yaw

stiffness depends on the distance between the mooring line attachment point and the centerline of the floater. Finally, the stiffness curves have been linearized in order to simplify the construction of the equivalent mooring systems.

Thus, after the installation of the floating bodies and their respective mooring systems, offset and decay tests were conducted to experimentally measure the stiffness and natural periods of the horizontal modes (i.e., Surge, Sway and Yaw).

The offset tests consist of applying a known force or moment and then measuring the linear (or angular) displacement. Decay tests were performed by introducing an initial linear or angular offset to the system and then releasing it to move freely.

Figures 6.11, 6.12 and 6.13 present the stiffness for Surge, Sway, and Yaw of the TLP. Note that, the nonlinear curves are presented using full-scale values. For Surge stiffness, with offsets in the range of [0 - 30] m, the differences between the nonlinear and linear approximations are insignificant.

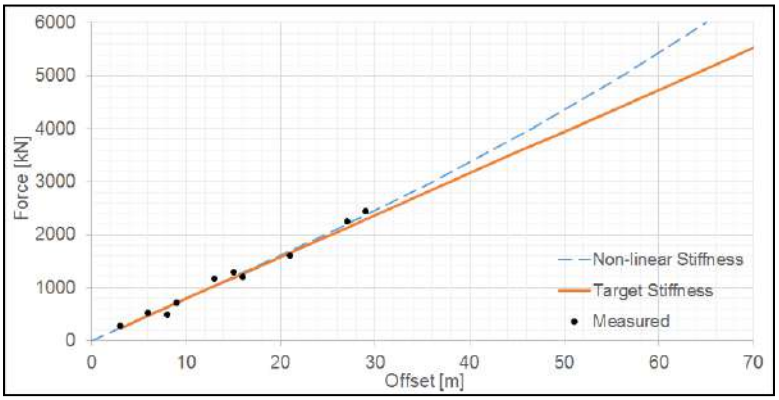

Figure 6.11 Surge stiffness of the TLP, nonlinear curve, linear approximation (target) and experimental values.

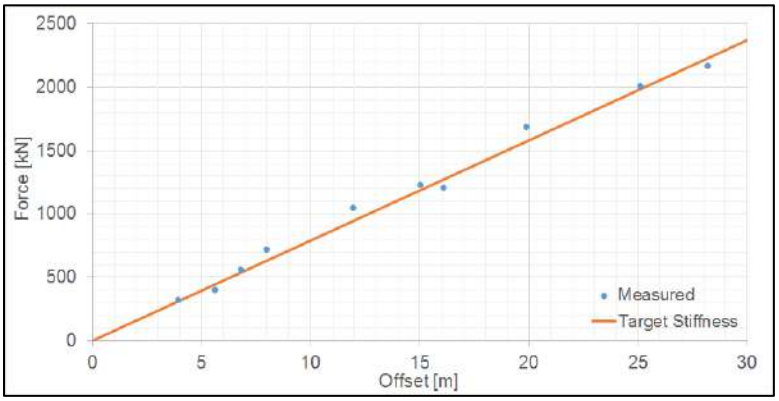

Figure 6.12 Sway stiffness of the TLP, target and experimental values.

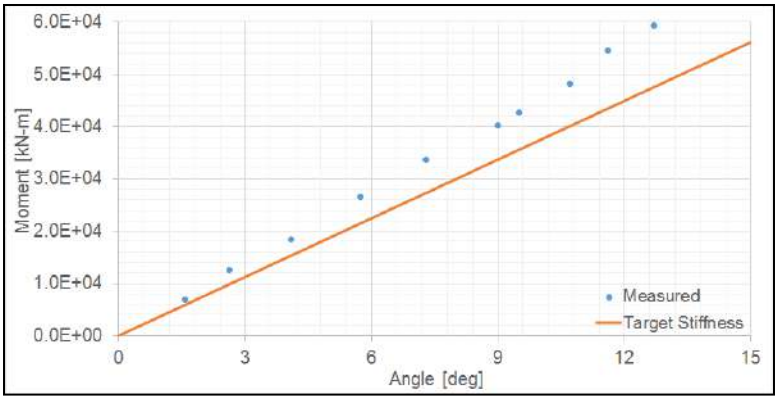

Figure 6.13 Yaw stiffness of the TLP, target and experimental values.

It is clear that the agreement with the target values is excellent for the cases of Surge and Sway. Because the Yaw stiffness depends on the position of the connection of the lines with the TLP, it was challenging to achieve better agreement. However, the results are acceptable.

Similarly, Figures 6.14, 6.15, and 6.16 present the stiffness for Surge, Sway, and Yaw of the TAD. Again, the nonlinear curves are presented using full-scale values. In this case, the nonlinear values of Surge and Sway stiffness are significantly higher. It is evident that the linear approximation does not represent the correct values for offsets larger than the range of [0 - 20] m. The agreement between the target and experimental values is excellent.

The hawser lines present nonlinear properties as shown in Fig. 6.17, however, to simplify the configuration of the hawser lines, the linear approximation shown in Fig. 6.17 was adopted. Table 6.5 presents the properties of the hawser lines of each hawser system used in the VIM tests.

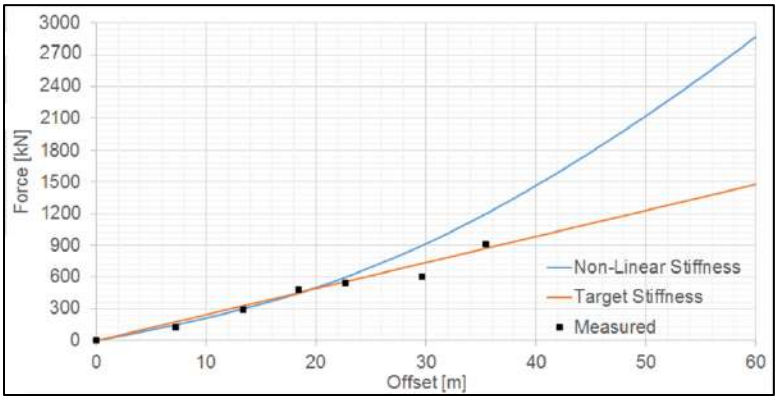

Figure 6.14 Surge stiffness of the TAD, nonlinear curve, linear approximation (target) and experimental values.

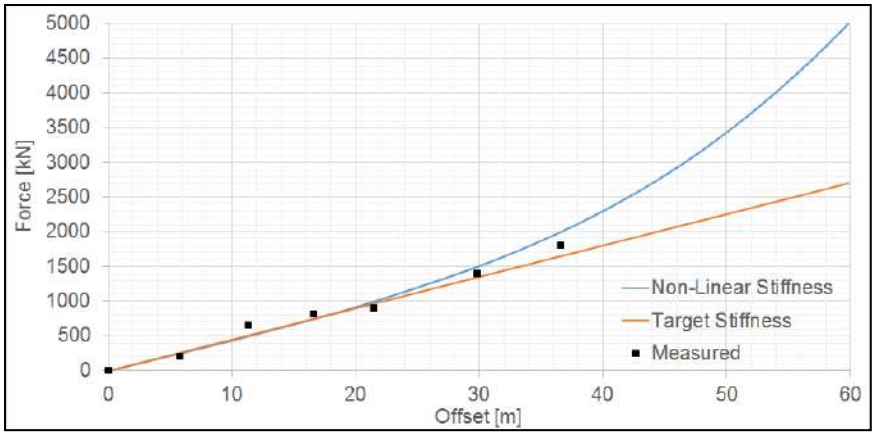

Figure 6.15 Sway stiffness of the TAD, nonlinear curve, linear approximation (target) and experimental values.

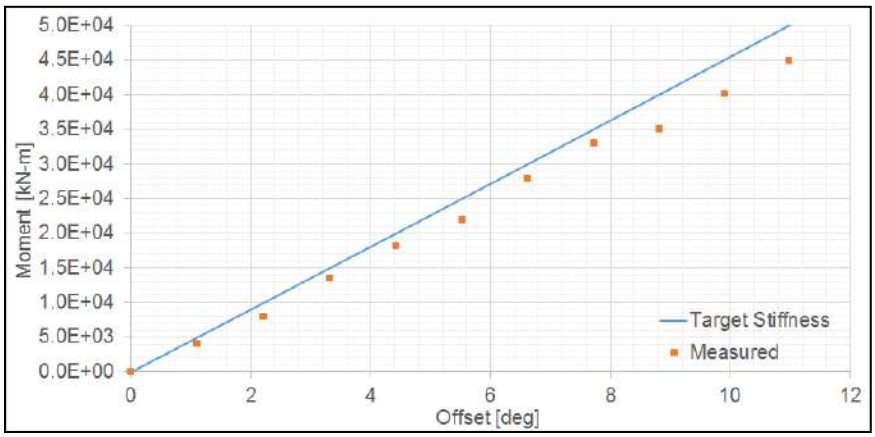

Figure 6.16 Yaw stiffness of the TAD, nonlinear curve, linear approximation (target) and experimental values.

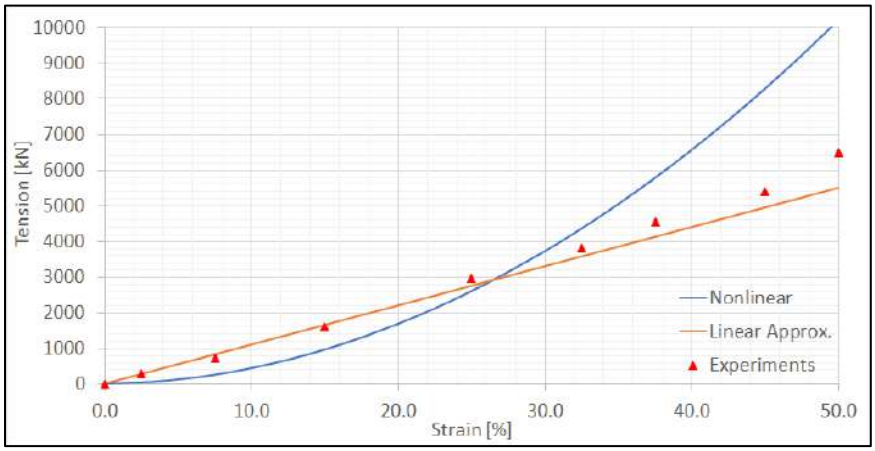

Figure 6.17 Axial stiffness of the hawser lines, nonlinear curve, linear approximation (target) and experimental values.

Table 6.5 Properties of the hawser lines of the four hawser system configurations**.**

Hawser line	H1	H2	H3	H4	H5	H6	H7	H8	H9
Initial length [m]	47.5	12.2	39.0	3.3	59.0	14.3	14.3	40	40
Pre-tension [kN]	865	220	842	363	940	496	396	1900	2456
Axial stiffness [kN]	116	116	116	116	116	116	116	116	179

Finally, Table 6.6 presents the values of the natural periods of the TLP and TAD for the single-body and multi-body connected by the hawser system cases. Note that, the four configurations of the hawser systems were tested.

Despite small variations, the hawser system does not modify the natural periods of the system significantly. In addition, Yaw motion has shown to be the most affected by the hawser configuration. However, these variations are small as well.

Note that the floaters connected by the hawser system present similar values for the natural periods of Surge and Sway. Yaw does not follow this trend, i.e., the natural periods of Yaw are different for the TLP and TAD.

In general, the values of the natural periods of the units when connected are smaller than the natural periods of the units in the single-body cases.

Table 6.6 Experimental and target values for the natural periods of the TLP and TAD

Case	Value	Surge		Sway		Yaw	
		TLP	TAD	TLP	TAD	TLP	TAD
Alone	Target	201	224	201	221	134	68.9
	Experimental	196	219	198	216	120	65.8
Coupled	Target	183	183	199	199	95.7	57.4
	Exp. HW1	176	174	194	196	87.5	52.8
	Exp. HW2	178	177	195	194	85.0	54.7
	Exp. HW3	174	173	197	198	84.0	56.1
	Exp. HW4	170	171	190	191	86.0	52.6

6.5 VIM TEST DESCRIPTION

The model tests were conducted in the current channel in the Laboratory of Waves and Currents (LOC) of COPPE/UFRJ. The current channel is 22 m in length, 1.4 m in width and 0.5 m in depth. Four electrical pumps generate the flow into the channel. An electronic module controls the RPM of the pumps and consequently the flow velocity in the channel. Finally, a propeller flowmeter measures the flow velocity. Table 6.7 presents the experimental and target values of the current velocities. In general, with a careful calibration of the current velocities, it is possible to achieve reasonable values of error. However, the turbulence intensity in the current channel is quite high. Unfortunately, there is no way to reduce these values without modification of the lab equipment.

Table 6.7 Experimental and target values of the current velocities of the model tests.

	Target values		Experimental values			
	Full-Scale [m/s]	Model Scale [m/s]	Mean [m/s]	Error [%]	Std. Dev. [m/s]	Turbulence Intensity [%]
V1	0.30	0.021	0.024	13.8	0.0047	19.6
V2	0.40	0.028	0.026	7.7	0.0049	18.6
V3	0.50	0.035	0.038	8.2	0.0044	11.5
V4	0.70	0.049	0.045	9.7	0.0054	12.1
V5	0.85	0.060	0.065	7.8	0.0068	10.4
V6	1.00	0.071	0.066	6.3	0.0062	9.3
V7	1.24	0.088	0.096	9.4	0.0080	8.4
V8	1.45	0.103	0.094	8.3	0.0069	7.3
V9	1.60	0.113	0.121	7.4	0.0076	6.3
V10	2.00	0.141	0.151	6.9	0.0097	6.4
V11	2.40	0.170	0.158	7.1	0.0103	6.5

The model test campaign is divided into four sections: TLP alone, TAD alone, TLP with TAD in a multi-body system without a mechanical connection between the floaters, and TLP with TAD connected by a hawser system. The components of the experimental apparatus are the scale models with the proper mass distributions and centers of gravity, the mooring

system of each floater and the hawser system as the connection between the floaters. Each mooring system and the metal pipe tower to support the vertical constraint for the TLP require support attached to the channel walls. Figure 6.18 presents the experimental setup for the TLP alone, TAD alone and TLP with TAD in the multi-body system without connection to the TLP, both upstream and downstream. Note that, for the single-body cases, the angle of attack is changed by rotating the entire system

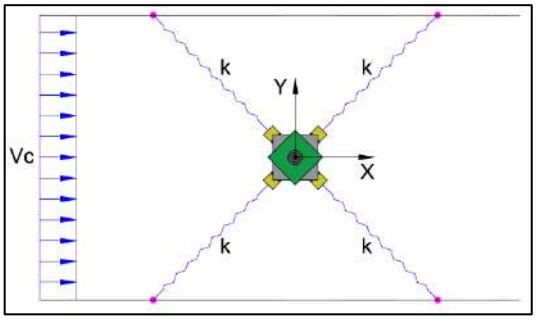

TLP alone

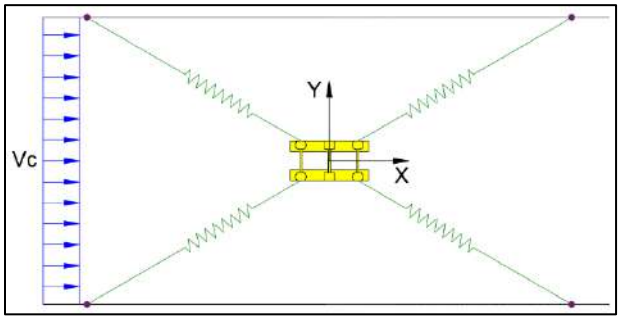

TAD alone

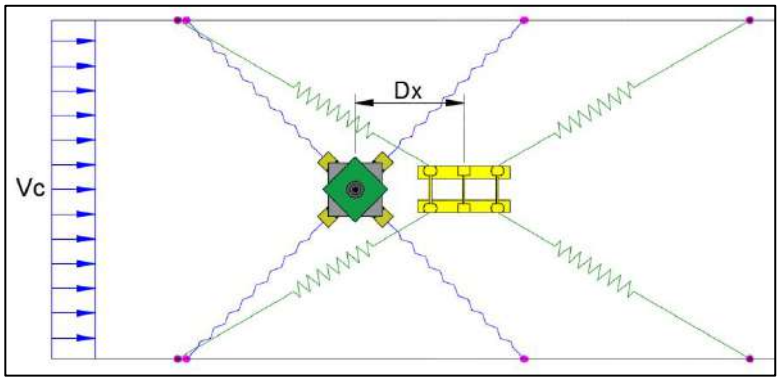

TLP with TAD without connection (TLP upstream and three distances Dx)

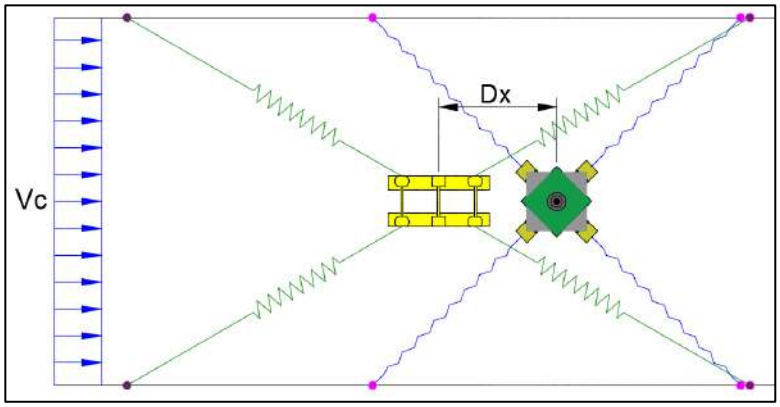

TLP with TAD without connection (TLP downstream and three distances Dx)

Figure 6.18 Experimental setup for the VIM tests – Part I.

Figure 6.19 presents the experimental setup for the TLP with TAD multi-body system connected by the hawser system considering the TLP upstream and downstream.

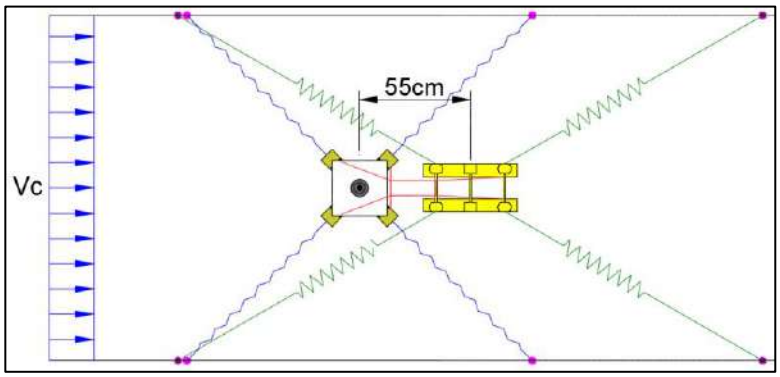

TLP with TAD connected by hawser system (TLP upstream)

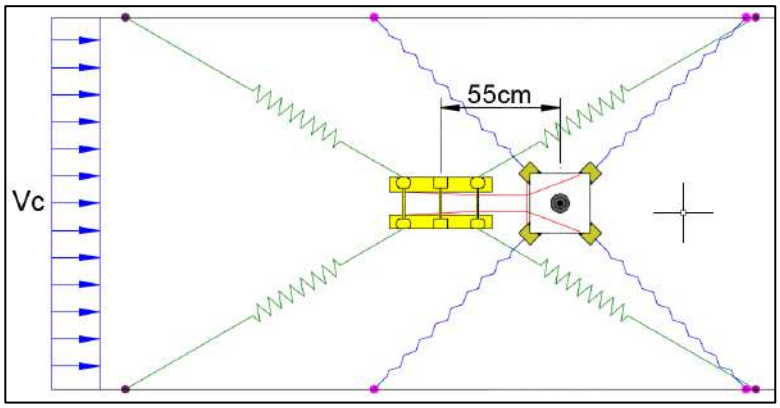

TLP with TAD connected by the hawser system (TLP downstream)

Figure 6.19 Experimental setup for the VIM tests – Part II.

The experimental setup was assembled to measure the motions developed by the floaters when subject to currents. The motions of the floaters were measured using Qualisys Track Manager (QTM) [73]. The QTM system is an optical tracking system that uses cameras with infrared (IR) light sources and passive markers fixed on the body. These markers are retroreflective spheres of a specific size. During measurement, the cameras flash IR lights at a specific frequency; the IR lights hit the spherical markers, and the lights reflect back to the cameras. The system computes the center point of each sphere and transmits this information in real-time to the software. Based on the coordinates defined and calibrated before the measurements, the QTM system can calculate the position of each marker in 3D. Note that,

the measurement of the motions of a body in six degrees of freedom requires at least three spherical markers.

Table 6.8 presents a summary of this experimental campaign.

RPM of four pumps controls the current velocity. Note that, when the current velocity is changed from one value to the next one, there is an interval of time, when the current velocity is "high-transient" The final data analysis of the time traces considers only the "steady" part of the measurements, i.e., without the motions induced by the current velocity in the "high-transient" interval of time. The "steady" part of the measurements represents at least 3-hours of full-scale time in all of the tests. Furthermore, each test was repeated twice.

In the case of the TLP alone, five angles of attack and 11 current velocities were tested, for a total of 110 VIM tests. For the TAD alone, three angles of attack and 11 current velocities, for a total of 66 VIM tests. For the case of the TLP with TAD in a multi-body system without a mechanical connection between the floaters, one angle of attack, three relative distances between the floaters and two relative positions were considered; in total, 132 VIM tests were conducted. For the case of the TLP with TAD in a multi-body system connected by the hawser system, one angle of attack, four hawser system configurations and two relative positions were considered; in total, 176 VIM tests were conducted on the current channel.

Table 6.8 Summary of the VIM experimental campaign.

Case	Tests description
TLP alone	11 velocities and 5 angles of attack 0°-45°@11.25°
TAD alone	11 velocities and 3 angles of attack 0°-180°@90°
TLP - TAD without connection (TLP upstream)	11 velocities and 3 relative distances between TLP and TAD
TLP - TAD without connection (TLP downstream)	11 velocities and 3 relative distances between TLP and TAD
TLP - TAD connected by hawser system (TLP upstream)	11 velocities and 4 hawser system configurations
TLP - TAD connected by hawser system (TLP downstream)	11 velocities and 4 hawser system configurations

6.6 EXPERIMENTAL RESULTS OF VIM TESTS

In this section, experimental data from the VIM test campaign are presented and discussed. As noted in previous sections, four general cases were considered: TLP alone, TAD alone, TLP-TAD multi-body system without mechanical connection and TLP-TAD multi-body system connected by the hawser system.

Figure 6.20 shows the coordinate systems for cases of the TLP alone and TAD alone. The global coordinate system is depicted in blue, and it is fixed to the current channel. The local coordinate system is depicted in red, and it is fixed to the floater. In all tests, the current flows toward the positive side of the x-axis. The current angle of incidence is measured as the counterclockwise angle between the x-axes of the two coordinate systems. Thus, the floaters and their respective mooring systems are located with the appropriate orientation to fix the angle of attack. The motions of the floaters are measured in relation to the global system.

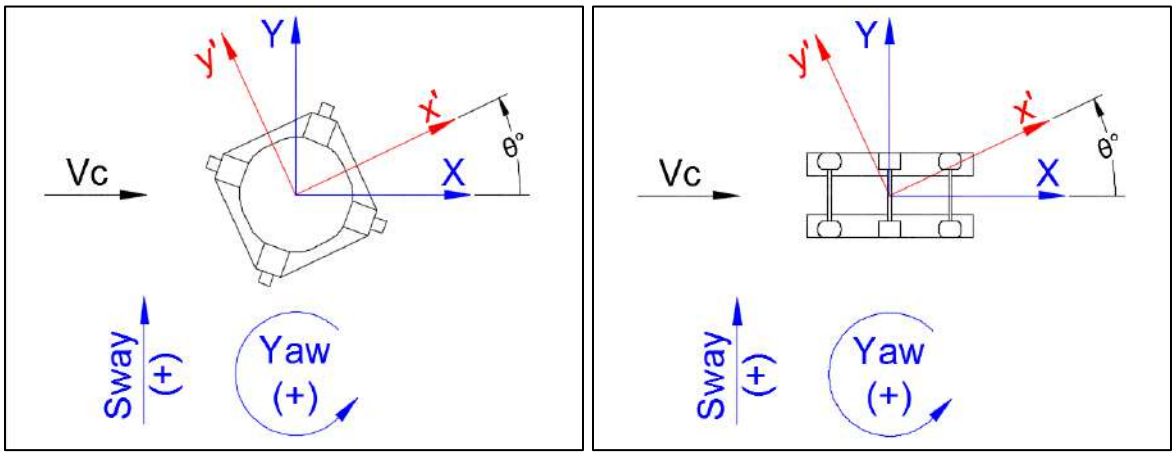

(A) (B)

Figure 6.20 Coordinate systems considered in the experimental tests for (A) TLP alone and (B) TAD alone. The global coordinate system is in blue, and the local one is in red.

Figure 6.21 presents the coordinate systems for the multi-body cases. In these tests, two coordinate systems fixed to the current channel were defined, one for each floater. The angle of attack is 0° for all of the cases. In addition, two sub-cases are considered: TLP upstream and TLP downstream. In cases without mechanical connection, three relative positions between the floaters were considered. In cases with a mechanical connection between the

floaters, four different configurations for the hawser system were analyzed. The motions of the floaters are measured in relation to their respective coordinate systems. Note that the coordinate systems presented in Fig. 6.21 are similar to those for the cases with the hawser system.

The origins of all of the coordinate systems fixed to the current channel are located at the initial position of the center of gravity of the respective floater. The origins of the coordinate systems fixed to the floaters are located at the position of the center of gravity of the respective floater.

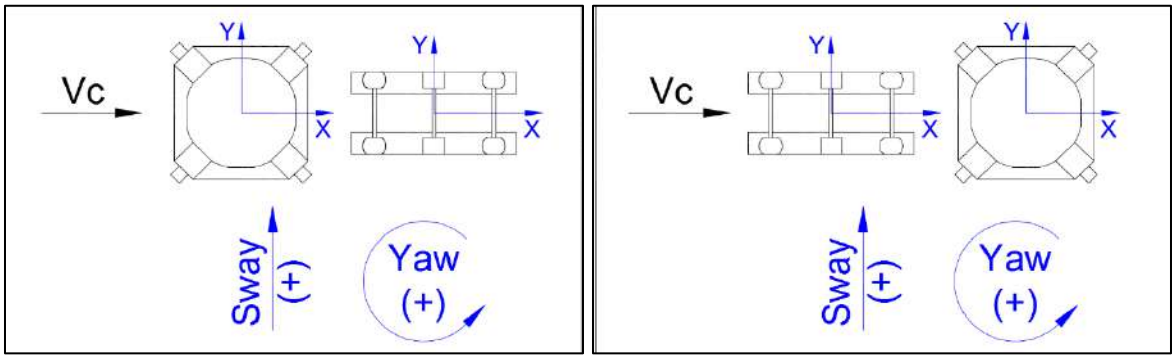

(A) (B)

Figure 6.21 Coordinate systems adopted in the VIM tests for multi-body cases for: (A) TLP upstream and (B) TLP downstream.

The results of the tests are presented by taking the statistics from the time traces of the motions of the floaters as follows.

$$A/D_{NOM} = \frac{\sqrt{2}\times\sigma(\bar{Y}(t))}{L_C} \quad 6.5$$

$$A/D_{MAX} = \frac{\bar{Y}_{MAX} - \bar{Y}_{MIN}}{2\times L_C} \quad 6.6$$

$$\overline{\psi_{MAX}} = \frac{\psi_{MAX} - \psi_{MIN}}{2} \quad 6.7$$

where $\sigma(\bar{Y}(t))$ is the standard deviation of Sway response $\bar{Y}(t)$, $\bar{Y}_{MAX}$ is the maximum value of $\bar{Y}(t)$, $\bar{Y}_{MIN}$ is the minimum value of $\bar{Y}(t)$, ψ_{MIN} is the minimum value of Yaw motion, ψ_{MAX} is the maximum value of Yaw motion and L_C is the characteristic length of each floater. Note that, the Sway motion $\bar{Y}(t)$ is defined as the linear motion along the y-axis of the global

coordinate systems and Yaw as the rotational motion around the z-axis of the global coordinate systems in all cases.

The characteristic length L_C is defined as the projected length of the column of the TLP or TAD. In the case of the TLP with square columns, L_C is evaluated as a function of the incident angle, as shown in Eqn. (6.8).

$$L_C = L_{TLP}\left(\left|sin\left(\frac{\pi}{4}-\theta\right)\right| + \left|cos\left(\frac{\pi}{4}-\theta\right)\right|\right) \quad 6.8$$

where L_{TLP} is the face dimension of the column and θ is the angle of attack, as shown in Fig. 6.22. In the case of the TAD, since the columns have different shapes, the section of the central column is considered to calculate the characteristic length. Thus, L_C for the TAD is a function of the incident angle, as shown in Eqn. (6.9).

$$L_C = A_{TAD}|cos(\theta)| + B_{TAD}|sin(\theta)| \quad 6.9$$

where A_{TAD} and B_{TAD} are the face dimensions of the TAD column rectangular section, as shown in Fig. 6.22. Table 6.9 presents the values of projected length for the TLP and TAD.

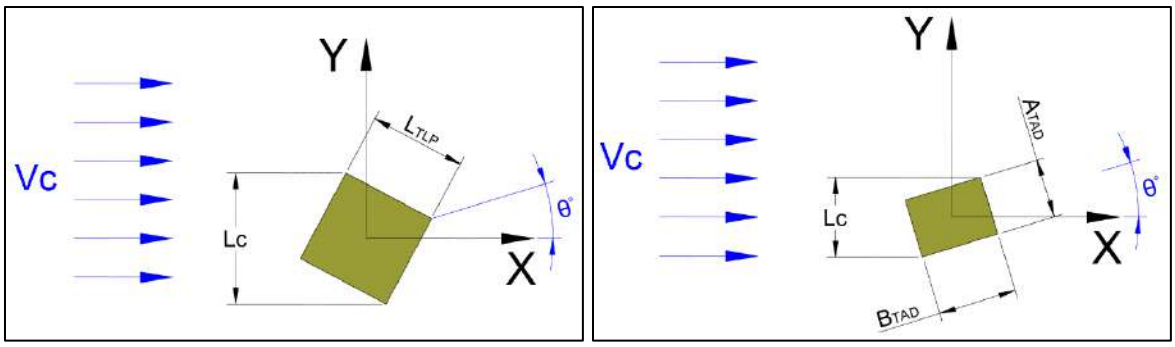

(A) (B)

Figure 6.22 Definition of characteristic length L_C for (A) TLP, and (B) TAD.

Table 6.9 Characteristic length L_C for TLP and TAD. (Full-scale data).

Parameter	TLP					TAD		
Angle of attack [deg.]	0.0°	11.25°	22.5°	33.75°	45.0°	0.0°	90.0°	180.0°
Characteristic length [m]	21.21	20.81	19.60	17.74	15.00	9.15	12.2	9.15

In addition, the current velocity V_C is represented by the non-dimensional reduced velocity V_R defined as follows:

$$V_R = \frac{V_C T_Y}{L_C} \qquad 6.10$$

where T_Y is the natural period in the transverse direction, e.g., Sway for θ=0°, and L_C is the characteristic lengths of the floater. Note that the natural periods considered for the calculations of V_R correspond to the experimental values of TLP and TAD alone presented in Tab. 6.6, for all cases. Table 6.10 presents the values of the current velocities and reduced velocities considered in this study.

Table 6.10 Reduced velocity V_R for TLP and TAD. (V_C values are full-scale)

V_C [m/s]	Angle of attack [deg.]							
	TLP					TAD		
	0.0°	11.25°	22.5°	33.75°	45.0°	0.0°	90.0°	180.0°
0.30	2.81	2.87	3.04	3.364	3.98	7.78	5.84	7.78
0.40	3.61	3.68	3.91	4.319	5.11	9.91	7.43	9.91
0.50	4.49	4.58	4.86	5.371	6.35	12.50	9.37	12.50
0.70	6.36	6.48	6.88	7.602	8.99	17.69	13.27	17.69
0.85	7.73	7.88	8.37	9.244	10.93	21.46	16.10	21.46
1.00	9.57	9.75	10.35	11.438	13.53	26.41	19.81	26.41
1.24	11.62	11.84	12.57	13.891	16.43	32.31	24.23	32.31
1.45	13.58	13.84	14.69	16.234	19.20	37.74	28.30	37.74
1.60	14.85	15.14	16.07	17.758	21.00	41.27	30.95	41.27
2.00	18.52	18.87	20.04	22.137	26.18	51.41	38.56	51.41
2.40	22.00	22.43	23.81	26.308	31.11	61.08	45.81	61.08

Moreover, the analysis of the floater motions is completed with a study in the frequency domain using the Power Spectral Density (PDS) calculated by Fast Fourier Transform (FFT). Finally, to visualize the order of magnitude of the motions about the platform sizes, trajectory plots in the XY plane are also presented.

6.6.1 TLP Alone

The results of VIM tests for the TLP alone are presented and discussed below. As mentioned in Section 6.5, five angles of attack and eleven current velocities were considered in this study.

Figure 6.23 presents the nominal A/D responses for Sway. Notably, the behavior of the TLP has a strong dependence on the angle of attack, i.e., a typical bell VIM curve is observed while at 0°, and the response of the TLP increases steadily at 45° with the reduced velocity, indicating galloping instabilities.

The behavior at 11.25°, 22.5° and 33.75° seems to be a combination of the trends described for 0° and 45° with some particularities. A typical VIM curve for 11.25°. However, the amplitudes of the motions are lower than those of the curve at 0°. In contrast, for 22.5° and 33.75°, the response increases steadily with the current. However, for these three angles of attack, the behavior at the last three velocities shows constant amplitude.

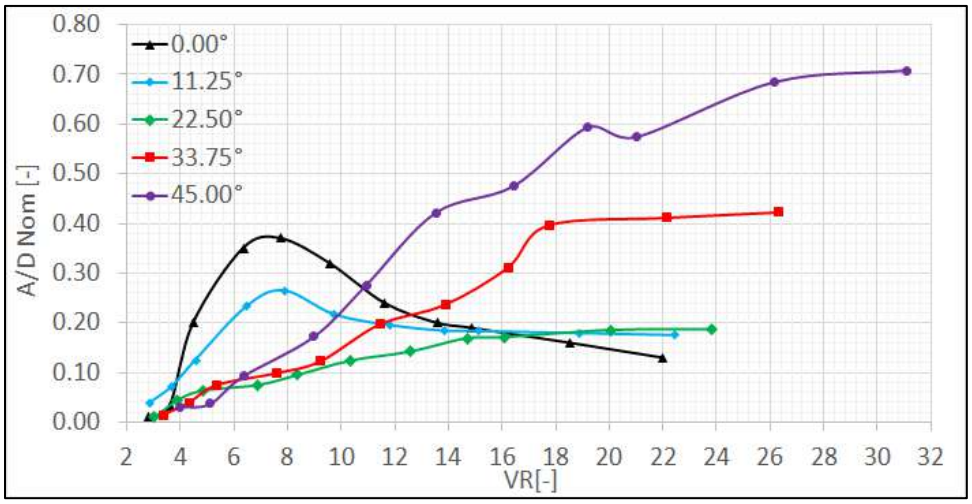

Figure 6.23 Nominal A/D for the TLP alone and several current angles of incidences: 0°, 11.25°, 22.5°, 33.75°, and 45°

Figure 6.24 presents the maximum A/D responses for Sway. The trends observed in these coefficients are similar to those of the nominal A/D response. However, the differences in terms of order of magnitude increase with the current velocity, i.e., the values of the maximum A/D and the nominal A/D are similar for low reduced

velocities, and, the values of the maximum A/D are considerably higher than the nominal A/D for high reduced velocities. This behavior occurs because the time series of the motions developed by the TLP have a sinusoidal shape at low velocities, and as the velocity increases, the shape of the time series becomes more irregular. Figure 6.25 illustrates this point.

Figure 6.26 presents the maximum Yaw response of the TLP alone for the five angles of attack. It is important to remark that the trend in the maximum Yaw response seems to be independent of the angle of attack, i.e., the response increases steadily with the reduced velocity for all angles of attack, indicating dominant galloping instabilities. The largest response is observed at 0°. No significant variations were found in the maximum responses for the other angles of attack.

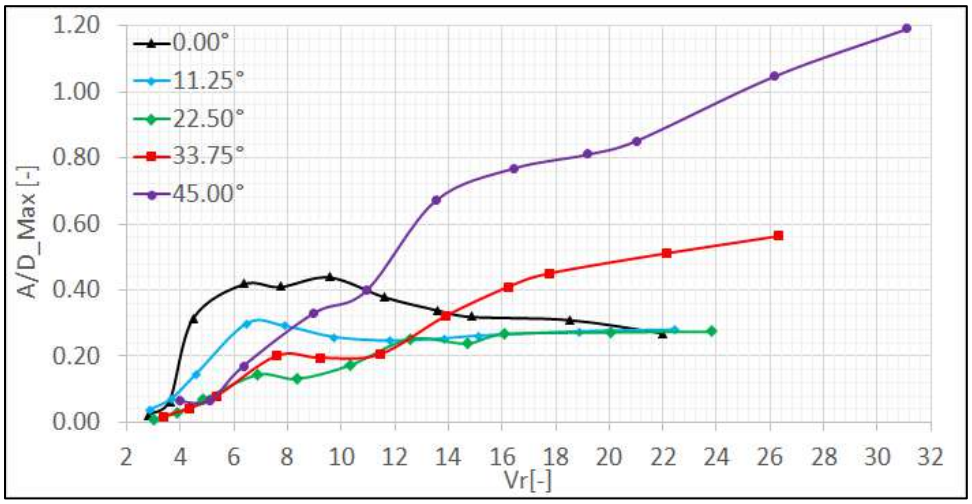

Figure 6.24 Maximum A/D for the TLP alone and several current angles of incidences: 0°, 11.25°, 22.5°, 33.75°, and 45°

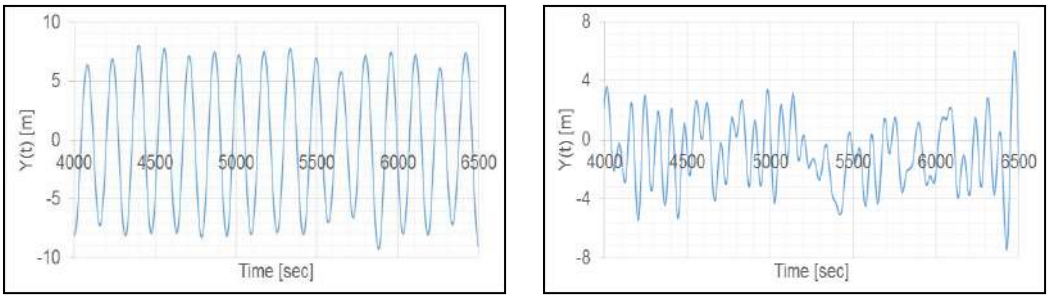

(A) (B)

Figure 6.25 Full-scale time series of Sway motion $\bar{Y}(t)$

(A) θ=0° and $V_R = 7.73$ (B) θ=0° and $V_R = 14.85$

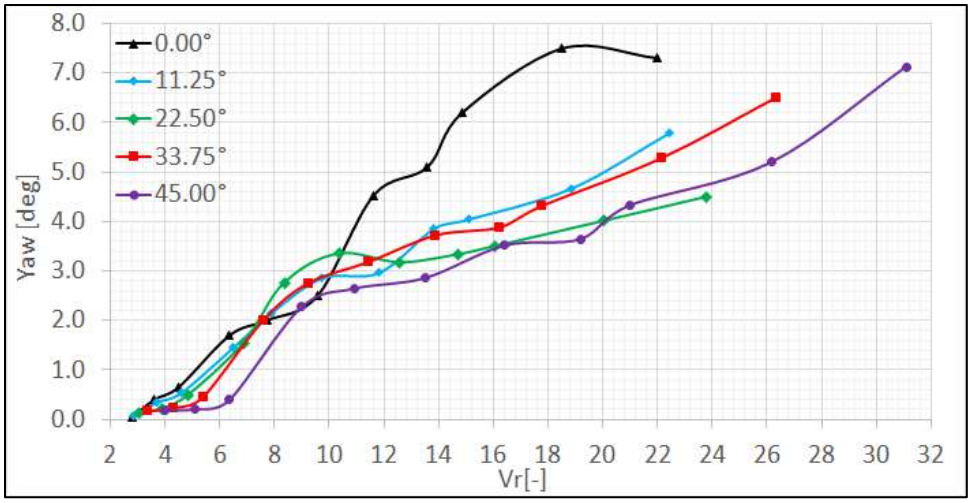

Figure 6.26 Maximum Yaw response for the TLP alone and several current angles of incidences: 0°, 11.25°, 22.5°, 33.75°, and 45°

Figure 6.27 presents trajectory plots of the horizontal motions of the TLP alone, considering six velocities and one angle of attack. Note that, the current travels in the direction of the positive side of the x-axis. It is very interesting to observe that the amplitude of the Sway motion increases with the reduced velocities in the range of [2 - 8], after which, it decreases with the reduced velocity for the range of [8 - 22]. In contrast, Yaw motion presents small values for low reduced velocities in the range of [2 - 8] and quickly increases with velocities in the range of [8 - 22].

Figure 6.28 presents the analysis of the motions developed by the TLP in the frequency domain for two angles of attack, namely 0° and 45°. For 0°, the PSD confirms that the response for Sway at low reduced velocities occurs at the natural frequency of the TLP. Consequently, the unit develops a resonant motion (i.e., VIM). As the velocity increases, some peaks at higher and lower frequencies are observed. Therefore, the motions of the TLP are a mix of VIM with galloping instabilities. The energy in Yaw motion is minuscule at low velocities; however, for high velocities, the energy of the rotational mode is widely spread across the entire range of frequencies.

At 45° degrees, the PSD shows that the energy of Sway motion is concentrated at very low frequencies. Consequently, there are no resonant motions or VIM. Since the higher peaks occur in regions far from the natural frequency, it is possible to conclude

that the TLP presents galloping instabilities. The same observations apply to Yaw motion at the same angle of attack.

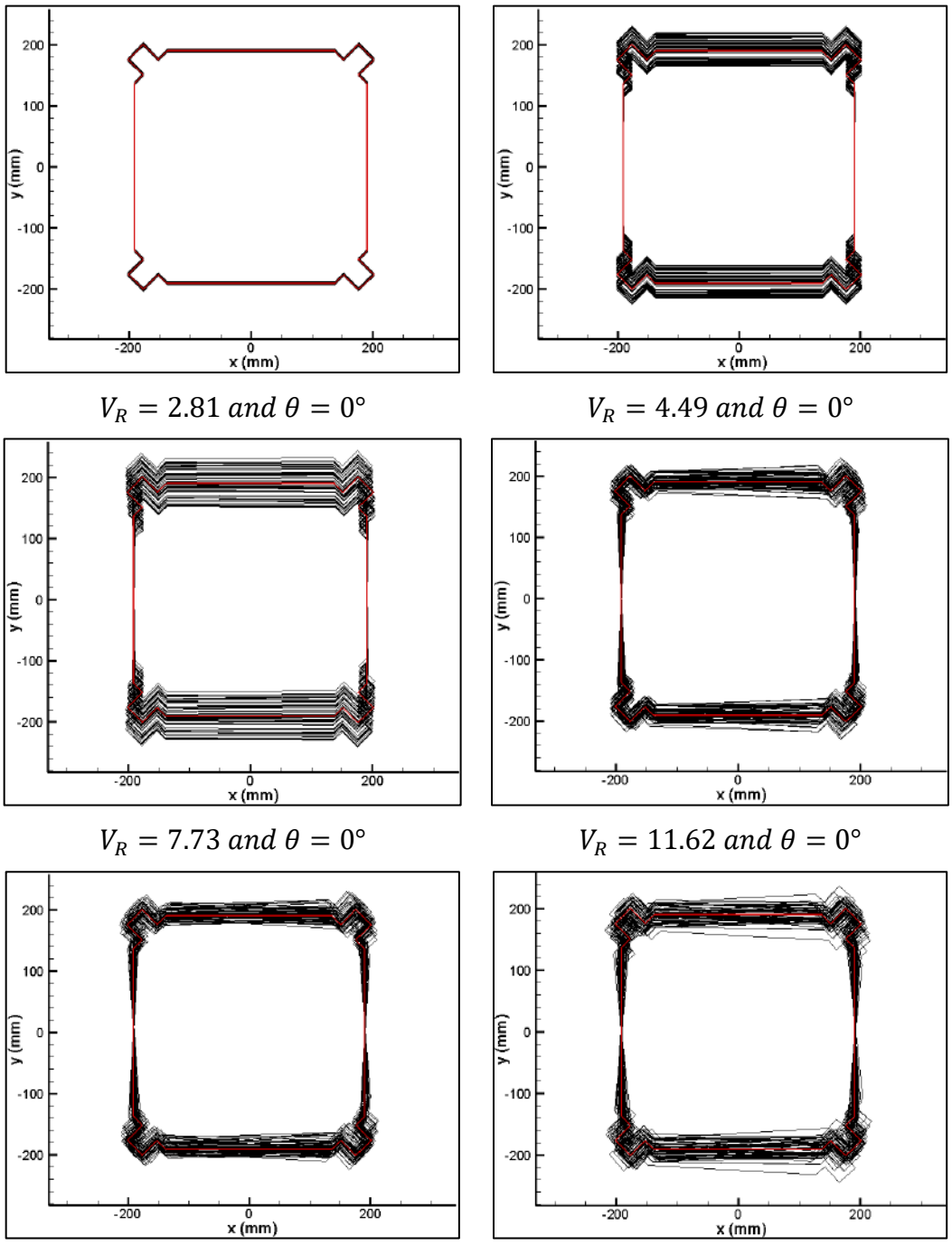

$V_R = 2.81\ and\ \theta = 0°$ $V_R = 4.49\ and\ \theta = 0°$

$V_R = 7.73\ and\ \theta = 0°$ $V_R = 11.62\ and\ \theta = 0°$

$V_R = 14.85\ and\ \theta = 0°$ $V_R = 22.00\ and\ \theta = 0°$

Figure 6.27 Trajectory plots of the motions of the TLP alone in the XY plane for θ=0° and different reduced velocities.

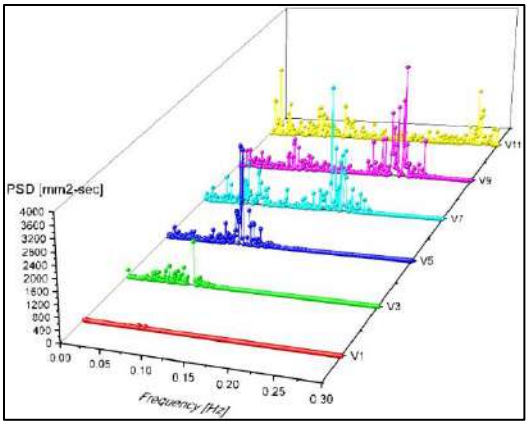

Sway of the TLP alone for θ=0°

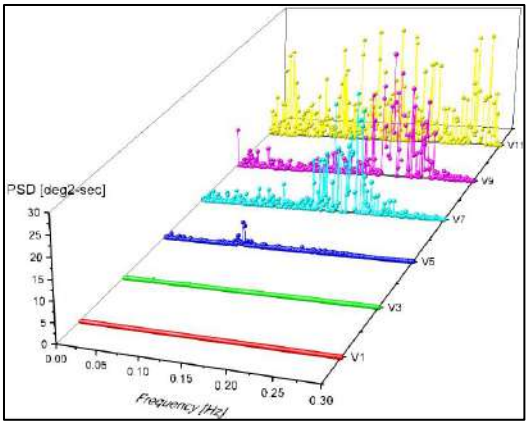

Yaw of the TLP alone for θ=0°

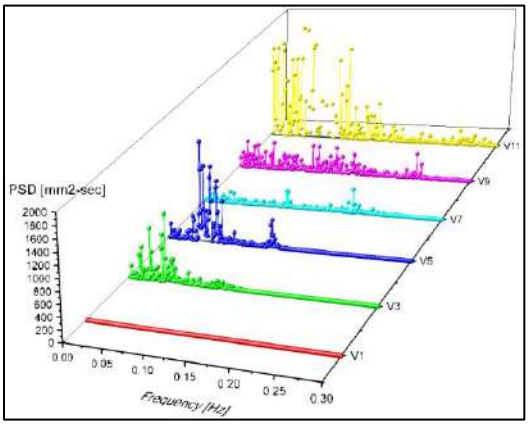

Sway of the TLP alone for θ=45°

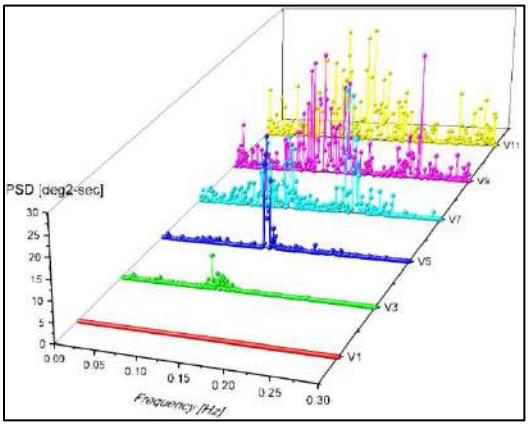

Yaw of the TLP alone for θ=45°

Figure 6.28 Power Spectral Density (PSD) of the motions of the TLP alone as functions of frequency and reduced velocity for θ = 0° and 45°

6.6.2 TAD Alone

The results of VIM tests for the TAD alone are discussed below. For this case, three angles of attack and eleven current velocities were considered.

Figures 6.29 and 6.30 present the nominal and maximum A/D responses for Sway, respectively. The motions developed by the TAD are considerably smaller than those of the TLP.

Previous studies, e.g. [95], have demonstrated that the length of the column is a relevant parameter to determine the order of the magnitude of the motion amplitude developed by a multi-column floater, i.e., floaters with smaller column lengths

develop smaller motion amplitudes. Note that, the column length of the TLP is approximately 3.4 times the column length of the TAD.

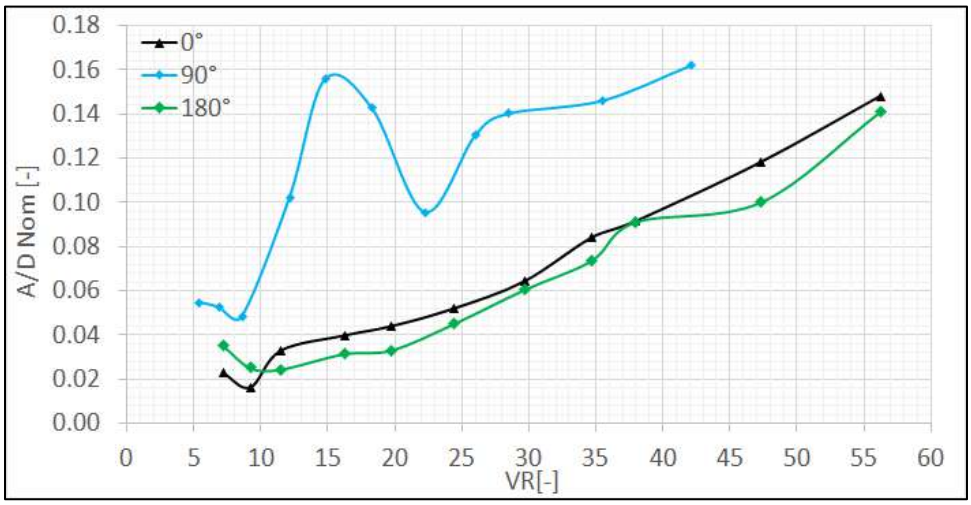

Figure 6.29 Nominal A/D for TAD alone and several current angles of incidences: 0°, 90°, and 180°

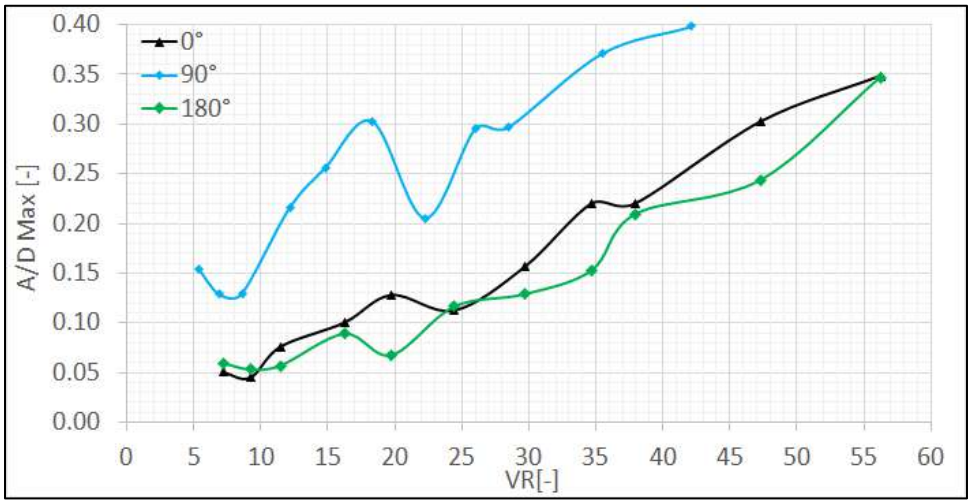

Figure 6.30 Maximum A/D for TAD alone and several current angles of incidences: 0°, 90°, and 180°

The amplitudes and trends in Sway motion at 0° and 180° are similar. Moreover, these motions increase steadily with the reduced velocity. This trend indicates that the TAD develops galloping instabilities with small amplitudes. The response of the TAD at 90° presents slightly higher amplitudes. However, the response is still considerably

smaller than that of the TLP. Despite some variations, the amplitude of the motions increases steadily with the current.

Figure 6.31 presents the maximum Yaw response for the TAD. Note that, the maximum angle reached by the TAD is approximately 2.7°, far from the 7.5° achieved by the TLP. In addition, for 0° and 180°, the amplitude of the Yaw motions seems to increase with the current velocity until $V_R = 35$, after which it slowly decreases. Finally, Yaw motion at 90° only increases with the velocity.

In general, no significant differences between the behavior of the TAD observed were found at 0° and 180°. Moreover, the motions developed by the TAD at 90° are significantly higher.

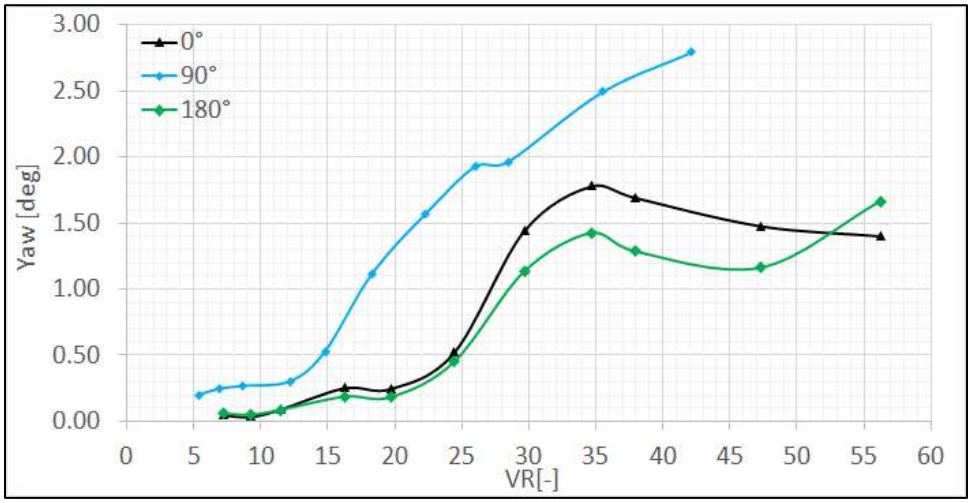

Figure 6.31 Maximum Yaw response for TAD alone and several current angles of incidences: 0°, 90°, and 180°

Figure 6.32 presents trajectory plots of the horizontal motions of the TAD alone considering six velocities and one angle of attack. Note that, the Sway and Yaw motions developed by the TAD are small relative to the size of the platform. In addition, it is noticeable that the motions increase with the reduced velocity.

Figure 6.33 presents the analysis of the motions developed by the TAD in the frequency domain for angles of attack of 0° and 180°. The Power Spectral Density (PSD) reveals that Sway motions developed by the TAD mainly occur at low

frequencies; the higher peaks occur at frequencies lower than 0.0045 Hz, which is the Sway natural frequency.

However, for Yaw motions, it is notable that the PSD does not present peaks and has a uniform distribution of energy with respect to frequency.

In addition, no relevant differences between the behavior of the TAD at 0° and 180° are observed.

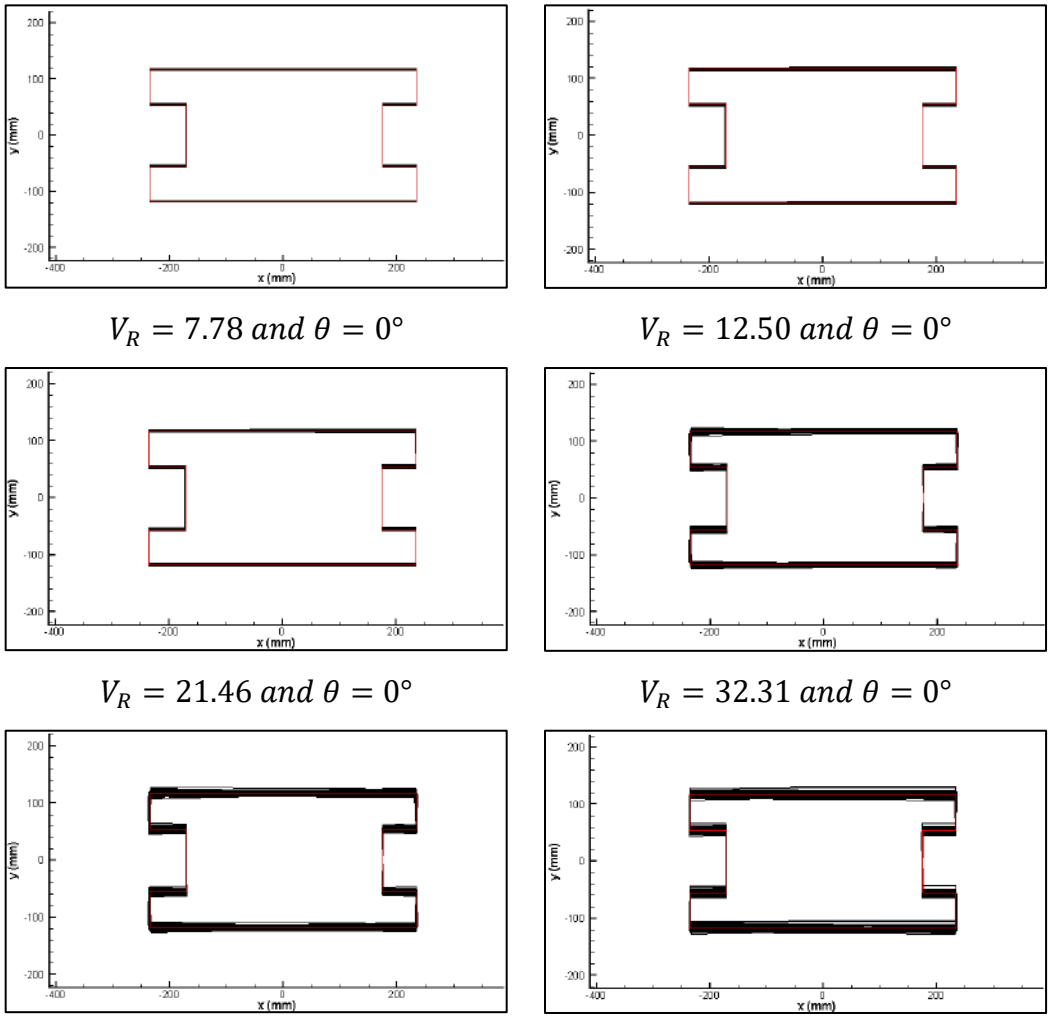

$V_R = 7.78\ and\ \theta = 0°$ $V_R = 12.50\ and\ \theta = 0°$

$V_R = 21.46\ and\ \theta = 0°$ $V_R = 32.31\ and\ \theta = 0°$

$V_R = 41.27\ and\ \theta = 0°$ $V_R = 61.08\ and\ \theta = 0°$

Figure 6.32 Trajectory plots of the motions of the TAD alone in the XY plane for θ=0° and different reduced velocities.

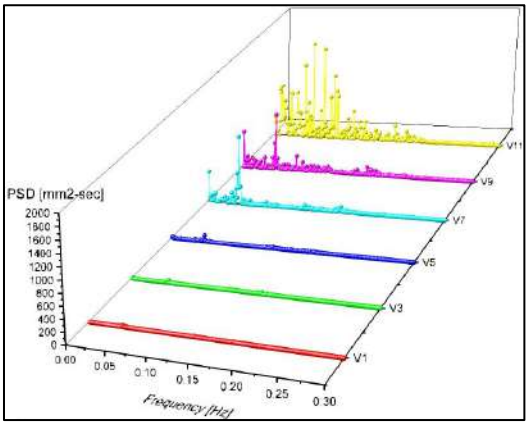

Sway of the TAD alone for θ=0°

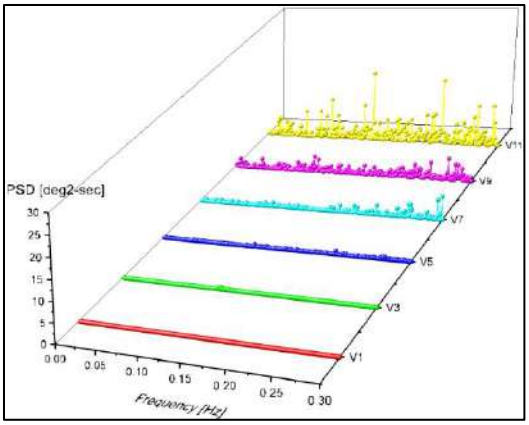

Yaw of the TAD alone for θ=0°

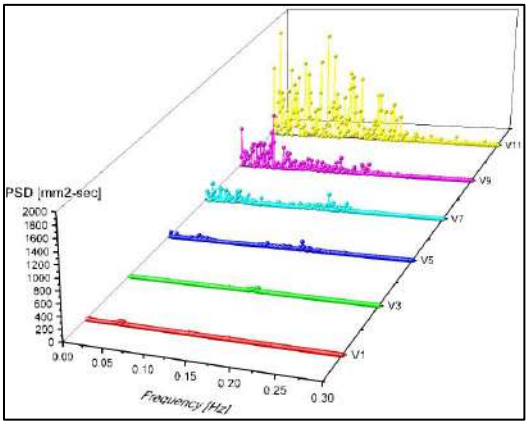

Sway of the TAD alone for θ=180°

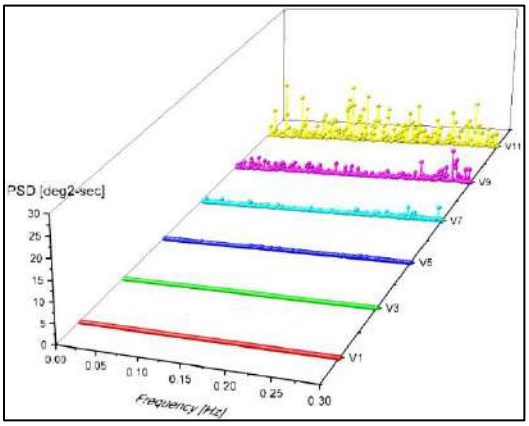

Yaw of the TAD alone for θ=180°

Figure 6.33 Power Spectral density of motions of the TAD alone as functions of frequency and reduced velocity for θ = 0° and 180°.

6.6.3 Multi-body System without Connection

In this section, the experimental results of the VIM tests with both floaters without a mechanical connection are presented. With the aim of investigating the influence of the distance and the relative positions between the floaters, two cases were considered: TLP upstream and TLP downstream. In each of these cases, three different distances between the floaters were considered. The distances are the same as those adopted in the analysis of current loads in Chapter V. See Table 5.5 and Fig. 6.18.

Figure 6.34 presents the nominal A/D, maximum A/D and maximum Yaw responses of the TLP in upstream and downstream positions for three different distances D1, D2, and D3. For a better comparison, the results for the TLP alone are

depicted together. Despite small variations, the results of the multi-body analysis with the TLP upstream and downstream did not present evidence of the influence of the distance between the TLP and the TAD on the motions of TLP.

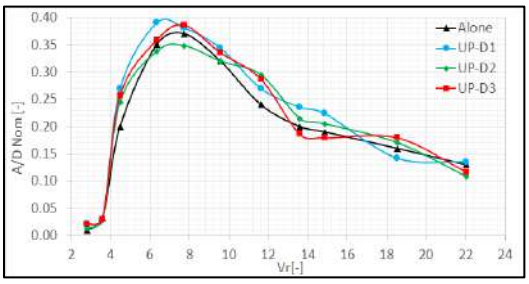

Nominal A/D for the TLP upstream

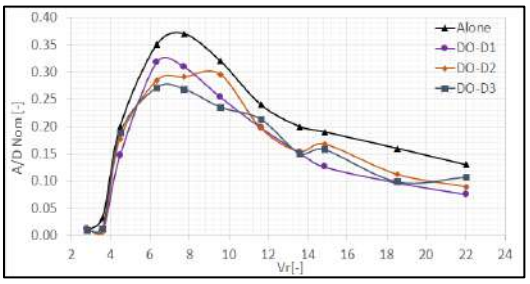

Nominal A/D for the TLP downstream

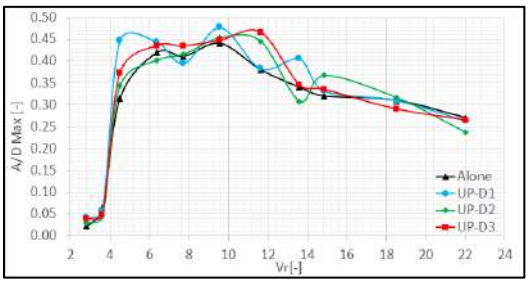

Maximum A/D for the TLP upstream

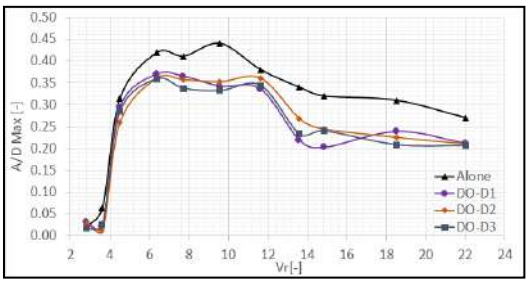

Maximum A/D for the TLP downstream

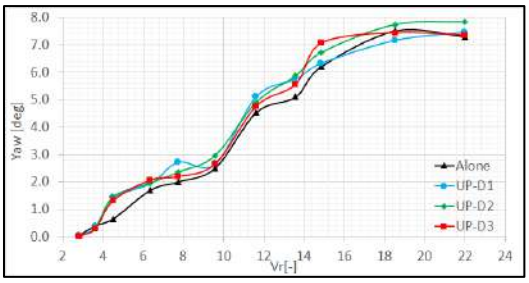

Maximum Yaw for the TLP upstream

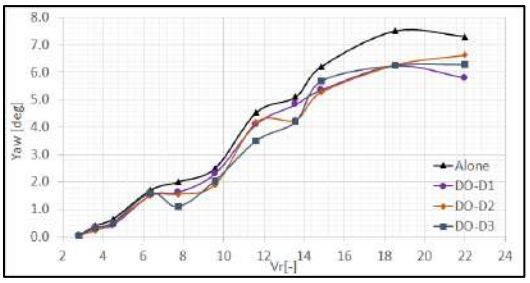

Maximum Yaw for the TLP downstream

Figure 6.34 Nominal A/D, maximum A/D and maximum Yaw responses for the TLP upstream and downstream from multi-body VIM tests with no connection between the floaters.

In general, the motions of the TLP upstream were slightly larger than those observed on the TLP alone. This effect is larger for the maximum A/D coefficient in the range of reduced velocities [4 - 14]. In contrast, the results from the tests with the TLP downstream were systematically lower than the results for the TLP alone, in terms of the motion amplitudes. Note that the differences between the TLP upstream

and TLP alone were considerably smaller than the differences between the TLP downstream and TLP alone. However, in both cases, the TLP upstream and TLP downstream cases, the trends of the curves are the same. Figure 6.35 presents trajectory plots of the horizontal motions of the TLP, comparing the single-body and multi-body cases with the TLP upstream and downstream.

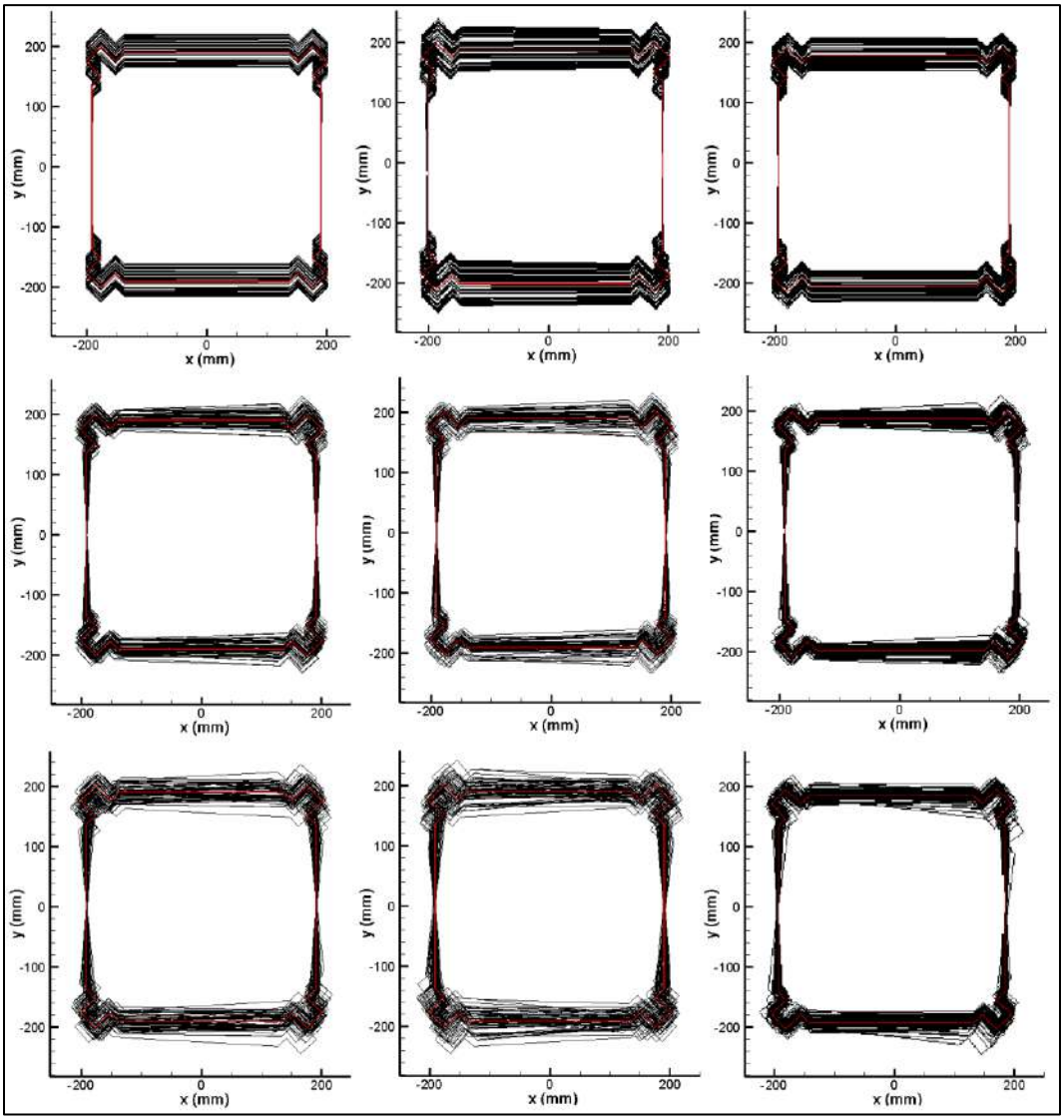

Figure 6.35 Trajectory plots of the motions of the TLP in the XY for cases alone, upstream and downstream without a mechanical connection. From left to right: TLP alone, TLP upstream and TLP downstream. From top to bottom: V3, V7, and V11.

The information presented in the XY plots is consistent with the statistical analysis. In general, while the motions with the TLP upstream are slightly higher than those with the TLP alone, the motions of the TLP downstream decrease slightly relative to those of the single-body case.

Figure 6.36 presents the analysis of the motions developed by the TLP in the frequency domain with the PSD for cases of TLP alone, TLP upstream and TLP downstream. The Power Spectral Density (PSD) confirms that the influence of the presence of the TAD on the behavior of the TLP is relatively small. Despite some minor variations, the distribution of the energy in frequency is essentially the same for the three cases. The resonance motions are observed for low reduced velocities, and as the current velocity increases, the spreading of the energy increases as well.

In the case of the TAD, the same cases are analyzed, thus, the TLP upstream test provides the information for the TAD downstream case, similarly, the TLP downstream case is now analyzed as the TAD upstream case, focusing on the motions developed by the TAD unit and how these motions are affected by the presence of the TLP hull. Figure 6.37 presents the nominal A/D, maximum A/D and maximum Yaw responses of the TAD in upstream and downstream positions for the three different distances (namely, D1, D2, and D3). In addition, the results for the TAD alone are depicted together. The results of the multi-body VIM tests show less influence of the TLP on the behavior of the TAD. However, as in the case of the TLP, the TAD presents slightly higher and lower movements for the upstream and downstream positions, respectively.

Furthermore, the relative distances between the floaters do not significantly influence the motions of the TAD unit. The most significant variations appear for Yaw motions of the TAD when it is in the downstream position in the range of [26 – 46] of reduced velocities.

In general, the motions of the TAD upstream were slightly higher than those observed for the TAD alone. In contrast, the results from the tests with the TAD downstream were systematically lower than the results of the TAD alone, in terms of the motion amplitudes. In addition, it is important to mention, that the trends of the curves are not modified by the presence of the TLP.

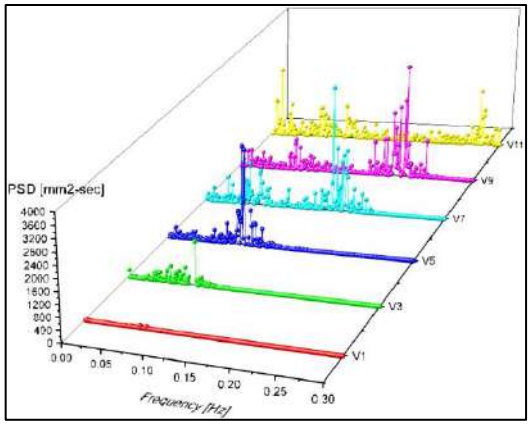

Sway of the TLP alone for θ=0°

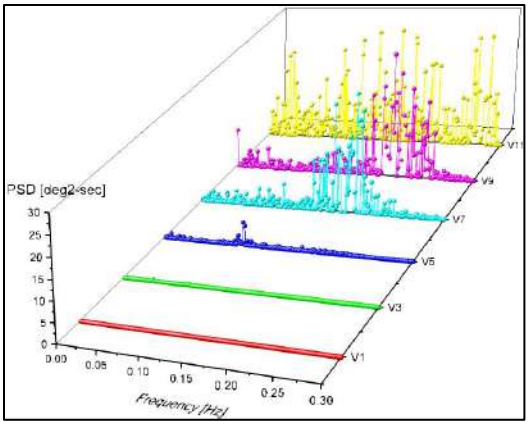

Yaw of the TLP alone for θ=0°

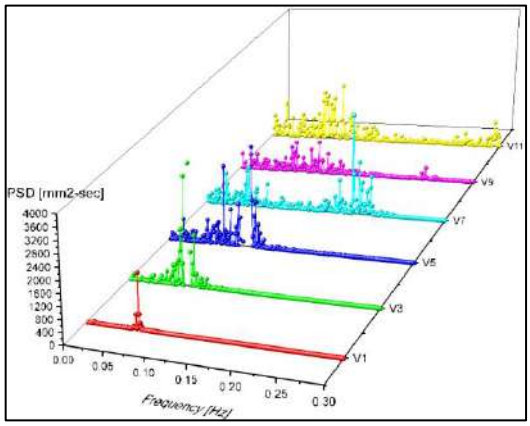

Sway of the TLP upstream

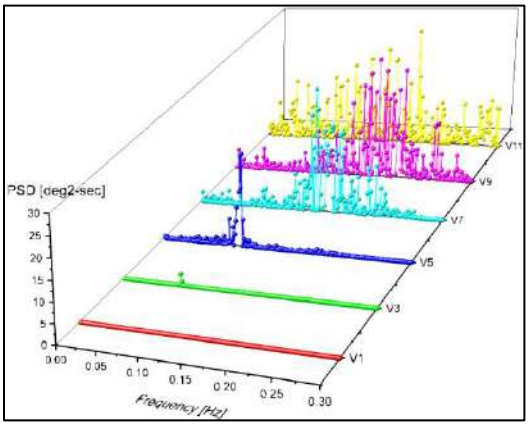

Yaw of the TLP upstream

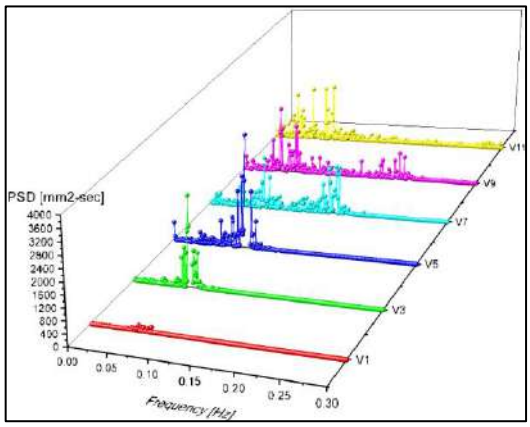

Sway of the TLP downstream

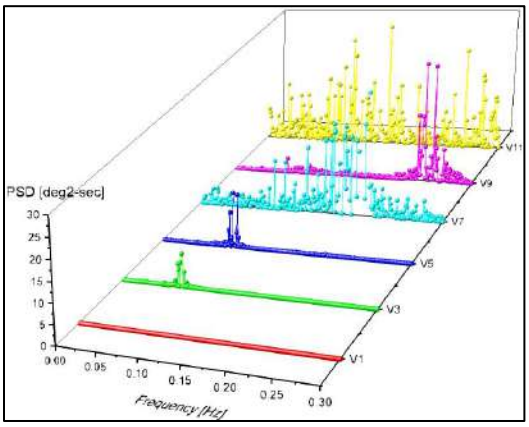

Yaw of the TLP downstream

Figure 6.36 Power Spectral Density (PSD) of the TLP motions for cases alone, upstream and downstream as functions of frequency and reduced velocity from multi-body VIM tests with no connection between the floaters.

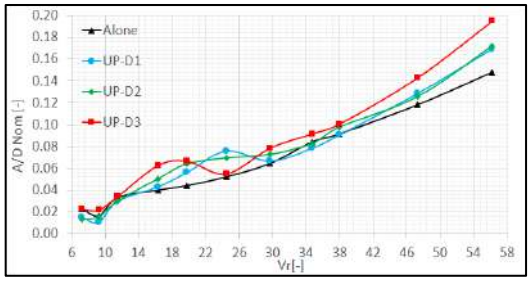

Nominal A/D for the TAD upstream

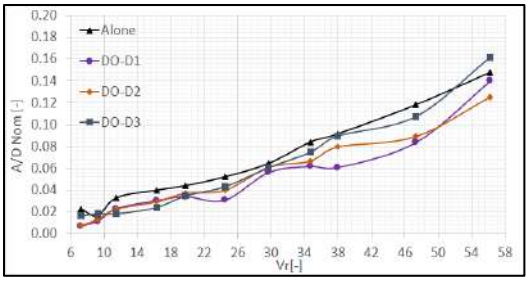

Nominal A/D for the TAD downstream

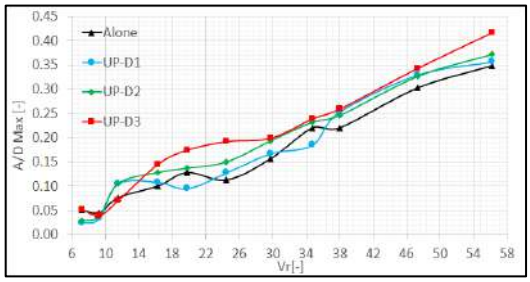

Maximum A/D for the TAD upstream

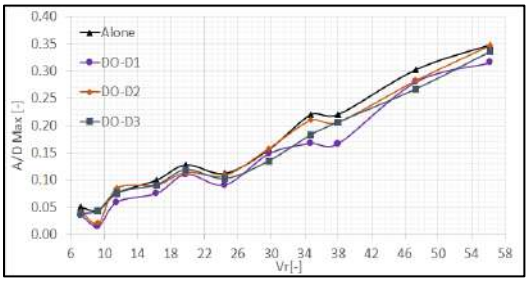

Maximum A/D for the TAD downstream

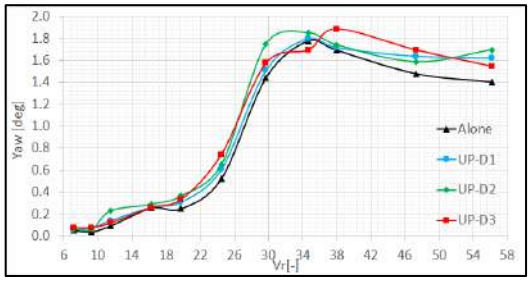

Maximum Yaw for the TAD upstream

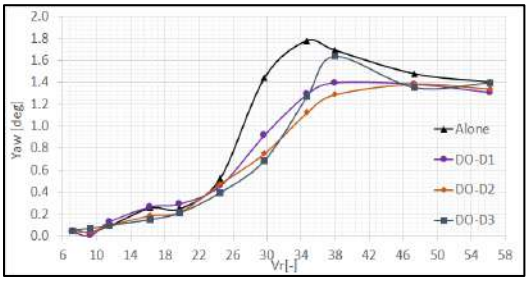

Maximum Yaw for the TAD downstream

Figure 6.37 Nominal A/D, maximum A/D and maximum Yaw responses for TAD upstream and downstream from multi-body VIM tests with no connection between the floaters.

Figure 6.38 presents the analysis of the motions developed by the TAD in the frequency domain with the PSD for cases TAD alone, TAD upstream and TAD downstream. The Power Spectral Density (PSD) confirms that the influence of the presence of the TLP on the behavior of TAD is minuscule. As in the case of TLP, the variations in the energy distribution in the frequency of both motions, Sway and Yaw, were small.

Figure 6.39 presents trajectory plots of the horizontal motions of the TAD, comparing the single-body and multi-body cases, with the TAD upstream and

downstream. No significant differences are found in the movements of three cases for low reduced velocities; however, for the highest velocities, these differences are large, particularly for the velocity V11 in Table 6.10.

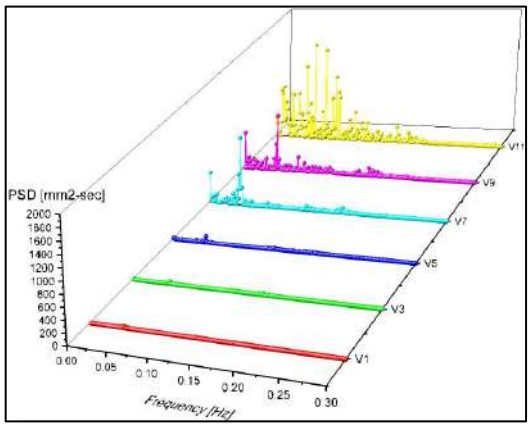

Sway of the TAD alone for θ=0°

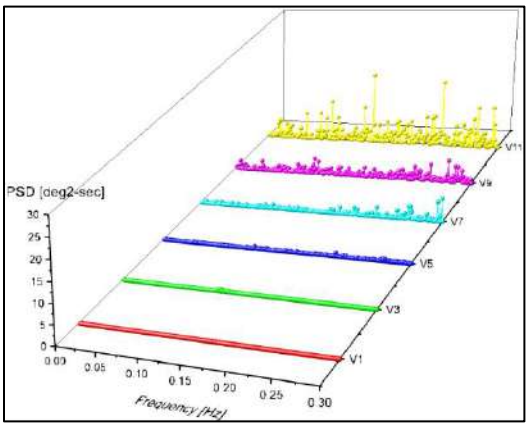

Yaw of the TAD alone for θ=0°

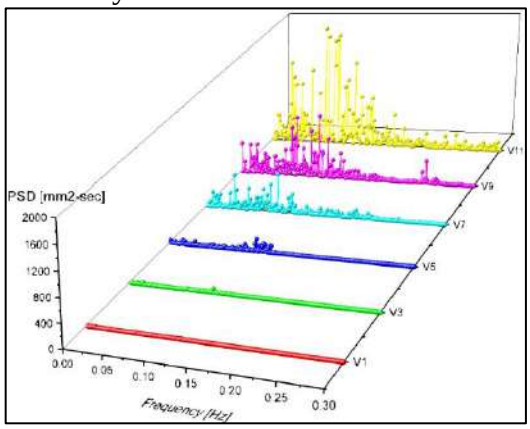

Sway of the TAD upstream

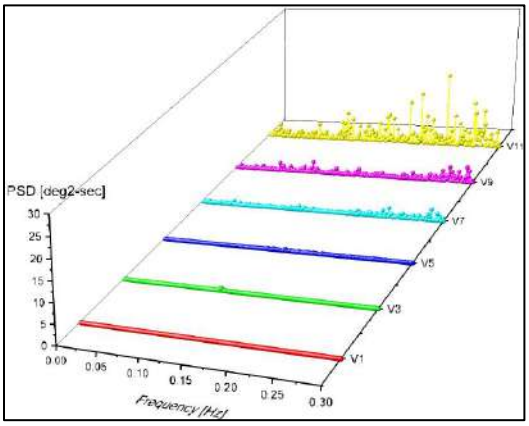

Yaw of the TAD upstream

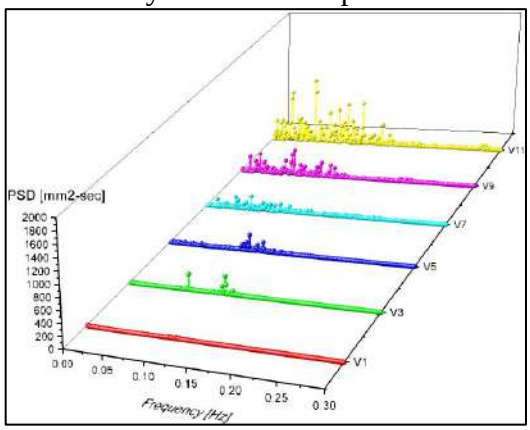

Sway of the TAD downstream

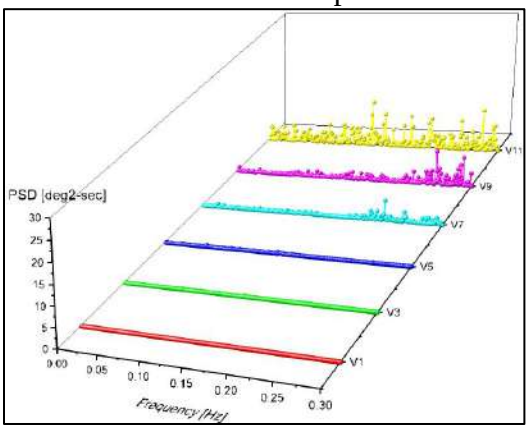

Yaw of the TAD downstream

Figure 6.38 Power Spectral Density (PSD) of the TAD motions for cases alone, upstream and downstream as functions of frequency and reduced velocity from multi-body VIM tests with no connection between the floaters.

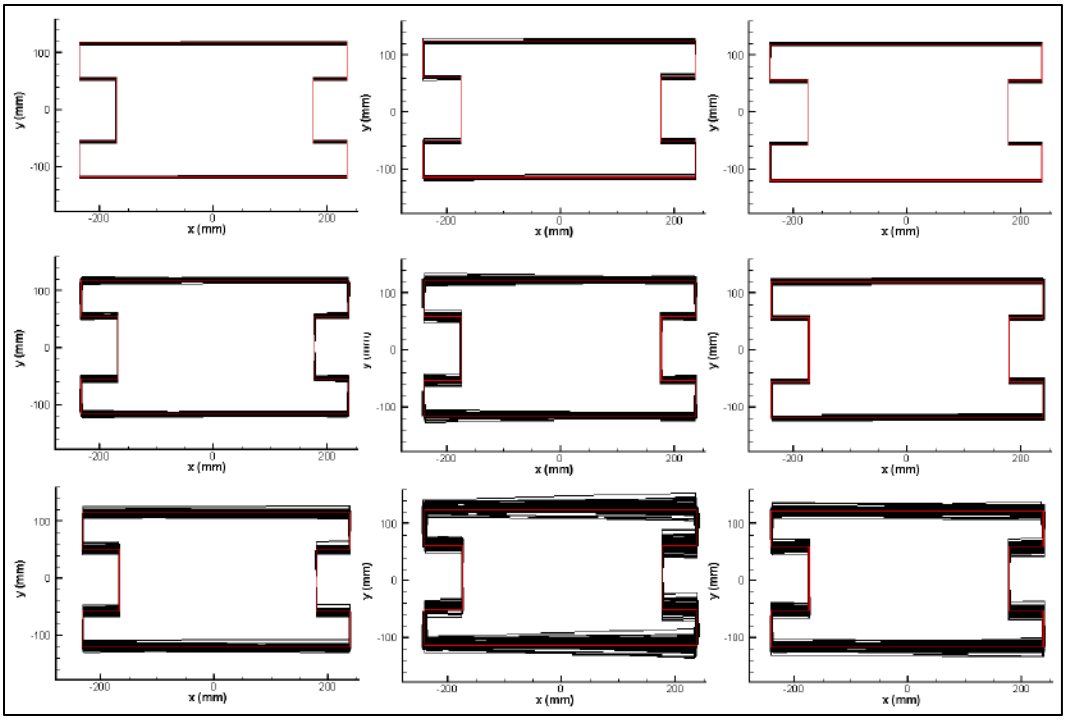

Figure 6.39 Trajectory plots of the motions of the TAD in the XY plane for cases alone, upstream and downstream without a mechanical connection. From left to right: TAD alone, TAD upstream and TAD downstream. From top to bottom: V3, V7, and V11.

6.6.4 Multi-body System with Hawser Systems

In this section, the experimental results of the VIM tests with both floaters connected by the hawser system are presented. With the aim of investigating the influence of the relative positions between the floaters, two cases were considered: TLP upstream and TLP downstream. In addition, four configurations of the hawser systems were tested. Details of the hawser configurations are presented in Section 6.3.3.

Figure 6.40 presents the nominal A/D, maximum A/D and maximum Yaw responses of the TLP in upstream and downstream positions for the four different hawser configurations HW1, HW2, HW3, and HW4. For a better comparison, the results for the TLP alone are depicted together.

A comparison of the behavior of the TLP alone with the TLP upstream and downstream reveals that the movements of the TLP, when it is connected to the TAD,

are smaller than in the single-body case. However, while the motions of the TLP upstream are slightly smaller, in the case of the TLP downstream, they are significantly lower. In addition, the trends of the curves of the three cases are similar. Furthermore, the variations between the different hawser configurations are small relative to the comparison with the variations between the single-body and multi-body cases.

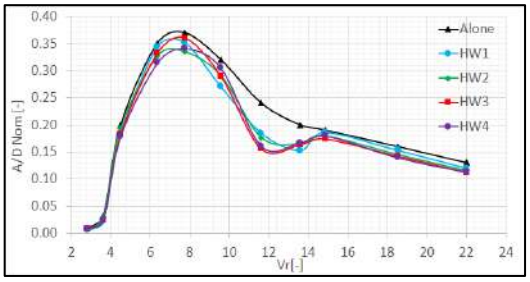

Nominal A/D for the TLP upstream

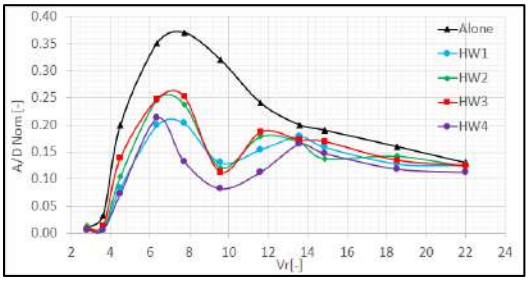

Nominal A/D for the TLP downstream

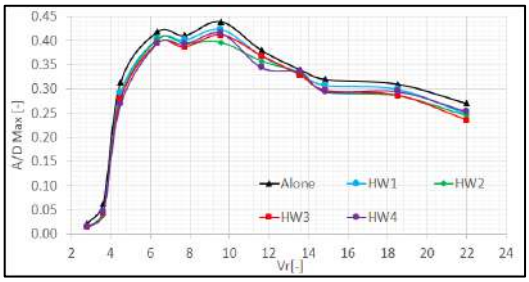

Maximum A/D for the TLP upstream

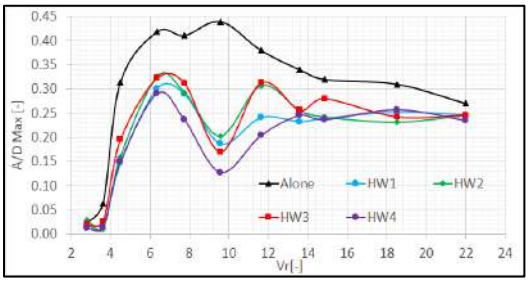

Maximum A/D for the TLP downstream

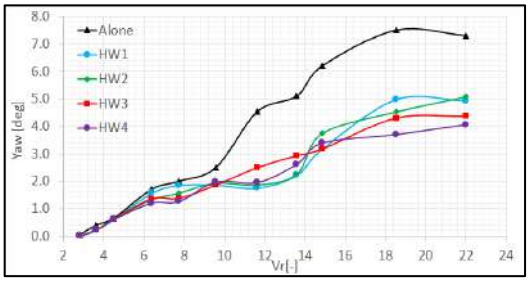

Maximum Yaw for the TLP upstream

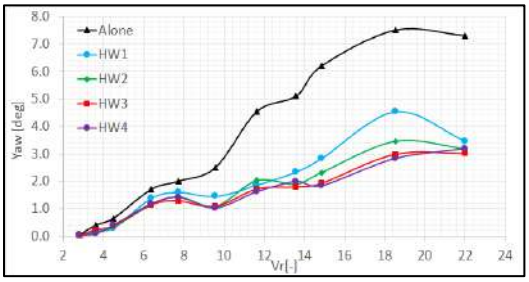

Maximum Yaw for the TLP downstream

Figure 6.40 Nominal A/D, maximum A/D and maximum Yaw responses for TLP upstream and downstream from multi-body VIM tests with the hawser system connecting the floaters.

Figure 6.41 presents trajectory plots of the horizontal motions of the TLP, comparing the single-body and multi-body cases connected by the hawser systems.

The trajectory plots show that the TLP downstream presents a significant reduction in both Sway and Yaw. In contrast, the differences between the TLP upstream and the TLP alone are considerably smaller.

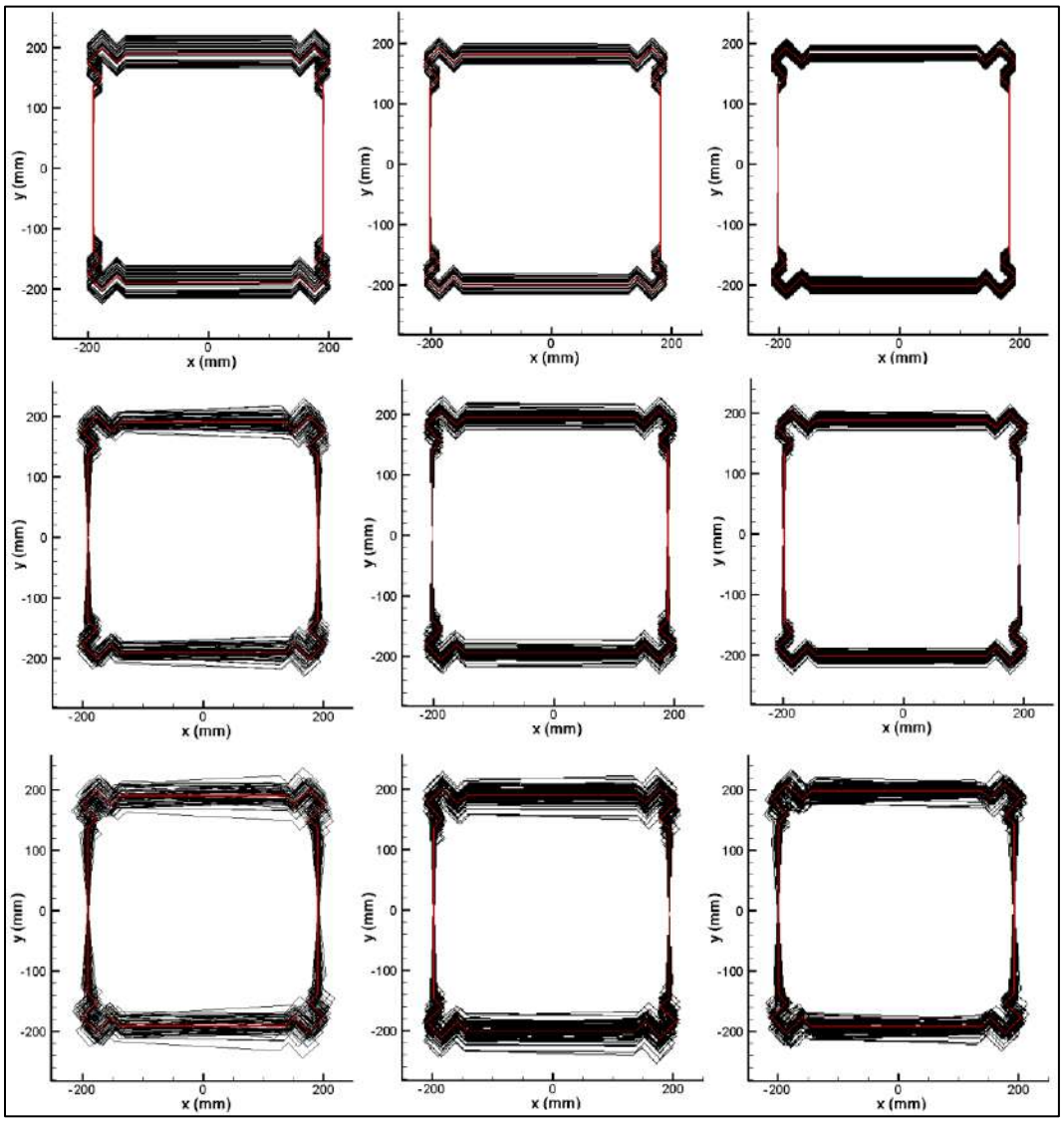

Figure 6.41 Trajectory plots of the motions of the TLP in the XY plane for cases alone, upstream and downstream with the hawser system HW1. From left to right: TLP alone, TLP upstream and TLP downstream. From top to bottom V3, V7, and V11.

Figure 6.42 presents the analysis of the motions developed by the TLP in the frequency domain with the PSD for cases TLP alone, TLP upstream and TLP downstream with the hawser systems HW1 connecting the floaters.

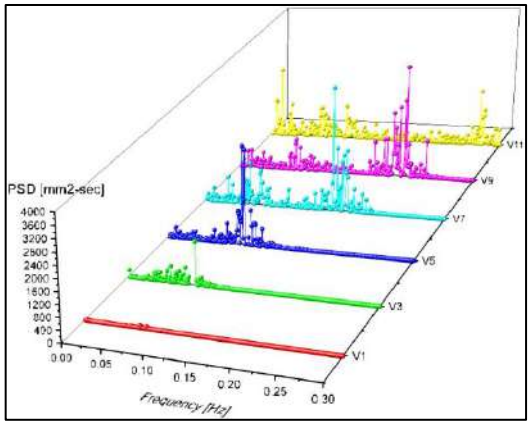

Sway of the TLP alone for θ=0°

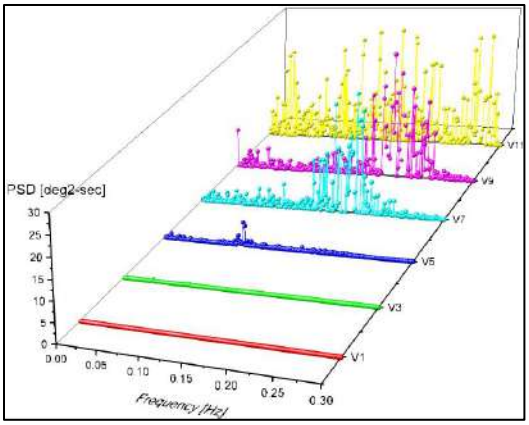

Yaw of the TLP alone for θ=0°

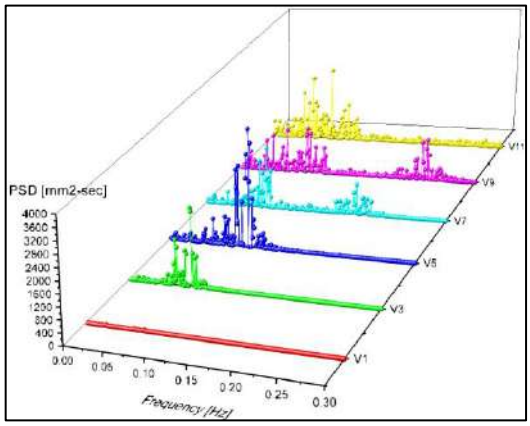

Sway of the TLP upstream

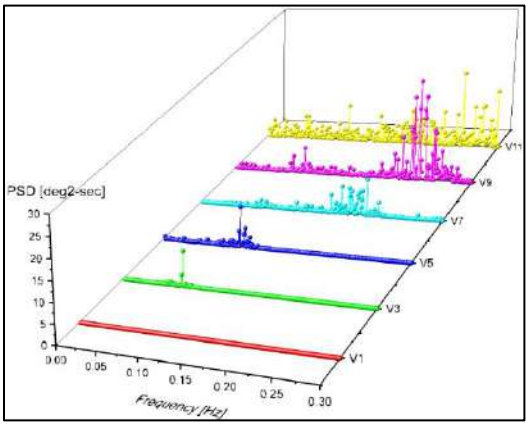

Yaw of the TLP upstream

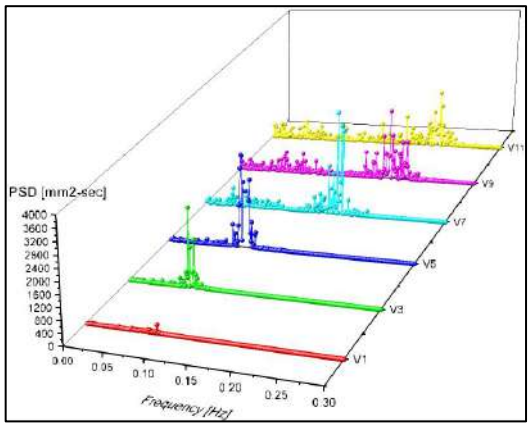

Sway of the TLP downstream

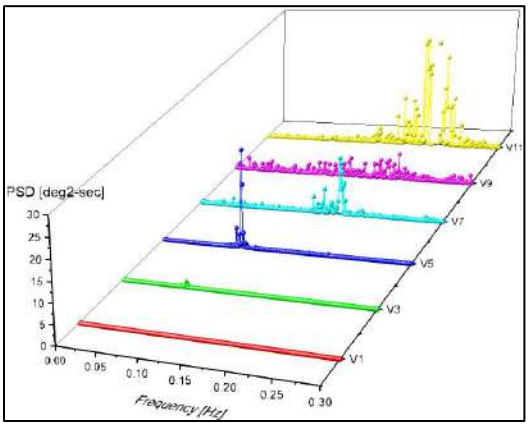

Yaw of the TLP downstream

Figure 6.42 Power Spectral density of motions of the TLP alone, upstream and downstream as functions of frequency and reduced velocity from multi-body VIM tests with the hawser system HW1 connecting the floaters.

Although the hawser systems present a strong influence on the order of magnitude of the motions developed by the floaters, no evidence exists that the hawser systems modify the trends of the curves. In addition, the Power Spectral Density (PSD) reveals small variations in the distribution of the energy in the horizontal modes of the TLP. The order of magnitude of the PSD varies because of the lower motion amplitudes. However, no significant differences were found in the frequency distribution between the alone, upstream and downstream cases.

Finally, this extensive study includes the analysis of the TAD and how the presence of the TLP and the hawser system modify its behavior with respect to the single-body case. Thus, Fig. 6.43 presents trajectory plots of the horizontal motions of the TAD, comparing the single-body and multi-body cases connected by the hawser systems HW1. In general, the motions of the TAD increase significantly. The motions of the TAD downstream present the highest variation, for both Sway and Yaw.

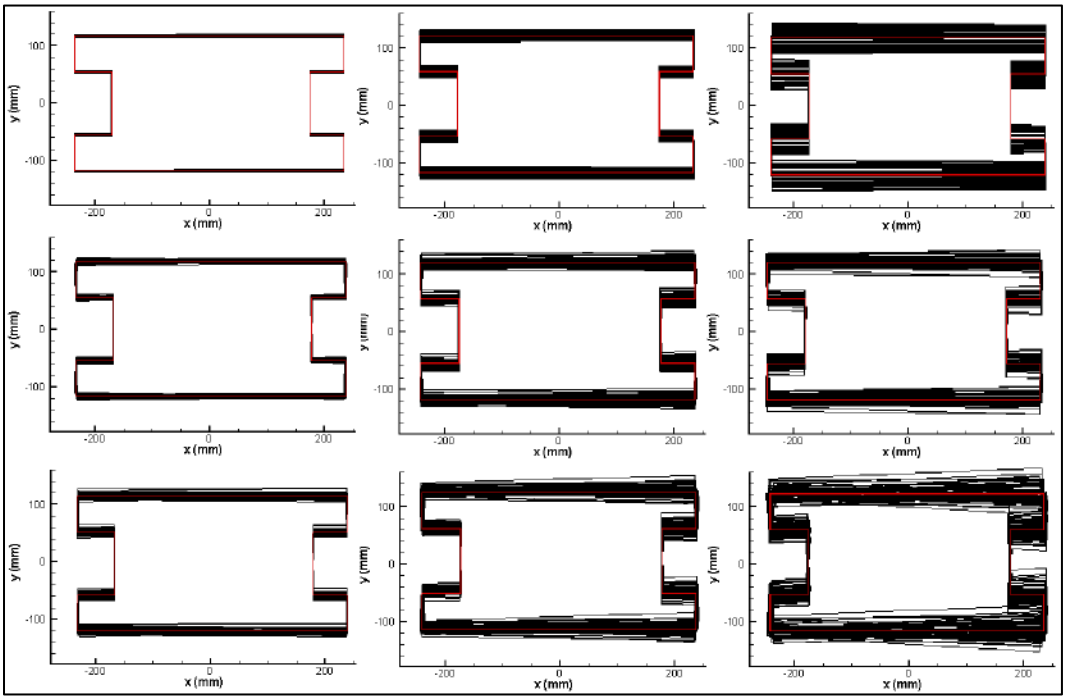

Figure 6.43 Trajectory plots of the motions of the TAD in the XY plane for cases alone, upstream and downstream with the hawser system HW1. From left to right: TAD alone, TAD upstream and TAD downstream. From top to bottom V3, V7, and V11.

Figure 6.44 presents the nominal A/D, maximum A/D and maximum Yaw responses of the TAD in upstream and downstream positions for the four different hawser configurations HW1, HW2, HW3, and HW4. For a better comparison, the results of TAD alone are depicted together. A comparison of the behavior of the TAD alone with the TAD upstream and downstream reveals that the movements of the TAD, when it is connected to the TLP, are significantly higher than for the TAD alone. These variations involve not only the order of magnitude of the motions of the TAD but also the trends of the response for Sway.

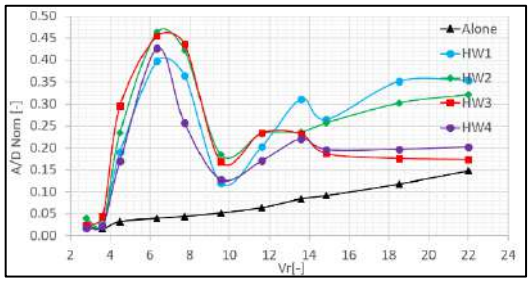

Nominal A/D for the TAD upstream

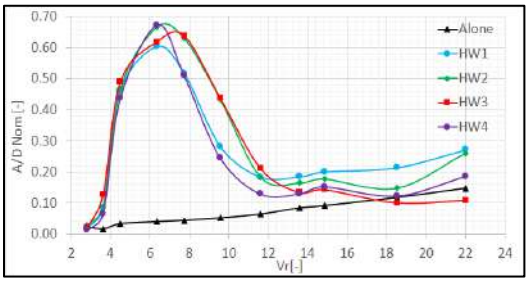

Nominal A/D for the TAD downstream

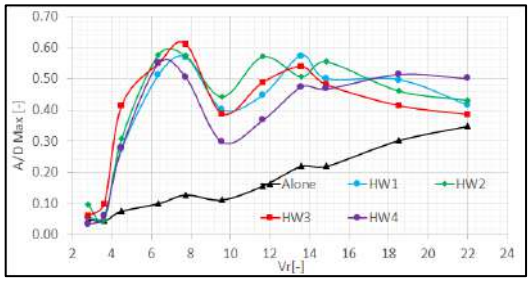

Maximum A/D for the TAD upstream

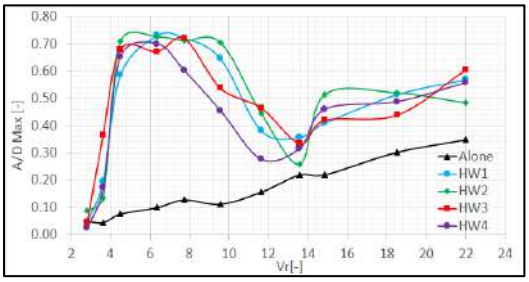

Maximum A/D for the TAD downstream

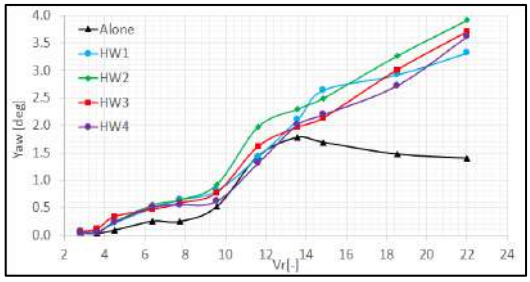

Maximum Yaw for the TAD upstream

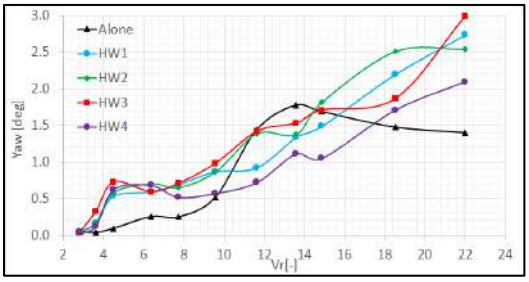

Maximum Yaw for the TAD downstream

Figure 6.44 Nominal A/D, maximum A/D and maximum Yaw responses for the TAD upstream and downstream from multi-body VIM tests with a hawser system connecting the floaters.

An analysis of the nominal and maximum A/D of the motion developed by the TAD reveals that the shapes of these curves are consistent with the motions of the TLP. This finding indicates that the TLP induces these larger motions on the TAD.

However, as shown in Section 6.7.3, the TLP does not induce significant motions on the TAD when a mechanical coupling does not connect the two units. Consequently, it is possible to conclude that the mechanical connection between the floaters is the largest generator of these induced motions.

Furthermore, the response of the TAD using different configurations of the hawser systems that connect this unit with the TLP shows that the impact of the configuration of the hawsers is limited.

Another important observation corresponds to the Yaw motion is that the variations in this mode are considerably smaller than those observed for Sway. However, for the TAD upstream case, the four configurations of the hawser system present significant amplitudes for reduced velocities in the range of [12 – 22]. In contrast, the TAD downstream case does not present this substantial increase in the angular amplitudes of motion.

Figure 6.45 presents the analysis of the motions developed by the TAD in the frequency domain with the Power Spectral Density (PSD) for cases of TAD alone, TAD upstream and TAD downstream.

The PSD confirms that the influence of the presence of the TLP connected by the hawser systems is significantly higher, not only in terms of the order of magnitude of the energy but also in the frequencies at which the response peaks. In addition, the differences increase with the velocity, i.e., the peaks for the velocities V9 and V11 present significant differences not only between the single-body and multi-body cases but also among the multi-body cases. The TAD upstream presents higher peaks at low-frequencies while the TAD is downstream presents peaks at high-frequency.

For Yaw motion of the TAD, the results show that the differences between the results for the upstream and downstream cases are small.

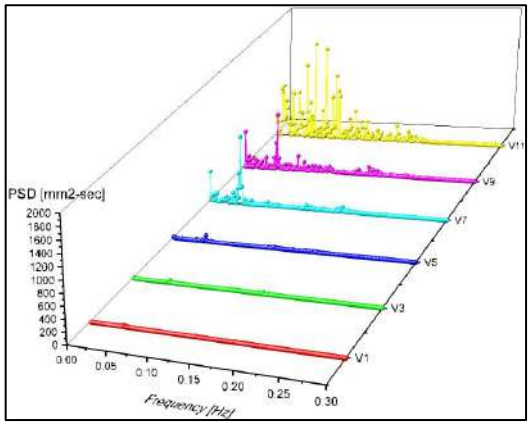

Sway of the TAD alone for θ=0°

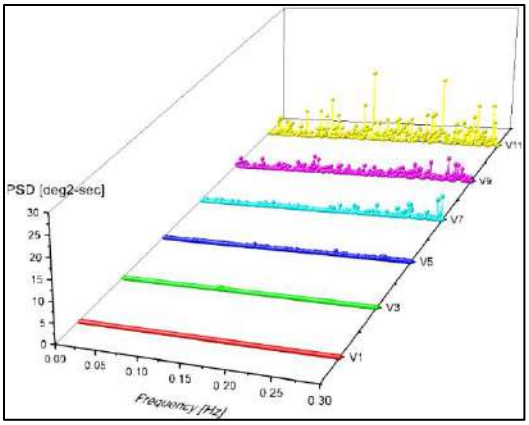

Yaw of the TAD alone for θ=0°

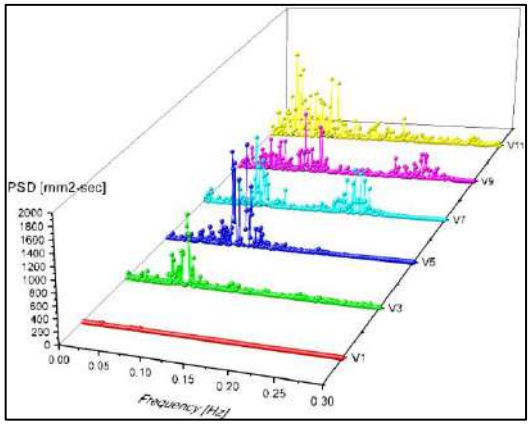

Sway of the TAD upstream

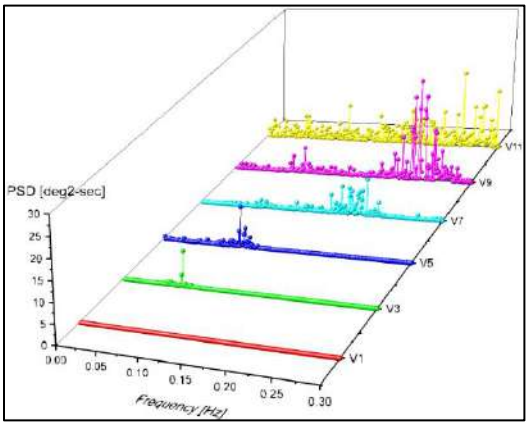

Yaw of the TAD upstream

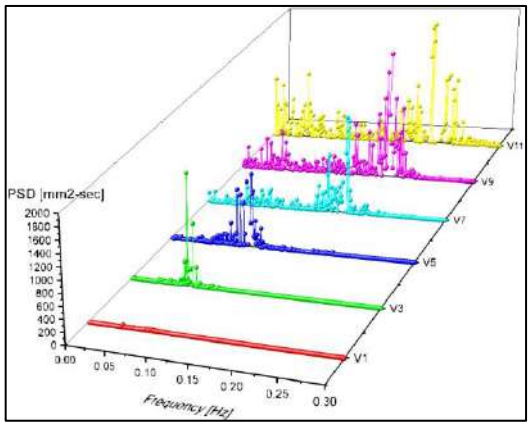

Sway of the TAD downstream

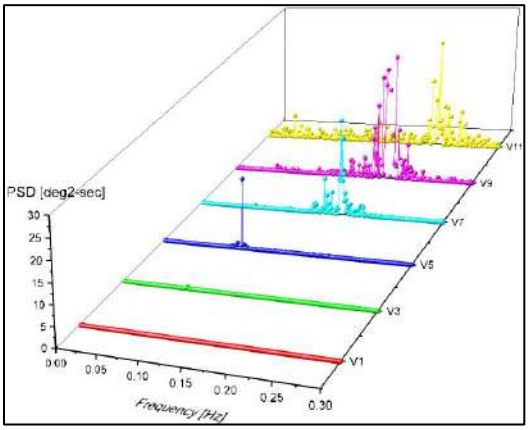

Yaw of the TAD downstream

Figure 6.45 Power Spectral density of motions of the TAD alone, upstream and downstream as a function of frequency and reduced velocity from multi-body VIM tests with the hawser system HW1 connecting the floaters.

6.7 CONCLUSIONS

Based on this extensive analysis of the current induced motions in the TLP-TAD multi-body system, the following conclusions are drawn:

- Although ultra-reduced scale models represent a significant challenge for calibration of the mass distribution, the position of the center of gravity and equivalent mooring systems, excellent results were achieved in the representation of these properties. Thus, experimental values of stiffness and natural periods for Sway and Yaw present excellent agreement with the target values. The arrangement for representing the TLP tendons has been shown as a powerful tool for the tests of deep draft TLPs in a shallow water channel.
- The experimental results present evidence that the current velocities and angles of attack have a strong influence on the dynamic behavior of the TLP. Thus, the TLP is susceptible to VIM and Galloping. For lower velocities and $\theta=0°$, VIM is predominant in the Sway response; and as the current velocity increases the TLP presents more galloping instabilities. For Yaw, the amplitude of the motion increases steadily with the current velocity, indicating galloping vibrations. For $\theta=45°$ the Sway motion presents a combination of VIM with galloping. An analysis in frequency domain reveals that Galloping is predominant for this angle of attack. In the case of Yaw, the motions increase steadily with the current velocity as well.
- The results of the tests with the TAD unit reveal that the semi-submersible develops relatively small motions for the whole range of current velocities. Yaw seems to be the critical degree of freedom since it is slightly higher for high current velocities. The behavior of the TAD at $\theta=90°$ shows that the motions developed by the TAD are significantly greater than the motions at the other angles of attack. No significant differences exist between $\theta=0°$ and 180°.
- The results of the multi-body analysis without mechanical connection reveal the weak influence of hydrodynamic interactions of the floaters on the motions developed by the units. Systematically, the motions of the unit in the downstream position are slightly lower than those of the single-body case. In contrast, the motions of the unit in the upstream position present a slightly higher response. For all of the cases, the

distances between the floaters did not modify the amplitude of the motions significantly.

- The results of the multi-body analysis with the hawser systems reveal that the influence of the configuration of the hawser lines on the motions developed by the TLP and TAD is slight.
- The TLP connected to the TAD by the hawser system presents smaller amplitudes of motions than those of the TLP alone. This effect is larger for the TLP downstream, for which a significant mitigation of the motions is observed. The TAD presents an amplification of the motions with the TAD upstream and downstream, and the highest amplification was observed with the TAD downstream.
- Although no relevant differences in the motion amplitudes were found between the four hawser system configurations, the differences between the behavior of the floaters in the connected and disconnected cases are relatively large. Therefore, it is evident that the hawser system can modify the behavior of the floaters significantly, mitigating the motions developed by the TLP and amplifying the motions of the TAD.

CHAPTER VII. VIM MITIGATION DEVICES

An extensive experimental analysis of innovative solutions to mitigate the current induced motions of the TLP is presented. Four mitigation devices were built and tested. The analysis includes decay tests to determine the variations in natural frequencies and damping ratios, VIM tests with constant current velocity to measure the induced motions, and current load tests to determine the average drag forces and moments. Comparisons between the TLP alone and with mitigation devices are performed for this study.

7.1 INTRODUCTION

The TLP unit analyzed in this work develops significant motions when subject to currents. Although the presence of the TAD connected to the TLP by a hawser system slightly reduces these motions, the TLP induces large motions on the TAD. As shown in Section 6.6.1, these motions occur even for low reduced velocities. Therefore, the mitigation of the motions developed by the TLP could improve the dynamic performance of both the TLP and the multi-body system.

The mitigation devices are analyzed using three different types of tests. First, decay tests were conducted for Sway and Yaw to investigate possible variations in the natural periods and damping ratios of the system due to the mitigation devices.

Second, VIM tests were performed to measure the dynamic motions of the TLP when subject to current; eleven current velocities and two angles of attack were considered in this model test campaign. The results of these tests identify the most efficient device in terms of reducing the movements developed by the TLP. In addition, the frequency analysis of the time traces shows how the mitigation devices modify the frequency of the motions.

Third, current load tests were conducted to measure the average drag forces and moments on the TLP. The results of these tests show the relation between the magnitude of the drag forces and the motions developed by the TLP.

7.2 VIM MITIGATION DEVICES

In the literature, several devices to mitigate the VIM on Spars can be found. However, information is lacking on the mitigation of motions on TLPs or deep draft semi-submersibles. Figure 7.1 presents the most common mitigation devices used in the reduction of current induced motions in cylinders.

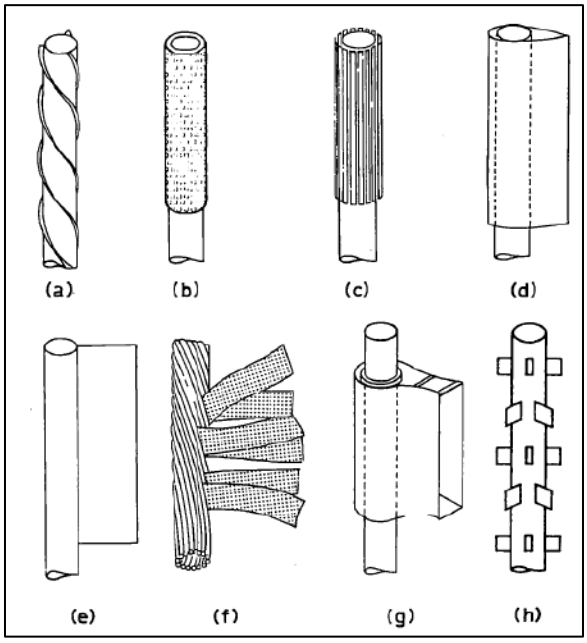

Figure 7.1 VIM mitigation devices for cylinders: (a) Helical strake, (b) Shroud, (c) Axial slats, (d) Streamlined fairing, (e) Splitter, (f) Ribboned cable, (g) Pivoted guiding vane, and (h) Spoiler plates [9]

Three of the VIM mitigation devices presented in Fig. 7.1 were adapted to the TLP square column. These are the shroud, the spoiler plates, and the helical strakes. In the case of the shroud, two configurations were tested, the first configuration with a square hole pattern and the second with a diamond hole pattern, as shown in Fig 7.2. Figure 7.3 presents the four VIM mitigation devices mounted on the TLP hull.

The mitigation devices were dimensioned by adapting the guidelines presented in [9], as summarized below.

Perforated shroud with square hole pattern:

- The length of the shroud side is 1.25 times the length of the TLP column side.

- The minimum depth of the shroud is equal to the distance between the top of the pontoon and the draft mark of operation.
- The shroud has 50 – 60% open area.
- The hole geometry is defined as squares with a side length equal to 0.073 times the TLP column side length.
- At least 15 holes are included in each row of the shroud face.

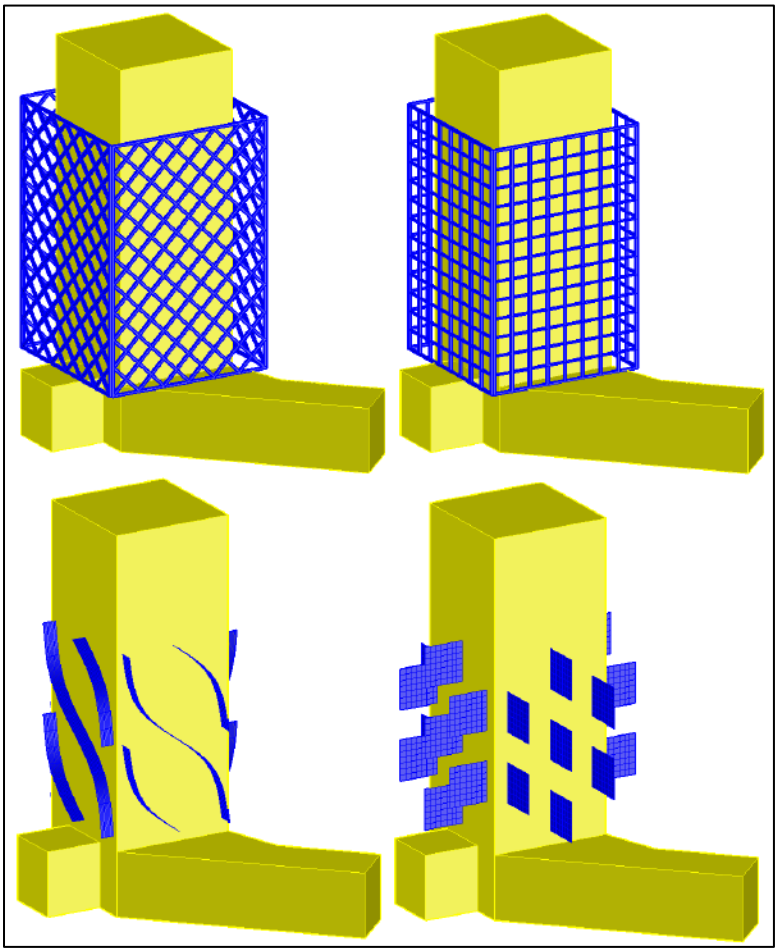

Figure 7.2 VIM mitigation devices for the TLP from left to right and from top to bottom: shroud with diamond holes, shroud with square holes, helical strakes, and spoiler plates.

Perforated shroud with diamond hole pattern:

- The length of the shroud side is 1.25 times the length of the TLP column side.

- The minimum depth of the shroud is equal to the distance between the top of the pontoon and the draft mark of operation.
- The shroud has 50 – 60% open area.
- The hole geometry is defined as diamonds with a side length equal to 0.066 times the TLP column side length.
- At least 16 holes are included in each row of the shroud face.

Helical strakes:

- The height of the strakes is 0.1 times the TLP column side length.
- Three strakes in a parallel helix pattern are used in each column face.
- The length of the strakes is equal to 0.5 to 1.0 times the TLP column side length.

Spoiler plates:

- The spoiler plate side has a length equal to 0.3 times the TLP column side length.
- Seven spoiler plates are used in each column face.
- The distance between the plates is equal to 0.4 times the TLP column side length.

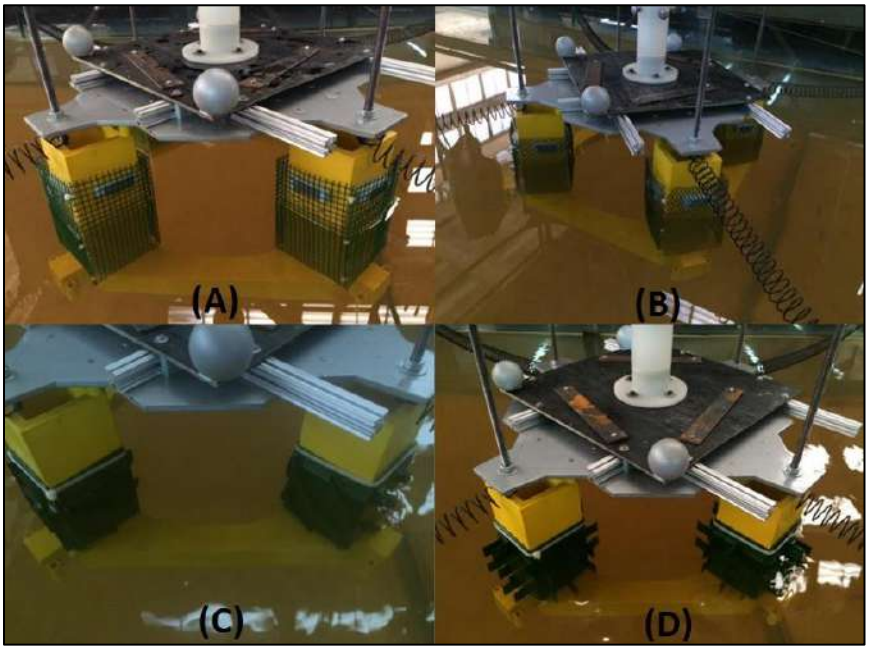

Figure 7.3 VIM mitigation devices for the TLP (A) shroud with square holes, (B) shroud with diamond holes, (C) helical strakes, and (D) spoiler plates.

7.3 DECAY TESTS

Decay tests were performed to measure the natural periods and to calculate the damping ratios of the TLP with the mitigation devices. Sway and Yaw were considered in the decay tests. Three repetitions for each mode were done for every configuration.

The decay tests started with a known static offset to the system, which is then released to oscillate freely. The oscillations are measured by the optical tracking system Qualisys [73]. The coordinate systems considered in the tests are described in Section 6.6.

Figure 7.4 and 7.5 present the decay tests for Sway and Yaw, respectively. The cases of the TLP alone, TLP with a shroud with diamond holes (SD), TLP with a shroud with square holes (SS), TLP with spoiler plates (SP), and TLP with strakes (ST) are depicted together.

The time traces were analyzed using the Fast Fourier Transform to estimate the natural periods of the oscillations. The damping was estimated by the method described in Appendix B.

Table 7.1 presents the summary of the natural periods and damping ratios for each configuration. Note that, the damping ratios are presented as percentages of the critical damping of each mode.

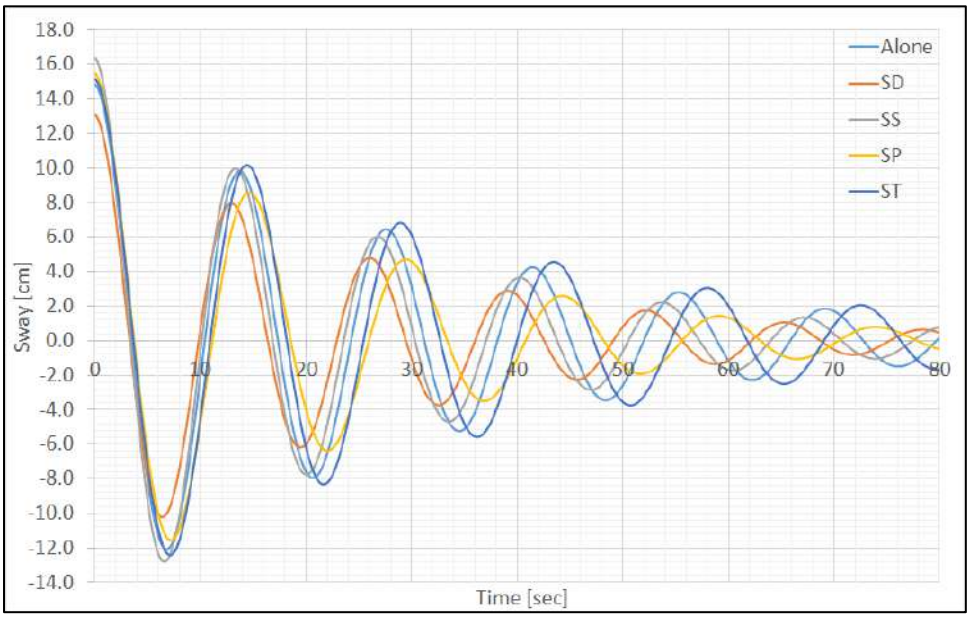

Figure 7.4 Decay tests for Sway of the TLP alone and the TLP with the mitigation devices.

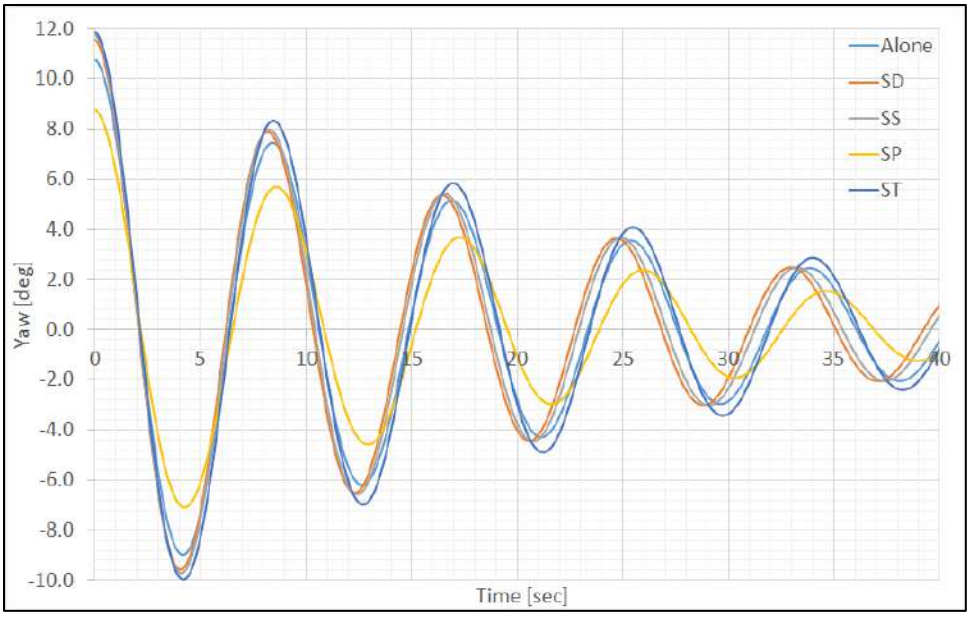

Figure 7.5 Decay tests for Yaw for the TLP alone and the TLP with the mitigation devices.

Table 7.1 Natural periods and damping ratios from decay tests.

Description	Natural periods [sec]		Linear damping ratios [%]	
	Sway	Yaw	Sway	Yaw
TLP alone	13.86	8.48	6.65	5.89
Diamond Shroud (SD)	13.08	7.25	8.03	6.13
Square Shroud (SS)	13.46	8.33	7.98	6.20
Spoiler Plates (SP)	14.82	8.68	9.51	6.94
Strakes (ST)	14.53	8.51	6.37	5.67

Based on these results, it is possible to conclude that the mitigation devices modify the natural periods and damping ratios of the TLP alone. However, the variations in the natural periods are relatively small, approximately ± 7.0% for Sway and ± 2.5% for Yaw. In contrast, the differences between the damping ratios of the mitigation devices are in the range of [-43% to 4%] for Sway and [-18% to 2.5%] for Yaw. Note that the spoiler plates present the highest damping ratio and natural periods, while strakes present the lowest damping ratios, and the shroud with diamond holes presents the lowest values for the natural periods.

7.4 VIM RESPONSE

This new experimental campaign was performed using the arrangement described in Section 6.5. The four VIM mitigation devices were tested one by one, using the same mooring system, current velocities and coordinate system reported in Chapter VI. Note that the inertia of the devices was neglected and kept the draft of the TLP constant. Two angles of attack were considered in this study: 0° and 45°.

Figure 7.6 presents a schematic representation of the experimental setup including the VIM mitigation devices. Note that, the devices were mounted directly on the columns of the TLP. Each test with a constant current velocity was repeated three times. Thus, 264 VIM tests were performed in the current channel of the LOC.

As described in Section 6.5, the VIM response of the TLP was measured using the Qualisys system [73]. As the current velocity is controlled by the RPM of four pumps, there is an interval of time in which the current velocity is "high-transient", and the final data analysis of the time traces considered only the "steady" part of the measurements, i.e., without the motions induced by the current velocity in the "high-transient" interval of time. The "steady" part of the measurements represents at least 3-hours of full-scale time in all tests.

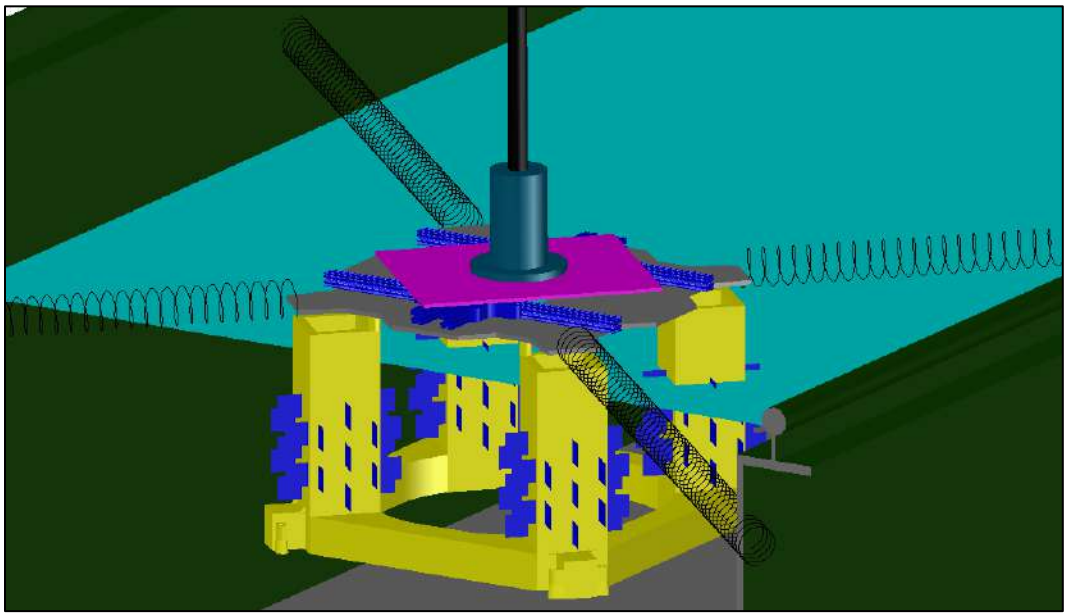

Figure 7.6 Experimental setup of VIM tests of the TLP using the mitigation devices. This figure shows the spoiler plates.

The VIM response was analyzed using the non-dimensional numbers described in Section 6.6, i.e., the reduced velocity, nominal A/D, maximum A/D and maximum Yaw response described in Section 6.6. These parameters depend on the natural period of Sway and the characteristic length of the floater.

Although the same mooring system was considered for all cases, the results of Section 7.3 reveal slight variations in the natural periods as shown in Table 7.1. In addition, as mentioned in Section 6.6, the characteristic length considered in the analysis of the TLP alone was a projected width of the column; consequently, this dimension changed due to the geometry of the mitigation devices. However, in order to have a better comparison between the experimental results for the TLP alone and with the mitigation devices, the values of reduced velocity and characteristic length of the TLP alone tests were adopted in the new tests.

Figures 7.7, 7.8 and 7.9 present the nominal A/D, maximum A/D, and maximum Yaw responses of the TLP with the mitigation devices. The angle of attack considered in the tests presented in these figures is 0° degrees. For a better comparison, the results for the TLP alone were included.

The shroud with square holes, shroud with diamond holes, and spoiler plates present excellent results. The mitigation achieved by using these devices is relatively high. In contrast, strakes on the TLP columns present the worst results; not only does it not mitigate the motions but also excites higher amplitudes, particularly for Sway.

Despite some small differences for a few reduced velocities, both shrouds present similar results. The shroud with diamond holes presents mitigation ratios in the ranges of [19% - 51%], [11% - 45%], and [2% - 58%] for the nominal A/D, maximum A/D, and maximum Yaw responses, respectively. The Shroud with square holes presents mitigation ratios in the ranges of [14% - 62%], [9% - 62%], and [2% - 69%] for the same parameters.

In general, both shrouds exhibit satisfactory performance for reduced velocities in the range of [5 - 10]. The maximum mitigation ratio in linear and angular motions was observed for reduced velocities of 7.73 and 22, respectively.

The spoiler plates present the best performance for both linear and rotational movements. Ratios of mitigations in the range of [25% - 78%], [15% - 68%], and [5% - 54%] for the nominal A/D, maximum A/D, and Yaw responses were observed, respectively. The best

performance in terms of linear motions was observed at the reduced velocity of 7.73; for rotational motion, the best performance was at the reduced velocity of 13.58. In general, spoiler plates present excellent results for the range of reduced velocities equal to [5 - 22].

The Sway motion of the TLP with strakes is as high as approximately 160% of the movements of the TLP alone. The worst performance is at a reduced velocity of 14.85. The Yaw motions increase by up to 50%, with the reduced velocity of 6.36 presenting the worst case.

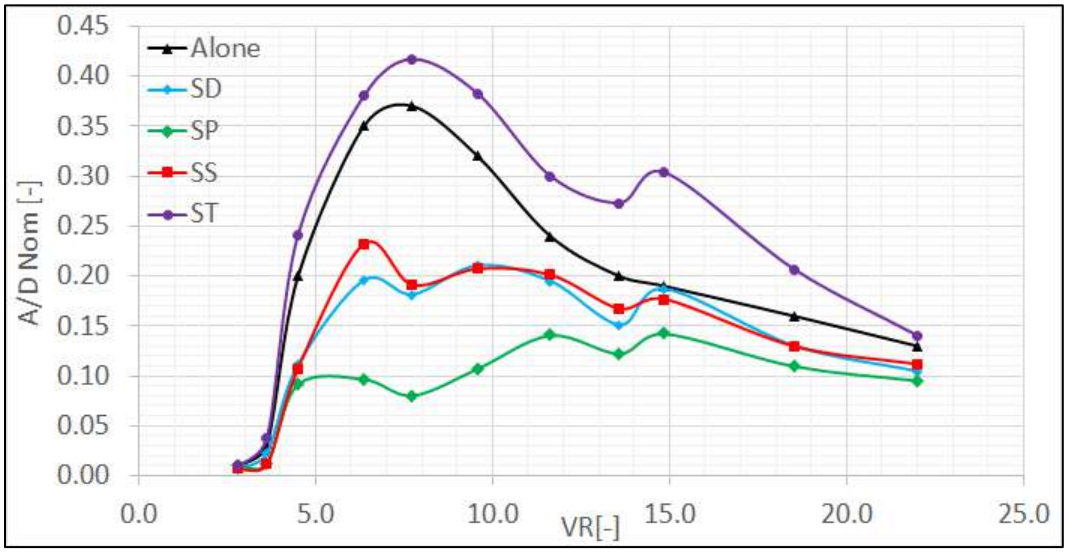

Figure 7.7 Nominal A/D response of the TLP for θ = 0° and the mitigation devices.

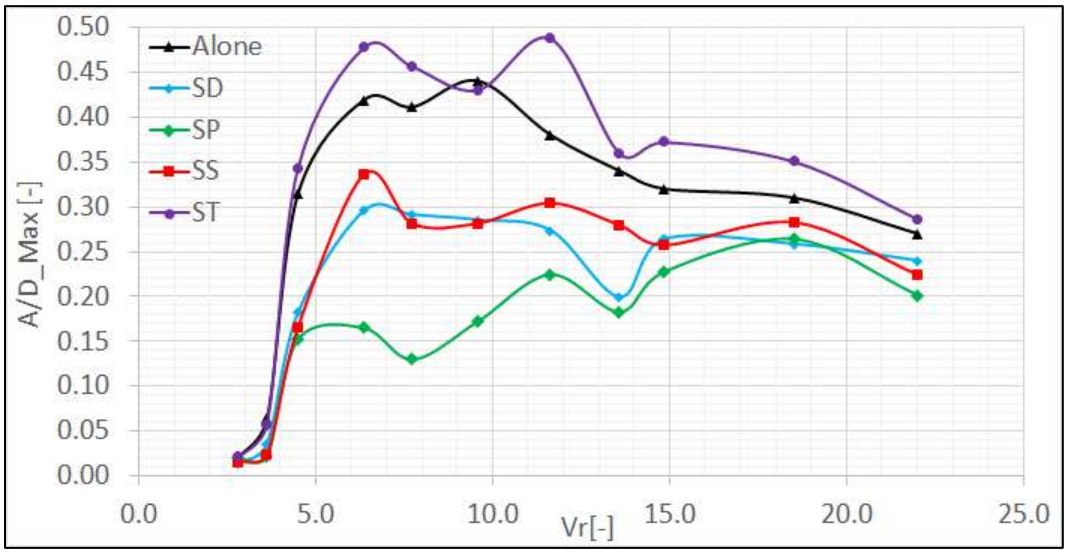

Figure 7.8 Maximum A/D response of the TLP for θ = 0° and the mitigation devices.

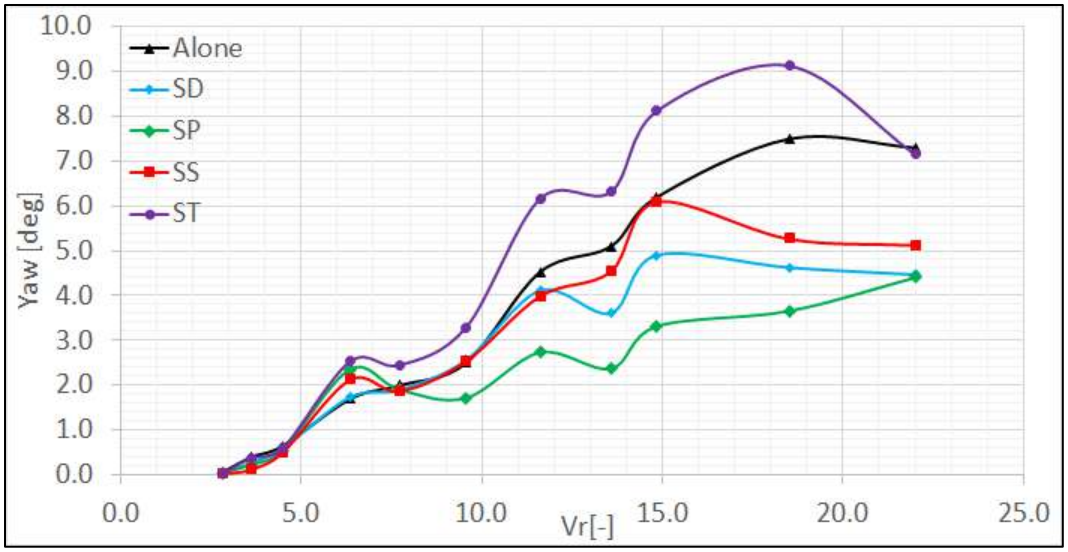

Figure 7.9 Maximum Yaw response of the TLP for θ = 0° and the mitigation devices.

Figures 7.10, 7.11 and 7.12 present the nominal A/D, maximum A/D and maximum Yaw responses of the TLP with mitigation devices for an angle of attack equal of 45°. In this case, the differences in the results between the mitigation devices are minor. However, the spoiler plates still present the best performance, while the strakes performed worst.

The spoiler plates present mitigation ratios in the ranges of [5% - 77%], [12% - 62%], and [3% - 74%] for the nominal A/D, maximum A/D, and maximum Yaw responses, respectively. Notably, the highest ratio of mitigation in linear and rotational motions corresponds to a reduced velocity of 5.11.

The shrouds with square and diamond holes present similar results for reduced velocities in the range of [0 – 10]. The shroud with diamond holes presents mitigation ratios in the ranges of [2% - 47%], [2% - 47%], and [1% - 51%] for the nominal A/D, maximum A/D, and maximum Yaw responses, respectively, while the shroud with square holes presents mitigation ratios in the ranges of [2% - 68%], [12% - 62%], and [3% - 74%] for the same parameters. In general, both shrouds present the best performance for reduced velocities in the range of [0 - 10].

At 45°, the strakes present better results; however, they still exhibit the worst performance. The nominal A/D is approximately 110% of the corresponding TLP alone value. The worst case occurs for at a reduced velocity of 14.85. For Yaw, the amplitude of the motions is higher than that of the TLP alone, reaching values as high as 137%.

In general, spoiler plates, shroud with diamond holes and shroud with square holes provide excellent performance.

For linear motions, average mitigation ratios of 45%, 30%, and 29% were found using SP, SD, and SS, respectively. For Yaw motion, the mitigation ratio has average values of 30%, 20% and 19% for SP, SD, and SS, respectively.

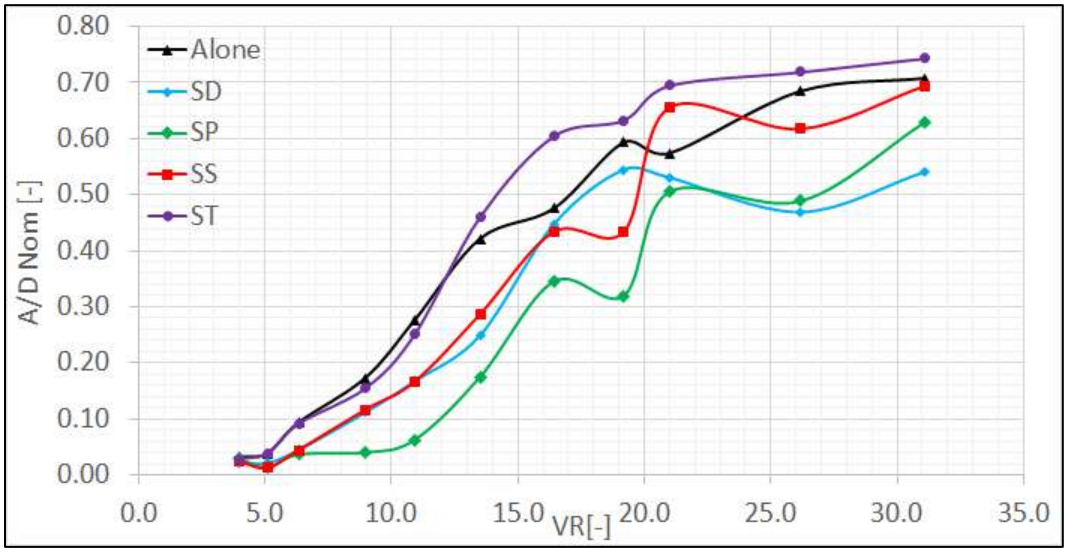

Figure 7.10 Nominal A/D response of the TLP for θ = 45° and the mitigation devices.

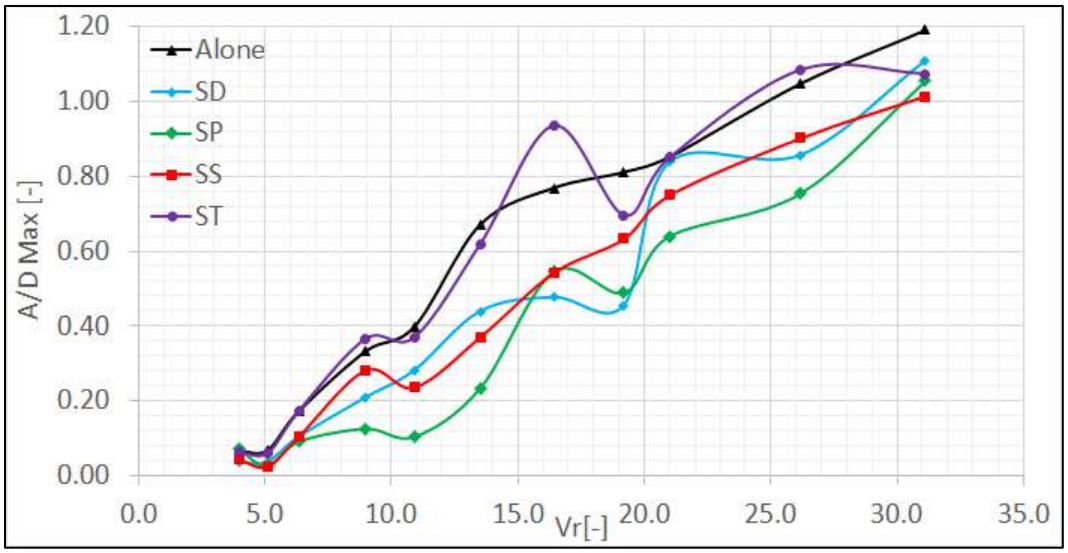

Figure 7.11 Maximum A/D response of the TLP for θ = 45° and the mitigation devices.

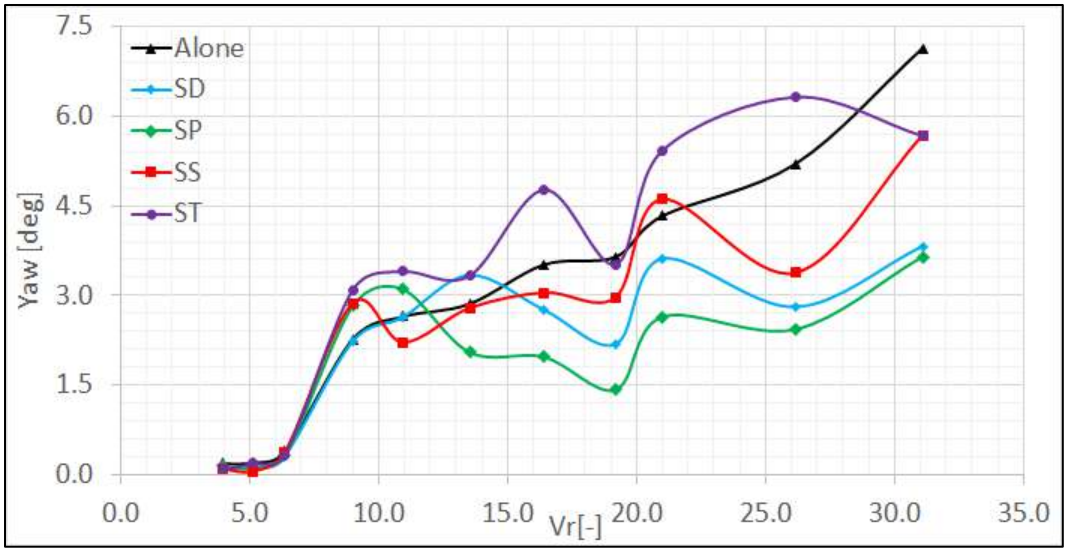

Figure 7.12 Maximum Yaw response of the TLP for θ = 45° and the mitigation devices.

The results obtained with strakes were singular, at both angles of attack and most of the reduced velocities, higher amplitudes of linear and angular motions were found. However, it is not possible to conclude that strakes, in general, are not a favorable option for TLPs. Further investigation into the geometrical parameters of the strakes is recommended to understand these results.

Figure 7.13 presents the XY plane motions of the TLP using the mitigation devices for the velocities V1, V3, V5, V7 and V11 of Table 6.7.

The Sway motion increases with the current velocity in the range of reduced velocities [V1 - V5]; this trend seems to be independent of the mitigation device; as shown in Fig. 6.27, this trend is observed on the TLP alone as well. In addition, for the same range of reduced velocities, slight Yaw angles are observed.

The TLP behavior for reduced velocities in the range of [V5 - V7] reveals that Sway motions decay and that Yaw motions increase rapidly with the current speed. Despite some small differences, similar trends were found on the TLP alone as well.

Another relevant observation is that both shrouds present similar behavior for all of the reduced velocities shown in Fig 7.10. In addition, a comparison of XY plane motions between spoiler plates and strakes reveals that the efficiency of the first is higher than that of the second one. The differences between shrouds and spoiler plates are relatively small.

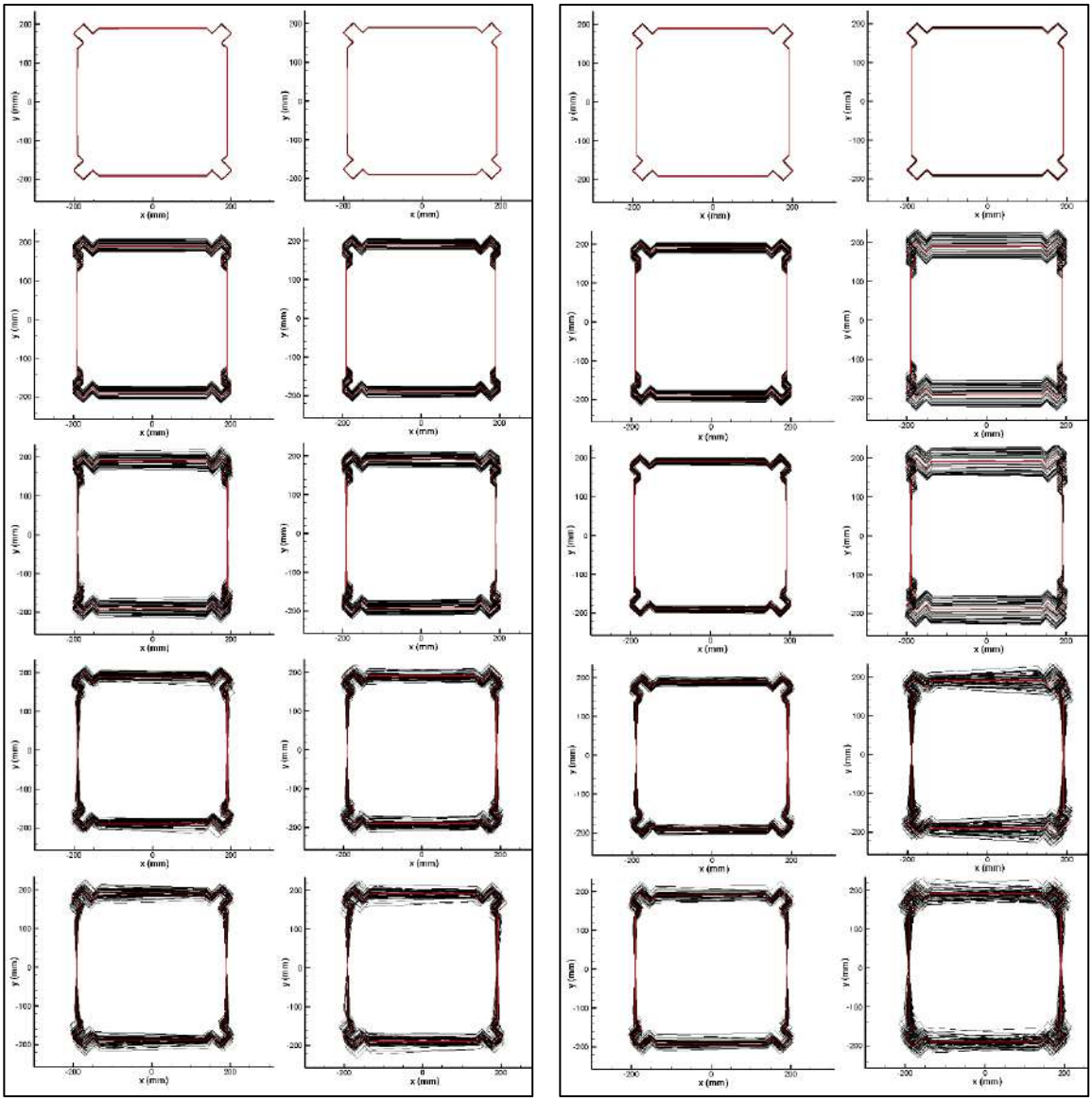

Figure 7.13 Motions in the horizontal plane XY for θ = 0°. Columns from left to right: shroud diamond, shroud square, spoiler plates, and strakes. Rows from top to bottom: V1, V3, V5, V7, and V11.

Finally, the study of the TLP motions with the VIM mitigation devices is concluded with an analysis in frequency domain. The Power Spectrum Density (PSD) is calculated by the Fast Fourier Transform (FFT) of the time traces. Figures 7.14 and 7.15 present the PSD for the TLP alone and the TLP with the mitigation devices for an angle of attack equal to 0° for Sway and Yaw motion, respectively.

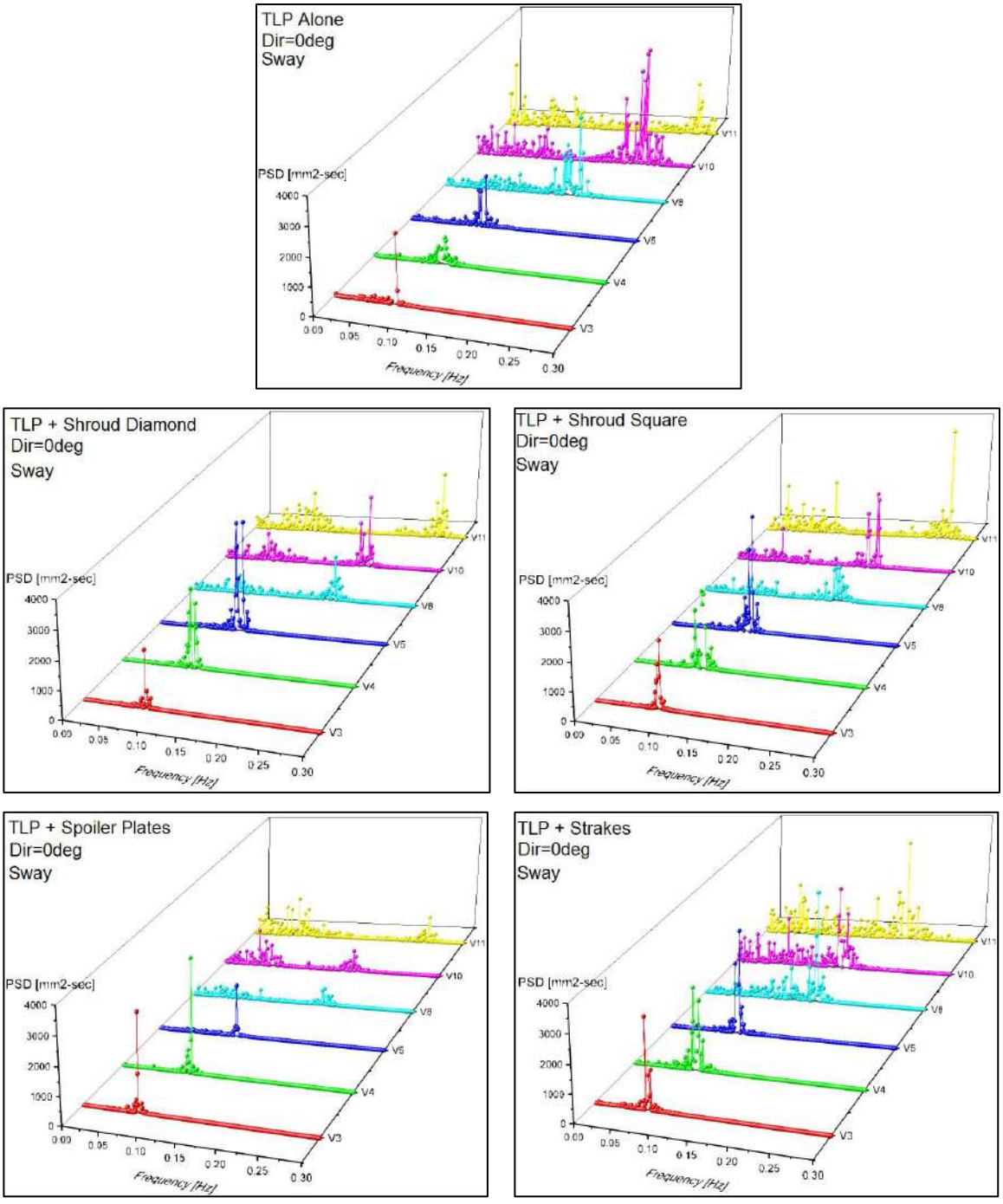

Figure 7.14 Power Spectral Density (PSD) from FFT of Sway motion of the TLP as functions of frequency and the reduced velocities V3, V4, V5, V8, V10, and V11.

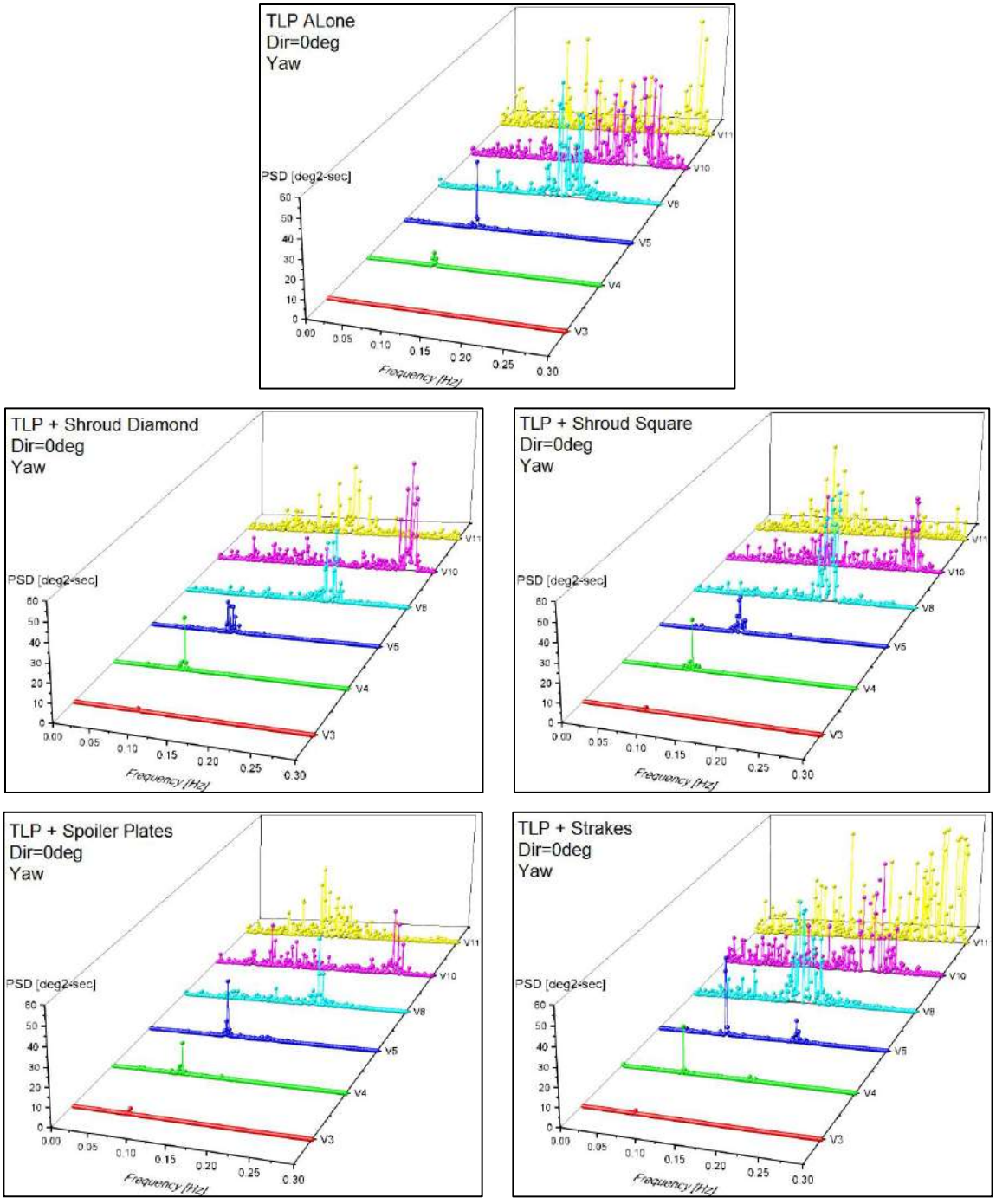

Figure 7.15 Power Spectral Density (PSD) from FFT of Yaw motion of the TLP as a function of frequency and the reduced velocities V3, V4, V5 V8, V10, and V11.

Notably, for Sway, the motions for the reduced velocities V3, V4, and V5 are concentrated in a small range of frequencies of [0.07 – 0.09] Hz. because the time traces for

these velocities present a regular periodic shape. A notable consequence of this fact is that the values of nominal A/D and maximum A/D are close to each other.

Note that this range of frequencies includes the Sway natural frequency of the TLP (approximately 0.08Hz). Consequently, this feature clearly defines a resonance motion. Note that, the phenomena called “lock-in” is not significantly modified by the presence of the mitigation devices. Furthermore, the mitigation of the motions observed in the statistical analysis is not a consequence of the modification of the frequency of the motions.

The PSD of Sway motions for reduced velocities V8, V10, and V11 reveals that the movements of the TLP occur over a wide range of frequencies. Consequently, the Sway motions can be defined as a combination of VIM and Galloping instabilities.

Notably, peaks exist at both low and high frequencies. The irregular shape of the time traces of the response and the significant differences between the nominal and maximum A/D confirm this observation. For this range of reduced velocities, the influence of the mitigation devices is more relevant. Significant differences are observed between the PSDs of the responses for the different devices. Finally, the mitigation of the motions of the TLP is consistent with the reduction of the magnitude of the peaks of the PSD for the different devices.

The analysis in frequency domain of the response for Yaw reveals interesting trends; for instance, the peaks of the energy increase steadily with the reduced velocity. In addition, the first three velocities present short-band frequency responses. However, the response for the last three velocities occurs in a wide-band frequency.

No significant variations appear between the TLP alone and with mitigation devices for velocities V3, V4, and V5. However, significant differences are observed for the last three velocities. The magnitude and the frequency of the peaks vary for all of the mitigation devices.

7.5 DRAG FORCES

Based on the information presented in Table 7.1, it is possible to conclude that the mitigation devices modify the natural periods and damping of the system. Consequently, it is reasonable to expect variations in the drag forces on the TLP as well, which is a critical issue for the dimensioning of mooring systems. Thus, the most convenient mitigation device

must have not only a high reduction ratio for the dynamic motions of the TLP but also a minimum impact on the drag forces on the TLP to reduce high static offsets on the TLP.

To measure the average current loading on the TLP with the mitigation devices, the experimental setup presented in Section 5.9 was used. Figure 7.16 presents a schematic representation of the TLP with the mitigation devices during the measurement of the current loads. The procedure of the tests is the same as that described in Section 5.9.

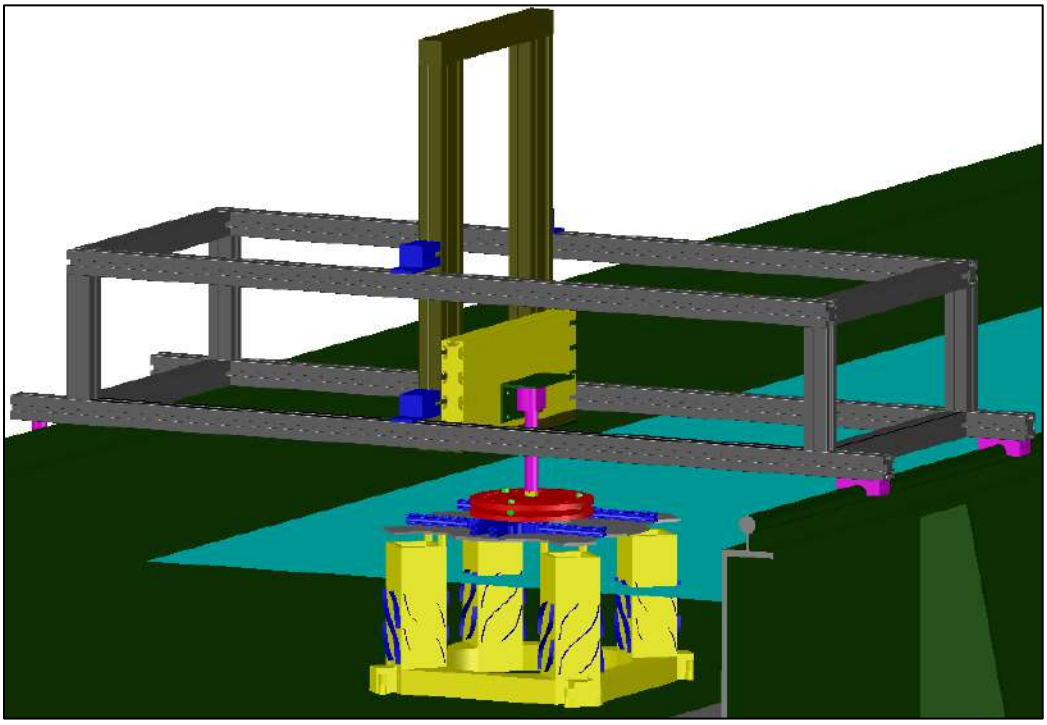

Figure 7.16 Experimental setup for the measurement of current loads on the TLP using the mitigation devices. The figure shows the strakes.

This new model test campaign considers the velocity V5 presented in Table 5.6, a range of current angles of attack [0° - 345°] in steps of 15° and two repetitions for each test. Consequently, a total of 104 tests were conducted.

Each test has a duration of 300 sec. in mode-scale time. The current load coefficients C_{FX}, C_{FY} and C_{MZ} were calculated using Eqns. (5.8) to (5.10). using the characteristic dimensions in Table 5.8 and considering the average values of forces and moments on the TLP.

Figures 7.17, 7.18 and 7.19 respectively present the current load coefficients C_{FX}, C_{FY} and C_{MZ} for the TLP with the four VIM mitigation devices. The results from the TLP alone were included in these figures to identify the variations due to the mitigation devices.

Based on the results presented in these figures, the influence of the mitigation devices on the global current loads on the TLP is confirmed. In general, the trends are clear for the three current load coefficients of each mitigation device. Surprisingly, both shrouds decrease the drag forces on the TLP for all angles of attack.

On average, reductions of 20% and 25% were observed for the shrouds with square and diamond holes, respectively. The variations between shrouds are significantly larger for C_{MZ}, for which average moment reductions of 53% and 29% appear for shrouds with square and diamond holes, respectively.

The results show that strakes and, in particular, spoiler plates, increase the current loads on the TLP. On average, C_{FX} and C_{FY} present values of approximately 115% of the loads on the TLP alone. Additionally, C_{MZ} presents values of approximately 142% and 130% of the loads on the TLP alone for the spoiler plates and strakes, respectively.

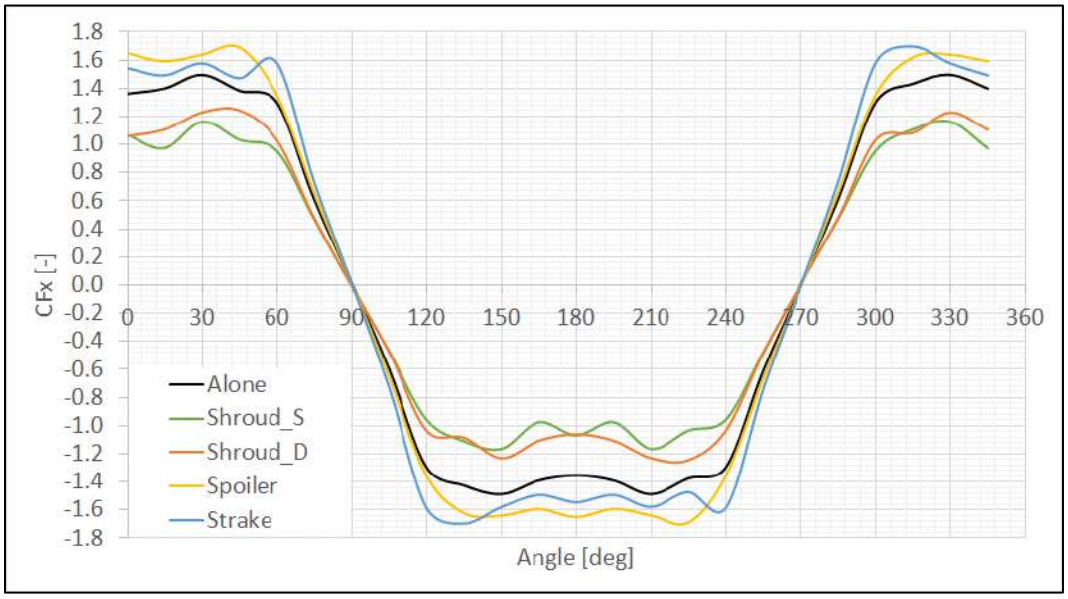

Figure 7.17 Variation of C_{FX} with angle of attack for the TLP alone and with mitigation devices.

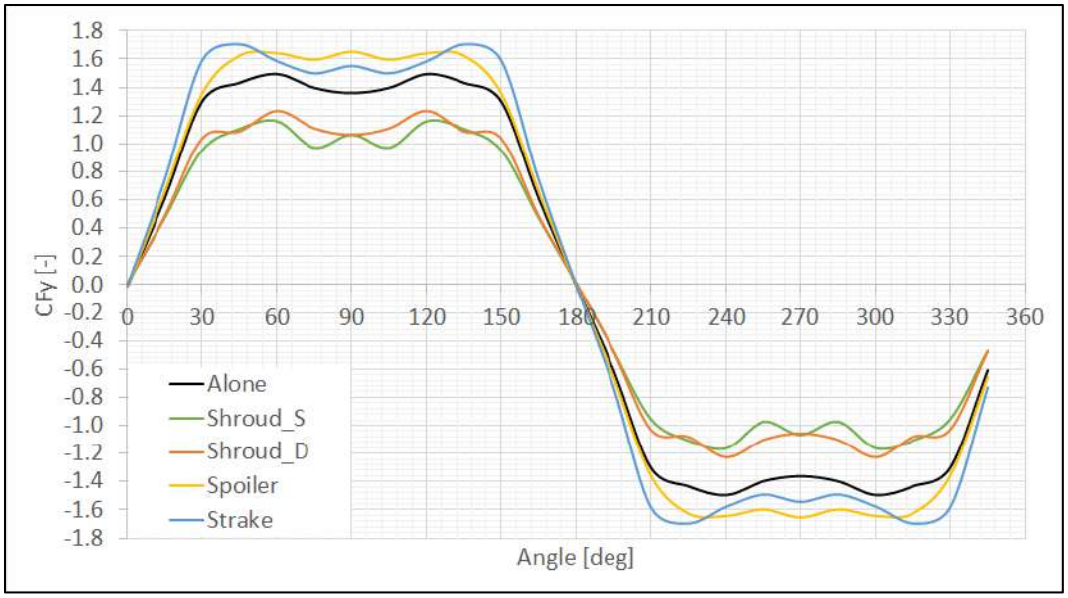

Figure 7.18 Variation of C_{FY} with angle of attack for the TLP alone and with mitigation devices.

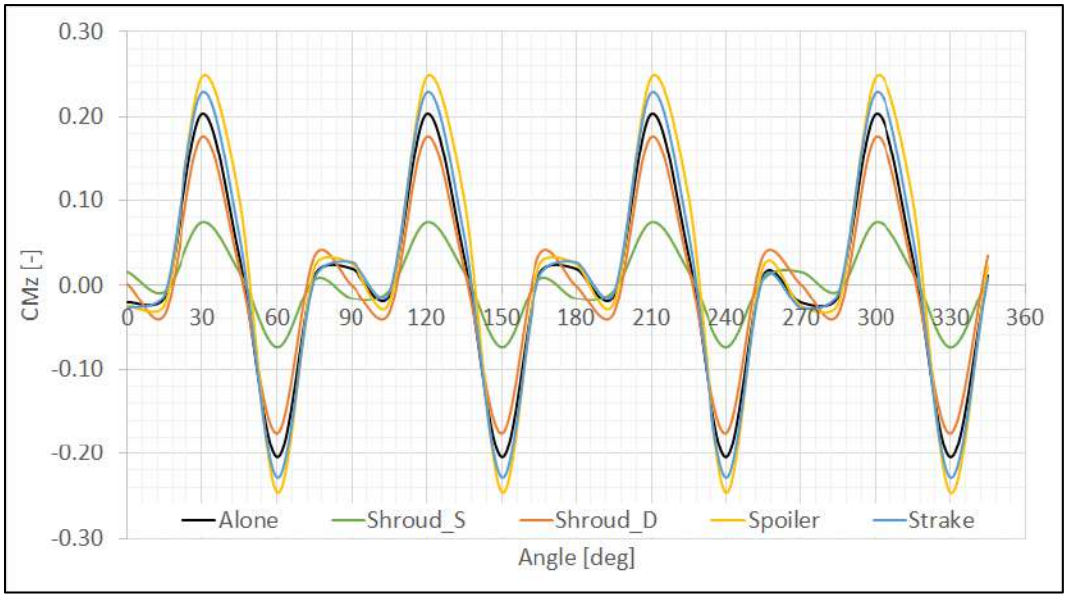

Figure 7.19 Variation of C_{MZ} with angle of attack for the TLP alone and with mitigation devices.

Therefore, based on this extensive study of VIM mitigation devices, it is clear that both aspects, the mitigation of motions and variations in drag forces, are independent. For instance, spoiler plates reduce the dynamic motions significantly and increase the drag

forces. Due to this fact, it is possible to conclude that there is not a direct relation between the average drag forces and current induced motions on the TLP.

At this point, considering that mitigation devices do not modify the natural period of the system significantly and consequently, the devices do not prevent resonant motions. Additionally, an increase in drag forces does not imply an increase in the motions developed by the TLP. Hence, the reason that the spoiler plates present the best performance could be considered undetermined. However, there is a final consideration that must be incorporated into this analysis: the damping.

As shown in Table 7.1, spoiler plates and both shrouds present high values of damping relative to that of the TLP alone. In addition, strakes present slightly lower values of damping than the TLP alone. Therefore, a direct correlation exists between the damping ratios and amplitudes of the motions of the TLP. The damping has shown to be the most relevant parameter in the mitigation of current induced motions.

Finally, despite the excellent performance of spoiler plates in motion mitigation, shrouds seem to be the most efficient devices in terms of drag reduction and motion mitigation. Note that the four mitigation devices were defined following the general guidelines described in Section 7.3. Thus, further analysis for optimization of the geometrical parameters of the devices can be conducted.

CHAPTER VIII. CONCLUSIONS

The present work examined the loads and motions induced by current and waves on the TLP-TAD multi-body system. The extensive experimental and numerical studies presented represent an effort to improve the understanding of the dynamic behavior of such a complex system. Thus, the most relevant results and conclusions of this research are summarized in the following section. Furthermore, some suggestions for future works are included.

8.1 WAVE-INDUCED LOADS AND MOTIONS

The study of wave induced loads and motions on the multi-body system includes an analysis of the first and second-order loads using frequency and time domain approaches in single-body and multi-body simulations considering regular and irregular waves.

The analysis of the first-order loads and RAOs indicates that there are not significant differences between the results obtained by the low-order and the higher-order panel methods when very fine grids are used. Furthermore, the higher-order method with coarse grids provides accurate results, and the low-order method requires a finer refinement on the body surfaces to provides reasonable accuracy, consequently, a longer processing time. Hence, higher-order method seems to be the most efficient in this type of analysis.

The comparison of the first-order loads between the single-body case and several multi-body cases reveals that the hydrodynamic coefficients of one floater are not affected by the presence of the other body. Consequently, the hydrodynamic interactions between the TLP and TAD are weak.

Time domain simulations using regular waves have demonstrated that the RAOs of the system are not linear, i.e., the RAOs depend on the amplitude of the exciting waves. In addition, the comparison of RAOs between the single-body and multi-body cases reveals slightly higher variations than those predicted by the frequency domain analysis. Finally, for most of the cases, the frequency domain predictions were conservative.

Time domain simulations using irregular waves have shown that frequency domain predictions are relatively accurate in the range of elementary wave frequencies. However, the predictions of the frequency domain approach are not in strong agreement with the time domain results for low and high frequencies. Moreover, no significant differences were found between the motions of the floaters in the single-body and multi-body time domain simulations. Therefore, the weak coupling effects for linear wave loads are confirmed.

In the analysis of second-order loads, the convergence between the direct and indirect method for low and high-frequency QTFs was achieved. The high-frequency QTFs are critical in terms of the body refinement and free surface discretization. In addition, the importance of the free surface has been confirmed for the high-frequency and the low-frequency QTFs, i.e., QTFs computed without the free surface integral present significant differences from the results in which this integral is considered. Finally, the indirect method has shown to be the most efficient in terms of computational time without loss of accuracy.

The comparison of QTFs between the single-body and multi-body simulations reveals significant hydrodynamic coupling effects, i.e., the differences between QTFs for the single-body and multi-body cases are high, particularly for the low-frequency QTFs.

In general, the predictions of the Newman approximation present poor agreement with the second-order QTFs. However, the analysis of the QTFs for a difference frequency equal to the natural frequency of the floaters shows that for the horizontal modes, the results of the Newman approximation are acceptable. Poor agreement is observed for the vertical modes.

Finally, two groups of time domain simulations were conducted. The first considers the low and high-frequency QTFs, whereas the second considers the Newman approximation for low-frequency QTFs and high-frequency QTFs were not computed. The results show that, for single-body cases, the differences between the two groups of simulations are minimal for the horizontal modes and relatively higher for the vertical modes, particularly for Pitch of the TLP. In contrast, the results for the multi-body cases reveal that the differences for horizontal modes are relatively higher and the differences for vertical modes. Therefore, based on these results it is recommended the use of the second-order QTFs in time simulations of the TLP-TAD multi-body system.

8.2 CURRENT LOADS

The study of current loads is divided into two groups: the experimental and the numerical analysis. In the experimental analysis, the entire experimental apparatus was built and tested to accommodate the particular characteristics of the current channel of the LOC. This arrangement can be used in future investigations to measure current loads on any other floater.

The results of the experimental tests reveal that the presence of the TAD does not affect the average current loads on the TLP. No significant differences were found for the cases, TLP alone, upstream, and downstream. Consequently, the shielding effects on the TLP loads due to the presence of the TAD are weak.

The results for the TAD for a similar test campaign reveal that the differences between the loads on the TAD upstream and downstream are relatively significant. The loads on the TAD in downstream positions are, in general, lower.

In general, for both floaters, the current load coefficients do not depend on the range of current velocities tested in the lab. In addition, the distance between the floaters has a minor impact on the current load coefficients in the multi-body cases.

The frequency domain analysis of the current loads shows that the forces on the TLP present the largest portion of their energy in frequencies that are close to the natural frequencies of this floater. Consequently, resonance motions could be expected in VIM tests. Although the results for the TAD show that the current loads on this floater present the highest energy at frequencies lower than the natural frequencies, the difference is not significant enough to conclude that resonance motions on the TAD are not expected.

The results of the extensive numerical analysis reveal that the differences in the Reynolds numbers and flow regimes between the model-scale and full-scale do not affect the average current loads on the TLP; the maximum difference is approximately 3%. In addition, the differences between full-scale and model-scale average loads on the TAD are slightly higher but never greater than 9%. Thus, scale effects are relatively small on the TAD as well.

The numerical analysis of the model-scale considering the walls and bottom of the channel demonstrate that there are significant blockage effects on the average current loads on both floaters due to the walls. In general, the dependence on the current load coefficients on the current velocities is weak in the full-scale and model-scale simulations.

8.3 CURRENT INDUCED MOTIONS

In the experimental analysis of the current induced motions on the TLP-TAD system, several contributions were made to the laboratory, such as the new experimental setup to test deep draft TLPs, semi-submersibles and multi-body systems.

Despite the tremendous challenges in the use of ultra-reduced scale models, a reasonable accuracy in the calibration of the physical properties of the floater was achieved. In addition, despite some small margins of error, the natural periods and stiffness properties based on full-scale data from real platforms can be represented properly with reasonable accuracy.

The influence of the current velocities and angles of attack on the behavior of the TLP was demonstrated. The TLP undergo Vortex Induced Motions (VIM) at 0°, however, at 45°, the trends of the motions correspond to Galloping Instabilities. Frequency domain analysis confirms these conclusions.

The TAD does not present significant motions for the whole range of current velocities analyzed in this model test campaign. This finding confirms the influence of the column length of the floater on the amplitude of the motions, i.e., floaters with longer columns are more susceptible to VIM and Galloping.

The analysis of the multi-body system without connection between the floaters reveals weak hydrodynamic coupling between the floaters. In general, the motions of the unit in a downstream position are slightly smaller. In contrast, the motions of the unit in an upstream position are slightly larger. In addition, as in the case of the average current load tests, the distance between the floaters has a marginal impact on the floater response, or at least it is challenging to establish a relationship between the distance between the floaters and the motion amplitude developed by the two floaters.

Finally, the analysis of the multi-body system with the connection between the floaters reveals two interesting characteristics of the motions developed by the floaters. First, the hawser system modifies the behavior of the floaters significantly. Second, changes in the configuration of the hawser systems seem to have little impact on the motions of the floaters.

In general, the TLP connected to the TAD develops considerably smaller motions. The mitigation is significantly larger for the case with the TLP downstream. In addition, the TAD develops considerably larger motions when connected to the TLP. The amplification is considerably larger for the case with the TAD downstream.

8.4 MITIGATION DEVICES

The experimental test campaign with VIM mitigation devices demonstrated that the dynamic behavior of the TLP can be significantly modified due to the presence of small appendages on the hull.

Decay tests show that the VIM mitigation devices do not alter the values of the natural periods of the TLP. In contrast, it is clear that these devices significantly modify the damping values.

The VIM tests reveal that spoiler plates are the most efficient mitigation devices in terms of reducing the amplitude of the motions developed by the TLP. Surprisingly, strakes present poor behavior, while shrouds present an excellent performance. Note that, no significant differences arise in the behavior of the TLP between the two shrouds.

The average current tests provide evidence that the presence of the VIM mitigation devices alters the average current loads on TLP. Thus, the spoiler plates and strakes present higher drag forces. In contrast, shrouds reduce the mean current loads.

In general, no direct relationship appears between mean drag forces on the fixed TLP and the dynamic motions developed by the unit. That is, a reduction of drag does not imply that the amplitude of the motions must be smaller. Furthermore, the frequency domain analysis reveals that the VIM devices do not modify the frequency of the oscillations, nor do they not modify the natural periods of the TLP. Consequently, these devices do not prevent “lock-in.”

Finally, the relationship between hydrodynamic damping generated by the mitigation devices and the amplitude of the motions developed by the TLP is clear. Therefore, based on these facts, it is possible to conclude that the damping is the most relevant parameter for the mitigation devices.

8.5 RECOMMENDATIONS FOR FUTURE WORKS

Although this thesis presents an extensive experimental and numerical analysis of the loads and motions induced by current and waves on the TLP-TAD multi-body system, there are many natural extensions of the present work, of which the following are suggested below.

- The results of this research have proved that the Newman approximation provides accurate results only for horizontal modes with natural frequencies lower than 0.005 Hz. Moreover, the Newman approximation presents poor results on vertical modes

of the TAD, and the omission of sum-frequency QTF implies underestimation on vertical modes of the TLP. Therefore, it is necessary to verify the impact of the second-order wave loads on the performance of the system and the mooring lines in operational and design phases using extreme seas and long-term fatigue analysis.

- With additional computational tools, a study of the differences between the transient average current loads from experiments, transient average current loads from numerical simulations and steady-state average current loads from numerical simulations could be performed to estimate the accuracy of the steady-state simulations.
- The VIM tests have shown that the mechanical connection has a tremendous impact on the system dynamic behavior of the system. The TAD develops very high amplitude when it is connected to the TLP. Consequently. A study to develop an alternative to the hawser system that can improve the dynamic behavior of the connected floaters is necessary to optimize the TLP-TAD multi-body system.
- Results of VIM tests have shown the strong influence of the current angles of attack, current velocity, column size of the floaters, the damping, and the mechanical connection between the floaters on the dynamic behavior of the multi-body system subject to currents. However, as mentioned in Section 2.6, the effects of waves combined with currents can modify the VIM motions significantly. Consequently, these effects could be investigated in future works.
- With the aim of mitigating the motions developed by the TLP in current, four mitigation devices were tested. Three of them present excellent results in terms of mitigation of the motions and drag forces. At this point, it is important to understand how the parameter of each mitigation devices can modify the VIM behavior of the platform to further optimizations

REFERENCES

[1] Ahilan, R.; Harrison, J.; 1993. *The Significance of Slowly Varying Forces on the Design of Catenary Mooring for Semi-submersible Units*. International Offshore and Polar Engineering Conference, Singapore.

[2] Ansys Inc.; 2016. *ANSYS CFX16.0 User Manual*.

[3] API Recommended Practice 2K, 2005. *Design and Analysis of Stationkeeping Systems for Floating Structures*. 3rd Edition.

[4] Armandei, M.; Fernandes, A. C.; 2012. *Stability Analysis of a Yawing Flat Plate into the Water Current*. OMAE2012-84164, Rio de Janeiro, Brazil.

[5] Armandei, M.; Fernandes, A. C.; 2014. *Torsional Instability of an Elastic Flat Plate due to Hydrodynamic Loads*. Journal of Mechanics, Vol 30, pp. 643–50.

[6] Armandei, M.; Fernandes, A. C.; Bakhshandeh, R. A.; 2016. *Hydroelastic Buffeting Assessment Over a Vertically Hinged Flat Plate*. Journal of Experimental Techniques, Vol 40, pp. 833-839.

[7] Bai, Y.; Tang, A.; O'sullivan, E.; Uppa, K. C.; Ramakrishnan, S.; 2004. *Steel Catenary Riser Fatigue Due to Vortex Induced Spar Motions*. OTC16629, Houston, Texas, USA.

[8] Bakhshandeh, R. A.; Armandei, M.; 2017. *Renewable Energy Harvesting by Vortex-Induced Motions: Review and Benchmarking of Technologies*, Journal of Renewable and Sustainable Energy Reviews, Vol. 70 pp. 193-214.

[9] Blevins, R.; 2001. *Flow Induced Vibration*. Krieger Publishing Company.

[10] Botker, S.; Karp, T.; Johannessen, T.; Chew, M.; 2001. *Wellhead TLP with Tender Assisted Drilling.* OTC 12988, Houston, Texas, USA.

[11] Cao, P.; Zhang, J.; 1997. *Slow Motion Responses of Compliant Offshore Structures*. ISOPE-97-07-2-119.

[12] Chakrabarti, S.; 1994. *Offshore Structure Modeling.* Advanced Series on Ocean Engineering.

[13] Chaudhuri, J.; 1993. *Design of Semi-Submersible Tender Assisted Drilling and Workover Systems for Harsh Weather Applications*. International Offshore and Polar Engineering Conference, Singapore.

[14] Chen, S.; Mahrenholtz, O.; 1992. *Dynamic Responses of Floating Twin Bodies in Beam Waves*. ISOPE-I-92-301. International Society of Offshore and Polar Engineers. San Francisco, CA, USA.

[15] Chen, X.; Molin, B.; Petitjean, F.; 1995. *Numerical Evaluation of the Springing Loads on Tension Leg Platforms*. Marine Structures, Vol 8, Issue 5, pp. 501 – 524.

[16] Chen, X.; 2007. *Middle-Field Formulation for the Computation of Wave Drift Loads.* Journal Engineering Math. Vol. 59, pp. 61-82.

[17] Choi, Y.; Hong, S.; 2002. *An Analysis of Hydrodynamic Interaction of Floating Multi-Body Using Higher-Order Boundary Element Method*. ISOPE-I-02-309, International Society of Offshore and Polar Engineers. Kitakyushu, Japan.

[18] Christiansen, P.; Cuvillier, G.; Hicks, N.; 1994. *Tender Assisted Drilling in the North Sea*. OTC7458, Houston, Texas, USA, 1994.

[19] Constantinides, Y.; Oakley, O.H.; Holmesn, S.; 2006. *Analysis of Turbulent Flows and VIV of Truss Spar Risers*. OMAE2006-92674, Hamburg, Germany.

[20] Croonenborghs, E.; Sauder, T.; Fouques, S.; Reinholdtsen, S.; 2013. *Comparison of Various Methods for the Assessment of Wind and Current Loads on a Semi-Submersible Platform*. OTC – 24399, Rio de Janeiro, Brazil.

[21] Cruz, R. E.; 2010. *Dynamic Simulation of Two Coupled Floating Bodies to Regular Waves*. M.Sc. Thesis. Federal University of Rio de Janeiro (UFRJ), Brazil.

[22] Dallinga, R.; Huijsmans, R.; Pinkster, J.; 1988. *Combined Statistics of First and Second-order Motion of Semi-Submersibles.* Boss Conference, pp. 733-754, Trondheim, Norway.

[23] Ding, Z.; Balasubramanian, S.; Lokken, R.; Yung, T.; 2004. *Lift and Damping Characteristics of Bare and Straked Cylinders at Riser Scale Reynolds Numbers*. OTC 16341, Houston, Texas, USA.

[24] DNV, 1996. *Guideline for Offshore Structural Reliability Analysis – Application for Tension Leg Platforms*. Technical Report.

[25] Dular, M.; Bachert, R.; 2009. *The Issue of Strouhal Number Definition in Cavitating Flow*. Journal of Mechanical Engineering, Vol 11. Pp. 666 – 674.

[26] Eatock-Taylor, R.; Hung, S.; 1985. *Wave Drift Enhancement Effects in Multi-Column Structures*. Applied Ocean Research. Vol. 7, pp. 128 – 137.

[27] Faltinsen, O. M.; Loken, A. E.; 1978. *Drift Forces and Slowly Varying Forces on Ships and Offshore Structures in Waves*. Norwegian Maritime Research, No. 1 pp. 2-15.

[28] Faltinsen, O; 1990. *Sea Loads on Ships and Offshore Structures*. Ocean Technology Series.

[29] Faltinsen, O.; Newman, J.; Vinje, T.; 1995. *Nonlinear Wave Loads on a Slender Vertical Cylinder. Journal of Fluid Mechanics*, Vol. 298, pp. 178 – 198.

[30] Fernandes, A. C.; Armandei, M.; 2014. *Phenomenological model for torsional galloping of an elastic flat plate due to hydrodynamic loads*. Journal of Hydrodynamics, Ser. B Vol 26, pp. 57-65.

[31] Fernandes, A. C.; Armandei, M.; 2014. *van der Pol-Duffing Modeling for Torsional Galloping*. OMAE2014-24013, San Francisco, CA, USA

[32] Fujarra, A.; Goncalves, R.; Rosetti, G.; Nishimoto, K.; 2010. *Mitigation of Vortex-Induced Motion (VIM) on a Monocolumn Platform: Forces and Movements*. JOMAE Vol. 132/041102-3.

[33] Fujarra, A.; Rosetti, G.; Wilde, J.; Goncalves, R.; 2012. *State-of-Art on Vortex-Induced Motion: A Comprehensive Survey After More than One Decade of Experimental Investigation*. OMAE2012-83561, Rio de Janeiro, Brazil.

[34] Goncalves, R.; Fujarra, A.; Rosetti, G.; Nishimoto, K.; 2010. *Mitigation of Vortex-Induced Motion (VIM) on a Monocolumn Platform: Forces and Movements*. Journal of Offshore Mechanics and Arctic Engineering, Vol. 132 p. 041102.

[35] Goncalves, R.; Rosetti, G.; Fujarra, A.; Oliveira, A.; 2012. *Experimental Study on Vortex-Induced Motions of a Semi-Submersible Platform with Four Square Columns, Part I: Effects of Current Incidence Angle and Hull Appendages*. Ocean Engineering 54, pg. 150-169.

[36] Goncalves, R.; Rosetti, G.; Fujarra, A.; Oliveira, A.; 2013. *Experimental Study on Vortex-Induced Motions of a Semi-Submersible Platform with Four Square Columns, Part II: Effects of Surface Waves, External Damping and Draft Condition*. Ocean Engineering 62, pg. 10-24.

[37] Goncalves, R.; Fujarra, A.; Rosetti, G.; Kogishi, A.; Koop, A.; 2015. *Effects of Column Design on the VIM Response of Deep-Draft Semi-Submersible Platforms*. ISOPE-I-15-701. International Society of Offshore and Polar Engineers. Hawaii, USA.

[38] Gueydon, S.; Duarte, T.; Jonkman, J.; Bayati, I.; Sarmento, A.; 2014. *Comparison of Second-order Loads on a Semi-submersible Floating Wind Turbine*. OMAE2014-23398, San Francisco, CA, USA.

[39] Gurley, K.; Kareem, A.; 1998. *Simulation of Ringing in Offshore Systems Under Viscous Loads*. Journal of Engineering Mechanics. Vol. 124, Issue 5, pp. 582 – 586.

[40] Huang, K.; Chen, X.; Kwan, C-T.; 2003. *The Impact of Vortex-Induced Motion on Mooring System Design for Spar-Based Installation.* OTC15245, Houston, Texas, USA.

[41] Huateclocque, G.; Rezende, F.; Waals, O.; Chen, X.; 2012. *Review of Approximations to Evaluate Second-Order Low-Frequency Load.* OMAE2012-83407, Rio de Janeiro, Brazil.

[42] Irani, M.; Finn, L.; 2004. *Model Testing for Vortex Induced Motions of Spar Platform*. OMAE2004-51315, Vancouver, Canada.

[43] Journee, J. M.; 2001. *Offshore Hydromechanics.* Delft University of Technology, Delft, The Netherlands.

[44] Kim, C.; 2008. *Nonlinear Waves and Offshore Structures*. Advanced Series on Ocean Engineering Vol 27.

[45] Kim, M.; 1991. *Second-Order Sum-Frequency Wave Loads on Large-Volume Structures*. Applied Ocean Research, Vol. 13, No. 6, pp. 287 – 296.

[46] Kim, Y.; Kring, D.; Sclavounos, P.; 1997. *Linear and Nonlinear Interactions of Surface Waves with Bodies by a Three-Dimensional Rankine Panel Method*. Applied Ocean Research, Vol 19, pp. 235-249.

[47] Koop, A.; Bereznitski, A.; 2011. *Model-Scale and Full-Scale CFD Calculations for Current Loads on Semi-Submersible*. OMAE2011-49204, Rotterdam, The Netherlands.

[48] Koop, A.; 2016. *Determining Side-By-Side Current Loads Using CFD and Model Tests*. OMAE2016-54344, Busan, South Korea.

[49] Koop, A.; Wilde, J.; Fujarra, A.; Rijken, O.; Linder, S.; Lennblad, J.; Haug, N.; Phadke, A.; 2016. *Investigation of Reason for Possible Differences Between VIM Response in the Field and in Model Tests*. OMAE2016-54746. Busan, South Korea.

[50] Lamas, F.; Fernandes, A. C.; Ramirez, M. A. M.; 2017. *Yaw Galloping of a TLWP Platform under High Speed Currents by Analytical Methods and its Comparison with Experimental Results*. OMAE2017-61909, Trondheim, Norway.

[51] Leverette, S.; Rijken, O.; Dooley, W.; Thompson, H.; 2003. *Analysis of TLP VIV Responses to Eddy Currents.* OTC15289. Houston, Texas, USA.

[52] Liu, Y.; 2016. *Research on Procedures to Estimate 3D Response of Vortex Induced Motion (VIM) of Multi-Column Floaters Based on 2D CFD Calculations*. M.Sc. Thesis. Delft University of Technology, Delft, The Netherlands.

[53] Maruo, H.; 1960. *The Drift of a Body Floating in Waves.* Journal of Ship Research, Vol. 4 No. 3

[54] Mathiesen, R.; 1989. *Tender Assisted Drilling – NPD Experience*. SPE-19248-MS. Offshore Europe, Aberdeen, UK.

[55] Matos, V.; 2009. *Slow Resonant Movements in the Vertical Plan of Semi-submersible Platforms*. D.Sc. Thesis. Federal University of Rio de Janeiro (UFRJ), Brazil.

[56] Matos, V.; Simos, A.; Sphaier, S.; 2011. *Second-Order Resonant Heave, Roll and Pitch Motions of a Deep-Draft Semi-Submersible: Theoretical and Experimental Results*. Ocean Engineering Vol 38 pp. 227 - 243.

[57] Mavrakos, S.; Chatjigeorgiou, I.; 2008. *Second-Order Hydrodynamic Effects on an Arrangement of Two Concentric Truncated Vertical Cylinders*. Marine Structures Vol 22 pp. 545-575.

[58] Menezes, F. G. T.; 2013. *Hydrodynamic and Structural Coupling of Multibody Floating Systems for Oil and Gas Production and Shipment*. D.Sc. Thesis. Federal University of Rio de Janeiro (UFRJ), Brazil.

[59] MIT.; 2006. *WAMIT User Manual - Version 6.4*. Massachusetts Institute of Technology, MIT, USA.

[60] Molin, B.; 1979. *Second-Order Diffraction Loads Upon Three-Dimensional Bodies*. Applied Ocean Research, Vol 1, pp 197-202.

[61] Molin, B.; Malenica, S.; 1995. *Third Harmonic Diffraction by a Vertical Cylinder*. Journal of Fluid Mechanics, Vol. 302, pp. 203 – 229.

[62] Molin, B.; Chen, X.; 2002. *Approximations of the Low-Frequency Second-Order Wave Loads*. Proc. 17th IWWWFB, Cambridge, UK

[63] Monroy, C.; Hauteclocque, G.; Chen, X.; 2013. *A Practical O(Δω) Approximation of Low Frequency Wave Loads*. OMAE, Nantes, France.

[64] Morgan, J.; Malaeb, D.; 1983. *Dynamics Analysis of Tension Leg Platforms*. Proceedings of the Second International Conference of Offshore Mechanics and Arctic Engineering, Paper No. 4, pp. 31 – 37, Houston, Texas, USA.

[65] Newman, J.; Lee, C.; 1967. *The Drift Force and Moment on Ships in Waves*. Journal of Ship Research Vol. 11. pp. 51 – 60.

[66] Newman, N.; 1974. *Second-order Slowly Varying Forces on Vessel in Irregular Waves*.

[67] Newman N.; 2005. *Second-Order Diffraction in Short Waves*. Journal of Ship Research, Vol 49, pp. 263-273.

[68] Ogilvie, T.; 1963. *First and Second-order Forces on a Cylinder Submerged Under a Free Surface.* Journal of Fluid Mechanics, Vol. 16 pp. 451 – 472.

[69] Ogilvie, T.; 1983. *Second-order Hydrodynamic Effects on Ocean Platform.* International Workshop on Ship and Platform Motions, University of California, USA.

[70] Orcina Ltd.; 2016. *Orcaflex User Manual - Version 10.0*. Orcina Limited, Cumbria, United Kingdom.

[71] Pinkster, J.; Oortmerssen, G.; 1977. *Computation of the First and Second-order Wave Forces on Oscillating Bodies in Regular Waves*. Proc. Second. Int. Conf. on Numerical Ship Hydrodynamics, Berkeley, CA, USA.

[72] Pinkster, J.; 1980. *Low Frequency Second-order Wave Exciting Forces on Floating Structures*. Ph.D. Thesis, Technical University of Delft, Delft, The Netherlands.

[73] Qualisys AB; 2006. *Qualisys Track Manager User Manual – Ver.1.10.2*. Gothenburg, Sweden.

[74] Rainey, R.; 1989. *A New Equation for Calculating Wave Loads on Offshore Structures*. Journal of Fluid Mechanics, Vol. 204, pp. 295 – 324.

[75] Rezende, F.; Chen, X.; Oliveira, A.; Menezes, F.; 2013. *A Comparison of Different Approximations for Computation of Second-order Roll Motions for a FLNG.* OMAE. Nantes, France.

[76] Richter, A.; Dutta, R; 1981. *Wind Forces on Square Sections with Various Corner Radii*. CIDECT Report 9D/84-21.

[77] Rijken, O.; Leverette, S.; 2009. *Field Measurements of Vortex Induced Motions of a Deep Draft Semi-submersible*. OMAE2009-79803, Hawaii, USA.

[78] Rivera, L. A. L.; 2012. *A Study on Parametric Resonances of a TLWP in Close Proximity to a FPSO in Regular*. M.Sc. Thesis. Federal University of Rio de Janeiro (UFRJ), Brazil.

[79] Roddier, D.; Finnigan, T.; Liapis, S.; 2009. *Influence of the Reynolds Number on Spar Vortex Induced Motions (VIM): Multiple Scale Model Test Comparison*. OMAE2009-79991, Hawaii, USA.

[80] Senjanovic, I.; Hadzic, N.; Tomic, M.; 2013. *Formulation of Consistent Nonlinear Restoring Stiffness for Dynamic Analysis of Tension Leg Platform and its Influence on Response.* Marine Structures 30, pp. 1-32.

[81] Shaker, F.; 1975. *Effect of Axial Load on Mode Shapes and Frequencies of Beam*. Tech. Resp. NASA TN D-8109.

[82] Silva, D. F. C.; 2012. *CFD Virtual Testing for Resistance, Wind and Current Loads on a Supply Boat*. OMAE2012-83108, Rio de Janeiro, Brazil.

[83] Simiu, E.; Scanlan, R. H.; 1986. *Wind Effects on Structures: An Introduction to Wind Engineering*. John Wiley & Sons, New York, USA.

[84] Steen, S.; 2012. *Experimental Methods in Marine Hydrodynamics - Lecture notes*, Norwegian University of Science and Technology NTNU, Norway.

[85] Stone, B.; Treu, H.; Wybro, P.; Wu, C.; 2005. *Tender Assisted Drilling on Deepwater Floating Production System*. SNAME Transaction, Vol 113, pp. 418 - 427.

[86] Takagi, M.; Arai. S.; Takezawa, S.; Tanaka, K.; Takarada, N.; 1985. *A Comparison of Methods for Calculating the Motion of a Semi-Submersible*. Ocean Engineering, Vol. 12 No. 1, pp. 45-97.

[87] Tan, J. H. C.; Magee, A.; Kim, J. W.; Teng, Y. J.; Zukni, N. A.; 2013. *CFD Simulation for Vortex Induced Motions of a Multi-Column Floating Platform.* OMAE2013-11117, Nantes, France.

[88] Tan, J. H. C.; Teng, Y.; Magee, A. R.; Ly, B. T.; 2014. *The Effect of Appurtenances on the VIM performance of a TLP for Southeast Asia*. OTC 24871, Kuala Lumpur, Malaysia.

[89] Tark, J. N K.; 2012. *Characteristics of Flow in the Wake Region of a Bluff Vertical Cylinder in The Presence of Wave, Currents and Combined Wave-Current Flows*. Ph.D. Thesis. National University of Singapore, Singapore.

[90] Teigen, P.; Przulj, V.; Younis, B.; 1998. *A CFD Investigation into the Effects of Incidence on Current Loading on Deep-Water TLP*. OMAE98-0523, Lisbon, Portugal.

[91] Teigen, P.; Sclavounos, P.; 2000. *Coupled Slow Drift Oscillations of a Mini-TLP and Barge*. OMAE2000/OSU OFT-4064. Joint Conference Energy for the New Millennium, New Orleans, LA, USA.

[92] Udoh, I. E.; Zou, J.; Vinayan, V.; 2014. *Hydrodynamic Interactions of TLP and TAD Moored in Close Proximity*. Proc. 19th Offshore Symp., Houston, Texas, pp.1-31.

[93] Van Dijk; Magee, A.; Perryman, S.; Gebara, J.; 2003. *Model Test Experience on Vortex Induced Vibrations of Truss Spars*. OTC 15242, Houston, Texas, USA.

[94] Vaz, G.; Waals, O.; Ottens, H.; Fathi, F.; Souef, T.; Kiu, K.; 2009. *Current Affairs: Model Tests, Semi-Empirical Predictions and CFD Computations for Current Coefficients of Semi-Submersibles.* OMAE2009-80216, Honolulu, Hawaii, USA.

[95] Waals, O.; Phadke, A.; Bultema, S.; 2007. *Flow Induced Motion of Multi Column Floaters.* OMAE2007-29539. San Diego, CA, USA.

[96] Xia, J.; Taghipour R.; 2012. *Feasibility of TLP with Tender Assisted Drilling for Northwest Australian Water – A Case Study*. OTC 23247, Houston, Texas, USA.

[97] Xu, X.; Yang, J.; Li, X.; Lu, H.; 2013. *Wave Drift Forces on Three Barges Arranged Side by Side in Floatover Installation*. OMAE2013-10737. Nantes, France.

[98] Yung, T.; Sandstrom, E.; Slocum, S.; Ding, Z.; Lokken, R.; 2004. *Advancement of SPAR VIV Prediction*. OTC 16343, Houston, TX, USA.

[99] Zdravkovich, M. M.; 2003. *Flow around circular cylinders - Vol 2: Applications*. London, UK, Oxford University Press.

Appendix A

Rather than limiting the analysis to six degrees of freedom for each floating body, modal analysis of the TLP tendons and TAD moored lines were performed. Three cases were analyzed: TLP alone, TAD alone and TLP-TAD connected by the hawser system presented in Section 3.3. For the TLP alone, tendon mode shapes were calculated analytically with the formulations described below.

Eqn. (A.1) gives the natural frequencies $f_{n_{TRANS}}$ of the transversal n-th shape mode of tensioned beams. This equation [81] originally developed for dry tensioned beams, was modified to include the added mass term.

$$f_{n_{TRANS}} = \frac{n^2 \cdot \pi}{2 \cdot L^2} \sqrt{1 + \frac{T \cdot L}{E \cdot I \cdot n^2 \cdot \pi^2}} \sqrt{\frac{E \cdot I}{M + A}} \tag{A.1}$$

where n is the n-th shape mode, L is the tendon length, T is the pre-tension in the tendons, E is the Young modulus of the tendons, M is the tendon mass per unit length, A is the added mass per unit length that Eqn. (A.2) approximates, and I is the area moment of inertia calculated with Eqn. (A.3).

$$A = \rho \cdot \pi \cdot \left(\frac{OD}{2}\right)^2 \tag{A.2}$$

$$I = \frac{\pi}{64} \cdot (OD^4 - ID^4) \tag{A.3}$$

where OD and ID are the outer and inner diameters, respectively.

The numerical results were calculated using Orcaflex software. For the TAD alone and TLP-TAD multi-body system, only the numerical approach was used. Figure A.1 presents the natural periods of the first 20 modes of the TLP tendons and TAD moored lines.

Note that, the T-Analytical and T-FEM curves are the results of the TLP tendons analysis, all the tendons present the same behavior. The MR1-FEM, MR2-FEM, MR3-FEM, and MR4-FEM curves are the results of the analysis of the TAD moored lines.

Figure A.2 presents the results for the TLP-TAD coupled system. The T1, T2, T3 and T4 curves represent the results for the TLP tendons. Note that, tendons that are symmetrical about XZ- plane

have the same behavior. The MR1, MR2, MR3 and MR4 curves present the results for the TAD moored lines.

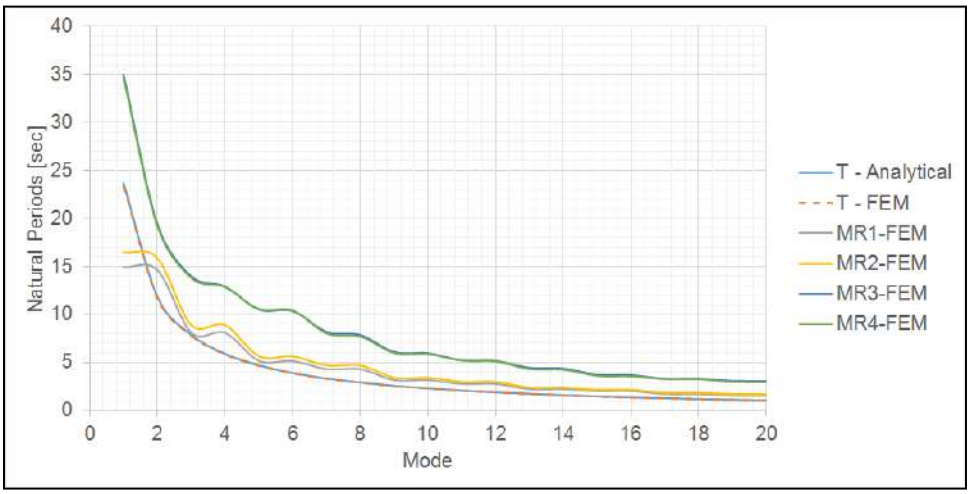

Figure A.1 Natural periods of the mode shapes of the TLP tendons and TAD moored lines.

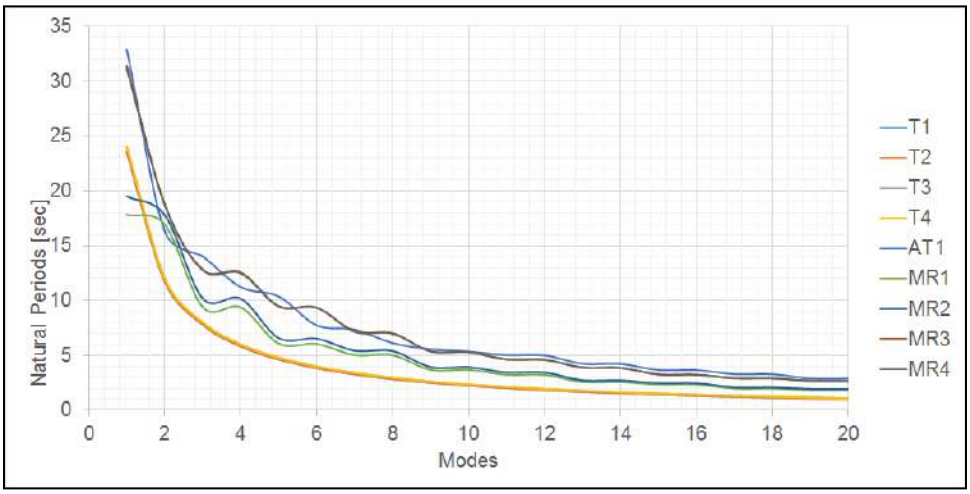

Figure A.2 Natural periods of the mode shapes of TLP tendons and TAD moored lines when the TLP and TAD are connected.

From these results, the following conclusions are reached:

- Numerical and analytical approaches present similar results. Moreover, the natural periods of the mode shapes for the TLP tendons present the same values for TLP alone and coupled TLP-TAD cases.

- The natural periods of the mode shapes of the TAD moored lines are slightly higher when the TAD is connected to the TLP.
- The range of the natural periods of the mode shapes of the TLP tendons and moored lines includes typical frequencies of random seas. However, the wave loads on moored lines are relatively small and affect only the section close to the free surface.
- Tendons and moored lines typically undergo current loads, and they are susceptible to vortex resonance (i.e., VIV). A structure develops vortex resonance if its natural frequency coincides with the vortex-shedding frequency given by Eqn. (A.4).

$$f_S = \frac{St \cdot V}{D} \tag{A.4}$$

where St is the Strouhal number. Typically, the value of St is assumed to be 0.2 for a circular cylinder, V is the free stream current velocity, and D is the structure diameter. Figure A.3 presents the vortex-shedding period for the TLP tendons and TAD moored lines, considering a uniform velocity profile.

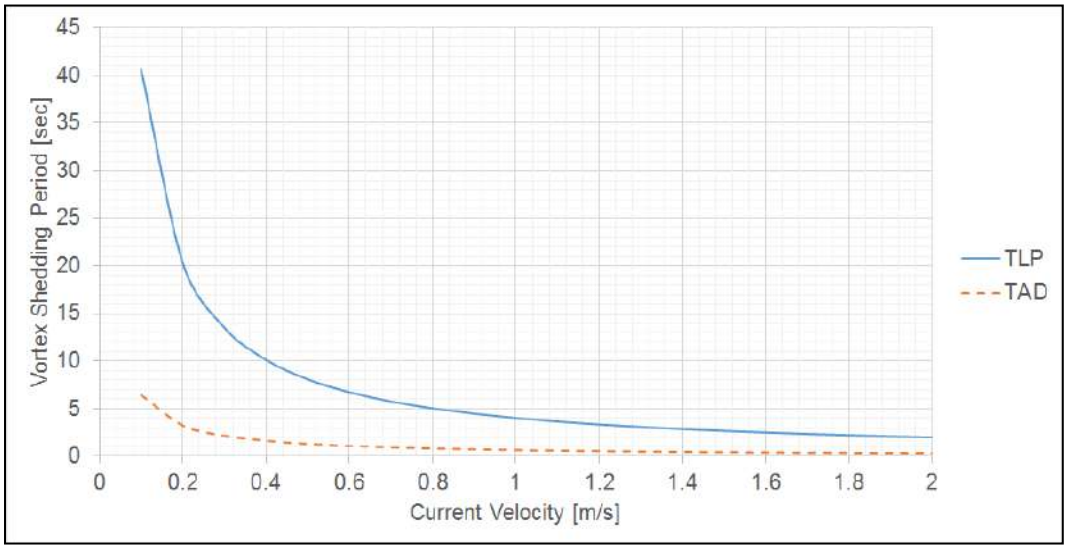

Figure A.3 vortex-shedding period for TLP tendons and TAD moored lines

Although this analysis contains important assumptions, it shows that the TLP tendons and, to a lesser degree, the TAD moored lines are susceptible to VIV. This problem requires a deeper analysis that is nevertheless outside of the scope of the present work.

Appendix B

In addition to the experimental tests described in Chapters V, VI and VII, decay tests were performed for the TLP and TAD unit for single-body cases to investigate the viscous damping.

From the recorded motion decay curves, the natural period and damping coefficients were derived. Two approximations to calculate the damping coefficients were considering, the linear damping method and the nonlinear damping method. Eqns. (B.1) and (B.2) present the analytical models considered in the analysis. Details of how to calculate the coefficients B, B_1 and B_2 can be found elsewhere [84].

$$A\ddot{x} + B\dot{x} + Cx = 0 \tag{B.1}$$

$$A\ddot{x} + B_1\dot{x} + B_2|x|x + Cx = 0 \tag{B.2}$$

Figure B.1 (A) presents the results of the decay test for Sway of the TLP. In addition, the results of both approximations are depicted together.

Despite some small differences, it is clear that the nonlinear damping is more consistent with the experimental data. Linear damping presents satisfactory results; however, some significant differences are observed in the range of [50 – 75] sec.

Figure B.1 (B) presents the results of the decay test for Yaw of the TLP. In this case, it is evident that the differences between the two analytical approaches are slight and that both provide excellent results. Figure B.2 presents the results of the decay test for Heave and Roll of the TAD. In the case of Heave, either linear or quadratic coefficients satisfactory agreement with the experimental values. In the case of Roll, the nonlinear model provides accurate results.

In summary, although the nonlinear damping method presents excellent results, requires further calculations and careful analysis to achieve the correct values of the coefficients $B_1$and B_2. The linear damping method seems to have reasonable accuracy, and it requires a simple analysis of the time series. Table B.1 presents the values of linear damping approximated from the experimental values for the 6 degrees of freedom of the TLP and TAD.

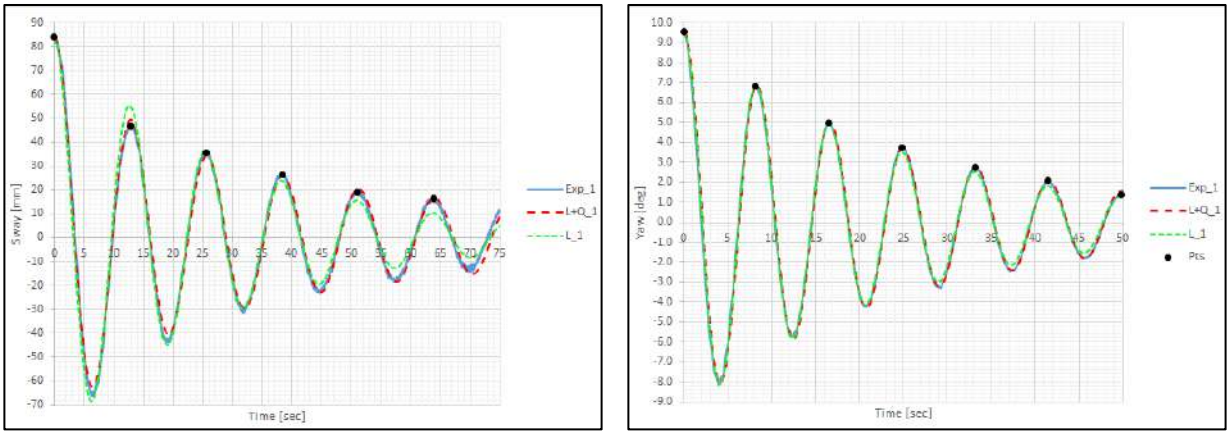

(A) (B)

Figure B.1 Decay tests for the TLP (A) Sway (B) Yaw.

Experimental results vs. linear and nonlinear damping approximations

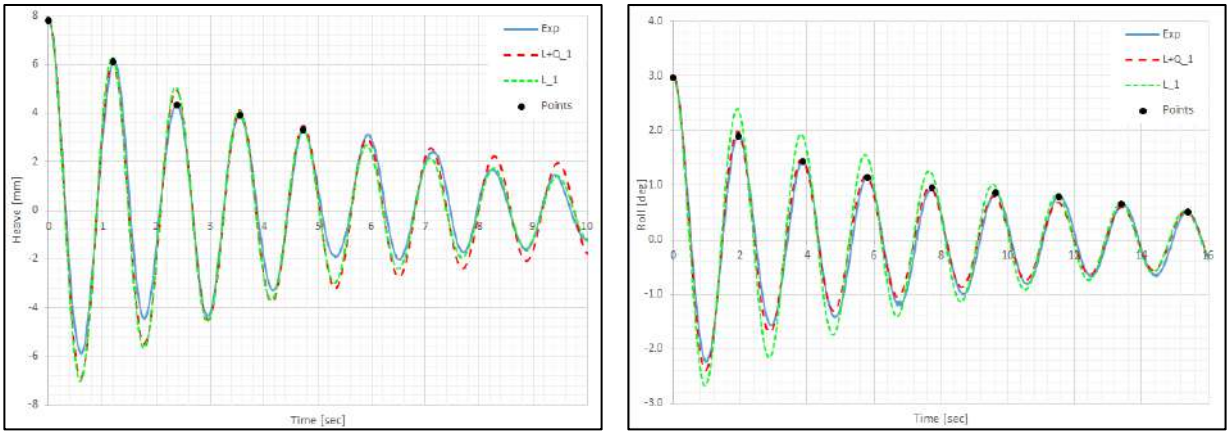

(A) (B)

Figure B.2 Decay tests of the TAD for (A) Heave (B) Roll.

Experimental results vs. linear and nonlinear damping approximations

Table B.1 Linear damping values approximated from experimental decay tests.

Mode	TLP	TAD
Surge	6.65%	7.10%
Sway	6.49%	6.20%
Heave	3.17%	3.40%
Roll	3.92%	3.35%
Pitch	4.12%	2.51%
Yaw	5.89%	3.74%

Appendix C

Figure C.1 Ultra-reduced scale model of the TLP.

Figure C.2 Ultra-reduced scale model of the TAD.

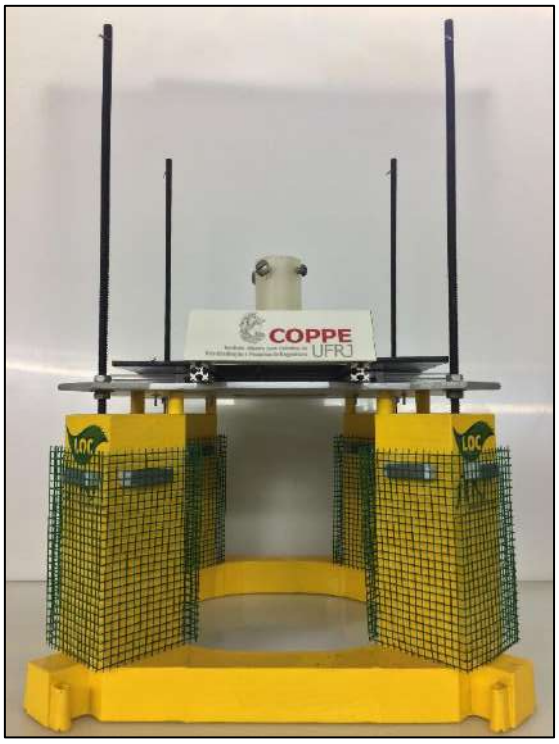

Shroud with square holes

Shroud with diamond holes

Helicoidal strakes

Spoiler plates

Figure C.3 VIM Mitigation devices for the TLP.

Figure C.4 Current load tests for the TAD in single-body case.

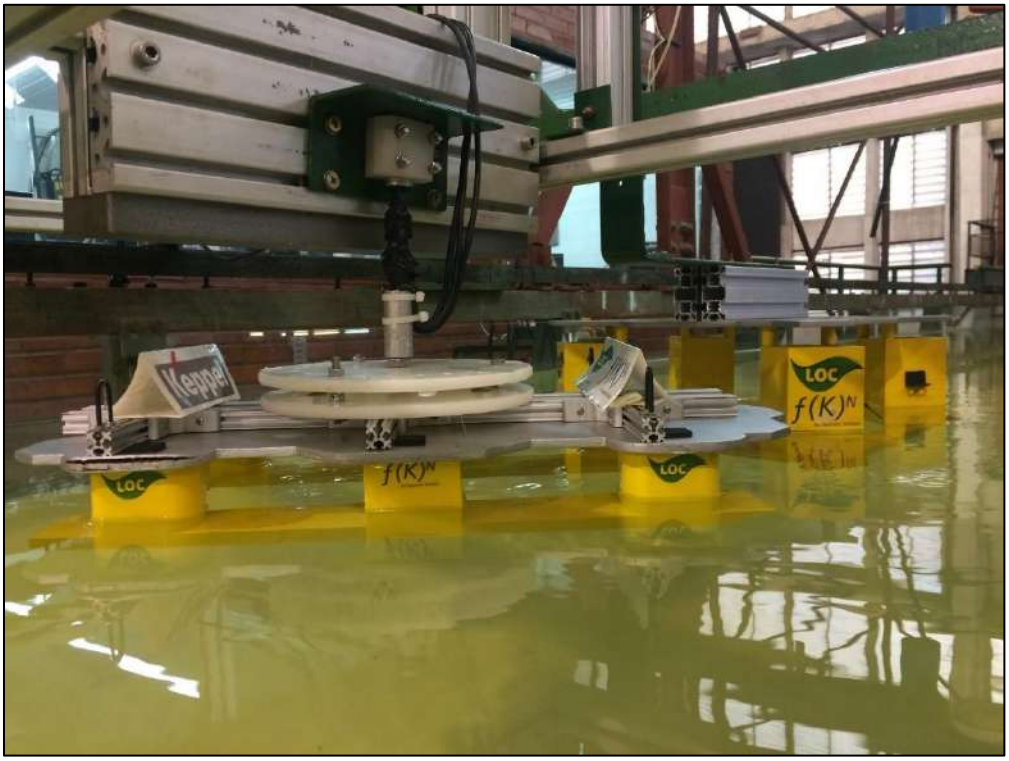

Figure C.5 Current load tests for the TAD Upstream in multi-body case.

Figure C.6 VIM test of the TLP.

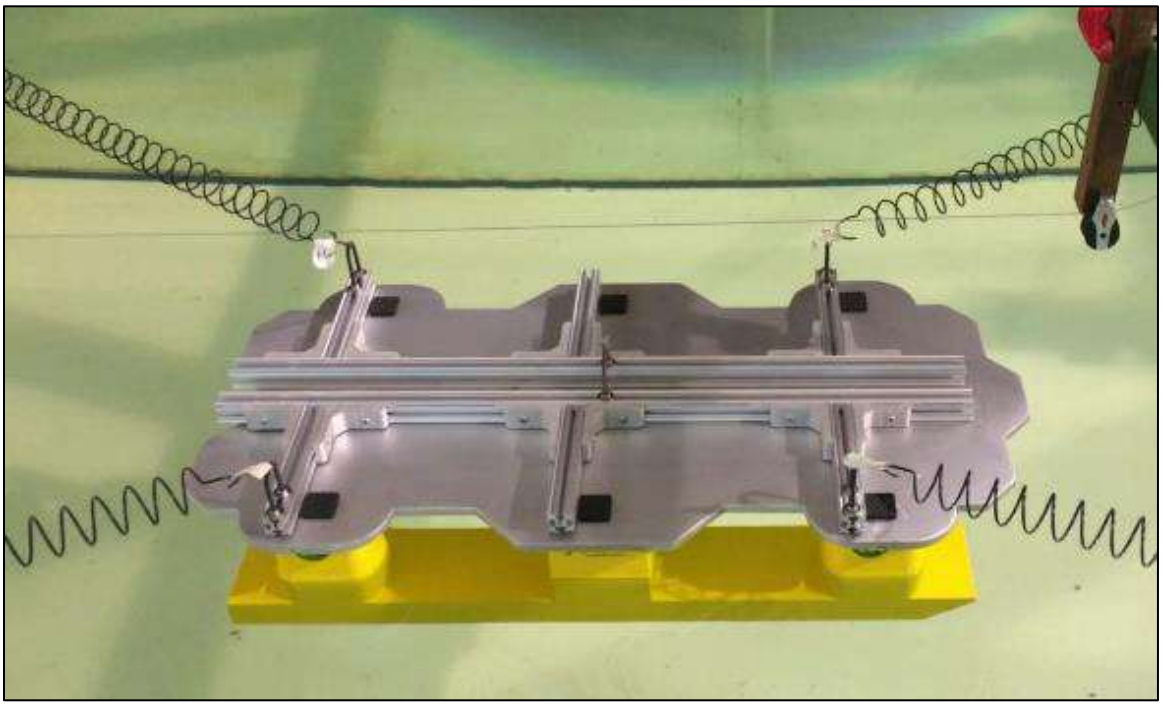

Figure C.7 VIM test of the TAD.

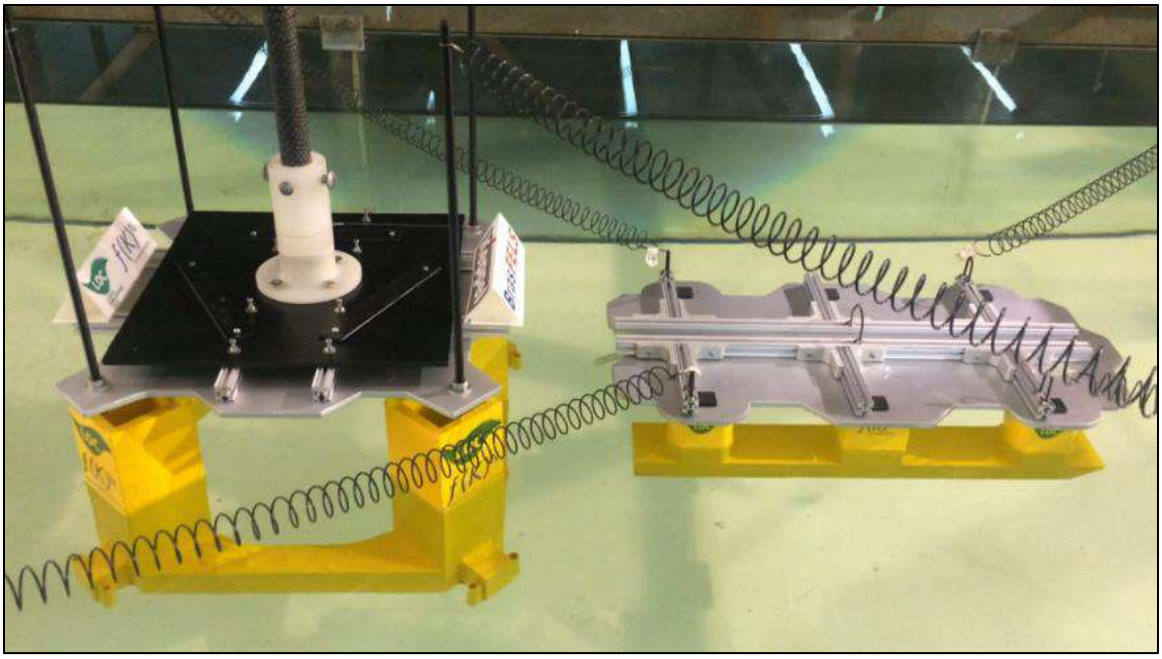

Figure C.8 VIM test of the TLP and TAD without a connection.

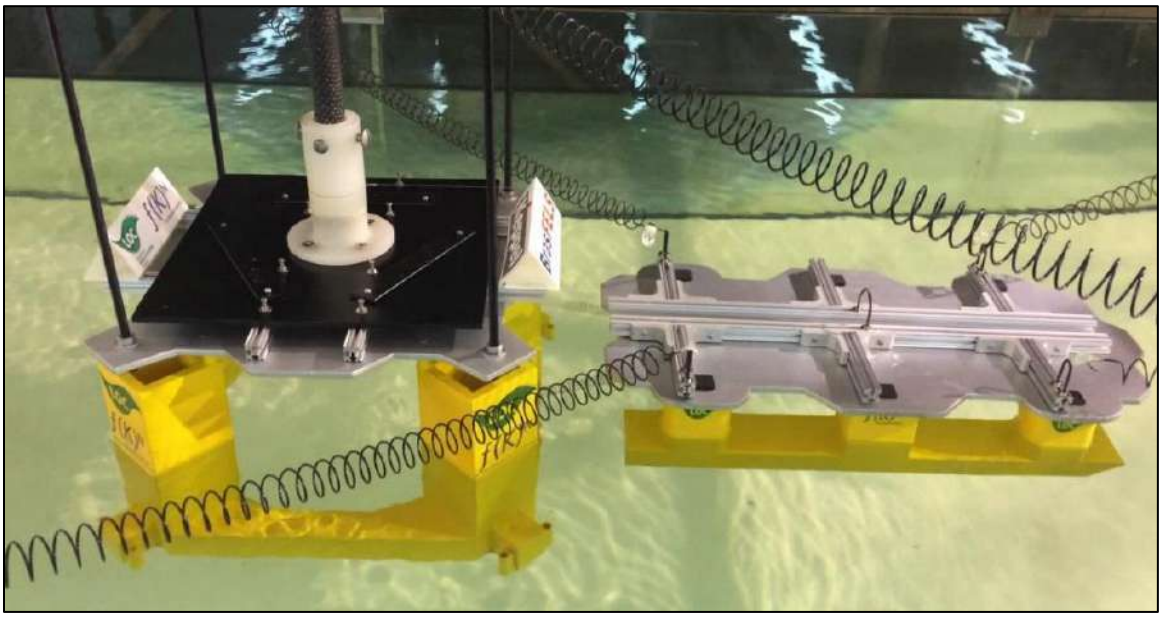

Figure C.9 VIM test of the TLP and TAD with a hawser system.